University of Glasgow

A Portable Metabolomics-on-CMOS Platform for Point-of-Care Testing

Valerio Francesco Annese

A Thesis submitted to

James Watt School of Engineering

University of Glasgow

in fulfilment of the requirements for the degree of

Doctor of Philosophy

February 2021

Abstract

Metabolomics is the study of the metabolites, small molecules produced during the metabolism. Metabolite levels mirror the health status of an individual and therefore have enormous potential in medical point-of-care (POC) applications. POC platforms are miniaturised and portable systems integrating all steps from sample collection to result of a medical test. POC devices offer the possibility to reduce the diagnostic costs, shorten the testing time, and, ultimately, save lives for several applications. The glucose meter, arguably the most successful example of metabolomics POC platform, has already demonstrated the dramatic impact that such platforms can have on the society. Nevertheless, other relevant metabolomic tests are still relegated to centralised laboratories and bulky equipment.

In this work, a metabolomics POC platform for multi-metabolite quantification was developed. The platform aims to untap metabolomics for the general population. As case studies, the platform was designed and evaluated for prostate cancer and ischemic stroke. For prostate cancer, new affordable diagnostic tools to be used in conjunction with the current clinical standard have are needed to reduce the medical costs due to overdiagnosis and increase the survival rate. Thus, a novel potential metabolic test based on L-type amino acids (LAA) profile, glutamate, choline, and sarcosine blood concentrations was developed. For ischemic stroke, where the portable and rapid test can make a difference between life and death, lactate and creatinine blood levels were chosen as potential biomarkers. All the target metabolites were quantified using an optical method (colorimetry).

The platform is composed of three units: the cartridge, the reader, and the graphical user interface (GUI). The cartridge is the core of the platform. It integrates a CMOS 16x16 array of photodiodes, capillary microfluidics, and biological receptors onto the same ceramic package. To measure multiple metabolites, a novel method involving a combination of replica moulding and injection moulding was developed for the monolithic integration of microfluidics onto integrated chips.

The reader is composed of a custom PCB and a microcontroller board. It is used for addressing, data digitisation and data transfer to the GUI. The GUI - a software running on a portable electronic device - is used for interfacing the system, visualise, acquire, process, and store the data.

The analysis of the microfluidic structures showed successful integration. The selection of the specific chemistry for detecting the analytes of interest was demonstrated to be suitable

for the performance of the sensors. Quick and reliably capillary flow of human plasma, serum and blood was demonstrated.

On-chip quantification of the target metabolites was demonstrated in diluted human serum and human plasma. Calibration curves, kinetics parameter and other relevant metrics were determined. For all the metabolites, the limits of detection were lower than the physiological range, demonstrating the capability of the platform to be used in the target applications.

Multi-metabolite testing capability was also demonstrated using commercially and clinically sourced human plasma. For multiplexed assays, reagents were preloaded in the microfluidic channel and lyophilised. Lyophilisation also improved the shelf-life of the reagents. Alternative configurations, involving the use of paper microfluidics, integration of passive blood filter and use of whole blood, were investigated.

The chracterisation of the platform culminated with a clinical evaluation for both the target applications. The same platform with minimal modification of the cartridge was able to provide clinically relevant information for both the distinct applications, highlighting the versatility of the platform for POC determination of metabolic biomarkers.

For prostate cancer, the platform was used for the quantification of the potential metabolic biomarker in 10 healthy samples and 16 patients affected by prostate cancer. LAA, glutamate and choline average concentrations were elevated in the cancer group with respect to the control group and were therefore regarded as metabolic biomarkers in this population. Metabolomic profiles were used to train a classifier algorithm, which improved the performance of the current clinical blood test, for this population.

For ischemic stroke, lactate determination was performed in clinically sourced samples. Clinical evaluation for ischemic stroke was performed using 10 samples from people diagnosed with ischemic stroke. Results showed that the developed platform provided comparable results with an NHS-based gold standard method in this population. This comparison demonstrated the potential of the platform for its on-the-spot use.

The developed platform has the potential to lead the way to a new generation of low-cost and rapid POC devices for the early and improved diagnosis of deadly diseases.

Author's declaration

Unless otherwise acknowledged, the content of this thesis is the result of my own work. None of this material has been submitted for any other degree at the University of Glasgow or any other institution.

Valerio Francesco Annese

Acknowledgements

This doctoral degree has been a life-changing experience, a long journey which would not have been possible without the support of many people. My gratitude cannot be expressed in these few lines, but I will give it a try.

First, I would like to recognize the invaluable guidance that my supervisor, Professor David Cumming, provided me during my study. His expertise and support were vital in inspiring me to think outside the box, from multiple perspectives to form a unique creative process. I would also like to pay my special regards to my second supervisors, Michael Barrett and Samadhan Patil, for their insight and assistance regarding metabolomics.

I'd also like to extend my wholehearted gratitude to all members, current and previous, of the Microsystem Technology Group. In particular, thanks to my dear friends Gianluca Melino and Claudio Accarino for making me feel at home. Thanks to James Grant for his encouragement, invaluable contribution, and practical suggestions for aspects of the work regarding fabrication and wire-bonding. Thanks to Srinivas Velugotla, Boon Cheah and Yash Shah which helped me navigate the topic at the beginning of my degree. Thanks to Christos Giagkoulovits, Mohammed Al-Rawhani and James Beeley for their support regarding the technical details of the chip. Thanks to Samadhan Patil, Chunxiao Hu, Ana-Maria Nastase and Andreea Stroia for their advice, guidance and laboratory space when performing biological experiments. Thanks to Ivonne Escorcia Carranza, Mitch Kenney, Vincenzo Pusino, Yasaman Alimi for your chats which helped me get through the journey. I am also indebted to who actively contributed to this thesis. Thanks to all of you for having welcomed me in this academic family. Without you, this journey would not have been the same.

The interdisciplinary nature of the project allowed me also to work in different environments, where I always found amicable and helpful people. I wish to express my deepest gratitude to staff and users of the James Watt Nanofabrication Centre, the Glasgow Laboratory for Advanced Detector Development, the laboratory in the Glasgow Biomedical Research Centre, the Beatson Institute for Cancer Research and the West Glasgow Ambulatory Care Hospital.

I wish to show my gratitude to the Engineering and Physical Sciences Research Council (EPSRC) for the financial support to this work.

I also wish to express my gratitude to all the people whose assistance was a milestone in the completion of this project.

Besides my academic life, I am incredibly grateful to my half, Martina, which is probably the only one which knows all the shades of this journey. We both started this journey, having only each other and a 20 kg piece of luggage. I know it has not been easy for her too, and I will always be grateful for being everything I could ever ask for. Thanks for being in my life.

I would also like to express my deepest gratitude to my parents and my brothers, for their endless love and support throughout my whole life. I would have never achieved my goals without your help.

I'd like to extend my thanks to my whole family, including grandparents, uncles and cousins, for being just the way they are.

I would also like to thank all my friends who have wished me well and believe in me.

Thanks to the University of Glasgow, Scotland, the Highlands, the castles, the sceneries, and landscapes, which I will always bring with me.

Thanks immensely to all of you,

Valerio

Outcomes of the Research Activity

My activity during my PhD research project led to the following outcomes:

Spin-out company (1)

The findings of this PhD research project have contributed to the creation of a spin-out company 'Multicorder DX Limited', of which I am co-founder and shareholder.
Multicorder DX has exclusive rights from the University of Glasgow to a portfolio of intellectual property that underpin this project. This portfolio comprises three pending patent applications and soft intellectual property on the design of several multimodal CMOS chips.

Filed patent (1)

A patent was filed on 08 April 2020 (application number: GB2005170.2) entitled 'Apparatus and method for biomarker detection'. The patent is mainly based on my research activity.

Publications in international journals (7)

1. **V.F. Annese**, S.B. Patil, C. Hu, C. Giagkoulovits, M. A. Al-Rawhani, J. Grant, M. Macleod, D.J. Clayton, L.M. Heaney, R. Daly, C. Accarino, Y.D. Shah, B.C. Cheah, J. Beeley, T.R.J Evans, R. Jones, M.P. Barrett, D.R.S. Cumming. 'A monolithic single-chip point-of-care platform for metabolomic prostate cancer detection'. Microsystems and Nanoengineering. In print.
2. C. Accarino*****, **V.F. Annese***, B.C. Cheah, M.A. Al-Rawhani, Y.D. Shah, J. Beeley, C. Giagkoulovitis, S. Mitra, and D.R.S Cumming. "Noise characteristics with CMOS sensor array scaling." Measurement 152 (2020): 107325. ***both authors contributed equally to this work.**
3. C. Hu, **V.F. Annese**, S. Velugotla, M. A. Al-Rawhani, B.C. Cheah, J. Grant, M. Barrett, and D.R.S. Cumming. "Disposable Paper-on-CMOS Platform for Real-time Simultaneous Detection of Metabolites." IEEE Transactions on Biomedical Engineering (2020).
4. C. Accarino, G. Melino, **V.F. Annese**, M.A. Al-Rawhani, Y.D. Shah, D. Maneuski, C. Giagkoulovits, J.P. Grant, S. Mitra, C. Buttar, D.R.S. Cumming. "A 64x64 SPAD Array

for Portable Colorimetric Sensing, Fluorescence and X-Ray Imaging". *IEEE Sensors Journal* (2019).

5. M.A. Al-Rawhani, C. Hu, C. Giagkoulovits, **V.F. Annese**, B.C. Cheah, J. Beeley, S. Velugotla, C. Accarino, J.P. Grant, S. Mitra, M.P. Barrett, S. Cochran, D.R.S. Cumming. "Multimodal integrated sensor platform for rapid biomarker detection." IEEE Transactions on Biomedical Engineering (2019).
6. G. Melino, C. Accarino, M. Riehle, M. Potter, P. Fineron, **V.F. Annese**, J. P. Grant, M. Al-Rawhani, J. Beeley, I.E. Carranza, and D.R.S Cumming, "Capsule endoscopy compatible fluorescence imager demonstrated using bowel cancer tumours." IEEE Sensors Journal (2020).
7. Y.D. Shah, J.P. Grant, P.W.R. Connolly, D. Hao, C. Accarino, X. Ren, M. Kenney, **V.F. Annese**, M.A. Al-Rahwani, K.G. Rew, Z.M. Greener, Y. Altmann, D. Faccio, G.S. Buller and D.R.S. Cumming. 'Ultralow light level color image reconstruction using high- efficiency plasmonic metasurface mosaic filters'. Optica.

Papers to be submitted in international journals (1)

1. S.B. Patil, **V.F. Annese**, C. Delles, P. Welsh, J. Dawson, M.P. Barrett and D.R.S. Cumming, "Testing utility of Multicorder: a CMOS based handheld platform to screen the stroke samples for the inflammation and kidney injury" to be submitted to PNAS, PLOS or Point of Care.

Book chapters (1)

1. S.B. Patil, **V.F. Annese**, D.R.S. Cumming. Commercial Aspects of Biosensors for Diagnostics and Environmental Monitoring. 2019. In Advances in Nanosensors for Biological and Environmental Analysis (pp. 133-142). Elsevier.

Publication in conference proceedings (1)

1. **V.F. Annese**, C. Hu, C. Accarino, C. Giagkoulovits, S.B. Patil, M.A. Al-Rawhani, J. Beeley, B.C. Cheah, S. Velugotla, J.P. Grant, and D.R.S. Cumming. The Multicorder: A Handheld Multimodal Metabolomics-on-CMOS Sensing Platform. 2019, June. In 2019 IEEE 8th International Workshop on Advances in Sensors and Interfaces (IWASI) (pp. 130-135).

Oral presentations (2)

1. **V.F. Annese** and D.R.S. Cumming. 'Development and clinical testing of a metabolomics-on-CMOS platform for prostate cancer'. Presented at 'Electronic and Nanoscale Engineering (ENE) away day'. 31 May 2019. The Lighthouse, Glasgow, UK. Best PhD student presentation award.
2. **V.F. Annese**, C. Hu, C. Accarino, C. Giagkoulovits, S.B. Patil, M.A. Al-Rawhani, J. Beeley, B.C. Cheah, S. Velugotla, J.P. Grant, and D.R.S. Cumming. The Multicorder: A Handheld Multimodal Metabolomics-on-CMOS Sensing Platform. 2019, June. In 2019 IEEE 8th International Workshop on Advances in Sensors and Interfaces (IWASI) (pp. 130-135).

Poster presentations (4)

1. **V.F Annese** and D.R.S. Cumming. 'Integration of microfluidics with CMOS technology for multi-metabolite sensing'. Poster presented at 'Electronic and Nanoscale Engineering (ENE) away day'. 18 June 2018. The Lighthouse, Glasgow, UK.
2. **V.F. Annese**, S.B. Patil and D.R.S. Cumming. 'CMOS/microfluidics hybrid microsystem for multiple metabolites sensing'. Poster presented at 'MegaMeet, the EPSRC Healthcare Technologies Conference'. 18 April 2018. The Playfair library hall, Old College, Edinburgh, UK.
3. **V.F. Annese**, S.B. Patil and D.R.S. Cumming. 'CMOS/microfluidics hybrid microsystem for multiple metabolites sensing'. Poster presented at 'Multicorder IAB Meeting', 2018. University of Glasgow, Glasgow, UK.
4. **V.F. Annese**, S.B. Patil and D.R.S. Cumming. 'Drop-on-demand inkjet printing for enzyme printing'. Poster presented at 'Multicorder IAB Meeting', 2017. University of Glasgow, Glasgow, UK.

Workshops (1)

1. 'Sensorthon' in partnership with Sensor City. 28 November 2019. The Royal Liverpool Hospital, Liverpool.

Table of Contents

List of Acronyms

4AAP	4-aminoantipyrine
ADC	Analog-to-digital converter
APD	Avalanche photodiode
ATP	Adenosine triphosphate
AUC	Area under the curve
CCD	Charge-coupled device
ChOx	Choline oxidase
CMOS	Complementary-MOS
CNN	Creatininase
CPGA	Ceramic Pin Grid Array
CTN	Creatinase
CVD	Cardiovascular disease
DI	Deionised
DNA	Deoxyribonucleic acid
ELISA	Enzyme-linked immunosorbent assay
FDA	Food and drug administration
FN	False negatives
FoM	Figure of merit
FP	False positives
FPN	Fixed pattern noise
Fps	Frames per second
FWHM	Full width half maximum
GC-MS	Gas chromatography MS
GDh	Glucose dehydrogenase
GlOx	Glutamate oxidase
Gox	Glucose oxidase
GP	General practice
GPIO	General-purpose input-output
GUI	Graphical user interface
HCl	Hydrochloric acid
HDL	High-density lipoprotein
HIV	Human immunodeficiency virus
HRP	Horseradish peroxidase
I/O	Input/output
IC	Integrated circuit
ICU	Intensive care unit
ID	Identification
IPA	Isopropyl alcohol
ISFET	Ion-sensitive field-effect transistor
IUPAC	International Union of Pure and Applied Chemistry
JWNC	James Watt Nanofabrication Centre
K2EDTA	Dipotassium ethylenediaminetetraacetic acid
KNN	K-nearest neighbours
LAA	L-amino acid
LAAOx	LAA oxidase
LaOx	Lactate oxidase
LC	Liquid chromatography
LDL	Low-density lipoprotein
LED	Light emitting diode
LFA	Lateral flow assay
LOD	Limit of detection

LOQ	Limit of quantification
LSB	Least significant bit
MEMS	Microelectromechanical system
MIS	Metal-insulator-semiconductor
MOSFET	Metal-oxide-semiconductor field effect transistor
MS	Mass spectroscopy
MSB	Most significant bit
MST	Microsystem technology
NAD	Nicotinamide adenine dinucleotide
NEMS	Nanoelectromechanical system
NEP	Noise equivalent power
NHS	National Health Service
NMOS	N-type MOS
NMR	Nuclear magnetic resonance
OXPHOS	Oxidative phosphorylation
PBS	Phosphate-buffered saline
PC	Personal computer
PCa	Prostate cancer
PCA	Principal Component Analysis
PCB	Printed circuit board
PDMS	Polydimethylsiloxane
PMMA	Poly(methyl methacrylate)
PMOS	P-type MOS
POC	Point-of-care
PPP	Pentose phosphate pathway
PSA	Prostate-specific antigen
PVA	Polyvinyl alcohol
RMSE	Root mean square error
RNA	Ribonucleic acid
ROC	Receiver operating characteristic curve
SaOx	Sarcosine oxidase
Sn	Sensitivity
SNR	Signal to noise ratio
Sp	Specificity
SPAD	Single-photon avalanche diode
SSE	Sum of squares error
SVM	Support Vector Machine
TCA	Krebs cycle
TCP/IP	Internet protocol suite
TN	True negative
TNR	True negative rate
TP	True positives
TPR	True positive rate
UART	Universal Asynchronous Receiver/Transmitter
UPLC-MS/MS	Ultra-performance liquid chromatography-tandem mass spectrometry
USB	Universal serial bus
UV	Ultraviolet
ZIF	Zero insertion force

Chapter 1: Introduction to the Research Project

1.1. Motivations

Point-of-care (POC) technology refers to all the miniaturised, portable, automatised devices capable of providing healthcare close to or near the patient [1]. In practice, POC platforms are portable diagnostic devices that can be operated by the general population in any location, including home, ambulance, hospitals, critical care facilities and remote locations. POC testing is a new emerging healthcare model. Nowadays, the most commonly used approach for testing in healthcare throughout the world is the centralised laboratory [1]. Typically, samples are collected by trained personnel from various locations, including general practice surgeries and hospitals. Samples are then transferred to a laboratory where they are analysed by trained personnel. Results are then communicated to the patient.

The use of POC devices simplifies the process of sample testing by providing an on-the-spot sample-to-answer test in a few minutes. POC provides results rapidly thereby saving time that would be spent with samples being transferred to the laboratory. There is no need to wait for a trained personal to run the tests and thus the results do not need to be transmitted and collected. POC platforms can therefore reduce the response of a test from hours/days to minutes [2]. Table 1.1 illustrates the two different processes in healthcare testing.

The rapidity and portability of POC testing might be more advantageous than laboratory testing in specific applications. The rapidity of POC testing can make a difference between life-or-death for applications requiring immediate availability of diagnostic data, such as sudden and acute medical conditions [2]. For instance, sepsis survival rate improves by 7.6% per hour of earlier diagnosis [3]. For acute cardiovascular events, such as ischemic stroke, early intervention within the so-called golden period (1-2 hours after the event) improves the survival rate by 80% [4].

Table 1.1 Comparison of of traditional testing vs POC testing.

	Traditional testing	**Poin-of-care testing**
Sample collection	Sample is collected by trained personnel in specilised facilities, including general practice, hospital, clinic, critical care.	Sample is collected by the user/carer anywhere, including home, ambulance, remote locations.
Analysis	Sample is analysed in a laboratory by trained personnel. Sample processing might be required.	Sample can be analysed anywhere by the user/carer. Minimal sample processing might be required.
Duration	From sample to answer in hours/days.	From sample to answer in minutes.

The portability of POC platforms has the potential to improve healthcare quality in rural and remote areas [1]. Testing infectious diseases in resource-poor locations, for instance, has the potential to save many lives by providing clinical information for conditions otherwise undiagnosed [1].

The need for rapid, adaptable and low-cost POC testing platform providing reliable and quick results have been outlined in pandemic scenarios [5]. The recent Covid-19 pandemic required population-wide strategies, including mass-testing and contact tracing, both potentially deliverable using POC technologies and challenging to implement when adopting centralised testing [5].

POC technology has the potential to reduce medical costs in some applications. For instance, in the case of prostate cancer (PCa), the widely used prostate-specific antigen (PSA) test, the current standard blood test for diagnosis, has been found to be unreliable. Fewer than one in three men with an elevated PSA will have PCa [6][7]. The high number of misdiagnosis due to PSA unreability can lead to unnecessary medical procedures (e.g. digital rectal examination, biopsy, etc). Besides being painful, invasive, and having the potential to cause complications, PSA downstream tests can be expensive [8], accounting for more than 70% of the medical costs associated with PCa screening. The adoption of a new blood test for PCa, supplementary to the PSA test, has the potential to reduce misdiagnosis, hence costs, and improve quality of health [9]. Candidate metabolic biomarkers have been identified for PCa. POC technology has the potential to enable detection of those candidate metabolomics biomarkers at a lower cost with respect to the equipment traditionally used for these analyses. Besides PCa, candidate metabolic markers have been identified for a variety of diseases. With its unique capability of describing the phenotype of the individual [10], [11], metabolomics - the study of the molecules produced by cells during the metabolism - is considered to have enormous potential in POC testing [12], [13]. While the study of metabolites is widely exploited in pharmacology [14], metabolomics for diagnostics and screening is very much research laboratory-based, mainly because the equipment traditionally employed for metabolomics is bulky and expensive [12], [15].

Metabolomics POC platforms have already demonstrated a dramatic social impact with handheld glucose meters forging 85% of the overall POC market [16]. To date, POC testing devices share a noteworthy market of approximately $21 billion [16]. It is projected that this market will keep growing in the next years, reaching an estimated value of $36 billion by 2025 [16]. North America market may witness the highest growth until 2024, although major

market growth is expected also in Europe, India, and Asia [16]. Currently, the market is dominated by a small number of well-established companies, including Roche, Abbott, Siemens, GE Healthcare and Medtronic [16].

Several limitations and challenges are slowing down the process of widespread of diagnostics POC devices in the market. The main challenges for the development of commercial POC platforms are discussed in the following.

Accuracy vs. Application. When a medical test is performed, the outcome typically yields to a positive (i.e. abnormal) or negative (i.e. normal) result with respect to a certain disease. Ideally, the test should be able to provide a certain and reliable result, with no false positive or negative. However, in practice this is not the case. Thus, the performance of the test is usually quantified by the diagnostic (or clinical) sensitivity, specificity, and accuracy (see Figure 1.1). The diagnostic sensitivity, also referred to as true positive rate (TPR), is the portion of positive samples correctly classified as positives [17] [18]. The diagnostic specificity, also known as true negative rate (TNR), is the portion of negative samples correctly classified as negatives [17] [18]. The diagnostic accuracy is the ratio between the sum of the true positive and negatives over the entire population [17].

The diagnostic capability mainly depends on two factors: the analytical performance of the sensor and the target analyte. Laboratory equipment has typically higher analytical performance than POC devices. This is because POC devices are more inclined to errors, interferences, outliers and device-to-device variability than laboratory equipment because they are operated in a variety of settings [2]. POC platform also uses unprocessed and readily available specimens (i.e. finger-prick blood, saliva, etc) and techquines aiming at reducing the cost of the test. Nevertheless, the POC platform must be capable of delivering satisfactory diagnostic performance with respect to the application.

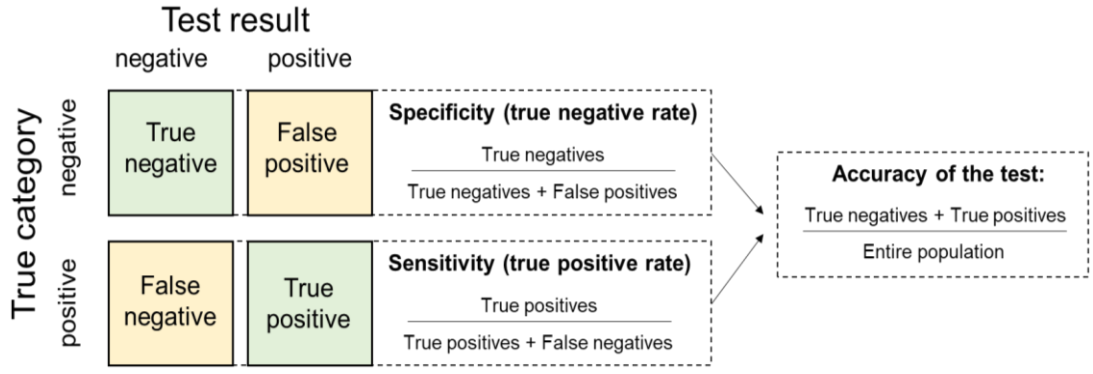

Figure 1.1 Schematic illustration of diagnostic specificity, sensitivity, and accuracy.

Multi-analyte platform. The demand for multi-analyte POC platforms with accuracy suitable for providing clinically relevant information is another relevant challenge in the field of commercial POC testing [1], [2]. Running multiple simultaneous tests can be required for many assays which are unreliable without control measurements. Multi-analyte platforms can also test a panel of biomarkers, enabling the use of classification algorithm and improving the accuracy of the test by performing additional supporting measurements [2]. Lastly, multi-analyte POC platforms are desirable because they avoid the need for manufacturing, use and disposal of several devices [1].

System integration. POC platforms are composed of different subsystems which need to be integrated. Subsystems also include sensors and biological reagents. Although both electronics and biology can rely on robust methods and procedures, their integration for a commercial purpose is still quite challenging. The procedures used for surface functionalisation is usually strongly dependent on the application. Recipes are usually tuned by experimental studies and empirical observation [19]. These limitations are particularly problematic for multi-analyte platforms, where multiple functionalisations of different sensing areas are required [20]. In this case, the procedures involved in the fabrication of the device must avoid crosstalk between different reaction zones [20].

Typically, reagents are biological molecules and it is fundamental to preserve their activity against non-ideal conditions of temperature, pH, humidity and time [2]. This might require strategies for the compensation of any sample-to-sample, test-to-test and device-to-device variability, loss in activity of the reagents, environmental conditions, external noise, transient effects and any other source of variability [2]. Furthermore, the POC should work with no or minimal sample pre-processing [2].

Cost of the platform. The trade-off between the cost of the platform and its frequency of use is another main challenge. The POC platform is required to be affordable by the final user but the affordability is related to its frequency of use. For instance, moder commercial glucose meters cost about £30, with a cost per test as low as £0.50. Glucose meters are used very frequently by the user (more than once a day), hence the very low cost. However, platforms used less frequently have an increased cost on the market. Typically, the reduction of the selling price can be achieved by employing appropriate mass-production strategies. However, the challenges illustrated above can require strategies which are not suitable for mass-manufacturing [21]. This discussion is addressed in detail in Paragraph 2.6.3.

1.2. Aims and Objectives

This research project is part of the 'Multicorder project' [22], [23], aimed at developing a broad-spectrum sensor platform by integrating several biosensors on a single device to sense the personal metabolome. The Multicorder project aims at developing a personal metabolome machine for precision healthcare. It is supported by the UK Engineering and Physical Sciences Research Council, with Professor David Cumming as the head of the project. Within the Multicorder project, many integrated sensing chips have been developed using the complementary metal-oxide–semiconductor (CMOS) technology.

In this frame, my PhD project consisted of developing and testing a POC platform for the quantification of metabolic biomarkers. The target metabolic biomarkers were detected using a colorimetric approach and were selected for two case studies: PCa and ischemic stroke. The former application aims to demonstrate the potential of a metabolomics based POC platform in a context where new diagnostic tools can improve the current clinical practice in terms of medical costs and survival rate. The latter application aims to show the potential of the device as a rapid diagnostic tool that can make a difference between life or death. The two case studies are intended as a proof-of-concept. The platform has the versatility and capability of adapting to a wide range of biological assays with no or minimal modifications. For the development of the platform, a CMOS chip developed within the Multicorder project, was employed. The CMOS chip integrates a 16x16 array of multi-sensor elements. Each element integrates a photodiode, a single-photon avalanche diode (SPAD) and an ion-sensitive field-effect transistor (ISFET). Only the photodiodes were used in this work. The specific objectives of this PhD project and the contributions for each of the completed task within the project are shown in Table 1.2.

Table 1.2 Table of contributions for this PhD project.

Chapter	Task / Activity	Main investigators
2, 3	Identification of a potential metabolic biomarker panel for prostate cancer	- **Valerio F. Annese** (literature survey) - Prof. Rob Jones[2] (discussion/validation)
2, 3	Identification of a potential metabolic biomarker panel for ischemic stroke	- **Valerio F. Annese** (literature survey) - Dr Samadhan Patil[1] (discussion/validation)
3	Design of the CMOS chip	- Dr Mohammed Al-Rahawani[1] - Dr Christos Giankulovitch[1] - Dr James Beeley[1]
3	Fabrication of the CMOS chip	Outsourced (Austriamicrosystems)
3	Development of the reader (hardware)	- Dr Mohammed Al-Rahawani[1] - Dr Christos Giankulovitch[1] - Dr Claudio Accarino[1]

3	Development of the reader (software)	**- Valerio F. Annese**
3	Development of the graphic user interface	**- Valerio F. Annese**
3	Enzymatic reactions modelling and simulations	**- Valerio F. Annese**
3	Embedded Platform testing	**- Valerio F. Annese**
4	Microfluidics design and modelling	**- Valerio F. Annese**
4	Integration of capillary microfluidics on the CMOS chip	**- Valerio F. Annese**
4	Packaging for multiplexed wet assays	**- Valerio F. Annese**
4	Characterisation of the microfluidic structures	**- Valerio F. Annese**
4	Spectral characterisation of the photodiode array	**- Valerio F. Annese** - Dr Mohammed Al-Rahawani[1] - Dr Christos Giankulovitch[1]
4	Characterisation of the cartridge	**- Valerio F. Annese**
4	Characterisation of sample flow in the microfluidic system	**- Valerio F. Annese**
5	Development of the experimental setup	**- Valerio F. Annese**
5	Assay formulations	- Well established in the literature
5	Assay optimisations for this platform	**- Valerio F. Annese**
5	Characterisation of the platform when measuring PCa-related metabolites in diluted serum	**- Valerio F. Annese**
5	Characterisation of the platform when measuring ischemic stroke-related metabolites in diluted serum	**- Valerio F. Annese**
5	Quantification of the test duration	**- Valerio F. Annese**
5	Reagents printing for microchannel functionalisation	**- Valerio F. Annese**
5	Reagents lyophilisation for microchannel functionalisation	**- Valerio F. Annese**
5	Quantification of the reagents shelf-life after lyophilisation	**- Valerio F. Annese**
5	Multiplexed assays in human plasma	**- Valerio F. Annese**
5	Multiplexed assays with paper microfluidics (2 metabolites)	- Dr Chunxiao Hu[1] (designed the work and performed experiments) - Dr Srinivas Velugotla[1] (developed the paper strips) **- Valerio F. Annese** (developed and applied functionalisation method of the paper strips)
5	Whole blood experiments	**- Valerio F. Annese**
6	Optimisation for clinical evaluation	**- Valerio F. Annese**
6	Clinical evaluation with PCa samples	**- Valerio F. Annese**
6	Clinical evaluation with ischemic stroke samples	**- Valerio F. Annese**
6	Multiplexed assays with PCa samples	**- Valerio F. Annese**
	Affiliation at the time of completion of the task: *[1]Microsystem Technology Group, James Watt School of Engineering, University of Glasgow.* *[2] Institute of Cancer Sciences, University of Glasgow, Beatson West of Scotland Cancer Centre, Glasgow.*	

145

1.3. Platform Requirements

This project aims to develop and characterise a portable metabolomics-on-chip platform for ischemic stroke and PCa. This raises the question: which are the requirements of the platform? This paragraph addresses this question with initial qualitative considerations. Quantitative requirements are then set in the next chapter, alongside the identification of strategies necessary to meet the criteria. Table 1.3 summarises the requirements of the platform developed in this research project.

The general requirements of a POC platform have been illustrated by the World Health Organisation [1], [13]. A POC test is required to be Affordable, Sensitive, Specific, User-friendly, Rapid & Robust, Equipment-free, Delivered [1]. Those specifications are generally referred to as ASSURED requirements [1]. In addition to the ASSURED requirements, there are two requirements specific to this research project: versatility and multi-analyte capabilities.

Affordability means that the platform must have a cost suitable for the general population. As already mentioned, the affordability of the platform depends on its frequency of use. We can assume that a platform designed for daily use should have a lower cost than a platform used, for instance, once a month. Evidence of this assumption is also provided by the cost of the POC platforms on the market.

Sensitivity and specificity are considered top-priority requirements [1]. The level of clinical sensitivity and specificity depend on the application. However, sensitivity and specificity levels similar (or better) than the current clinical standard are expected.

User-friendliness. The POC platform is required to be user-friendly, meaning that a member of the general population should be able to use it with a minimal set of instructions without any previous training. The user-friendly requirement implies that the platform must be easy to use, intuitive and largely automatised.

Rapidity & Robustness. The POC platform is required to provide a rapid result. By comparison with the POC devices currently on the market, we can assume that the test must have a duration in the order of minutes.

The POC platform is required to be robust. The platform must have strategies in place to standardise the measurement and provide reliable and replicable results against device-to-device and sample-to-sample variability. The platform should also recognise when a test is

invalid and have strategies in place to 'fail safely', for example by notifying the user that the result is not trustworthy.

Equipment-free. The POC platform is required to be equipment-free, meaning that the platform must be capable of running the test without any external equipment required. The World Health Organisation also illustrates that the platform must be delivered, meaning that it must be possible to safely transport and ship the platform to the final user.

Versatility. This work is part of a larger vision and employs a sensor platform which integrates additional sensors. Although the metabolomic biomarkers targeted in this work needs to be specific to address the case studies, the developed methods and procedure must apply to a larger variety of detection methods and biomarkers.

Multi-analyte testing. The platform also requires to be capable of multi-analyte testing. Multi-analyte testing means that the platform must have the potential to perform multiple measurements (involving different biomarkers or/and control measurements) within a single test routine.

Table 1.3 Requirements of the platform.

Requirement	**Definition**
Affordability[1]	The platform and the single test must have a cost suitable for the general population (depending on its frequency of use).
Sensitivity[1]	The platform must have the capability of providing clinically relevant measurement (high true positive rate).
Specificity[1]	The platform must be specific for a determined application (high true negative rate).
User-friendly[1]	The general population must be capable of operating the platform with a minimal set of instructions.
Rapid[1]	The platform must provide the result in minutes.
Robust[1]	The platform must have solutions in place to standardise the measurement against device-to-device and sample-to-sample variability. The platform should also be capable of failing safely.
Equipment-free[1]	No external equipment must be necessary to run the test. The platform should be portable, ideally handheld.
Delivered[1]	The platform must be suitable for transport and shipping.
Multi-analyte capability[2]	The platform must be capable of measuring multiple metabolic biomarkers at the same time.
Versatility[2]	The platform should be capable of accommodating several applications with minimal modifications.

[1] Requirement outlined by the World Health Organization.
[2] Requirement for this specific project.

1.4. Thesis Outline

The present thesis work is divided into seven chapters. A flow chart of the research project in Figure 1.2 guides the reader through the thesis. A brief description of the following chapters is also provided below.

Chapter 2 sets the quantitative requirements of the platform. This is achieved by discussing relevant scientific literature and devices on the market. The literature review mainly focuses on five topics, namely enzyme-based biosensors, integrated optical sensors, microfluidics, metabolomics and POC systems.

Chapter 3 describes the development of the embedded platform. All the units composing the platform are singularly analysed, reporting the design and the development stages.

Chapter 4 presents the development and characterisation of microfluidics. It illustrates the properties of the developed microfluidics, the spectral properties of the colorimetric reagents and the characterisation of the sensor array.

Chapter 5 illustrate results related to the quantification of the proposed metabolic biomarkers for both PCa and ischemic stroke in diluted serum using the developed platform. This chapter also demonstrates the capabilities of the platform for simultaneous multi-metabolite quantification.

Chapter 6 presents the clinical evaluation of the platform. Results related to the quantification of the proposed metabolic biomarkers for both PCa and ischemic stroke in clinically sourced samples of human plasma are presented.

Chapter 7 concludes this research work by summarising the main findings and discussing potential future work.

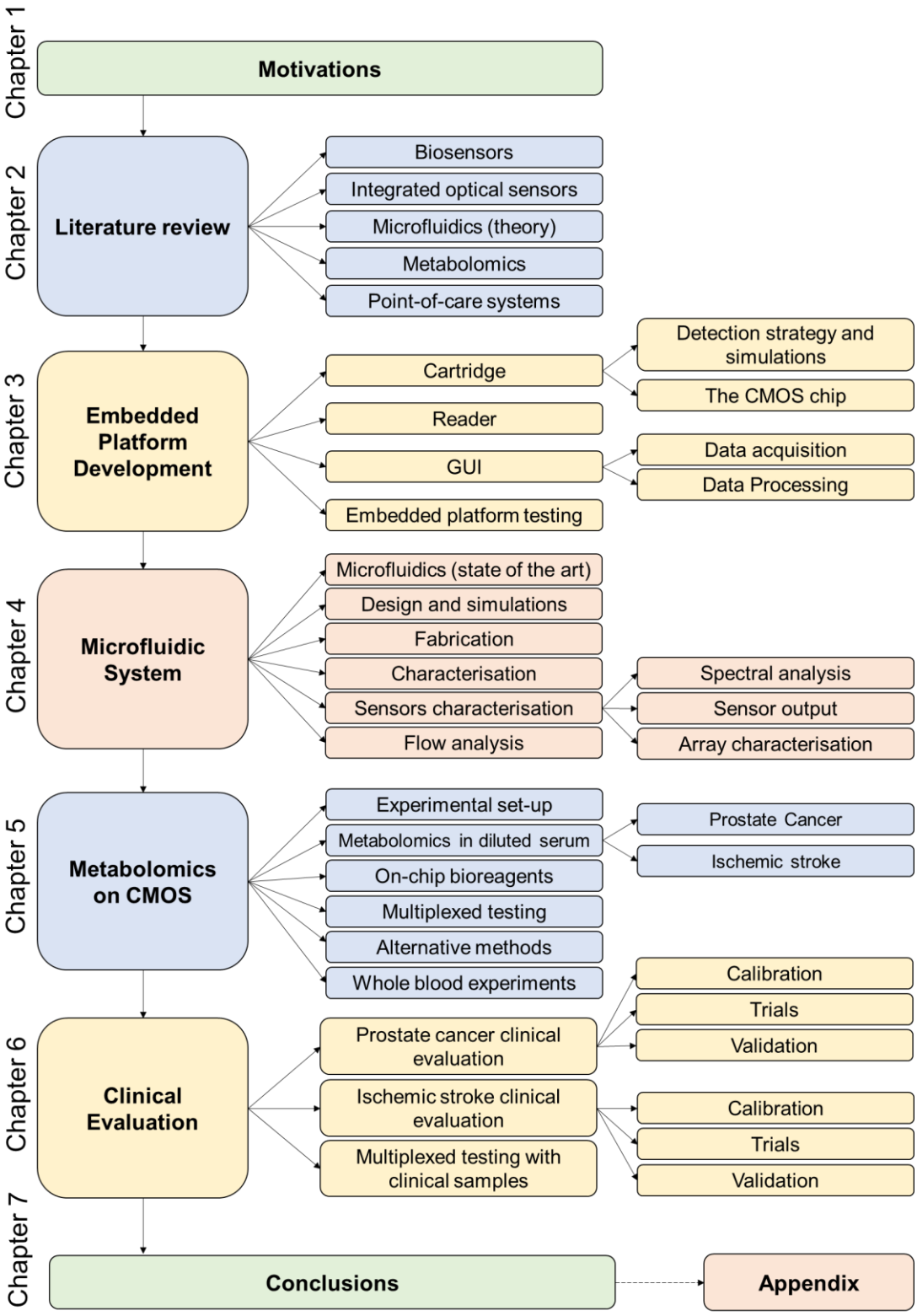

Figure 1.2 Flow chart of the research project.

Chapter 2: Application Background

2.1. Introduction

This chapter aims to set quantitative requirements for the platform. Strategies necessary to address the requirements are also discussed. This is done by providing theoretical knowledge and discussing the relevant state of the art. Table 2.1 recapitulates the objectives and the requirements of this work for ease of reading.

Five main topics are analysed in this chapter. The first theme herein discussed is biosensors. The section is mainly oriented to integrated enzyme-based optical biosensors. The second topic discussed, integrated optical sensors, illustrates the complementary metal-oxide-semiconductor (CMOS) technology, and provides theoretical knowledge on optical sensors. The third theme examined in this chapter is microfluidics. Theoretical knowledge is provided in this chapter. The state of the art and the discussion about its integration with the integrated circuit is discussed in Chapter 4. The fourth aspect herein covered is metabolomics, with a special focus on the case studies of this platform, i.e. PCa and ischemic stroke. The final aspect herein discussed is POC platforms for healthcare. Both experimental and commercial POC apparatuses are discussed, presenting challenges, limitations, and successful examples of the technology.

Table 2.1 Summary of objectives, applications, and requirements of the platform.

Requirement	Definition
Objective	Development and characterisation of a metabolomics-on-CMOS platform
Applications	- Ischemic stroke - Prostate cancer
Requirements	- Affordability - Sensitivity - Specificity - User friendly - Rapid - Robust - Equipment-free - Delivered - Multi-analyte capability - Versatility

2.2. Biosensors

A biosensor is a device that couples one or more molecular recognition elements (biological receptors or reagents) with a transducer to convert a biological response into an electric signal [24]–[26]. A biosensor usually aims to detect or quantify a target substance, namely the analyte, typically restrained into a sample. The reasons for their rapid evolution since the development of the first biosensor by Clark and Lyon in 1962 [27], include the wide range of applications, including defence, healthcare, security, pharmaceuticals, food safety and quality, environmental monitoring [28], and their higher performance if compared to traditional bulky instrumentation regarding specificity, sensitivity, cost, rapidity, multiplicity and portability [28]. As shown in Figure 2.1, a biosensor can be usually divided into the following essential elements [28]:

- *the bioreceptors*, the biological elements that specifically recognise the target analyte;
- *the transducer*, the system capable of converting the physical changes accompanying the interaction between analyte and bioreceptor into a measurable electric signal;
- *the front-end*, an electrical circuit responsible for signal conditioning (amplification, filtering, digitisation) and reading.

The elements mentioned above are mutually connected. The target analyte depends on the application. Nucleic acids, proteins, metabolites, ions, antigens, pollutants are just a few examples of the potential target analyte. Accordingly, the bioreceptor is selected for interacting with the analyte with a high degree of selectivity and specificity. Examples of bioreceptors are enzymes, antibodies, nucleic acids, proteins, aptamers [29]. The transducer is selected for detecting the modification in chemical, biological or physical properties of the sample or the environment induced by its interaction with the organic reagents. Finally, the front-end depends on the specific application and the selected transducer.

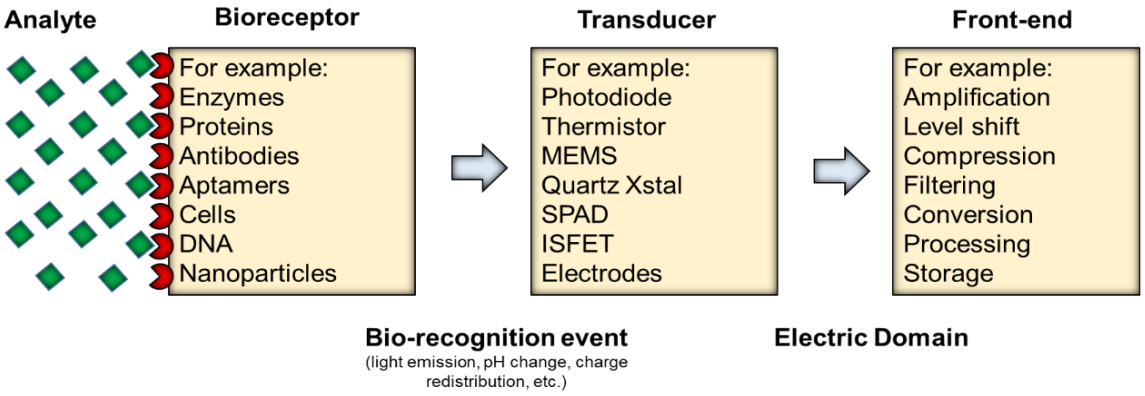

Figure 2.1 Schematisation of a generic biosensor. Reproduced and modified from [30].

2.2.1. Enzyme-based biosensors

The use of biomolecules rather than synthesised molecules as bioreceptor is becoming a priority in modern biotechnology [31]. There are several advantages when using biomolecules. They are usually easier to obtain than synthetic molecules [32], exhibit high specificity and selectivity of binding [28] and can be labelled by fluorescent probes [32]. Knowledge and procedures for biomolecules manipulation are also well-established [32]. Among all types of bio-molecules, enzymes have found widespread use in biosensors because of their inherent specificity, selectivity and catalytic properties [33].

Enzymes are folded chains of amino acids which catalyse specific reactions transforming a substrate into a product by lowering the activation energy of the reaction. This is achieved by inducing transition states with lower free energy, as shown in Figure 2.2 [24], [34].

The model of 'the lock and the key" provides an intuitive explanation of the high selectivity of enzymes [35]. Enzyme and substrate might be conceptualised with complementary geometric shapes that fit precisely into one another. Today, this model has been overcome due to some limitations but intuitively describes the specificity of the binding [36].

According to the Michaelis-Menten theory [24], [34], which illustrates the kinetics of enzyme action, the reaction sequence can be described as:

$$E + S \underset{k_{-1}}{\overset{k_{+1}}{\rightleftarrows}} ES \xrightarrow{k_{+2}} P \qquad (2.1)$$

Where E is the enzyme, S is the substrate, ES is the bound complex, P is the product, k_{+1}, k_{-1} and k_{+2} are the rate constants (typically $k_{+1} > k_{-1}, k_{+2}$) [24]. By calculating the rate equations of the reaction, applying the boundary conditions and after mathematical manipulations reported in [24], it is possible to derive the Michaelis-Menten equation (Figure 2.3):

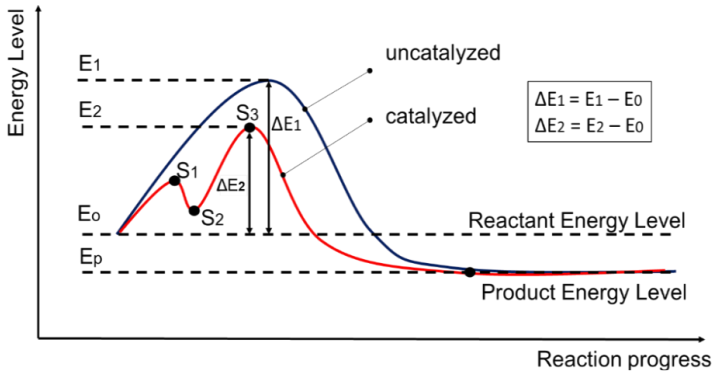

Figure 2.2 Due to the introduction of transition states (S_1, S_2, S_3), the catalysed reaction has lower activation energy than the one of the uncatalysed reaction ($\Delta E_2 < \Delta E_1$). Reproduced and modified from [24].

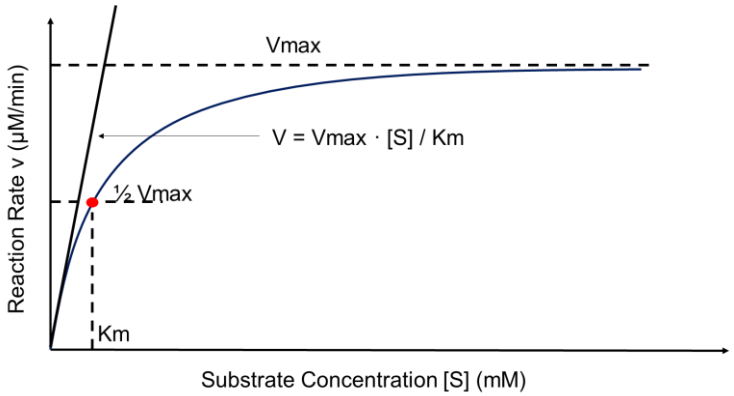

Figure 2.3 Reaction rate vs substrate concentration (Michaelis-Menten model) [24].

$$\frac{d[P]}{dt} = v = k_{+2}[ES] = \frac{k_{+2}[S][E]_0}{[S] + K_m} = \frac{V_{max}[S]}{[S] + K_m} = \frac{V_{max}}{1 + \frac{K_m}{[S]}} \quad (2.2)$$

$$K_m = \frac{k_{-1} + k_{+2}}{k_{+1}} \approx \frac{k_{-1}}{k_{+1}} \ (\text{when } k_{+2} \gg k_{-1}) \quad (2.3)$$

Where v is the rate of the reaction, [X] denotes the concentration of X, $[E]_0$ is the initial concentration of the enzyme, V_{max} is the maximum rate of reaction (occurring when the substrate completely saturates the enzyme), and K_m is the Michaelis constant (typical values 10^{-1}:10^{-5} M) defined in Equation (2.3).

There are two general approaches to enzymatic substrate estimation: end-point analysis or rate measurement analysis [37]. The end-point method compares the condition of the sample or the environment before and after the chemical reaction is completed.

Differently, the rate measurement analysis employs the Michaelis-Menten equation. By monitoring the initial rate of the reaction v_o by an appropriate transduction method with known V_{max}, K_m and $[E]_0$, it is possible to calculate the initial concertation of the substrate $[S]_0$ as:

$$[S]_0 = \frac{v_0 K_m}{V_{max} - v_0} \quad (2.4)$$

This estimation method is usually quicker than the alternative approach based on the reaction endpoint because it is required only to monitor the first part of the reaction.

There are mainly two types of biosensors: electrochemical and physical [38]. Electrochemical biosensors detect alterations of the charge distribution of the sample or environment [38]. Amperometric, potentiometric, impedimetric and voltametric are the most common electrochemical biosensors. pH biosensing usually performed thoroughly integrated pH sensors such as the ion-sensitive field-effect transistors (ISFET), are also a

widespread electrochemical sensing technique [2]. Among electrochemical detection methods, amperometric is probably the most commonly used approach [39].

Amperometric sensors generate a current flow proportional to the concentration of the analyte [39]. This class of biosensors use a catalytic electrode, classically platinum, for the oxidation of specific chemical species (e.g. hydrogen peroxide or NADH) generated alongside an enzymatic reaction [40]. The electrode where the oxidation takes places is called the working electrode (anode). The potential of the working electrode is kept constant with respect to a reference electrode for the oxidation of the desired species, hydrogen peroxide in this example. Generated electrons from the oxidation of the target species create a detectable current and are usually recombined on the counter electrode (cathode), classically made of silver/silver chloride (Ag/AgCl).

Physical biosensors detect modifications of the physical properties or condition of the sample or environment [38]. Calorimetric, mechanical, and optical biosensors are the most common physical biosensors. Calorimetric biosensors detect heat exchange accompanying the reaction of the analyte with the bioreceptors. Mechanical biosensors usually detect mass modifications of the biological component after the interaction with the bioreceptors. Optical biosensors usually employ a light sensor which detects a variation of the optical properties of the sample or the environment. They can mainly be divided into three categories according to the principle of operation: bioluminescence, fluorescence, and absorbance [38].

Bioluminescent biosensors use specific bioreceptors (e.g. luciferase) selected to produce photons when interacting with the substrate. The light production mechanism involves biochemical reactions relying on the oxidation of the substrate [41]. When the light-producing reactions are chemical (inorganic reagents, e.g. luminol), this phenomenon is usually referred to as chemiluminescence [41]. The setup of a generic bioluminescence-based biosensor is described in Figure 2.4(a). The interaction of the bioreceptors and the analyte within the sample produces the generation of photons, usually with a wavelength λ_{lum} in the visible or near-infrared range [41]. Light production is omnidirectional. Produced photons can be sensed by an optical sensor typically operated in a dark environment.

Fluorescent biosensors use specific bioreceptors (e.g. fluorophore) selected to produce a change in the fluorescence properties when interacting with the target analyte. Fluorescence is the emission of light that occurs after the absorption of light that is typically of shorter wavelength [42]. The setup of a generic fluorescence-based biosensor is described in Figure 2.4(b). Unlike bioluminescence, fluorescence requires incident excitation radiation.

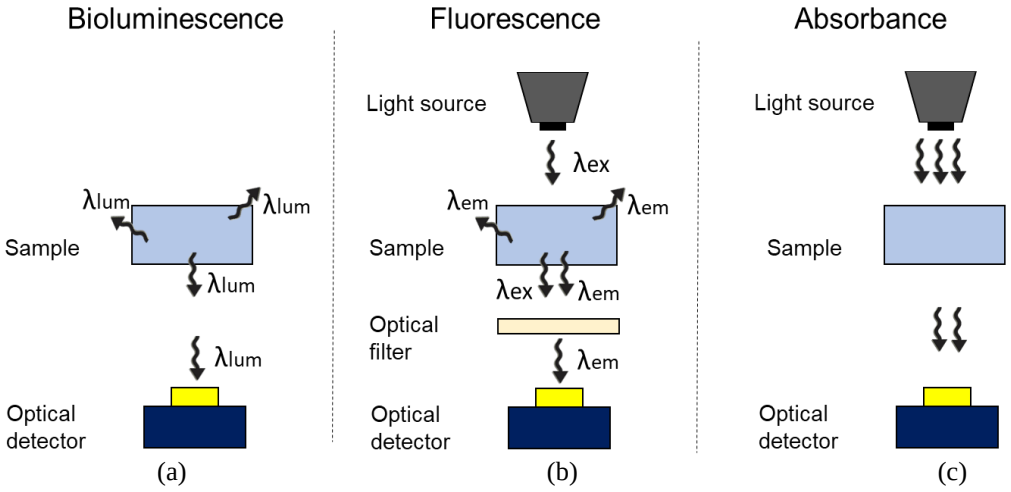

Figure 2.4 Working principle of (a) bioluminescence-based biosensors, (b) fluorescence-based biosensors and (c) absorbance-based biosensors.

A light source emitting excitation light with a wavelength λ_{ex} is used to illuminate the sample. Due to the reaction between analyte and bioreceptors within the sample, photons with a wavelength λ_{em} are omnidirectionally emitted. The emitted photons can be sensed using an optical sensor, typically preceded by an optical filter cancelling out the excitation light.

Absorbance-based biosensors use bioreceptors to produce a change in the light absorbance of the sample when interacting with the target analyte [39]. Since the change in the absorbance property of the sample is usually measured only for a selected range of wavelengths, absorbance-based biosensors are also referred to as colorimetric.

The setup of a generic colorimetric biosensor is described in Figure 2.4(c). A fixed wavelength is shone on the sample under test. The wavelength is typically selected to be a compromise between the responsivity of the detector and the peak absorption of the light-absorbing species in the visible range. Light transmitted thorough the sample is then monitored with an optical sensor during the chemical reaction. The intensity of the incident light is kept constant and usually in a linear region of the optical sensor dynamic range.

2.2.2. Discussion on the detection methods

Electrochemical and optical biosensors have shown comparable performance [43]. However, when considering integrated solutions for multi-analyte sensing, there are some aspects to be considered. To date, mass-produced optical sensors have good performance at affordable costs, mainly driven by the consumer electronics industry. Arrays of optical sensors with variegated dimensions (e.g. camera and imagers) can be easily manufactured.

Related bio-chemistry accompanying the optical transduction is also robust and well-established [43]. Platforms utilising optical modalities also have a great deal of potential for customisation due to the large numbers of probe molecules available [43]. The main issue related to optical biosensors is the necessity of samples pre-processing such as blood pre-filtration since red cells and other large molecules can create noise and artefacts [43].

Electrochemical platforms, such as amperometric devices, are less convenient to miniaturise. First, the selection of the metals used for the electrodes is crucial [44]. Some of the metals to be used in amperometric sensing are incompatible with standard manufacturing processes and need to be deposited after fabrication in cleanroom facilities [45]. The consequent need for additional fabrication steps, which can also be purchased as service, can lead to an increased cost of the platform. Additionally, the working principle of amperometric sensors creates challenges when designing an array of amperometric sensors for multiple assays due to potential interferences related to other chemical species nearby of the potential window used for the oxidation of the target compound [45].

With reference to the requirements of this platform outlined in Table 1.3, the electrochemical methods have a lower multi-analyte capability than the optical methods. For this reason, an optical detection mechanism was selected for the developed platform. Among the optical detection methods, a colorimetric approach has been adopted in this work. The reasons leading to this selection are illustrated in the following discussion (summary in Table 2.2).

For its ease-of-use bioluminescence is an excellent candidate to achieve non-invasive live-cell imaging. The absence of a light source simplifies the required setup and also eliminates the risk of photobleaching, which is the permanent photochemical modification of a probe molecule due to light exposure [46]. Photobleaching is an intrinsic property of the receptors and it is usually preponderant when exposing the dye probe to wavelength in the range 360–440nm [42], [47]. It also depends on the intensity of the light source, on the duration of the exposure and the concentration of the receptors [47].

However, bioluminescence suffers from its low-brightness nature largely caused by the slow turnover of bioreagents and the omnidirectionality of light production [42]. Bioluminescence intensity is strictly limited by the number of substrate molecules being catalysed by the bioluminescent protein [46]. To increase the chance to sense the produced light, bioluminescence is usually used over samples with macroscopic volume and detected with high-performance optical transducers. Furthermore, optical transducers are typically operated with long exposure times, which limit the spatiotemporal resolution of the

measurement [41]. Bioluminescence is therefore not adequate for this PhD project as the platform requires small sample volumes (in the µL scale). The adequate temporal resolution of the measurement is also needed for a correct estimation of the reaction rate.

One major advantage of fluorescent probes with respect to bioluminescence is that they can be brighter than bioluminescent proteins [46]. The intensity of the emitted light can also be increased by increasing the excitation light intensity. The difference between the exciting and emitted wavelengths makes these biosensors highly specific and suitable for the quantification of very low concentration of analytes [42].

Nonetheless, photobleaching is a limiting factor for fluorescence measurements [42]. On one hand, this is because the wavelength of the light excitation source is typically in the range of wavelength where photobleaching is more preponderant [42]. On the other hand, this is due to the use of high-intensity excitation light [47]. The use of a high-intensity excitation light also requires the use of an optical filter with a high rejection coefficient. The necessity of a high-performance optical filter makes fluorescent biosensor expensive, especially in the case of miniaturised platforms. Fluorescence is not adequate for this project as the cartridge needs to be affordable, ideally disposable. The integration of an optical filter for fluorescence biosensing would increase the cost of the cartridge. Also, the necessity of a filter between the sample and sensor would implicitly undermine the usage of other sensors on the cartridge (ISFET). A fluorescence approach is therefore incompatible with the versatility requirement.

Colorimetry is easy to operate, affordable and suitable for multi-metabolite sensing. Colorimetric sensors have lower selectivity when compared to bioluminescent and fluorescent biosensors. This is because any impurity within the sample can affect the light absorbance and interfere with the sensing. Colorimetric sensors are also not suitable for sensing analytes with a low concentration (in the range of pM, nM). Photobleaching is also an issue for colorimetric sensors [48]. However, this might be minimised by using wavelength where the effect is less evident (e.g. > 450 nm) , a light source with irradiance intensities in the range of tens of $\mu W/cm^2$ and limiting the duration of the light exposure to a few minutes [47]. Colorimetry is the most promising approach for the target applications as it is a trade-off among all the requirements. The target analytes of this platform have a blood concentration in the µM to mM range (this is discussed in the metabolomics section of this chapter), which is suitable for colorimetric detection. The platform is also required to be affordable and easy to operate. For these reasons, the colorimetric method is the most suitable for this project and it was adopted for the development of this platform.

Table 2.2. Comparison of different optical detection methods. The suitability of the detection methods against the requirements of this project was scored (low, medium, high) and justified. Scores were assumed by literature investigation and only apply for this project.

Requirement	Bioluminescence	Fluorescence	Colorimetry
Affordability	High (Easiest setup)	Low (Light source and expensive filter required)	Medium (Light source required but no filter)
Sensitivity	Low (Light glow has low intensity)	High (Suitable for nM to mM concentrations)	Medium (Suitable for µM to mM concentrations)
Specificity	High (Detection method is very specific)		Medium (Impurities might affect the measurement)
User-friendly	High (The user only requires inserting the sample, regardless of the detection method)		
Rapid	High (The initial reaction rate can be used to estimate substrate concentration)		
Robust	High (Controls tests can be run to increase the reliability of test)		
Equipment-free	High (The setup of the test can be integrated into a single equipment-free platform)		
Delivered	Medium (All the detection methods employ biological reagents which might require particular care when transported)		
Multi-analyte capability	Medium (Lateral crosstalk might be an issue. Large sample volume also required)	Medium (Lateral crosstalk might be an issue. The necessity of the filter complicates the monolithic integration)	High (Lateral crosstalk is lower - light is mostly unidirectional)
Versatility	High (Electrochemical sensors on the platform can be used)	Medium (Electrochemical sensors on the platform cannot be used)	High (Electrochemical sensors on the platform can be used)

2.2.3. Colorimetric biosensors

Since colorimetry was adopted in this work, a more detailed description of colorimetric biosensors is proposed in this paragraph.

The working principle of colorimetric sensors can be dived in two simultaneous phenomena: enzymatic reaction and reaction transduction [40]. The enzymatic reaction stage groups all the chemical reactions taking place. The most commonly employed enzymes belong to the oxidation and dehydrogenase classes [40]. For example, let us consider integrated enzyme-based biosensors for the determination of glucose. Today, glucose meters are the most popular portable quantitative platform employed in healthcare [2]. Glucose meters are mainly based on Glucose Oxidase (GOx), commonly employed in both amperometric and colorimetric biosensors [40]. GOx has a very high glucose selectivity, is easy to obtain, low-cost and very stable to pH, temperature and storing-time [40]. In the presence of water and oxygen, glucose reacts with GOx, producing gluconic acid and hydrogen peroxide [49]:

$$\text{Glucose} + H_2O + O_2 \xrightarrow{Glucose\ Oxidase\ (GOx)} Gluconic\ acid + H_2O_2 \quad (2.5)$$

Cofactors (e.g. flavin adenine dinucleotide), can be used in combination with GOx. At this stage, there might be different strategies for the reaction transduction [40].

Absorbance biosensors employ an additional reaction step introduced to interact with hydrogen peroxide and produce light-absorbing species. O-dianisidine and the system phenol/4-aminoantypirine (4AAP) are two well-established probes [49]. They are both oxidised by hydrogen peroxide in the presence of a catalysing enzyme, namely peroxidase (HRP), as reported in the following [49]:

$$o-d\text{ianisidine (reduced)} + H_2O_2 \xrightarrow{Peroxidase\ (HRP)} o-d\text{ianisidine (oxidised)} + H_2O \quad (2.6)$$

$$Phenol + 4-AAP + H_2O_2 \xrightarrow{Peroxidase\ (HRP)} Quinone-imine + 2H_2O \quad (2.7)$$

Both oxidised o-dianisidine and quinone-imine have higher extinction coefficient than the initial solution, resulting in a higher absorbance around 450 - 500 nm. At this stage, an optical sensor can be used as a transducer to monitor the variation of the absorbance. Beyond the example of glucose, similar chemistries based on oxidation enzymes can be used to measure different analytes.

Colorimetric bioassays employ the Beer-Lambert law which states that the optical absorbance A of a solution depends on the concentration of the light-absorbing species [P], its extinction coefficient ε and the optical length h [50] :

$$\varepsilon \cdot h \cdot [P] = A = -\log T = -\log \frac{I}{I_0} \quad (2.8)$$

Where T is light transmittance, I is the transmitted light and I_o is the incident light. Figure 2.5 illustrates the Beer-Lambert law. The absorbance is directly proportional to the concentration of the light-absorbing species. Hence, a high concentration of analyte (in the order of µM) is required in order to create a detectable signal. Usually, ε, h and [P] are measured in $Lcm^{-1}mol^{-1}$, cm and $molL^{-1}$, respectively. During the reaction, the absorbance changes and its profile can be referred to as a(t). The quantities ε and h are usually constant; thus, a(t) is proportional to the concentration profile of the light-absorbing species, referred to as [p(t)]. By differentiating the time-domain Beer-Lambert equation and plugging-in Michaelis-Menten equation (2.2), the following relation can be demonstrated:

$$a(t) = \varepsilon \cdot h \cdot [p(t)] \rightarrow \frac{da(t)}{dt} = \varepsilon \cdot h \cdot \frac{d[p(t)]}{dt} = \varepsilon \cdot h \cdot \frac{V_{max}}{1 + \frac{K_m}{[S]}} \quad (2.9)$$

where the notation mentioned above has been preserved. Beer-Lambert law is limited by the phenomenon of photobleaching for high concentrations of the light-absorbing species and high light intensities.

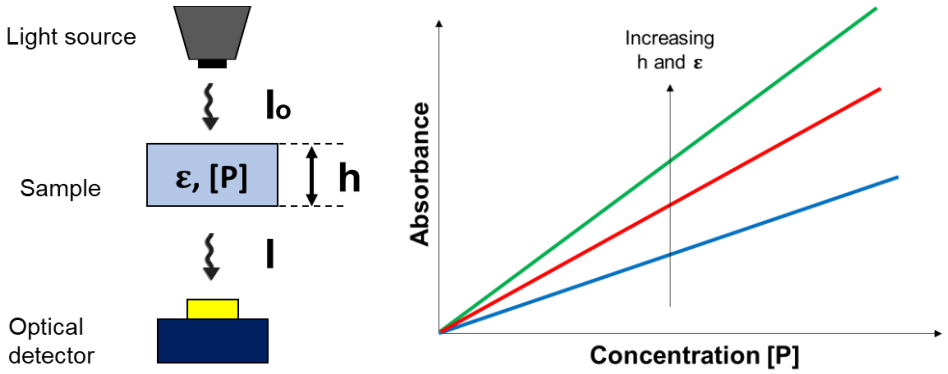

(a) (b)

Figure 2.5 (a) Setup for colorimetric measurement. (b) Illustration of Beer-Lambert law.

2.2.4. Integration of the bioreceptors

Many approaches for the integration of the bioreceptor with the sensor have been developed. Currently, immobilisation and lyophilisation are the most commonly used approaches [51]. Reagent immobilisation defines a set of procedures aiming to link the reagent to a substrate [51]. Reagent immobilisation has shown several advantages with respect to the reagent in a liquid state, including higher stability, easier shipment, easier process control, multi-enzyme processes, convenient handling, reusability [51].

Immobilisation methods can be dived into physical methods and chemical methods. Physical methods include reagent entrapment, absorption and microencapsulation [51]. Reagent entrapment involves the cross-link of the reagent with a polymer (e.g. alginate) [51]. Differently, reagent absorption methods allow the non-covalent link of the reagent with a substrate. This can be achieved by hydrophobic interactions, hydrogen bonding and Van der Waals forces [51]. Microencapsulation refers to the encasement of the reagent in semi-permeable polymer membranes with variable micrometric porosity. On the other hand, chemical methods include covalent attachment, cross-link, ionic binding and conjugation by affinity ligands [51]. A detailed description of protocol and techniques for enzyme immobilisation is reported in [51].

Reagent lyophilisation is also a widespread technique, especially in commercial devices [2]. Lyophilisation, also known as freeze-drying, is a process in which water is removed from a product by direct sublimation. Freeze-drying is today a well-established technique, vastly employed by pharmaceutical industries to preserve drugs. Freeze-drying improves the stability of the biological sample over temperature, pH and time [52], [53]. The sublimation of the water content is obtained by controlling the temperature and pressure of the sample

[54]. Usually, this is performed following a cycle, such as the one shown in Figure 2.6(a). Typically, the compounds to be freeze-dried are initially in a liquid state (state A in Figure 2.6(a)). The process of lyophilisation starts with freezing the solution (state B). The freezing temperature depends on the specific composition of the solution (typical value: -50^{o}C to -80^{o}C). A low freezing temperature ensures that almost all the water content is in the solid state. Subsequently, the pressure of the chamber is reduced to 1-2 mPa through vacuum pumping (state C). The sublimation typically takes place partially during the permanence in state C and during the slow transition from state C to D, during which the temperature is gradually brought to room temperature. Figure 2.6 (b) shows an example of the product of the freeze-drying process of a glucose oxidase based solution [55].

Timings, temperatures and pressure are usually selected according to the application [54]. Cryoprotective compounds, such as glycerol or sugars, can be used to optimise the process [54]. Freeze-dried enzymes have similar properties to immobilised ones [51]. However, there is no physical attachment of the molecules to the surface, so, once solubilised in the appropriate media, the reagent resembles its liquid form and does not allow reusability [51]. Thus, this technique has been used in conjunction with microstructures [53], [56]. Once lyophilised into the microstructure, the bioreceptor is confined and trapped in the physical structure [53], [56]. The reagents are then rehydrated by the sample itself once introduced [52], [53], [56].

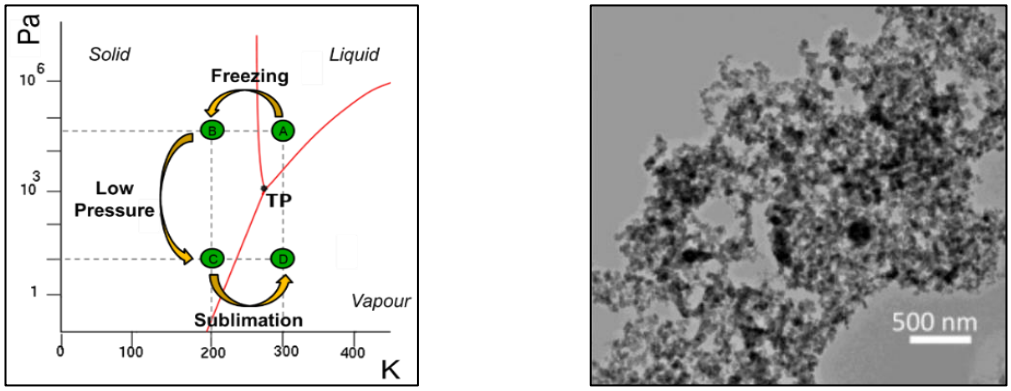

(a) (b)

Figure 2.6 (a) Working principle of the freeze-drying process. (b) Freeze-dried solution containing glucose oxidase. Reproduced from [55].

2.2.5. Biosensors metrics

The performance of a biosensor is usually assessed by a set of parameters. The main metrics are illustrated in Table 2.3. Other metrics have also been standardised but are omitted in this review since unnecessary for the comprehension of this work. Additional readings in [49], [57]–[60] are suggested for a comprehensive description.

Table 2.3 Main biosensor metrics.

Metric	Definition	Relation	Eq.
Linear Range	It defines the range where the output of the sensor (y) shows a linear behaviour i.e. it is proportional to the substrate (x) by a constant (S) and has an offset (c) [57].	$y = S \cdot x + c$	(2.10)
Analytical Sensitivity (S)[1]	It quantifies the enhancement of the output signal (Δy) when increasing the quantity to be measured by a certain level (Δx) [37].	$S = \frac{\Delta y}{\Delta x}$	(2.11)
Analytical Selectivity[1]	It is defined as the ratio of the desired product formed to the undesired product formed expressed in moles [37].	$\frac{Desired\ product\ (moles)}{undesired\ product\ (moles)}$	(2.12)
Baseline (c)	It defines the offset c of the calibration curve [37]. It is also referred to as blank measurement or control.	$c = (y - S \cdot x)_{x=0}$	(2.13)
Absolute error (e)	It is the absolute difference between the test result (x_i) and the true value to be measured (X) [60].	$e = \lvert X - x_i \rvert$	(2.14)
Relative error ($e_{\%}$)	It is the relative difference between the test result (x_i) and the true value to be measured (X) [60].	$e_{\%} = \frac{\lvert X - x_i \rvert}{X} \cdot 100$	(2.15)
Root mean square error (RMSE)	It is the square root of the mean of the square of all of the errors [61].	$\sigma = \sqrt{\frac{\sum_i e_i^2}{N}}$	(2.16)
Sum of squares error (SSE)	It is the sum of the squared differences between each observation and its mean (μ) [62].	$SSE = \sum_i (x_i - \mu)^2$	(2.17)
Precision (σ)	It defines the closeness of agreement between independent results obtained by applying the experimental procedure under stipulated conditions. A measure of precision is the standard deviation (σ) over N repeated measurements (x_i) [60].	$\sigma = \sqrt{\frac{\sum_i (x_i - \mu)^2}{N}}$	(2.18)
Resolution (R)	It is defined as the smallest change in the concentration of an analyte required to bring a change in the biosensor response and therefore it is expressed in molarity [57].	$R = \frac{\sigma_{ctrl}}{S}$	(2.19)
Analytical Accuracy (acc.) [1]	It is the closeness of agreement between a test result and the true value. It is calculated as the average error (absolute or relative) over N measurements.	$acc = \left(\frac{\sum_i \lvert X - x_i \rvert}{N}\right)$	(2.20)
Limit of detection (LOD)	It defines the minimum detectable concentration by the biosensors. It is calculated as the sum of the mean (μ_{ctrl}) and 3.3 times the standard deviation (σ_{ctrl}) of the control measurements [58].	$LOD = \mu_{ctrl} + 3.3\sigma_{ctrl}$	(2.21)
Limit of quantification (LOQ)	It defines the minimum quantifiable concentration by the biosensors. It is calculated as the sum of the mean and 10 times the standard deviation of the control measurements [58].	$LOD = \mu_{ctrl} + 10\sigma_{ctrl}$	(2.22)
Correlation coefficient (R)	It measures the linear correlation between two sets of variables x and y. It has a value between -1 and 1 [63]	$R(x,y) = \frac{Cov(x,y)}{\sigma_x^2\ \sigma_y^2}$	(2.23)

[1] Analytical sensitivity, specificity and accuracy express different concepts than the diagnostic (or clinical) sensitivity, specificity and accuracy of the test, already defined in Chapter 1.

2.3. Integrated Optical Sensors

A colorimetric approach was selected for this platform. Thus, a light source and optical sensors are required to measure the absorbance change of the sample accompanying the enzymatic reaction. Typically, colorimetric probes show light absorbance change in the visible spectrum. Regarding the portability requirement of this platform, a commercial light-emitting-diode (LED) was used as the light source in this work. Therefore, the required optical sensor must be capable of measuring light with intensity in the order of µW to mW (typical light intensities for commercial LEDs [64]) and wavelengths in the visible range.

2.3.1. CMOS technology

In this work, the integration of optical sensors onto the same substrate was achieved using the complementary metal-oxide-semiconductor (CMOS) technology. CMOS is today's leading manufacturing process for the fabrication of integrated circuits. Developed for the first time in the 60s by C. Sah. and F. Wanlass (Fairchild Semiconductor), in fifty years CMOS technology was adopted for the fabrication of 99% of integrated circuits [65]–[67]. CMOS technology has the capability of integrating sensors, including optical sensors, with read-out electronics on the same silicon chip.

Read-out circuitry developed in CMOS technology mostly use a combination of metal-oxide-semiconductor field-effect transistors (MOSFET) in different configurations to perform signal conditioning, including biasing, amplification and switching operations. The most important property of semiconductors is that their conductivity can be varied over a vast range by adding regulated quantities of impurity atoms into the semiconductor crystal [65]. This process is generally referred to as doping. To increase the concentration of free electrons, silicon can be doped with an element with a valence of 5, such as phosphorus [65]. The resulting material is an n-type semiconductor. Similarly, to increase the concentration of holes, silicon can be doped with an element with a valence of 3, such as boron [65]. The resulting material is a p-type semiconductor. A single silicon crystal can be doped differently in different regions.

Figure 2.7 shows a schematic cross-section of an NMOS and a PMOS, fabricated with a CMOS process. The process usually starts with a polished single crystal silicon wafer, doped with p-type impurities (p-type substrate is assumed in this description). N-wells are then fabricated on the substrate.

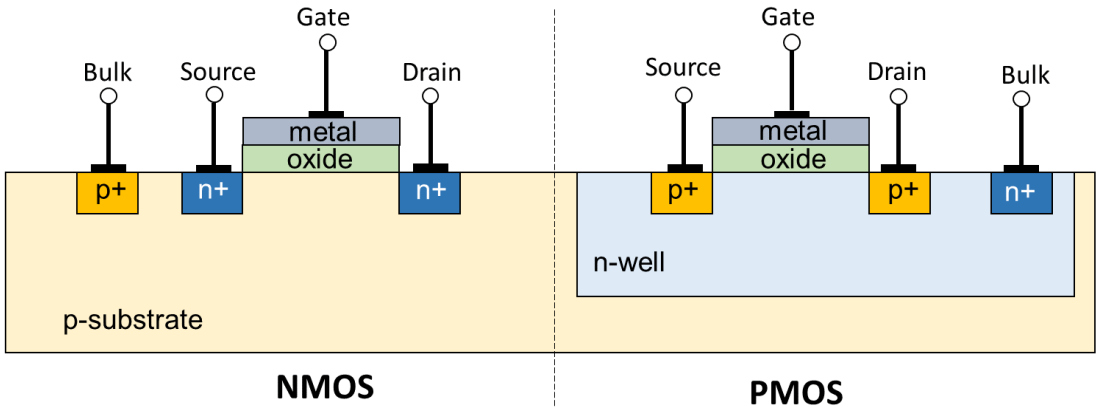

Figure 2.7 Cross-section of two transistors in a CMOS gate. The figures assume the use of a p-type substrate and an n-well process. The schematic is a simplified version of the device and does not include all the material layers. Dimensions are not in scale. Well implants are expected to have rounded edges. Reproduced and modified from [65].

For this aim, a SiO_2 layer is grown onto the substrate and selectively etched over desired areas. Donor atoms (n-type impurities) are subsequentially implanted in the desired exposed areas. The silicon dioxide layer is then removed after the implant is completed. Similar lithographic steps are employed for the fabrication of a high resistance polycrystalline silicon (polysilicon) gate separated from the substrate by a thin silicon dioxide layer. Aluminium metal contacts are also used to interconnect bulk, source, drain and gate with other structures. At the end of the process, passivation layers (typically silicon nitride and polyimide) are used to protect the structure. Passivation layers are etched over the pads to enable wire-bonding connections to external instrumentation.

CMOS-based systems have been used for both digital and analogue applications. In the digital world, CMOS technology is in use for microprocessors and memories, for example. Antennas, sensors, signal processing circuitry (filtering, amplification, etc.) have been implemented with the same technology. Besides being scalable, reliable and low-cost, there are also technological advantages of CMOS-based chips, including its immunity against noise and low static power consumption [65].

2.3.2. Photodetectors

Optical detectors are devices capable of converting optical radiation into a detectable electric signal and have been successfully integrated with CMOS technology. There are many ways of interaction of electromagnetic radiation with material [68]. However, typically there are two main categories of photodetectors: thermal and photonic [68]. There are also further

classes of photodetectors which are widely described in the literature [68]. In thermal photodetectors, the absorption of light causes an increase in the device temperature with the consequent variation of a temperature-dependent physical parameter (e.g. the electrical conductivity) [68]. Whereas, in photonic detectors, photons interact directly with the electrons in a material [68].

The photon detection process can be further divided into internal and external [68]. In detectors exploiting an internal photonic effect, photo-excited carrier (electron or hole) remains within the sample. On the other hand, in sensors utilising an external photonic effect, also known as the photoemissive effect, the incident photon causes the emission of an electron from the surface of the absorbing material [68]. The capability of internal photonic detectors of handling electrons within the device makes them usually the first choice for integrated systems. This was also the case for this project. The diagram in Figure 2.8 summarises the main categories of photodetectors.

The photoelectric effect requires a minimum of photon energy to be triggered. If the energy of the incident photons is greater than the band-gap energy of the semiconductor, each absorbed photon can produce an electron-hole pair. The photon energy E is given by:

$$E = h\,\upsilon = h\frac{c}{\lambda} \tag{2.24}$$

Where h is the Planck constant, υ is the optical wave frequency, c is the light speed, and λ is the wavelength. Therefore, the photonic detectors have a maximum wavelength, beyond which they cannot operate.

Photodiodes are one of the most commonly used internal photonic detectors and have also been employed in this project. The principle of operation of a photodiode is based on a p-n junction. A p-n junction is formed on the same silicon crystal by creating two adjacent regions doped with p-type and n-type impurities. [65]. At the interface, due to the rapid recombination of diffused carriers from the n to the p region and vice versa, a depletion region is established [65].

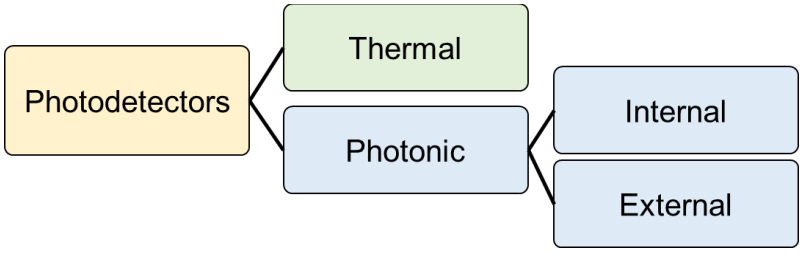

Figure 2.8 Main photodetectors categories.

In the depletion region, there is no free charge carrier, and an electric field is created, called built-in potential [65]. The built-in potential opposes the diffusion of holes into the n region and vice versa, acting as a potential barrier [65].

Photodiodes are p-n junctions and can be operated in both photoconductive and photovoltaic mode [68]. The photoconductive mode involves reverse biasing of the p-n junction, as shown in Figure 2.9. In this mode, when the junction is illuminated (for example, from the p-side), the photons absorbed in the depletion region can statistically produce electron-holes pairs. The generated carriers are separated, under the action of the electric field generated by the reverse bias: the electrons move towards the n zone and the holes toward the region p. Light can also be absorbed outside the depletion region and the carriers generated outside the depletion region are separated by diffusion. The diffusion current is a limiting factor in the response speed of the p-n photodiode, and it can be reduced by widening the depletion region. The extension of the depletion region can be controlled by tailoring structure conformation, doping concentrations, and the biasing.

Photodiodes operated in photovoltaic mode do not have any applied bias. The photocurrent generation is such as the one presented for the photoconductive mode, but the extension of the depletion region is exclusively due to the built-in-potential.

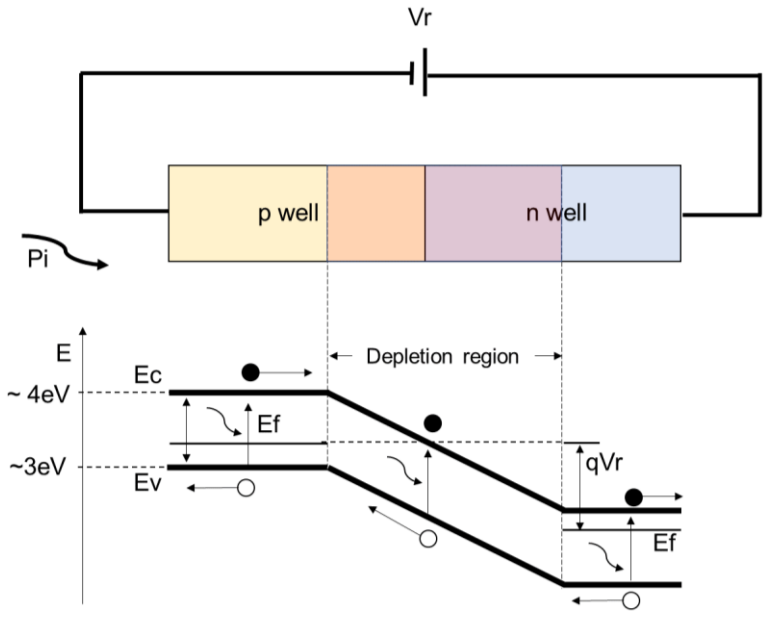

Figure 2.9 Schematic representation of a photodiode in photoconductive mode. Dimensions are not in scale. V_r: bias voltage; E_c: conduction band; E_v: valence band; E_g: energy gap (for undoped silicon E_g = 1.14eV); E_f: Fermi level; q: elementary charge. Reproduced and modified from [68].

The equivalent circuit of a silicon photodiode is shown in Figure 2.10 [69][70]. The model is composed of an ideal current source, an ideal diode (D_1), a capacitor (C_j), and two resistors (R_{sh} and R_s) connected as in the figure. The diode represents the p-n junction. C_j and R_{sh} represent the junction capacitance and resistance, respectively. Although an ideal photodiode should have an infinite R_{sh}, actual value ranges from 10 to 1000 MΩ [70]. R_s represents the resistance due to the connections. The ideal current source represents the contribution of the photogenerated current I_p. I_p is proportional to the incident optical P_i and the responsivity of the optical detector R_s:

$$I_p = R_s P_i \tag{2.25}$$

Using the above equivalent circuit, the output current (I_o) is given by the following equation [70]:

$$I_0 = I_p - I_d - I_{Rsh} \tag{2.26}$$

If I_{Rsh} is negligible, the above equation can be rewritten as [69]:

$$I_0 = R_s P_i - I_s(e^{\frac{qV_d}{kT}} - 1) \tag{2.27}$$

Where the first addend of the second member is given by equation (2.25) and the second addend is the diode equation. In the diode equation, I_s represents the saturation current of the diode, V_d is the voltage across the diode, q is the elementary charge (~ $1.6 \cdot 10^{-19}$C), k is the Boltzmann constant, T is the temperature in Kelvin.

Figure 2.11 illustrates the photodiode characteristic [69]. In dark conditions ($P_i = 0$), the photodiode characteristic is similar to the curve of a diode (see curve 1) [69]. However, when the photodiode is illuminated ($P_i > 0$), the characteristic function shifts downwards (see curve 2). Increasing the light intensity produces a further shift of the characteristic (see curve 3) [69].

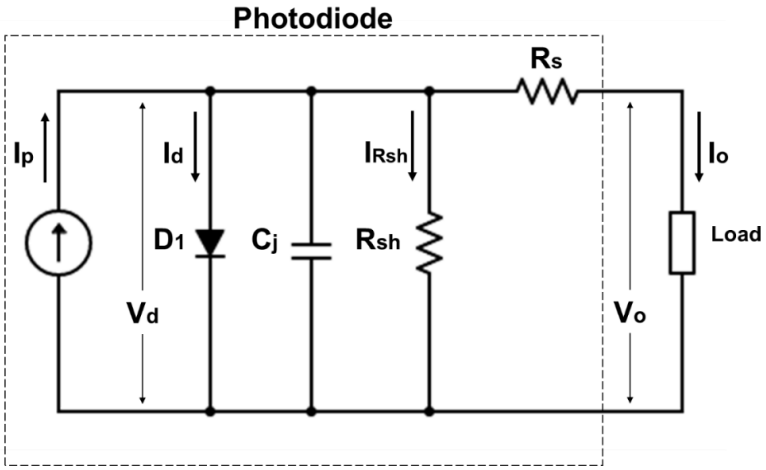

Figure 2.10 Photodiode equivalent circuit. Reproduced and modified from [69].

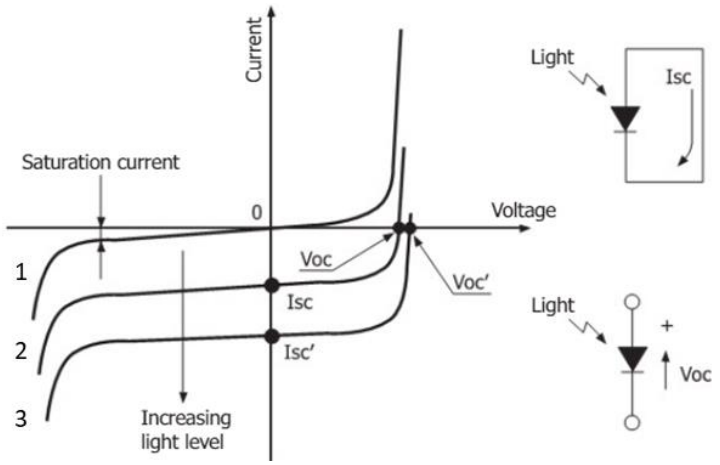

Figure 2.11 Photodiode characteristic I-V curves. V_{oc}: open-circuit voltage. I_{sc}: short circuit current. Reproduced and modified from [69].

A photodiode is subject to various noise sources that degrade its performance. Noise sources place a limit on the ability of subsequent detection electronics to detect small signals from the photodiode [71], [72].

Specifically, the current flowing in a photodiode can be mainly divided into three components: the photogenerated current I_p, the background current, and the dark current. The three components can be considered additive. I_p is generated by the absorbed light and is the desired output of the device. The background current is the undesired current due to background radiation absorbed by the device. Therefore, this component depends on the environment where the sensor operates. The dark current is undesired current observed even in the absence of incident radiation.

There are many adding phenomena contributing to the dark current. Because of the stochastic nature of the mechanism generating noise, noise sources are usually described with statistical values such as power spectral density and root mean square value [73]. In the absence of electrical bias, the absolute minimum internal noise is the thermal noise, also known as Johnson noise or Nyquist noise [68]. Thermal noise is found in all resistive materials, including semiconductors, and depends on temperature, resistance, and the operating bandwidth of the device [65]. With the same notation illustrated above, the root mean square of current fluctuation due to thermal noise ($i_{th,rms}$) is given by the following equation:

$$i_{th,rms} = \sqrt{\frac{4kT\Delta f}{R_L}} \tag{2.28}$$

Where Δf is the operating bandwidth of the device and R_L is the load of the photodiode [74].

Any other form of internal noise, usually depending on the bias, is referred to as excess noise [68]. In general, a bias voltage across the photodetector increases excess noise. Shot noise and flicker noise are the two main causes of excess noise [68]. Shot noise is related to the discrete nature of the electric charge. The root mean square of the current fluctuation due to shot noise ($i_{sh,\,rms}$) is given by:

$$i_{sh,rms} = \sqrt{2qI_{avg}\Delta f} \tag{2.29}$$

Where the same notation as above are maintained and I_{avg} represent the average signal current flowing in the diode [71]. As shown in Figure 2.11, a saturation current (I_s) is expected under reverse bias and in dark condition. The saturation current is due to the diffusion of minority carriers. The saturation current of the device and depends on the conformation of the p-n junction, including doping levels and extension of the depletion region. Typical values of the saturation current are in the order of nA [75]. A mathematical model of the saturation current is illustrated in [75].

Flicker noise is associated with the presence of potential barriers at the contacts, interior, or surface of the semiconductor. Flicker noise is also known as 1/f noise due to its spectral density, being less evident at a higher frequency. The root mean square current due to flicker noise can be approximated by the following empirical equation:

$$i_{\frac{1}{f},rms}(f) = \sqrt{\frac{K\, {I_d}^{\beta}\Delta f}{f^{\gamma}}} \tag{2.30}$$

Where I_d is the diode current, K, γ and β the empirical device coefficients depending on the fabrication process and doping profile, f is the operating frequency [76], [77].

All the above mechanism illustrated above are independent and contribute to the noise floor of the photodiode. The resulting root mean square current ($i_{n,\,rms}$) can be expressed as:

$$i_{n,rms} \approx \sqrt{{i_{th,rms}}^2 + {i_{sh,rms}}^2 + {i_{\frac{1}{f},rms}}^2} \tag{2.31}$$

Therefore, while at low frequencies flicker noise dominates the power spectral density, broadband noise mechanisms prevail at a higher frequency. There are also additional sources of dark noise for photodiodes, including, generation-recombination (g-r) noise, leakage current and impact ionisation current [71]. A detailed discussion about dark current contributors can be found in [71], [78].

In the last decades, photodiodes experienced a profound revolution. Improved materials and architectures allowed the development of new types of photodiodes for specific

applications [79]. The photodiode material is usually selected in accordance with the operation wavelength. Silicon photodiodes are a common choice in application with an operating wavelength in the visible range [79]. Silicon photodiodes, widely fabricated with the CMOS technology, have been used for several applications, including imaging and biosensing.

In imaging applications, an array of photodiodes is typically used. A CMOS image sensor array is typically formed by the sensor array, row and column selectors, analogue signal processors timing and control [80]. The sensor array is a grid of sensors, each capable of producing a photogenerated current [81]. Each element of the array (usually referred to as a pixel) also integrates readout electronics. Pixel circuits are mainly divided into active pixels or passive pixels. A review on pixel circuits for imaging is reported in [80]. The readout method has an important influence on sensor performance [80]. Typically, the output of each pixel is usually addressed by row and column selectors [80]. To date, CMOS image sensors have been used for a varied range of applications, including vision systems, space, automotive, medical applications [80].

Photodiodes used for biosensing are typically coupled with biological receptors for the optical detection of the target analyte. Photodiodes have successfully been employed for the development of bioluminescent [82], fluorescent [83] and colorimetric sensing [84]. The review illustrated in Paragraph 2.6.1 includes several additional examples of the use of photodiodes for biosensing.

2.3.3. Photodetectors metrics

A set of metrics, here briefly discussed, are currently used for comparing different devices.

Quantum efficiency (η) is defined as the number of carriers generated per incident photon. Formally, η can be expressed as [72]:

$$\eta = \frac{\frac{I_P}{q}}{\frac{P_i}{h\upsilon}} \tag{2.32}$$

However, it is more practical to express the quantum efficiency as the ratio between the optical power P_a absorbed by the material and the incident optical power P_i [68]:

$$\eta = \frac{P_a}{P_i} \tag{2.33}$$

This expression can also be expressed as a function of the transmitted power P_t [68]:

$$P_a = P_i - P_t = P_i - P_i e^{-\alpha w} \rightarrow \eta = 1 - e^{-\alpha w} \quad (2.34)$$

Where α is the light absorption coefficient of the material and w is the depth of the substrate. The wavelength λ_c corresponding to $\alpha = 0$ and consequently $\eta = 0$ is called cut-off wavelength: the device is unresponsive for any $\lambda > \lambda_c$.

Responsivity (R_s), which has also been previously introduced, is defined as the ratio between the output current of the device and the incident light power determined in the linear region of response. Formally, R_s can be defined as [72]:

$$R_s = \frac{I_p}{P_i} \quad (2.35)$$

If the detector has a voltage output rather than a current, responsivity can be defined as the ratio of output voltage and optical power. This leads to units of V/W. If a photodiode is combined with some detector electronics generating a voltage output, the output voltage is the photocurrent times the trans-impedance of the electronics. Responsivity also depends on the wavelength of the incident light and is related to quantum efficiency as follows [72]:

$$\eta = \frac{h\upsilon}{q} R_s \quad (2.36)$$

Dynamic range quantifies the working range of the sensor considering the power of the incident light [85].

Spectral range quantifies the working range of the sensor considering the wavelength of the incident light [85].

Gain is the ratio between the output current of the device and the photogenerated current inside the device [72]. In some photodetectors, such as p-n junctions, the maximum possible gain is 1. In other devices, where a carrier multiplication effect is in place (such as avalanche photodiodes), the gain can be higher than one.

Noise equivalent power (NEP) is defined as the amount of light required to produce a signal to noise ratio (SNR) equal to 1 [72]. NEP depends on the light wavelength.

Detectivity (D)* provides a representation of the noise level in a photodetector independently by its active area A and is formally defined as [72]:

$$D^* = \frac{\sqrt{A}}{NEP} \quad (2.37)$$

Dark current, as previously introduced, defined as the electrical noise detectable in the absence of light [72].

Other metrics have also been standardised but are omitted in this review, since unnecessary for the comprehension of this work. Additional readings in [68], [71], [72] are suggested for a full description.

2.3.4. Other photodetectors

Besides photoconductors and photodiodes, many other photodetectors have been successfully developed [68]. It is beyond the scope of this work to thoroughly review all the implemented photodetectors. However, the most commonly used photodetectors are briefly described, and their advantages and disadvantages are discussed.

Photodiodes are an attractive choice for all those applications aiming to miniaturisation, low-cost and easy usage. However, they have no amplification effect, and their gain is usually lower than 1.

For use requiring high sensitivity, avalanche photodiodes (APD) are a common choice [68], [71], [72]. APD are photodiodes (p-n or p-i-n junctions) with an internal mechanism of signal amplification through an avalanche process. They are typically biased at a large reverse voltage (see Figure 2.12(a)). The high electric field in the depletion region accelerates the photo-generated carriers which generate secondary electron-hole pairs through impact ionisation. Thus, the output of the device is the primary photocurrent multiplied by a factor M. The photocurrent multiplication has a random nature, and this introduces additional sources of noise. Every electron-hole pair is generated in a random location, so they do not experience the same multiplication. Also, the multiplication effect amplifies both background and dark current. More sophisticated APD structures have been proposed to optimise the device metrics. However, APD manufacture requires very uniform doping profiles, more complex designs, and a large reverse bias, usually resulting in higher fabrication complexity and costs.

An APD operated in the ‘Geiger mode’ is known as a single-photon avalanche diode (SPAD) [86]. SPADs are p-n junctions operated with a reverse bias voltage largely above the breakdown voltage of the device (point 1 in Figure 2.12(b)). Due to the multiplication mechanism, a single initial photogenerated carrier can trigger a self-sustaining avalanche due to impact ionisation effects. Thus, a single photon can initiate a large internal current flow. The avalanche can be quenched by reducing the bias voltage (see point 3 in Figure 2.12(b)). At this biasing point, the avalanche is no longer self-sustained and is quenched [87]. Quenching circuits are typically used to decrease the voltage across the diode.

SPADs are usually employed in high-speed applications and are a common choice for detecting low light intensity (for instance lower than 1 nWcm^{-2} at 550 nm) [85]. They are also a popular choice in applications requiring high responsivity and high quantum efficiency [85], [86]. Although they share similar limitations with APDs, SPADs currently suffer from poor sensitivity due to noise and low fill-factors.

Although photodiodes, APDs and SPADs are all based on p-n junctions, they have structural differences designed to optimise their performance in their respective operation modality. A review illustrating the structural differences of these devices can be found in [87].

Photomultipliers tubes (PMTs) are also among the most-sensitive photodetectors for the visible light [72]. However, they are challenging to miniaturise; therefore, due to their high operating voltages, fragility, size and cost, there are many challenges to be addressed for their integration [72].

Charge-coupled devices (CCDs) are probably the biggest competitor of CMOS technology for image sensing applications [72]. A CCD is an array of metal-insulator-semiconductor or metal-oxide-semiconductor which can detect, store and transfer photogenerated charge. CCDs have high spatial resolution, low noise and high sensitivity [80].

However, CMOS outstands CCDs in terms of speed, integration capabilities, lower power consumption and capability of random access to single pixels [80], [88]. CMOS sensors and CCDs have comparable fabrication costs. However, CMOS usually requires a less complex read-out electronic, which can result in a less-expensive system [80], [88], [89].

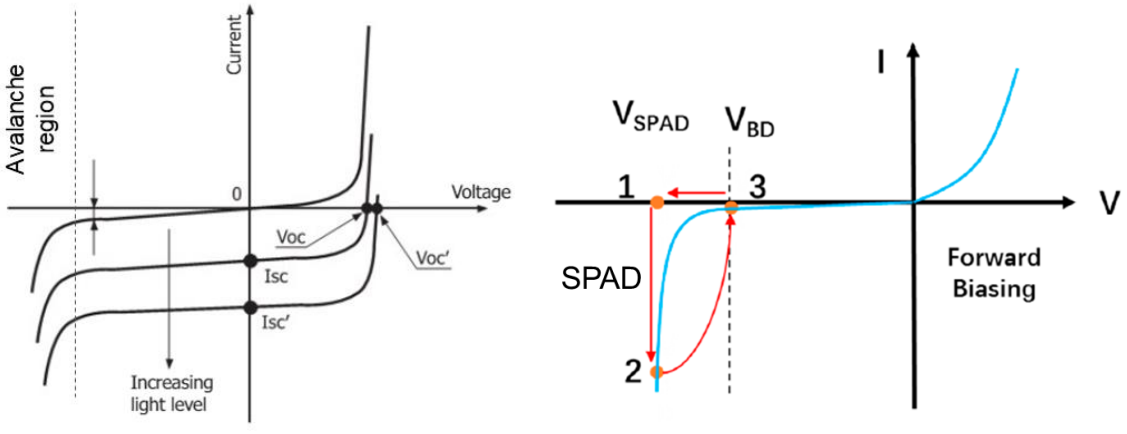

(a) (b)

Figure 2.12. (a) Avalanche region showed in the photodiode characteristic I-V curves. Reproduced and modified form [69]. *(b) Operating principle of the Geiger mode. Reproduced and modified from* [87].

2.4.Metabolomics

One of the most promising fields of application of lab-on-chip platforms is metabolomics. Metabolomics is the study of the relative variation of the collection of small molecules (<1500 Da), known as metabolites, produced by cells during the metabolism [90]. The increasing interest in metabolomics is related to its capability of describing the phenotype and providing a 'functional readout of the physiological health of an organism' [11]. Metabolomics, together with the probably more well-known genomics, transcriptomics, and proteomics, belongs to the omics sciences. Omics studies aim to identify, characterise, and quantify all biological molecules that are involved in the structure, function, and dynamics of a cell, tissue, or organism [91]. More precisely, genomics studies the structure, function, evolution and mapping of nucleic acids and aims at the characterisation and quantification of genes that guide the development of proteins with the aid of enzymes and messenger molecules [91]. Transcriptomics is the study of the collection of all messenger RNA molecules in a single cell, tissue, or organism [91]. Proteomics is the science that studies the sum of all cell, tissue or organism proteins as related to their biochemical properties and functional roles, as well as their modifications during the life of the organism [91].

Metabolomics is affected by both genetic and environmental factors and, therefore, can bridge the gap between genotype and phenotype [11]. Metabolomics and other omics sciences are complementary, and their integration is a promising research challenge [92]. The study of the metabolome is also considered to be more promising than other omics science. This is because, unlike other omics studies, metabolic pathways are highly conservative in mammalian species meaning that studies carried out on laboratory animals can be easily related to humans [92]. An analysis of metabolomics can be carried out on a variety of biological fluids and tissue types and can use a variety of different platforms of technologies [91]. Currently, more than 114,000 metabolites have been detected and quantified in human fluids, tissues or organs in different concentrations [90]. Among the human fluids, blood metabolome is probably the most attractive one because of its intrinsic physiological stability and collection convenience [90]. Blood is made up of two components: a cellular component (red/white cells and platelets) suspended into a liquid component, namely plasma [90]. Plasma can be obtained from blood by centrifugation or filtration. The serum is also a body fluid obtainable by removing the clotting agents from plasma.

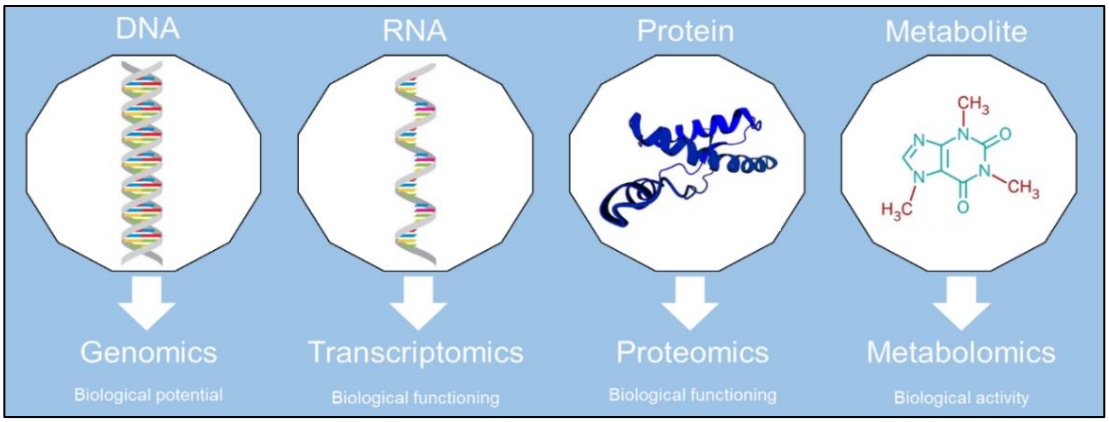

Figure 2.13 Metabolomics reflects the phenotype of an organism. Modified from [93].

Blood, plasma and serum contain a variety of organic and inorganic substances such as proteins and peptides, nutrients, electrolytes, organic wastes and a variety of other small molecules suspended or dissolved [90]. The biological composition of plasma and serum is very similar and includes more than 4200 metabolites [90]. Unknown metabolites, expected to be discovered in support of metabolic pathways still not completely understood, are referred to as metabolic dark matter [94].

Four different conceptual approaches are widely adopted: target analysis, metabolite profiling, metabolomics, and metabolic fingerprinting [11]. Target analysis and metabolite profiling aim to quantify, respectively, a small set of known metabolites and a larger set of compounds (both identified and unknown) using a single analytical technique [11]. Differently, metabolomics employs complementary methodologies to quantify as many metabolites as possible. Finally, metabolic fingerprinting looks for a specific metabolite in a large sample population by comparing specific features.

Due to the huge diversity of chemical structures, there is no single technology available to analyse the entire metabolome [90]. Although over the past two decades several techniques have been employed for metabolic profiling [90], nuclear magnetic resonance (NMR) and spectroscopy and mass spectrometry (MS) are the traditionally used approaches for metabolomics profiling [14], [94], [95]. NMR spectroscopy quantifies analyses based on their response to a radio-frequency excitation [90]. Differently, MS quantifies analyte based on their mass-to-charge ratio (m/z) by transforming the analyte molecules into a charged (ionised) state, with subsequent ion analysis and any fragment ions formed during the ionisation process [96]. There are several types of MS, depending on the technique for ionisation and ion analysis [96]. The most used MS techniques in metabolomics are gas

chromatography MS (GC-MS) and liquid chromatography MS (LC-MS). GC-MS provides molecules separation basing on their volatility at several temperatures. Differently, LC-MS provides separation depending on the solubility of the molecule in various solvents (e.g. water, methanol, acetonitrile, isopropyl alcohol, and hexane) [96]. Each technique has advantage and disadvantages when compared to the others, as summarised in Table 2.4. For additional details about the techniques mentioned above, [95]–[98] are suggested.

Nevertheless, they are often complementary since some analytes are solely quantifiable with a single technique. N. Psychogios et al. in [90] estimated that NMR is capable of quantifying only 1.2% of the human serum metabolome. Several MS techniques, all together, can instead obtain data on 84% of the serum metabolome [90]. Among the MS techniques, the authors in [90] suggest using LC-MS for human serum metabolomics. Metabolomics has been applied to a vast variety of applications: human and animal health, biomarker discovery, pharmacometabolomics, environmental monitoring are just some of them [14].

It is a shared vision that metabolomics has a large and still partially untapped potential in healthcare, where the large metabolome information can be combined by machine learning and classification algorithms [11], [14], [92], [93]. Currently, metabolomics is exploited mainly for pharmacology. The best-selling drugs on the market today act on the metabolic pathway by enzyme, inhibitors or any other suitable mean [14]. There is evidence that metabolomics can potentially be employed for the diagnosis and monitoring of the most deadly diseases, including cancer, cardiovascular diseases (CVD) and dementia [12]. In line with the aim of the present project, a focus is provided for metabolomics applied to PCa and ischemic stroke.

Table 2.4 Comparison of most commonly used techniques for metabolomics [14].

	NMR	**GC-MS**	**LC-MS**
Start-up cost	> $1 million	> $150k	> $300k
Quantitative	✓	✓	✓
Destructive	x	✓	✓
Limit of detection (LOD)	5 µM	0.5 µM	0.5 nM
Test time (per sample)	5 min	20-40 min	20-40 min
Sample volume	0.1 – 0.5 mL	0.1 – 0.2 mL	10 – 100 µL
Automated	Fully	Partially	Partially
Organic molecules	✓ (most of them)	✓ (most of them)	✓ (most of them)
Inorganic molecules	x	✓ (some of them)	✓ (some of them)
Novel compounds identification	✓	x	x

2.4.1. Metabolomics for cancer

One in two people will develop cancer at some point in their lifetime [13], [99]. The World Health Organization estimates more than 18 million cases of cancer and more than 9.5 million cancer-related deaths worldwide, only in 2018 [13]. Although frequency and survival rate are considerably variable with the cancer type, there is consistent evidence that patients diagnosed at an early stage are more likely to survive [13], [99]. For some cancer types, screening programs have already dramatically improved the survival rate. In the UK, the NHS cervical and bowel cancer screening programs have reduced mortality by 70% and 15%, respectively [100], [101]. However, there are other types of cancer where the scientific community is in desperate need of new criteria and tools [7].

Metabolomics has a largely untapped potential in the field of oncology [14], [102]. Cancer cells have a different metabolism than healthy ones [103]. The altered metabolism of cancer cells, together with their accelerated metabolism and the parallel angiogenesis, produce substantial and detectable modifications in the entire human metabolism [104]. Cancer-related metabolites accumulate in human body fluids [105], and their altered levels act as indicators or biomarkers to diagnose or monitor the disease [14], [105]. It has been demonstrated in the scientific literature that the use of a panel of metabolites rather than a single biomarker has the potential to perform better than the current clinical standard [106]. Leichtle et al. [107], for instance, have developed a multi metabolomics marker model which was superior to the conventional tumour marker CA 19-9 in differentiating between pancreatic cancer, pancreatitis, and healthy controls. Similar results have also been achieved for breast cancer [106]. Besides, Wang et al. [108] have demonstrated that it is possible not only to diagnose but also to monitor oesophageal cancer stage by quantifying 12 metabolites in tissue.

The main metabolic difference in cancer cells is how they use glucose to produce energy [103]. Cancer cells usually proliferate from one aberrant cell to more than $2 \cdot 10^9$ cells per cm^3 and modify their metabolic pathways to sustain their proliferative capacity [109]. In cells, energy is usually stored using a series of 'building' (anabolic) processes and released through a series of 'breaking-down' (catabolic) mechanisms. In the presence of O_2 (aerobic conditions), healthy human cells transform glucose into energy under the form of adenosine triphosphate (ATP). This process is carried out through a series of biological processes, including the Krebs cycle (TCA) and the oxidative phosphorylation (OXPHOS), producing residual CO_2 and water. Usually, this process provides 36 ATP molecules per glucose

molecule processed [103]. In the absence of oxygen (anaerobic or hypoxic conditions), energy is obtained from different processes leading to the production of lactate, which is later released outside the cell as a reaction residue. In parallel, glucose is also used for the pentose phosphate pathway (PPP), which influences DNA replication [110].

Glutamine metabolism – the second most used nutrient after glucose – is also used to provide energy after being converted in glutamate through the glutaminolysis cycle [110]. TCA and OXPHOS are also related to the synthesis of fatty acids, primarily through the production of citrate-related Acetyl-CoA.

In cancer cells, the standard mechanisms mentioned above are altered [103], [109], [110]. Even in the presence of oxygen, glucose is mainly converted to lactate for energy production [110]. This mechanism is usually referred to as the Warburg effect [103]. The process is less efficient when compared to the normal cycle since it only produces 4 ATP molecules per glucose molecule [103]. The consequent increase in lactate secretion has been linked to the capability of the cancer cell to accelerate the generation of new blood vessels (angiogenesis) [110]. On the one hand, angiogenesis helps cancer cells to receive increased levels of nutrients. On the other, it provides an easy way for aberrant cells to invade new tissues and create metastasis [110]. Aiming to compensate for the glucose-related ATP production, glutamine intake is also increased in cancer cells. Glutamine is converted into glutamate which, when in excess, is also released by the cell [110]. The upregulated glutamine-glutamate cycle also boosts fatty acid synthesis [110]. Increased synthesis of nucleic acids and fatty acids has been linked to cell proliferation [110]. Metabolic differences related to energy production and usage from glucose and glutamine are schematically represented in Figure 2.14. Additional metabolic modifications have been discovered in cancer cells and reviewed in the literature [103], [109], [110]. Among them, cancer cells take advantage of ample supply of amino-acids, especially in the L-type form, vastly more abundant in humans with respect to D-type amino acids [111]. The progression of cancer is associated with increases in L-amino acids (LAA) uptake by cancer cells, also obtained by modifying the specific transporters [112]. Choline metabolism is another well-established modified pathway [113]. In many cancer types, the increase of choline and choline-related metabolites have been related to a modification in choline-related enzymes and transporters [113]. Understanding cancer metabolism led to the development of specific drugs acting on critical metabolic pathways proven essential for cancer cells [109], [114].

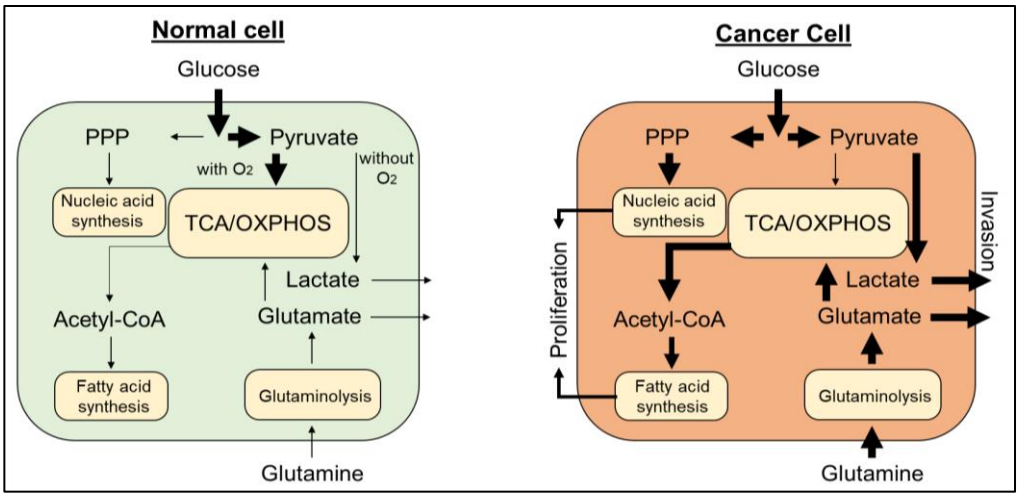

Figure 2.14 Schematic representation of metabolic differences between a normal cell (left) and a cancer cell (right). Bold arrows indicate an upregulated pathway. Reproduced and modified from [110].

Statins such as Simvastatin and Atorvastatin, for instance, act on the metabolic pathways for fatty acid synthesis [109]. Methotrexate, another anticancer approved agent, operates on the nucleic acid synthesis [114]. L-asparaginase is also an approved anticancer agent used in clinical practice to treat leukaemia by acting on asparagine metabolism [115]. Alongside the approved drugs, an increasing number of compounds are in clinical and pre-clinical trial stages [114]. A detailed review of cancer metabolism for therapeutic purposes has been published by U.E. Martinez-Outschoorn et al. [114].

Understanding cancer metabolism also provided essential knowledge for cancer diagnosis and monitoring. Several metabolites have been linked to cancer. Currently, a selection of marked metabolites is being used in clinical testing for imaging purposes [116]. Positron Emission Tomography scanning is used to image cancer after the intake of labelled metabolites such as, for example, Fludeoxyglucose, C-acetate, C-choline, F-choline, C-pyruvate [116]. Labelled metabolites are usually stable isotope and are selected because expected to accumulate more in cancer cells due to their upregulated intake [116].

Table 2.5 presents a review of metabolites linked to cancer. Interestingly, there is some crossover between the metabolic profiles. The set of the most recurrent metabolites, independently by the sample, have been summarised in Table 2.5. Confirming what previously described, the table highlights a set of metabolites crucial for cancer cells such as glucose/lactate, glutamine/glutamate, amino acids, and choline/choline-derived metabolites.

998 *Table 2.5 Cancer-related metabolites documented in the scientific literature.*

Cancer	Sample	Metabolites
Breast	Serum*	2-hydroyglutarate [104], acetoacetate [117], beta-alanine [104], choline [118], fatty acid [119], glucose [120], glutamate [104], [117], glutamine [104], glycerol [117], glycerophosphocholine [118], histidine [117], [120], linoleic acid [119], lipids [120], mannose [117], n-acetyl glycoprotein [117], palmitic acid [119], phenylalanine [117], phosphocholine [118], pyruvate [117], steriatic acid [119], xanthine [104]
	Tissue**	acetoacetate [121], histidine [121], glycerol [121], mannose [121], phenylalanine [121], pyruvate [121], linoleic acid [122], glutamate [121], glutamine [122], myoinositol [106], phosphoethanolamine [106], taurine [106], asparagine [115], [123], isoleucine [122], threonine [122]
	Urine	4-hydrolyphenylacetate [124], 5-hydrixyindoleacetic acid [124], homovanillate [124], urea [124]
Colorectal	Serum*	2-Hydroxybutyrate [102], alanine [125], arginine [106], aspartic acid [102], [125], choline [126], cystamine [102], cysteine [106], fatty acid [106], glucose [106], glycin [126], glycine [125], histidine [125], inositol [126], isoleucine [125], kynurenine [102], lactate [126], leucine [126], lysine [125], methionine [125], oleamide [106], phenylalanine [126], phosphocholine [126], pyruvate [127], sarcosine [125], taurine [126], threonine [126], tryoptophan [127], [128], tyrosine [125], [127], ultralong fatty acids [129], uridine [127], valine [125]
	Tissue**	2-aminobutyrate [130], 2-Hydroxybutyrate [130], 2-oxobutyrate [130], 5-Hydroxytryptamine [130], arginine [130], betaine [130], fatty acid [131], [132], glutamic acid [130], glutamine [131], [132], indoxyl [130], lactate [127], linoleic acid [130], N1-acetylspermidine [130], N-acetyl-5-hydroxytryptamine [130], nicotinic acid [130], proline [126], [130], symmetric dimethylarginine [130], threonine [130], uracil [130], urea [131]–[133], xanthine [130]
Pancreatic	Serum*	3,6-dihydroxy-5-cholan-24-oic acid [107], 3-hydrolybuterate [106], 3-hydrolyisovalerate [106], 3-Hydroxybutyrate [134], [135], 3-hydroxyisovalerate [134], acetone [134], [136], alanine [137], arachidonic acid [138], arachidyl carnitine [139], butanoic acid [138], chenodeoxycholic acid [139], choline [137], citrate [136], creatine [134]–[136], cysteine [138], ethanol [134], formate [134], [136], glucose [134], [137], glutamate [134], glutamine [134], [138], glycerol [134], glycerol 2-phosphate [137], glycerol 3-phosphate [137], Glycholic acid [107], glycodeoxycholic acid [107], hydroxybutyrate [136], hypoxanthine [138], isoleucine [135], lactate [135], linoleic acid [137], lipids [136], lysine [138], malate [137], mannose [134], medium-chain acylcarnitines [140], myoinositol [137], N-acetyl glycoprotein [136], N-methylalanine [138], oleoyl carnitine [107], phenanthrenol [138], phenylalanine [134], [138], phosphatidylcholine [106], proline [134], quinaldic acid [139], sitosterol [139], tauro(ursodeoxy)cholic acid [138], tetradecanal oleamide [139], triglycerides [135], trimethylamine-N-Oxide [135], tyrosine [138]
	Tissue**	Alanine [108], arachidonic acid [141], asparagine [108], choline [108], citrate [142], fatty acid [142], glutamic acid [108], glutamine [141], glycerophosphocholine [143], ketones [142], lactate [108], leucine [108], lysine [141], lysophosphatidylcholine [144], N-methylalanine [141], phenylalanine [141], phosphatidylcholine [144], phosphocholine [143], sphingolipid [142], sphingomyelin [144], taurine [108], tauro(ursodeoxy)cholic acid [141], valine [108]
Ovarian, uterus, cervix	Serum*	2-Piperidinone [105], glycin [106], lysophosphatidylcholine [105], pyrimidine [106], tryoptophan [105]
	Urine	1-methylguanine [145], histidine [146], ketones [147], lactate [147], methylxanthine [145], mucin [146], N4-acetylcytidine [146], Nucleotide [146], proline [145], pseudouridine [146], pyridylacetic acid [145], succinic acid [146], theophylline [145], tryptophan [105], urate-3-ribonucleoside [146], uric acid [145], urocanic acid [145]

Prostate	Serum*	Alanine [148], [149], androsterone sulfate [150], arachidonoyl amine [150], arginine [148], [151], cholesterol [150], choline [152], citrate [148], [153], creatinine [154], [155], cysteine [150], dimethylheptanoyl carnitine [150], fatty acid [148], formate [150], glucose [151], glutamate [148], [150], glycine [150], isolithocholic acid [150], leucine [150], lysine [150], [151], phenylalanine [151], [156] phosphocholine [150], proline [148], testosterone sulfate [150]
	Tissue**	Alanine [156], arginine [157], asparagine [156], cholesterol [150], [157], [158], choline [150], [156], [159], citrate [150], cysteine [157], fatty acid [150], glutamate [150], glutamine [150], glycerol [150], [156], glycine [150], [159], lactate [150], [156], lactate [160], [161] leucine [71], myoinositol [156], phenylalanine [150], phosphocholine [150], [156], proline [150], [156], pyrimidine [150], [156]
	Urine	Alanine [156], choline, [156], citrate [156], creatinine [150], cysteine [150], fatty acid [150], glycerol [150], lactate [156], phosphocholine [156], pyrimidine [150]
Oesophageal	Serum*	adenosine monophosphate [162], NAD [162], acetoacetate [106], acetone [106], asparagine [157], aspartate [106], beta-hydrolybutyrate [163], citrate [163], creatine [106], cysteine [106], glucose [162], glutamate [106], glutamine [163], histidine [106], lactate [106], lactic acid [163], LDL [106], leucine [106], linoleic acid [163], lysine [163], methionine [163], myristic acid [163], phenylalanine [164], tryptophan [163], tyrosine [163], valine [163], VLDL [106],
	Tissue**	Acylcarnitines [165], carnitine [165], fatty acid [165], lysophosphatidylcholine [165]
Lung	Serum*	6-diaminopimelate [166], cholesteryl acetate [166], choline [167], fatty acid [167], [168], glutamine [169], lysophosphatidylcholine [166], [168], N-succinyl-2 [166], octanoylcarnitine [166], phosphatidylcholine [166], phosphatidylserine [166], sphingomyelin [168]
	Tissue**	Choline [170], fatty acids [170], glutamine [171]
Brain	Tissue**	arachidonic acid [141], glycerophosphocholine [141], lactate [141], lysophosphatidylcholine [141], phosphatidylcholine [141]
	CBF***	2-aminopimelic acid [172], citric acid [172], isocitric acid [172], methionine [172], serine [172], tyrosine [172], valine [172]
Leukaemia	Serum*	Acetone [173], alanine [173], arginine [173], cholesterol [173], [174], choline [173], creatine [173], cysteinyl-glycine [175], formate [173], glucose [173], glutamate [175], glycerol [174], histidine [173], lactate [173], [174], leucine [173], lysine [173], lysophosphatidylcholine [175], myoinositol [173], phenylalanine [173], phosphatidylcholine [175], phosphocholine [174], proline [173], pyruvate [174], trimethylamine-N-Oxide [173], tyrosine [173], uric acid [174], uridine [174], valine [173]
	Tissue**	Asparagine [123], [176], glutathione [177]

* This group includes blood, serum, or plasma
** This group includes tissue, cells or locally collected biological fluid (e.g. secretions)
*** Cerebrospinal fluid

999

Table 2.6 Summary of metabolic cross-over between the metabolic profiles.

Analyte	Breast	Colorectal	Pancreas	Ovarian, Uterus, Cervix	Prostate	Oesophageal	Lung	Leukaemia	Brain
asparagine	✓		✓		✓	✓		✓	
choline	✓	✓	✓		✓		✓	✓	
cysteine		✓	✓		✓	✓		✓	
fatty acid		✓	✓		✓	✓	✓		
glucose	✓	✓	✓		✓	✓		✓	
glutamate	✓		✓		✓	✓		✓	
glutamine	✓	✓	✓		✓	✓	✓		
histidine	✓	✓		✓		✓		✓	
lactate		✓	✓	✓	✓	✓		✓	✓
leucine		✓	✓		✓	✓		✓	
lysophosphatidylcholine			✓	✓		✓	✓	✓	✓
phenylalanine	✓	✓	✓		✓	✓		✓	
phosphocholine	✓	✓	✓		✓			✓	
proline		✓	✓	✓	✓			✓	
tyrosine		✓	✓		✓	✓		✓	✓
valine		✓	✓		✓	✓		✓	✓

2.4.2. Metabolomics for prostate cancer

PCa has the highest cancer incidence for male subjects in the UK (26 % in 2014), and it is expected to rise in the next 15 years, as the population ages [178]. In accordance with other cancer types, there is consistent evidence that patients diagnosed at an early stage are more likely to survive cancer. PCa patient 5-years survival rate is nearly 100% when the tumour is detected in a localised initial stage [178]. The same rate decreased to 34% when the tumour is diagnosed in a late metastatic stage [178]. This difference in the survival rate underlines the necessity of PCa screening program. Most PCa cases are diagnosed with a prostate-specific antigen (PSA) blood test, usually in combination with digital rectal examination, biopsy and imaging [150]. Once diagnosed, PSA is also used to monitor and assess the evolution of the disease [150]. This prediction has been related to the high false-positive rate of the PSA test: only less than one in three subjects with increased PSA will have PCa [7]. PSA test also misses about 15% of cancers [7]. Currently, a PSA-based screening program remains controversial because of the number of false positives. This could unnecessarily deteriorate the quality of life of healthy subjects and increase clinical costs without significantly reducing mortality [179]. Besides being invasive, digital rectal examination and biopsy can even potentially miss cancer due to tumour heterogeneity [150]. As a

consequence, several additional biomarkers are now being explored to improve the performance of the current clinical procedure [150].

Metabolomics is being explored to address this necessity [150]. Lohkov et al. [150], for instance, have demonstrated that a set of metabolites from plasma can potentially discriminate PCa better than PSA. Specifically, in a group of 30 healthy controls and 40 subjects affected by PCa, they demonstrated that increased levels of carnitine-related metabolites discriminated cancer and healthy groups with sensitivity and specificity of 94.6% and 96.4%, respectively. They performed better than the PSA test, which scored a sensitivity of 35% and a specificity of 83.3% on the same samples. In a similar study, Zhang et al. [150] also provided a set of metabolites with diagnostic potential comparable to PSA.

Table 2.7 demonstrates that metabolomics can be applied to PCa in all the stages of the disease, from early diagnosis to the stage assessment. Here, the link between PCa and metabolites have been broken down to four sub-categories. The first category groups all the metabolites which have been linked to PCa risk or recurrence. The second category groups all the metabolites which have shown diagnostic capability. This is usually assessed by comparing the metabolome of a healthy control group with one of the people recently diagnosed with PCa. The third category groups all the metabolites which have shown the capability of discriminating a malignant from a benign tumour. This is usually determined by comparing the metabolome of people diagnosed with a malignant PCa with subjects diagnosed with a benign PCa. The fourth category groups all the metabolites which have shown the capability of providing information about cancer stage, including the presence of eventual metastasis, usually evaluated by comparing the metabolome of people affected by PCa in several stages.

Among the metabolites relevant to PCa, it is worth highlighting that the serum concentration of LAA is typically increased in PCa group, except for alanine and lysine showing a decreased level in late-stage cancer. Glutamate and choline, also demonstrate a very close link with PCa, being relevant in all the stages of the disease [148], [152]. A correlation between sarcosine and PCa is still a controversial topic. At this stage, there are studies both approving [150], [156], [157] and disapproving [180] serum sarcosine as a metabolic biomarker for PCa. Certainly, this topic requires further study.

Table 2.7 Summary of metabolites which have been linked to PCa in literature, divided according to sample type (serum, tissue**, urine) and cancer stage.*

Metabolite	Sample	Risk or recurrence	Diagnosis	Malignancy	Staging
Alanine[LAA]	Serum*		↔ [149]		↓ [148]
	Tissue**			↑ [156]	
	Urine			↑ [156]	
Androsterone sulfate	Serum*		↑ [150]		
	Tissue**				
	Urine				
Arachidonoyl amine	Serum*		↑ [150]		
	Tissue**				
	Urine				
Arginine[LAA]	Serum*			↑ [151]	↑ [148]
	Tissue**				↑ [157]
	Urine				
Asparagine[LAA]	Serum*				
	Tissue**			↑ [157]	↑ [156]
	Urine				
Carnitine	Serum*		↔ [150]		
	Tissue**				
	Urine				
Cholesterol	Serum*				↑ [150]
	Tissue**				↑[150]
	Urine				
Choline	Serum*	↑ [152]	↑ [152]		
	Tissue**		↑ [150], [156]	↑ [150], [156]	↑ [150], [157], [159]
	Urine		↑ [156]	↑ [156]	
Citrate	Serum*	↔ [148]		↔ [148]	↓ [148], [181]
	Tissue**	↓ [150]	↓ [150]	↓ [150]	
	Urine		↓ [156]		↓ [156]
Creatinine	Serum*	↑ [154]			↑ [155]
	Tissue**				
	Urine			↓ [150]	
Cysteine[LAA]	Serum*	↔ [150]			
	Tissue**			↑ [157]	
	Urine	↔ [150]			
Fatty acid	Serum*	↔ [148]		↔ [148], [150]	↔ [148]
	Tissue**				↔[150]
	Urine			↔ [150]	
Formate	Serum*			↔ [150]	↔ [150]
	Tissue**				
	Urine				
Glucose	Serum*			↑ [151]	
	Tissue**				
	Urine				
Glutamate[LAA]	Serum*	↔ [148]	↑[150], [182]	↑ [148], [151], [182]	↑ [148], [150], [156], [182]
	Tissue**		↔ [150]	↑ [150]	↑ [156]
	Urine				
Glutamine[LAA]	Serum*		↑ [150]		
	Tissue**	↔[150]	↔[150]		
	Urine				
Glycerol	Serum*				
	Tissue**		↑[150], [156]	↔ [150]	↑ [156]
	Urine		↑ [150], [156]		↑ [156]
Glycine[LAA]	Serum*		↑ [150]		
	Tissue**			↑ [150]	↑ [159]
	Urine				
Isolithocholic acid	Serum*		↓ [150]		
	Tissue**				
	Urine				
Lactate	Serum*		↑ [160], [161]		
	Tissue**		↑ [150], [156]	↑ [156]	
	Urine		↑ [156]	↑ [156]	
Leucine[LAA]	Serum*				↑ [150]
	Tissue**			↔ [150]	↑ [156]
	Urine				
Lysine[LAA]	Serum*		↔ [150]	↑ [151]	↓ [150]
	Tissue**				
	Urine				
	Serum*				

Myoinositol	Tissue**			↑ [157]	↑ [150], [156]
	Urine				
Phenylalanine^{LAA}	Serum*			↑ [151]	↑ [156]
	Tissue**				↑ [150]
	Urine				
Phosphocholine	Serum*		↔ [150]		
	Tissue**		↑ [150], [156]	↔ [150]	↑ [156]
	Urine		↑ [156]		
Proline^{LAA}	Serum*			↑ [148]	↑ [148]
	Tissue**		↑ [150]		↑ [156]
	Urine				
Pyrimidine	Serum*				
	Tissue**		↓ [156]		
	Urine		↓ [150], [156]		
Sarcosine	Serum*		↑ [149]		
	Tissue**		↑ [150]	↑ [150], [156], [157]	↑ [150], [156], [159], [183]
	Urine			↑ [150], [156], [157]	↑ [156], [157], [159], [183]
Serine^{LAA}	Serum*				
	Tissue**				↓ [157]
	Urine				
Spermine	Serum*				↓ [119], [150], [157]
	Tissue**	↓ [150]	↓ [156]	↓ [156]	↓ [119], [150], [157]
	Urine		↓ [156]	↓ [156]	
Taurine^{LAA}	Serum*				↑ [156]
	Tissue**			↔ [150]	↑ [150]
	Urine				
Tryptophan	Serum*	↔ [148]		↔ [148]	↑ [148]
	Tissue**				
	Urine				
Tyrosine^{LAA}	Serum*				↔ [150]
	Tissue**				
	Urine				
Urea	Serum*	↔ [148]		↔ [148]	↑ [148], [153], [155]
	Tissue**				
	Urine				
Valine^{LAA}	Serum*			↑ [151]	↑ [150]
	Tissue**		↓ [156]		
	Urine				
Xanthine	Serum*			↔ [148]	↑[148], [157]
	Tissue**				
	Urine				
Testosterone sulfate	Serum*		↓ [150]		
	Tissue**				
	Urine				

↑: increased concentration level
↓: decreased concentration level
↔: altered concentration level but the trend is not easily reportable
* This group includes blood, serum, or plasma
** This group includes tissue, cells or locally collected biological fluid (e.g. secretions)
^{LLA} Amino acid, mainly present in human blood in its l-type

2.4.3. Metabolomics for cardiovascular diseases

Globally, CVDs are the leading cause of death, claiming almost 18 million lives each year [13]. CVDs group a variety of conditions related to the hearth and blood vessels. CVDs might be divided into chronic and acute diseases. Chronic CVDs, including rheumatic heart disease, congenital heart disease, coronary heart disease, are long term diseases. Differently, acute CVDs include usually severe and immediate failure events. Acute events such as stroke and heart attacks are mainly caused by a blockage that prevents blood from flowing correctly [13]. Among acute CVDs, ischemic stroke is the second leading cause of death and the third

leading cause of disability [184]. Ischemia is the sudden death of brain cells due to lack of cell oxygenation [184]. This is usually related to a cardiovascular accident where blood vessels are blocked or ruptured [184].

Metabolomics is a powerful tool also for CVDs [185]. It is well-known that a high lipid profile, excess of long-chain amino-acids and high glucose concentration in the blood increase the risk of acute CVDs [13], [185]. Therefore, monitoring lipid profile, including cholesterol, high-density lipoprotein (HDL) and low-density lipoprotein (LDL), is now standard practice in the clinical environment to evaluate the risk of acute events [186].

Lactate also has a clinical significance in acute cardiac patients and is clinically used for patient stratification [187]. Authors in [187] suggest that patients with acute CVDs with an admission lactate blood level lower than 2 mM usually have a better prognosis. Lactate has been strongly related to acute inflammation and also gives account for any hypoxia condition [188], [189]. The importance of lactate for critically ill patients is well-known, and today it is the clinical practice to monitor lactate levels in intensive care units (ICU) [190].

Besides lactate, serum creatinine is a diagnostically significant metabolic marker for acute conditions [189]. Creatinine is also clinically used in ICUs for critically ill patients [154], [191]. On top of these well-established metabolomic biomarkers for CVDs, several additional metabolites have been linked to cardiovascular events and reported in Table 2.8.

Table 2.8 A selection of metabolites and related cardiovascular disease.

CVD	Sample	Metabolites
Risk	Serum	Betaine [192], branched-chain amino acids (BCAA) [185], cholesterol [193], choline [192], HDL [193], LDL [193], TMAO [185], [194], short-chain dicarboxylacylcarnitine (SCDA) [185]
Heart failure	Serum	BCAA [185], acylcarnitines [185], fatty acids [185], glucose [185], ketones [185]
Myocardial infection	Serum	Creatine [195], fatty acid [195], glucose [195], glutamate [195], glycerol [195], lactate [195], phenylalanine [195], phosphoethanolamine [195], pyrimidine [195], succinate [195], taurine [195], triglycerides [195], tyrosine [195]
Hearth attack	Serum	Ceramide [192], cholesterol [192], choline metabolism [192], triacylglycerol [192]
Ischemic stroke	Serum	Acetic acid [196], alanine [189], aspartate [189], betaine [196], [197], carnitine [189], choline [192], [197], choline-related pathways [189], citric acid [189], [196], creatinine [189], cysteine [189], formate [189], free fatty acids [192], glutamate [189], glutamine [189], glycine [189], homocysteine [189], lactate [189], [196], phenylalanine [189], proline [189], pyruvate [189], pyruvic Acid [196], serine [189], threonine [189], tryptophan [189], [196], tyrosine [189], uric acid [189], valine [189], [196]

2.4.4. Other metabolomics applications

There are many other healthcare applications where metabolomics could have a dramatic impact. It is beyond the scope of this work to review all the healthcare applications where metabolomics shows untapped potential. However, a few more uses are listed here to emphasise that metabolomics still has impressive unexploited potential.

Metabolomics could be employed for Alzheimer's disease early diagnosis, currently affecting more than 5 million people in the US only [198]. A large number of serum metabolites, including choline [198], valine [198], carnitine [198], serine [198], have been linked to the disease. Serum metabolic profile could serve as an additional tool to increase the accuracy of diagnostic, to predict the disease progression [198].

Metabolomics has also been linked to sepsis [199]. Globally, 31.5 million people develop sepsis each year, and this figure is expected to increase as the population ages [200]. Sepsis is both the most expensive condition to treat (US$ 24 billion) and the leading cause of death in US hospitals, with a fatality rate ranging from 30% to 50%, depending on its severity [200]. Early diagnosis is crucial in sepsis, as where survival is reported to decrease by 7.6% with every hour of delay in the initiation of therapy [3]. There are many metabolites which have been linked to sepsis. Lactate, above all, is currently being used in clinical settings for sepsis diagnosis [199], [201]. Also, increased blood levels of 3-hydroxybutyrate [201], [202], acetate [201], acetoacetate [201], acylcarnitines [201], citrate [201], glucose [201], [202], isobutyrate [202], linoleic acid [201], lysophosphatidylcholine [201], malate [201], myoinositol [202], o-acetylcarnitine [202], phenylalanine [202], pyruvate [201], urea [202], and decreased blood levels of kynurenine [201], methanol [202], propylene glycol [201], ribitol [201], ribonic acid [201], valine [202] have been linked to sepsis.

On top of all the mentioned applications, metabolomics has also been shown to be relevant for other widely spread diseases such as acute coronary syndrome, asthma, cardiovascular diseases, hepatitis, Parkinson's disease, rheumatoid arthritis, exotic diseases, acute renal injury [12]. In summary, at present metabolomics is very much research laboratory-based and needs to move out of academic laboratories and into the clinic [12], [15].

2.5. Microfluidics

A single miniaturised and automated diagnostic system made up of multiple integrated biosensors, actuators, and electronic interfaces is called lab-on-chip [28], [203]. Lab-on-chips incorporates numerous laboratory tasks onto a small device and has many advantages than standard benchtop equipment. The main benefits of lab-on-chips are the speed of analysis, ease of use, low reagent and sample consumption, high-throughput processing and high reproducibility due to automation and standardisation [30]. Lab-on-chip devices integrate all steps 'from sample to answer' and, for this reason, they are promising for addressing environmental and medical challenges [31]. A lab-on-chip device is typically more complex than a biosensor and it is composed of (i) multiple receptors, (ii) multiple transducers, (iii) multiple readouts and a (iv) sample handling system [31]. The previous sections have already discussed receptors, transducers, and readouts. Therefore, this section is dedicated to the sample handling system.

Microfluidics is the study of microstructures capable of handling small quantities of fluids. Many microfluidic structures have been successfully used for a range of fluidic operation in lab-on-chip platforms [204]. Microfluidic channels are microstructures which confine the fluid and allow it to move in a controlled path. Microfluidic elements for controlling the flow of the fluid in the microchannel have been developed, including pumps (active and passive) and valves [205]. Microfluidic mixers are microstructures designed to favour the mixing of two different fluids [205]. Microfluidic elements are usually combined to create microfluidic networks. Currently, microfluidic networks can reach very high complexity level integrating channels, valves, pump and mixers [206].

In this work, capillary microchannels with rectangular cross-section were used. No microfluidics pump or mixers were employed. Therefore, this paragraph will focus on microfluidic theory for capillary and laminar flow regime. Additional resources for an overview of microfluidic elements are here suggested [205], [207], [208].

In microfluidic structures, the flow is primarily laminar, meaning that the behaviour of the liquid can be decomposed into a series of infinitesimal layers flowing on top of each other without mixing. The Reynolds number (Re) is typically used to define the flow regime in a microfluidic structure. The Reynolds number is defined as the following:

$$\mathrm{Re} = \frac{\text{Inertial Forces}}{\text{Viscous Forces}} = \frac{\rho u l}{\eta} = \frac{u l}{\nu} \tag{2.38}$$

Where ρ is the fluid density (kgm^3), u is the velocity of the fluid in the structure (m/s), l is a characteristic linear dimension of the structure (m/s), η is the dynamic viscosity of the fluid (Pa·s), and ν is the kinematic viscosity of the liquid (m^2/s) [209]. For a microstructure, $l \approx 10^{-6}$ so Re < 1. Turbulent flow is present when Re > 4000 while when Re < 2000 the flow is laminar.

The study of the fluid kinematics is usually carried out using the Navier-stokes equation. A generic particle with mass m and velocity v is influenced by several independent forces (F_j):

$$m\frac{dv}{dt} = \sum_j F_j \rightarrow V^{-1}m\frac{dv}{dt} = V^{-1}\sum_j F_j \rightarrow \rho D_t v = \sum_j f_j$$
$$\sum_j f_j = \begin{cases} \rho\delta_t v_x & \text{1D Flow} \\ \rho\{\delta_t v + (v \cdot \nabla)v\} & \text{3D Flow} \end{cases} \quad (2.39)$$

Where V is the considered volume, f is the force density and D_t is the material time-derivative defined as [208]:

$$D_t = \begin{cases} \delta_t, & \text{1D Flow} \\ \delta_t + (v \cdot \nabla), & \text{3D Flow} \end{cases} \quad (2.40)$$

The final form of the Navier-Stokes equation can be calculated by inserting the complete expression for the force densities:

$$\rho\delta_t v_x = -\delta_x p + \eta\left(\delta_y{}^2 + \delta_z{}^2\right)v_x + f_x \quad \text{1D Flow} \quad (2.41)$$

$$\rho\{\delta_t v + (v \cdot \nabla)v\} = -\nabla p + \nabla^2 v + \{\rho g + \rho_{el}E\} \quad \text{3D Flow} \quad (2.42)$$

Where, in the second member, the first term is the pressure-gradient force density, the second term is the viscous force density, and the third term is the body force density.

One of the methods for resolving the Naiver-Stokes equation is represented by the Hagen-Poiseuille equation, valid in static conditions and in a rigid straight structure when a pressure gradient Δp (Pa) is applied [208]:

$$\Delta p = R_h Q \quad (2.43)$$

Where R_h is the hydraulic resistance (kg/ m^4s), and Q is the flow rate (mole of fluid passing through a section in a unit of time, m^3/s). There is a formal equivalence between the Hagen-Poiseulle and the 2nd Ohm's law. The hydraulic resistance depends both on the geometry of the structure both on the viscosity of the fluid. Specifically, for rectangular channels with height h, length L and depth w the R_h is:

$$R_h = \frac{12\eta L}{\left\{1 - 0.63\left(\frac{h}{w}\right)\right\}h^3 w} \quad (2.44)$$

R_h is generally high for microfluidic structures due to height h and the width w having micrometric dimensions [208].

In the absence of externally applied pressure and with channel height and width in the order of hundreds of micrometres, the liquid can spontaneously move due to cohesive forces within the liquid and adhesive forces between the liquid and its surroundings. This effect is commonly referred to as capillary action [210]. With reference to Figure 2.15, the capillary pressure gradient (Δp) is related to the property of the fluid and the geometry of the microchannel [208]:

$$\Delta p = \gamma\left(\frac{\cos\Theta_b + \cos\Theta_t}{h} + \frac{2\cos\Theta_s}{w}\right) \tag{2.45}$$

Where Θ denotes the contact angle of the different materials employed and γ the surface tension. According to equation (2.45), when w << h, the capillary pressure gradient depends only on w and the microchannel can even be left open [211], [212].

Under the assumption of laminar, steady-state flow, and in the absence of gravitational effects, the position of the advancing liquid l(t) can be obtained by manipulating Equation (2.44) and Equation (2.45) [208], [213]:

$$l(t) = h\sqrt{\frac{\Delta p}{6\eta L}\left(1 - 0.63\frac{h}{w}\right)t} \tag{2.46}$$

Where Δp is the capillary pressure gradient, R_h is the hydraulic resistance, Q is the flow rate, η is the dynamic viscosity, L is the microchannel length. Equation (2.46) can be used as a designing equation when developing capillaries.

Many different methods have been used to fabricate microfluidic structures and integrate them with integrated circuits. A review of microfluidic fabrication and integration is reported in Chapter 4.

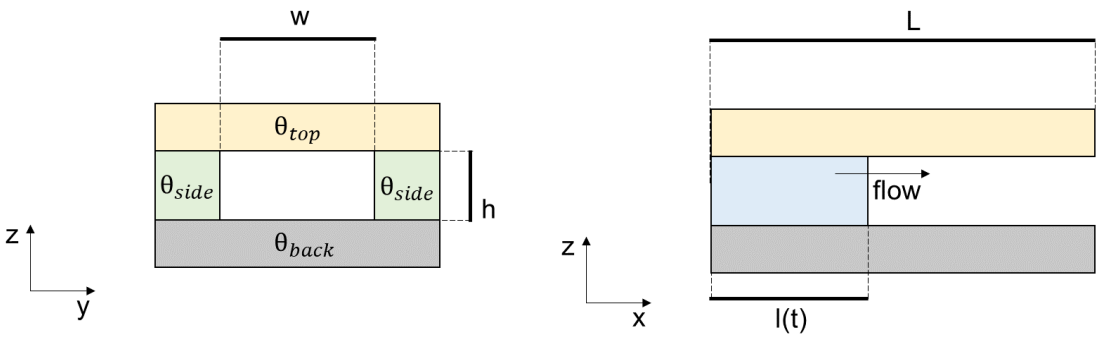

Figure 2.15 Schematic representation of a passive rectangular microfluidic channel.

2.6. Point-of-care Systems

By potentially being useful for all the major causes of death [12], [13], metabolomics social impact would be impressive if it was untapped for masses through POC platforms [10]. The main advantages and challenges of POC systems have already been examined in Chapter 1. Particularly, the potential of such technologies for saving lives, time and money have been already discussed. The main technological and practical challenges slowing down the widespread of these technologies have also been analysed. In this section, a more in-depth literature review is proposed for both experimental and commercial POC devices.

2.6.1. Review of POC platforms

Authors in [1] illustrate the key design components of a POC device which include user interface, sample delivery device, reagent storage strategy, reaction cell, sensors to detect the measurement reaction, control and communication system, data management storage.
POC testing has been employed to a variety of samples, including tissue, urine and blood [39]. Among them, blood testing is particularly interesting because the concentration of specific biomarkers in the blood is directly related to the physiological state of the body. Therefore, testing blood is often used for preventions, identification and monitoring for a variety of diseases [39]. Blood, especially in a small volume, is also particularly easy to obtain for the majority of conditions [39].
POC can be qualitative or quantitative [1]. Qualitative POC platforms usually do not provide a numerical result [199]. Typically, the output of this platform is only a binary result (i.e. positive or negative). Lateral flow assays (LFAs), introduced in 1988, are the most popular qualitative POC platforms [2]. LFAs are cellulose-based devices consisting of a strip, a sample pad, a reagent pad, and a test line. The sample is introduced at the sample pad. It migrates to the reagent pad via capillary forces, where bioreagents conjugated to the target analyte are immobilised. The formed antigen/antibody product continues to flow along the strip where is subsequently captured by a final biorecognition molecule. The result interpretation is usually a visual-coloured indicator.
There are many advantages of LFAs. The inherent properties of the paper support capillary flowing; thus, no pumping or complicated fluidics is required [1]. Also, LFAs only requires a small sample volume, no sample pre-processing and the waste can be conveniently incinerated [1]. Besides, the device is usually low-cost and can accommodate easy

functionalisation techniques. On the other hand, LFAs are challenging to use for multiple testing and have low sensitivity [1].

Quantitative POC devices aim to provide a numerical measurement of the level of the target analyte. LFAs can be extended form qualitative to quantitative by the use of a coupled reading instrumentation [1]. However, quantitative POC platforms require sensors [1]. Then, it should not be surprising that CMOS technologies and lab-on-chip platforms are vastly used for the development of quantitative POC systems [1].

POC platforms, very often supported by IC, have been used for a variety of healthcare applications including genomics, proteomics, and metabolomics. Other applications not discussed in this review also include biophysical analysis, cell separation and sorting, material and drug delivery, drug testing, and organs-on-chip [214]. Table 2.9 summarises the review on POC platforms proposed in this paragraph.

Genomics POC platforms. POC testing in genomics and transcriptomic targets DNA and RNA [2]. Numerous methods have been proposed for detecting and amplifying the presence of nucleic acids [2]. The most commonly used process is the polymerase chain reaction which creates billions of copies of a DNA sequence by iterative replications [215]. POC testing in genomics and transcriptomic is particularly essential for detecting and identifying virus, bacteria, fungi, microbes, pathogens [2], necrotic and aberrant cells [1]. A significant challenge remains in integrating blood pre-treatment with DNA and RNA detection in a low-cost, robust and user-friendly platform [1].

Proteomics POC platforms. POC testing in proteomics targets proteins, including enzymes, antibodies, and hormones [2]. Modern POC devices utilise immunoassay technology, which includes antigen-antibody binding [2]. These assays target protein biomarkers such as PSA for PCa, troponin I for CVDs, and bacterial and viral infection-related markers such as HIV, influenza, chlamydia, and hepatitis [2]. Most methods for protein analysis are based on the enzyme-linked immunosorbent assay (ELISA) method [1]. In traditional ELISA tests, colorimetric, fluorescent readout signals are used to visualise the interaction of the target protein to the specific recognition molecule [1]. ELISA analysis usually requires several washing steps which creates additional complication when designing a POC device [1]. ELISA can be implemented on both LFA-based POC and quantitative platforms [1]. LFA-based ELISA test has been demonstrated to be convenient to develop [1]. However, work is now under development for creating multiplexed protein assays on qualitative platforms [1], [216]. Authors in [216], for instance, propose a CMOS-

based device able to differentiate between serum samples containing either, neither, or both rabbit anti-mouse (RAM) antibodies and/or anti-HIV antibodies using a gold-nanoparticle promoted silver enhancement immunoassay. The authors claim that the proposed platform is the first step in creating a mass-manufacturable POC tool capable of multi-proteins quantification [216]. Several platforms have been developed for PSA detection [217]. Electrochemical [218], optical [219], [220], cantilever-based [221] and other suitable sensors [221] have also been successfully employed for PSA quantification, recently leading to the first FDA approved POC PSA test [181]. Despite the need for new tools and standards for PCa, the development of POC remains confined to PSA detection because PSA-based functionalisation techniques are very stable and convenient.

Metabolomics POC platforms. POC platforms for metabolic biomarkers have also been developed. The development of POC platforms for metabolomics is mainly driven to the cost and bulkiness of the equipment typically used for metabolites quantification. This also led to the development of commercial colorimetric and fluorescence assay kit to be used in combination with a spectrophotometer [222]. The current panel of metabolites most often targeted is wide and include glucose, amino acids, choline, sarcosine, lactate, creatinine, cholesterol and triglycerides, [2]. Besides glucose meters, today well-established, the interest of the research community is moving towards different metabolites.

Biosensors for the quantification of amino acids profile, with particular reference to L-types, which are more relevant for humans, have been documented in the literature [223]. The bioreagents typically include L-amino acids oxidase (LAAOx), which can oxidase any type of LAA while producing hydrogen peroxide [49]. Both electrochemical and optical methods have been used for the quantification of LAA with a similar performance [223]. Among the targeted amino acids, glutamate is one of the most popular, especially for its link to neurodegenerative diseases [224]. Glutamate biosensors typically employ glutamate oxidase (GlOx) [49]. The interest in the quantification of choline is related to its involvement in several diseases [225]. Choline biosensors typically employed the specific enzyme choline oxidase (ChOx), which oxidases choline while producing hydrogen peroxide. The produced hydrogen peroxide has been used to develop both electrochemical and optical biosensors [225]. Similarly, sarcosine oxidase (SaOx) and lactate oxidase (LaOx) have been developed [2]. Authors in [226], for instance, employ SaOx for the colorimetric determination of sarcosine in the urine. Authors here demonstrate that the developed assay is capable of differentiating people with PCa from the healthy group [226]. However, the authors employ

a benchtop spectrophotometer to run the experiment, thus no integrated platform has been achieved here [226]. Both electrochemical and optical methods have been used for lactate sensing [2][227]. Creatinine level is being currently tested for renal deficiencies [2]. The chemistry involved in creatinine biosensing is slightly more complicated since it involves creatininase (CNN) and creatinase (CTN) to convert creatinine in sarcosine. Sarcosine is then measured by employing SaOx [228]. POC platform monitoring lactate, cholesterol, triglycerides, and other lipids are getting progressively popular for the management of CVDs [2].

Authors in [229] demonstrate the use of a CMOS sensor and an LED to provide comparable results to a commercial spectrophotometer for the colorimetric determination of bacterial concentrations. This work shares a similarity with the work presented in this thesis regarding the setup utilised and the colorimetric approach. However, the work in [229] uses a commercial CMOS sensor and no microfluidic integration was achieved. Similarly, authors in [230] employ a CMOS sensor to quantify H_2O_2 using a colorimetric approach. However, also in this case, there is not monolithically integration and the samples are retained into reaction cuvettes.

Multi-analyte metabolomics POC platforms. Lab-on-chip devices are also being developed for quantifying multiple compounds [231]. Authors in [232], for instance, present a microfluidic lab-on-chip quantifying human body metabolites, using sub microliter droplets as reaction chambers. Authors demonstrate the suitability of the platform for glucose, glutamate, and pyruvate individually [232]. The lab-on-chip takes advantage of an electrowetting chip which transport and mix the sample and the reaction for the initiation of a colorimetric reaction [232]. The reaction takes place in microchannel fabricated by Teflon, perylene and glass. Chemistry and working principle developed in this work are very similar to the one adopted in this research project. However, the platform is not integrated and a single external photodiode is used to monitor the absorbance during the reaction [232]. The developed lab-on-chip also does not allow parallel assays [232]. PDMS microfluidic channels have been employed on the CMOS-based spectrophotometer system reported in [233]. The system was used for the determination of glucose, uric acid, and cholesterol. However, PDMS microfluidics is developed onto a glass substrate. The integration of microfluidics with the sensor array was not achieved in this work [233]. A more complex PMMA-based system has been developed by authors in [234] for the quantification of sorbic acid. Also in this case, microfluidic chip and sensors are two physically separated units.

Table 2.9 State of the art of IC-based POC platforms.

Analytes (examples)	Common techniques	References
DNA and RNA (e.g. from virus, bacteria, fungi, aberrant cells)	Polymerase chain reaction. Detection methods: electrochemical.	[1], [2], [215]
Proteins (e.g. enzymes, antibodies, antigens, hormones, etc.)	Enzyme-linked immunosorbent assay (ELISA). Detection methods: optical and electrochemical.	[1], [181], [216]–[221]
Metabolites (e.g. LAA, glutamate, choline, sarcosine, lactate, creatinine, etc).	Enzyme-based assay. Detection methods: optical and electrochemical.	[49], [223], [232], [233], [224]–[231]
Other biomarkers (e.g. cells)	Various	[1], [2]

2.6.2. Market Review

Sensing devices currently on the market for biomedical applications can be mainly divided into in-home or in-laboratory based diagnostics. While the market for in-home care monitoring has proliferated, the rate of acceptance of the new biosensors for the hospital or laboratory-based diagnostics has been comparatively lower [16].

In-home POC devices are designed to be used by the generic public. This category of devices usually requires no or minimal sample pre-treatment, are cheaper, more robust and have a higher degree of portability. In-home POC can also take advantage of personal mobile devices such as smartphone or tablet for processing or data storage [235]. LFAs are the most commercially available tools for POC in-home testing [199]. Modern portable pregnancy tests are probably the widest spread example of LFA [2]. Semi-quantitative PSA lateral flow strips are also available on the market to help to diagnose PCa [221], [236]. However, glucose biosensors seem to have forged the most significant market share for in-home POC platforms [16]. Glucose biosensors account for approximately 85% of the entire biosensors market [2]. Most diabetics now regulate their condition at home by self-testing their blood with hand-held glucose meters [2]. Typically, two types of glucose sensors are commercially available in the market, namely electrochemical and optical. For effective management and to record patient history, most modern glucometers now have memory storage and computer interfaces so that the patients can keep track of their blood glucose levels over a period of time, and the data can then be shared with clinicians to prescribe a better course of medical treatment.

Whatever the working principle, glucose market is so vast that standardisation agencies published a set of guidelines for their development. The most commonly cited guideline for

glucose meter is from the International Organisation for Standards stating that the relative error of the measurement for glucose concentrations < 4.2 mM should be lower than 15% (95% confidence interval). The same quantity should be lower than 20% for glucose concentrations > 4.2 mM [1]. The Clinical and Laboratory Standard Institute indicates a requirement for meter results to be within 12.5% of laboratory results [1]. The Food and Drug Administration (FDA) has stipulated a maximum discrepancy of 10% between meter results and laboratory analysis [1]. Worryingly, independent studies indicated that not all the meters on the market are complainant with these recommendations [237].

Cholesterol monitoring devices are also finding new demand world-wide, and this biosensor segment is expected to grow at a rate of around 8% over the next five years [16]. There is also an increasing instance of disorders due to obesity and hormonal imbalance, creating an escalation of cholesterol levels in the blood.

In-laboratory based diagnostics are designed to be used by trained personnel. This category of devices can require sample pre-processing and can be more expensive and less portable than the previous class. In-laboratory based diagnostics usually aim to reduce the time patients spend in the emergency department and accelerate the clinical decision. They are also used for bedside testing or patients with reduced mobility. Acute conditions, such as stroke and sepsis, also gain advantages from the quick test provided by POC testing. A remarkable example of the category is the i-STAT by Abbott. The i-STAT is a ‘handheld blood analyser for with-patient testing aimed at improving the quality, cost, and operational efficiency of health’ [238]. The device is very versatile and allows to diagnose acute conditions in minutes. The i-STAT cartridges are available for a range of clinical tests, including cardiac markers, lactate, coagulation, blood gases, chemistries and electrolytes, and haematology [238].

The most successful commercial POC device capable of DNA sequencing is probably the CMOS-based Ion Torrent platform by Thermo Fischer Scientific [239]. The platform uses an ISFET sensor array together with the polymerase chain reaction technique [239]. First, the genome sequence is divided into millions of fragments, which are attached to beads allocated in microwells. Microwells are iteratively washed with solutions containing one of the four bases (adenine, cytosine, guanine, and thymine). When a test base attaches to its complementary base, hydrogen ions are released and sensed by the pH sensor. By iterating the washing step and by repeating the test over millions of pH sensors, it is possible to reconstruct the sequence of the molecule under analysis.

Figure 2.16 shows devices based on different technologies for biomedical applications, including optical, pH, amperometric, electrochemical nano-mechanical and thermal sensors [16]. Table 2.10 provides some examples of the currently available biosensors for the detection, diagnosis and monitoring of biomedically relevant analytes [16].

2.6.3. Discussion on platform affordability

Basing on the market review illustrated above, it is now possible to define the requirement about the cost of the platform. With reference to Table 2.10, glucose meters have a very low cost because they are used very frequently (more than once a day) by people affected by diabetes. However, the platform developed in this work target applications where the frequency of use is expected to be lower. Other platforms on the market have increased costs for both the reader and the test. The cost of the reader for these platforms ranges from £ 250 to £ 5200, while the cost per test is in the range of £1.5 - £10. For both the target applications of this work, we can assume a frequency of usage of once every three months (per patient). This is similar to other multi-analyte platforms in the market, such as Accutrend Plus (Cobas-Roche) and CardioChek PA (PTS diagnostics) – see Table 2.10.

Table 2.10 Examples of commercial POC platforms. Devices information have been retrieved from the respective websites of the platforms. Reproduced and modified from [16].

Device	Analyte/test	Sensor type	Assay time	Cost per test /reader
i-stat (*Abbott*)	Multiple: (Troponin I, O_2, Glucose, lactate, pH, Hematocritmany)	Electrochemical	2-5 min	T: £ 10 R: £ 5200
MiniOn (*Nanopore technology*)	DNA sequencing	Nano-pore	-	T: n.d. R: £1000
CoagMax (*Microvisk*)	Blood viscosity	Micro-cantilever	-	n.d.
Contour (*Bayer*)	Glucose	Electrochemical (GDH)	< 30 s	T: < £ 0.5 R: £ 30
Optimum (*Abbott*)	Glucose	Electrochemical (GDH/NAD)	< 30 s	T: < £ 0.5 R: £ 30
Accu-check Performa (*Roche*)	Glucose	Electrochemical (GDH/PQQ)	< 30 s	T: < £ 0.5 R: £ 30
Accutrend Plus (*Cobas-Roche*)	Tot. Cholesterol Triglycerides Glucose, Lactate	Optical (absorbance)	30 s	T: < £ 1.5 R: £ 250
CardioChek PA (*PTS diagnostics*)	Total cholesterol, HDL, triglycerides, glucose, LDL, Ketones, Creatinine	Optical (absorbance)	2 min	T: £ 7.50 R: £ 700
Cholestech LDX (*Alere*)	Cholesterol, HDL, glucose, triglycerides, LDL, ALT , AST and hs-CRP	Optical (absorbance)	5 min	T: £ 8.50 R: £ 950
DCA Vantage (*Siemens Healthineers*)	HbA, HbF, HbS, HbC, HbE in urine	Immunological	-	T: £ 9.11 R: £ 4000
In2it (*Provalis*)	HbS and HbD	Boronate affinity	-	T: £ 6 R: £ 1500
Q-POC (*Quantum DX*)	HPV or Tuberculosis or STI	Functionalised Nanowire FET	20 min	T: $ 10 R: $ 1000

Figure 2.16 Reproduced and modified from [16]. *(a) i-STAT (Abbott), (b) In2it (Provalis), (c) coagmax (Microvisk), (d) Q-POC (Quantum Dx), (e) Cholestech (Alere), (f) Optium (Abbott), (g) Genome sequencer (Ion torrent), (h) DCA Vantage (Siemens), (i) Contour (Bayer), (j) MiniOn (Nanopore technology), (k) CardioChek PA (PTS diagnostics), (l) Prototype from DNA electronics, (m) Accutrend Plus (Cobas-Roche).*

Therefore, similar costs requirement can also be set. Specifically, maximum target costs for the reader and cartridge were assumed to be £5200 and £10, respectively.

The cost of the reader can be easily met by using off-the-shelf electrical components. However, the maximum target price of the cartridge is a challenging requirement. This is because the disposable cartridge integrates CMOS sensors, biological reagents, and microfluidic systems. The requirement can potentially be met when cartridges are mass-produced but, in this project, cartridges were not mass-produced. However, the methods and procedures developed in this project must be suitable for mass-production.

The cost of the cartridge could be reduced by integrating reusable sensors in the reader rather than in the cartridge. However, with reference to the versatility requirement, a reduction of the functionalities of the platform is not advised at this stage. It is also worth outlining that the platform can be used for many applications, meaning that only one reader can be used for several applications. This can produce additional cost savings.

Thus, the cartridge was developed with integrated CMOS sensors. Optimisation strategies aiming to reduce the cost for specific applications can be investigated as part of future works.

2.7. Summary of the Chapter

In conclusion, the quantitative requirements of the POC platform have been discussed and set in this chapter. Strategies required to meet the requirements have also been identified. Table 2.11 summarises the discussion.

Table 2.11 Summary of the quantitative requirements of the platform. The strategies identified to address the requirements are also summarised.

Requirement	Criterion	Strategy
Affordability	- Reader cost < £5200[1]. - Test cost < £10[1].	- Use well-established techniques for sensors and readout. - Use processes suitable for mass-scale production (e.g. CMOS, moulding, enzyme printing). - Use colorimetry
Sensitivity	- Ischemic stroke: results comparable to NHS standard. - PCa: specificity ≥ 0.32 [18][2]. - Relative error of the measurement in the order of 15-20%[3].	- Use well-established detection methods. - Optimise the platform to achieve the requirement. - Evaluate the platform with clinical samples.
Specificity	Develop a biomarker panel specific to PCa and ischemic stroke	- Identify and use multiple biomarkers. - Discuss biomarkers with experts. - Test the biomarker with clinically sourced samples.
User-friendly	- Use blood/plasma/serum[1,2]. - Minimal sample pre-processing[1,2]. - Low sample volume (tens of µL)[1,2]. - Plug and play device[1].	- Integrate sensors, fluidics and biological reagents. - Use blood/serum/plasma. - Develop the platform to be used with a small volume. - Develop an intuitive user interface. - Minimise user operations.
Rapid	- Complete test in minutes[1].	- Estimate substrate from initial reaction rate.
Robust	- Compensation of sample-to-sample and device-to-device variations. - Capable of detecting failure[1].	- Develop a solution to standardise the measurement (controls). - Develop strategies for the safe failure of the platform (e.g. invalidate result).
Equipment-free	- No other external equipment required for running the test.	- Embed all the required equipment into the platform.
Delivered	- Reagents must have shelf-life in the order of weeks/months[1].	- Develop established strategies for reagent stabilisation and storage (lyophilisation).
Multi-analyte capability	- Measure 2 or more metabolites at the same time[1,2].	- Use multiple sensors (array). - Develop a sample handling system (microfluidics).
Versatility	- Demonstrate multiple biomarker detection. - Potential use of other sensors.	- Use custom CMOS chip. - Integrate fluidics monolithically. - Beware of other possible use of the platform (e.g. use ISFET). - Demonstrate platform usage with multiple biomarkers.

[1] Assumed from market review.
[2] Assumed from the literature review.
[3] Assumed form glucose meters guidelines.

Chapter 3: Embedded Platform Development

3.1. Introduction

The present chapter describes the development of the proposed embedded platform. Requirements, simulations, fabrication, and design consideration are also discussed. Table 3.1 illustrates the contribution to each activity discussed in this chapter.

The platform is composed of a cartridge, a reader, and a graphical user interface (GUI) – see Figure 3.1. The cartridge is the core of the platform. It is meant to be disposable when mass-produced, but it has been reused in this project due to limited resources. It integrates the CMOS chip, passive microfluidics, and on-chip reagents onto a ceramic package. In this chapter, the sensing platform is illustrated. Microfluidics and bioreceptors integration is illustrated in the next chapter. The cartridge is designed for the colorimetric detection of multiple metabolites. This raises the question of whether the cartridge requires a single sensor or more sensors organised into an array format.

Typically, a biosensor with one transducer provides a single result. An apparatus containing multiple sensors can deliver multiple or single results. Image sensors, for example, provide multiple readings. Multiple readings can be combined for providing a lower number of readings.

Table 3.1 Table of contributions for the activity presented in this chapter.

Task / Activity presented in Chapter 3	Main investigators
Identification of a potential metabolic biomarker panel for prostate cancer	**- Valerio F. Annese** (literature survey) - Prof. Rob Jones[2] (discussion/validation)
Identification of a potential metabolic biomarker panel for ischemic stroke	**- Valerio F. Annese** (literature survey) - Dr Samadhan Patil[1] (discussion/validation)
Design of the CMOS chip	- Dr Mohammed Al-Rahawani[1] - Dr Christos Giankulovitch[1] - Dr James Beeley[1]
Fabrication of the CMOS chip	- Outsourced (Austriamicrosystems)
Development of the reader (hardware)	- Dr Mohammed Al-Rahawani[1] - Dr Christos Giankulovitch[1] - Dr Claudio Accarino[1]
Development of the reader (software)	**- Valerio F. Annese**
Development of the graphic user interface for both acquisition and data analysis	**- Valerio F. Annese**
Enzymatic reactions modelling and simulations	**- Valerio F. Annese**
Platform testing	**- Valerio F. Annese**
Affiliation at the time of completion of the activity: [1]*Microsystem Technology Group, James Watt School of Engineering, University of Glasgow.* [2] *Institute of Cancer Sciences, University of Glasgow, Beatson West of Scotland Cancer Centre, Glasgow*.	

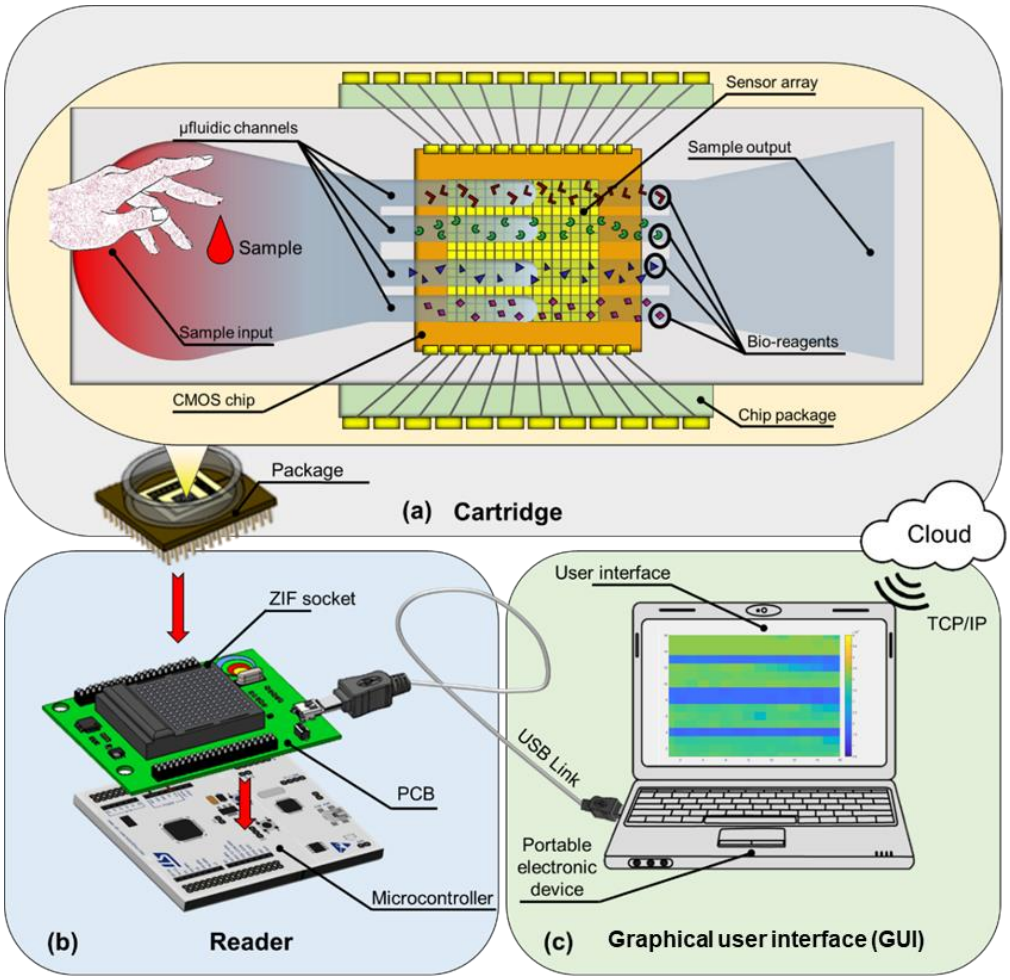

Figure 3.1 The overall architecture and components of the developed platform: (a) the cartridge, (b) the reader, and (c) the GUI. This is a high-level diagram and it is not in scale.

When combined altogether, data coming from multiple sensors can be used to provide a single output. Microstructures, such as microfluidic channels, can provide physical separations allowing to confine target reactions in different zones of a sensing area. For example, authors in [240] use a microfluidics-based device for simultaneous testing of a plurality of separate nucleic acids in a barcode-like layout. Also, authors in [241] disclose an apparatus capable of performing test and controls at the same time from the same sample. The developed platform uses an array of optical detectors. Similarly to [240] and [241], this platform aims to perform multiple simultaneous measurements. Thus, the use of an array of optical detectors is the most suitable configuration for this platform. The use of multiple independent sensors has also the potential to reduce the fixed-pattern-noise of the array and improve the overall SNR of the measurement [242].

The optical detectors used in this work were custom developed. Arguably, the use of a commercial camera chip for this project would have also been possible. However, it is worth stressing once again that this work is part of a larger vision aiming to develop a multimodal platform. As such, the use of a commercial camera chip would have reduced the functionalities of the platform to optical detectors only and would have not satisfied the versatility requirement. The use of a custom sensing platform enabled the integration of other sensors (i.e. ISFET) to be used in conjunction with optical sensors. The use of electrochemical and optical sensors at the same time on this platform has been demonstrated by other members of my research group [243]. This would not have been possible with a commercial camera chip.

The cartridge connects to the reader through a zero-insertion force (ZIF) socket. The reader is composed of a custom printed circuit board (PCB) and a commercial microcontroller board. It is employed for sensors addressing and data digitisation. It also handles raw data and sends them in real-time to the GUI through USB link.

The GUI is a software running on a portable electronic device. It allows user interaction as well as data visualisation, analysis, and storage. The platform can also take advantage of the TCP/IP capability of the portable electronic device for uploading the result of the test onto a cloud-based storage platform.

3.2. The Cartridge

The cartridge integrates the CMOS chip, one or more biorecognition elements and the passive microfluidics (illustrated in the next chapter). All the parts are integrated onto a ceramic chip package. Figure 3.2 shows a diagram of the cartridge with four microfluidic channels.

3.2.1. Target applications

The platform is meant to be versatile and capable of adapting to a wide range of biological assays with no or minimal modifications. However, two case studies have been selected to demonstrate the diagnostic capability of the platform.

The first proposed application of the platform is PCa diagnosis. This application aims to demonstrate the potential of POC platforms for early diagnosis of deadly diseases, especially for use where the current standard lacks reliability.

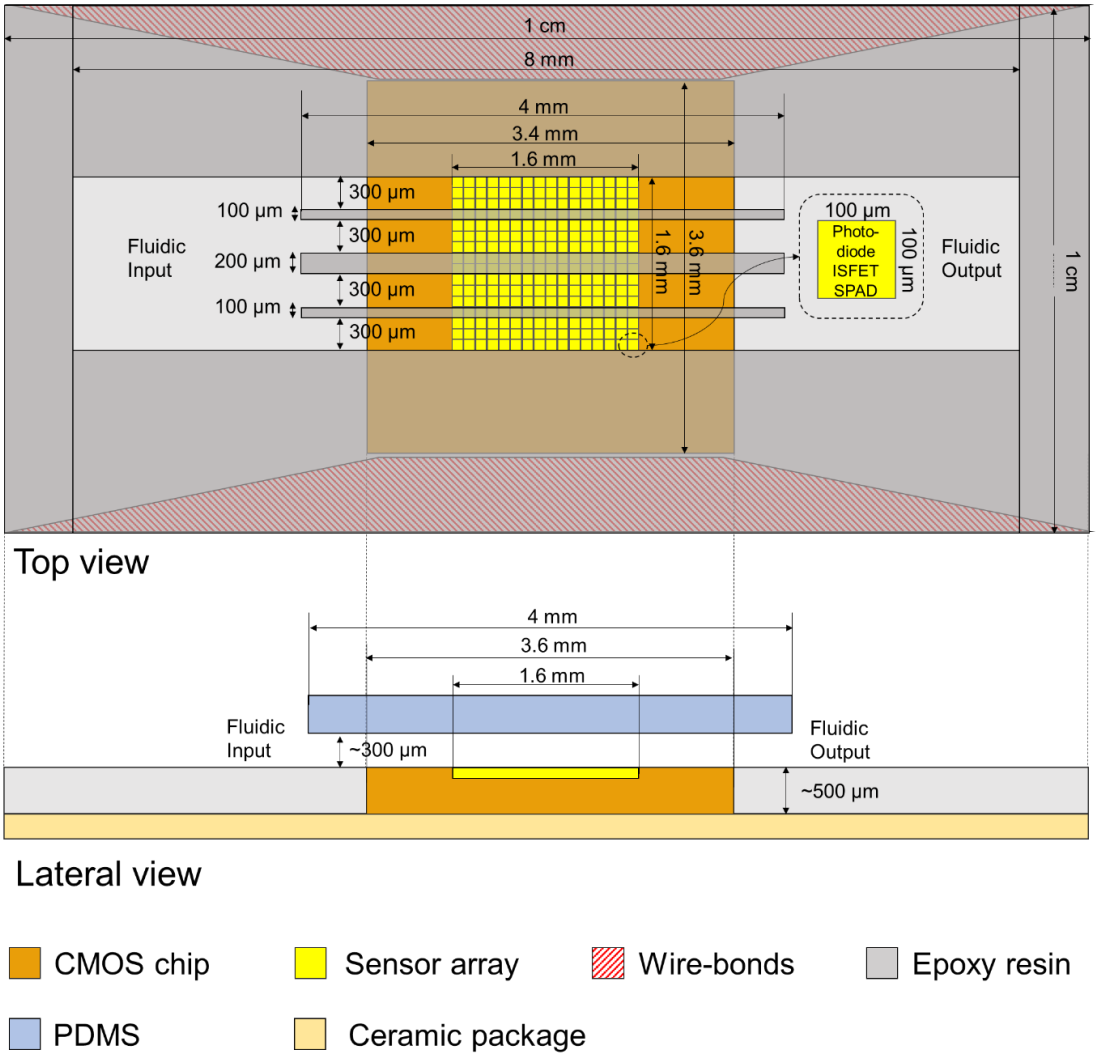

Figure 3.2 Top view (top) and later view (bottom) of the cartridge. Biological reagents have been omitted in the schematic for clarity. The diagram is in scale. Further microfluidic structures have been analysed and developed in this project.

As introduced in Chapter 2, the current standard alone, PSA blood testing, is not reliable enough, and invasive methods are usually used in conjunction with the blood test. In this frame, the proposed platform is suggested for the quantification of metabolic biomarkers to be used in conjunction with the PSA testing for non-invasive improved diagnosis. Four analytes have been selected for this application, namely total LAA, glutamate, choline, and sarcosine. The selection of the metabolites panel is based on the literature review presented in Chapter 2. Subsequently, the metabolites review has been discussed with a team of cancer researchers, led by Prof. Robert Jones, professor of clinical cancer research at the University of Glasgow. The team of cancer researchers have recognised that there is merit in the selected metabolites panel, although metabolomics is still a relatively unexplored field in PCa. The

relation between LAA, glutamate, choline, and sarcosine and PCa are well-known to the research community. The correlation between sarcosine and the disease is still controversial, and this study can shed light on the contentious matter. The development of such a platform has the potential to provide additional information which, together with PSA testing, can improve the early diagnosis of PCa.

The second proposed application of the platform is the diagnosis of ischemic stroke. With this application, the aim is to highlight the potential of POC platforms for acute medicine, where timing is vital. Two metabolites have been selected for this application, namely creatinine and lactate. The selection of the metabolites is based on a similar procedure involving literature review and discussions with experts in the field including Dr Samadhan Patil, lecturer of medical engineering at the University of York, and Prof Jesse Dawson, professor of stroke medicine at the Institute of Cardiovascular & Medical Sciences, University of Glasgow.

In summary, six tests have been selected for this research project, LAA, glutamate, choline, sarcosine, lactate, and creatinine. It should be clarified that the total profile of LAA is not a single metabolite but, throughout this work, it will be referred to as a metabolite.

3.2.2. Detection strategy for the target metabolites

All the selected metabolites were detected with a colorimetric approach using specific enzymes interacting with the target analytes for producing hydrogen peroxide. The adopted enzymatic reactions are reported in the following [49]:

LAA: $\mathrm{L-amino\ acid} + H_2O + O_2 \xrightarrow{L-amino\ acid\ oxidase\ (LAAOx)} \alpha - oxo\ acid + NH_3 + H_2O_2$

Glutamate: $\mathrm{Glutamate} + H_2O + O_2 \xrightarrow{Glutamate\ Oxidase\ (GlOx)} 2 - oxoglutarate + NH_3 + H_2O_2$

Choline: $\mathrm{Choline} + H_2O + O_2 \xrightarrow{Choline\ oxidase\ (ChOx)} betaine + H_2O_2$

Sarcosine: $\mathrm{Sarcosine} + H_2O + O_2 \xrightarrow{Sarcosine\ oxidase\ (SaOx)} glycine + formaldehyde + H_2O_2$

Lactate: $\mathrm{Lactate} + O_2 \xrightarrow{Lactate\ oxidase\ (LaOx)} pyruvate + H_2O_2$

Creatinine:

$$\begin{cases} \mathrm{Creatinine} + H_2O \xrightarrow{Creatininese\ (CNN)} creatine \\ \mathrm{Creatine} + H_2O \xrightarrow{Creatinase\ (CTN)} Sarcosine + Urea \\ \mathrm{Sarcosine} + H_2O + O_2 \xrightarrow{Sarcosine\ oxidase\ (SaOx)} glycine + formaldehyde + H_2O_2 \end{cases}$$

The produced H_2O_2 is proportional to the concentration of the analyte of interest. The production of H_2O_2 was monitored by a colorimetric probe which changes its absorbance property depending on the H_2O_2 level. Two different probes were employed, namely

o-dianisidine and the system phenol/4-aminoantipyrine (4AAP). The target reaction for H_2O_2 are reported below:

$$\boldsymbol{O-dianisidine}: o-d\text{ianisidine (reduced)} + 2H_2O_2 \xrightarrow{Peroxidase\ (HRP)} o-d\text{ianisidine (oxidised)} + 2H_2O$$

$$\boldsymbol{Quinone-imine}: Phenol + 4AAP + 2H_2O_2 \xrightarrow{Peroxidase\ (HRP)} Quinone-imine + 2H_2O$$

Thus, for each selected test, at least two enzymatic reactions are required. However, the ratio of the concentration of the enzymes within the same reaction chain can be tuned. In this work, an increased level of HRP was adopted. According to the Michaelis-Menten model, this ensures that when H_2O_2 is produced, it is promptly used for the oxidation of the probe. Consequently, the reaction rate of the entire reaction chain can be approximated to the slower reaction, i.e. the one leading to the production of hydrogen peroxide. There are two main parameters to be considered in the selection of the hydrogen peroxide probe, namely the extinction coefficient and the wavelength absorbance range. Commercially sourced o-dianisidine and quinone imine have extinction coefficients of 7.5 $mM^{-1}cm^{-1}$ and 12 $mM^{-1}cm^{-1}$ at 500 nm, respectively [222]. The effective extinction coefficient for this platform has been measured and reported in Figure 4.13. Table 3.2 summarises the selected panel of metabolites together with their physiological range, the enzymes employable for their colorimetric determination, and related kinetics constants.

3.2.3. Simulations of colorimetric reactions

Method. A Matlab-based model for the simulation of a generic colorimetric assay was developed and used for preliminary assessment of the platform requirements. The simulations aimed to identify critical parameters in the development of the platform.
The implemented simulation employed the Michaelis-Menten model and rate-equations to simulate the enzymatic-reaction.

Table 3.2 Summary of the target metabolites to be measured by colorimetric method.

Analyte	**Physiological range (µM)**	**Application**	**Enzyme**	**Km (mM)** [49]
LAA profile	1700 - 4600 [244]	↑ in PCa	LAAOx	0.17 - 116.5
Glutamate	40 - 150 [244]	↑ in PCa	GlOx	0.15 - 10
Choline	10 - 40 [245]	↑ in PCa	ChOx	0.05 - 213
Sarcosine	0 - 20 [246]	↑ in PCa	SaOx	0.01 - 142.3
Lactate	300 - 2000 [247]	↑ in stroke	LaOx	0.039 - 103
Creatinine	100 - 150 [248]	↑ in stroke	CNN CTN SaOx	0.17 - 350 0.034 - 53.2 0.01 - 142.3

Beer-Lambert's law was then applied for estimating light absorbance and light transmittance. Michaelis-Menten equation and Beer-Lamber law are reported here for ease of reading:

$$\frac{d[P]}{dt} = \frac{V_{max}}{1 + \frac{K_m}{[S]}} \tag{3.1}$$

$$A = -\log T - \log\frac{I}{I_0} = \varepsilon \cdot L \cdot [P] \tag{3.2}$$

Where [P] is the concentration of the product, V_{max} is the maximum rate of the reaction, K_m is the Michaelis-Menten constant, [S] is the concentration of the substrate, A is the light absorbance, T is the light transmission, I_o is the light intensity from the light source, I is the light intensity transmitted from the sample, ε is the extinction coefficient, L is the optical length (in this work L coincide with the height of the microfluidic channel). Numeric values used in the simulations are summarised in Table 3.3.

The simulation assumed that light with constant power and fixed wavelength is shone onto an ideal photodetector (i.e. one with unity quantum efficiency). The wavelength was in the absorbance range of the H_2O_2 probe (i.e. around 500 nm) and adequate for the maximum responsivity of the ideal photodetector. The model also did not include any source of noise. The implemented Matlab model is reported in Appendix A.

Results. Figure 3.3 summarises the primary simulated outcomes. The results of the simulations led to several design considerations. Primarily, it is clear from Figure 3.3(a) that the trend of light transmission over time is not linear. Substrate concentration is the unknown parameter that the system aims to quantify.

Generally, the reaction rate increases with the substrate concentration. As shown in Figure 3.3(b), the reaction rate is the highest at the beginning of the reaction, and it progressively decreases until the end of the reaction. The reaction duration is not known apriori and depends on all the platform variables.

Table 3.3 Simulation parameters.

Parameters	Simulation value /range	Reference
[S]	0 – 200 µM	Target range – worst case (see Table 3.2)
K_m	3.5 – 9.5 mM	Typical values for oxidation enzymes [49]
V_{max}	5 - 30 μMs^{-1}	Typical values for oxidation reactions [49]
ε	4 - 11 $mM^{-1}cm^{-1}$	Typical values of commercial colorimetric probes [222]
L	50 - 750 µm	Typical heights of microfluidic channels [249]

Kinetics constants, namely K_m and V_{max}, also have a significant impact on the system response. Specifically, the reaction rate increases when K_m is reduced, or V_{max} is increased. K_m and V_{max} typically depend on the selected chemistry and the concentration of the individual reagents employed. Generally, K_m depends on the specific enzyme and cannot be easily modified. However, V_{max} can be adjusted by varying the concentration of the enzymes. The rate of light transmittance is also higher when increasing the extinction coefficient, which depends on the selected light-absorbing species and the working wavelength chosen. With all the kinetics variables fixed, the light transmittance trend and the estimated reaction rate are also strongly affected by the optical length of the system.

The following design considerations can be made, based on the results of the simulations:

- A rate-analysis approach for the estimation of the substrate concentration is viable with the adopted chemistry since different levels of the substrate correspond to different initial reaction rates. This method was then selected.
- ε, K_m and V_{max} have to be tuned when designing the optimal reaction to avoid saturation and match the range of the analyte to be measured.
- Strictly from the reaction point of view, the optical length L has to be maximised to ensure the sensor can easily detect the drop in absorbance. However, there is a trade-off between maximising L and microfluidic performance, which will be discussed later.

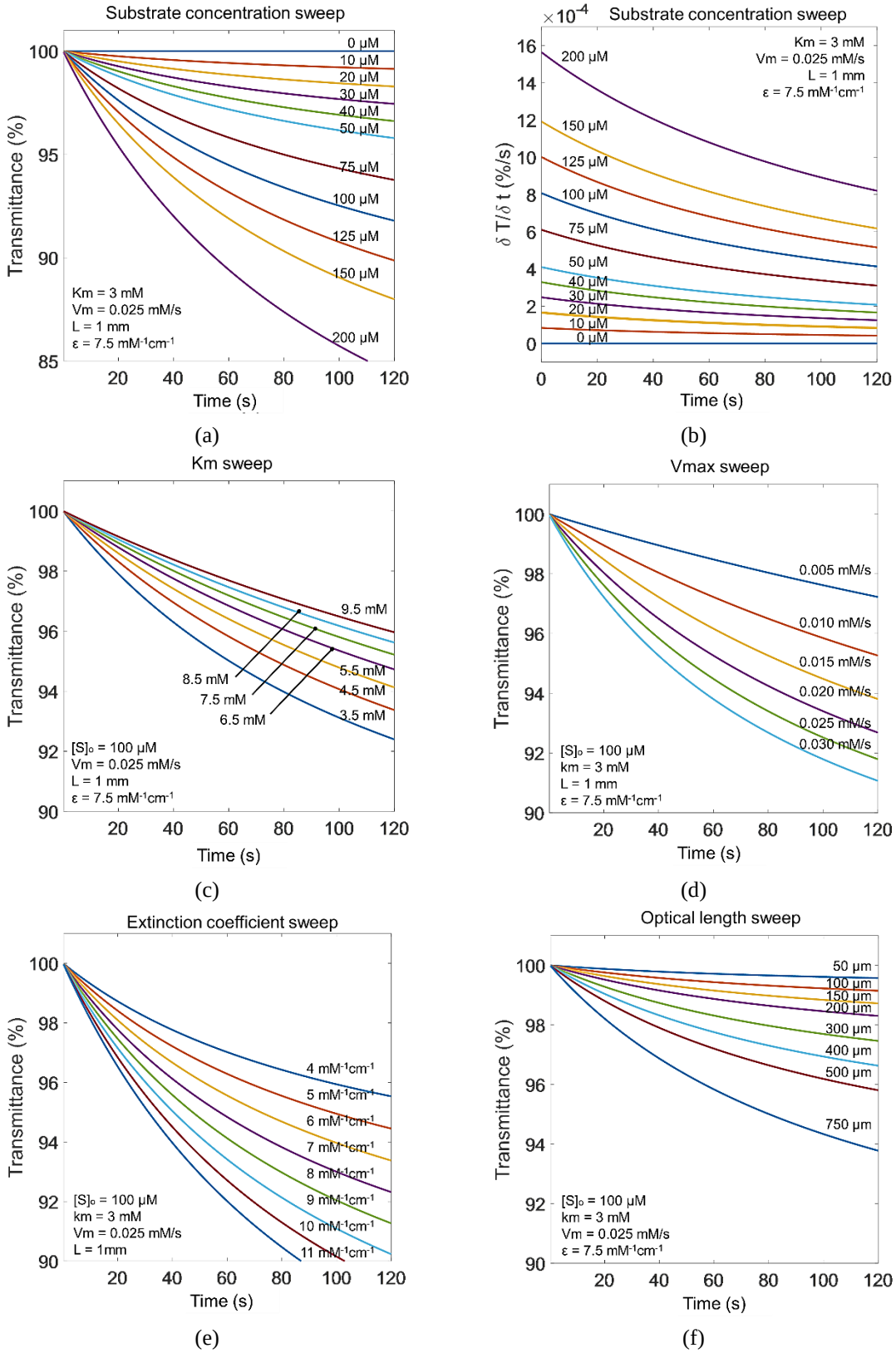

Figure 3.3 Simulated colorimetric assays. (a) Transmission and (b) reaction rate with substrate concentrations sweeping from 0 µM to 200 µM. (c) K_m sweep from 3.5 mM to 9.5 mM. (d) V_{max} sweep from 5 µMs^{-1} to 30 µMs^{-1}. (e) Extinction coefficients sweep from 4 to 11 mM^{-1}cm^{-1}. (f) Optical length sweep from 50 µm to 750 µm. Simulations parameters are shown in Table 3.3

3.2.4. The Multicorder chip

This research project is part of the project Multicorder project. The Multicorder project led to the development of several CMOS-based chips for measuring the personal metabolome. A particular version of the developed chip herein referred to as the CMOS chip, has been employed in this project. The CMOS chip was designed by a group of researchers from the Microsystem Technology (MST) group at the University of Glasgow. Dr M.A. Al-Rawhani was the principal designer [85].

The CMOS chip, presented in Figure 3.4(a), is a 16x16 array of multi-sensors elements, herein also referred to as pixels or clusters. Each multi-sensor element integrates a photodiode, an ISFET and a SPAD. Within the cluster, sensors are aligned in the north-south direction, as shown in Figure 3.4(b). The interface electronics can address sensors individually or simultaneously [85]. Each cluster has a size of 100×100 μm^2. Thus, the whole array occupies a total area of approximately 1.6×1.6 mm^2, in the centre of the chip. The entire chip occupies an area of 3.4x3.6 mm^2 (see Figure 3.4(c),(d)). The electronic circuitry embedded into the cluster is mainly located on the west side of the sensors. Sixty-four pads are equally distributed on the west and east side of the chip. Alignment marks (crosses and squares) are symmetrically placed on the north and the south side of the multi-sensor array.

The CMOS process selected for the design of the chip was the 0.35 μm high voltage process with four metal layers (‘H35B4’ technology). The constraints leading to the selection of this technology are linked to the presence of SPADs on-chip, requiring a high reverse bias voltage. Mainly, the H35B4 process enables the use of a deep n-well that allows the SPADs to operate at a high breakdown voltage with minimal interference with other close devices.

A schematic representation of the cluster manufacture with the selected technology is presented in Figure 3.4(e). The schematic representation is not in scale (information about layer thickness is confidential), and some design structures have been omitted for the sake of clarity. The fabrication of the chip was outsourced to Austriamiscrosystems (a different company for manufacturing the CMOS chip might be used in future). After the manufacture, bare chips were diced and sent to the MST group.

The CMOS chip and different iterations of the chip within the same project have been employed in related works. The ISFET array of the CMOS chip has been employed to quantify on-chip urea [243], [250], and glucose [243], [251]. However, many challenges associated with the use of the ISFET arrays had to be addressed by additional post-fabrication of the chip [252].

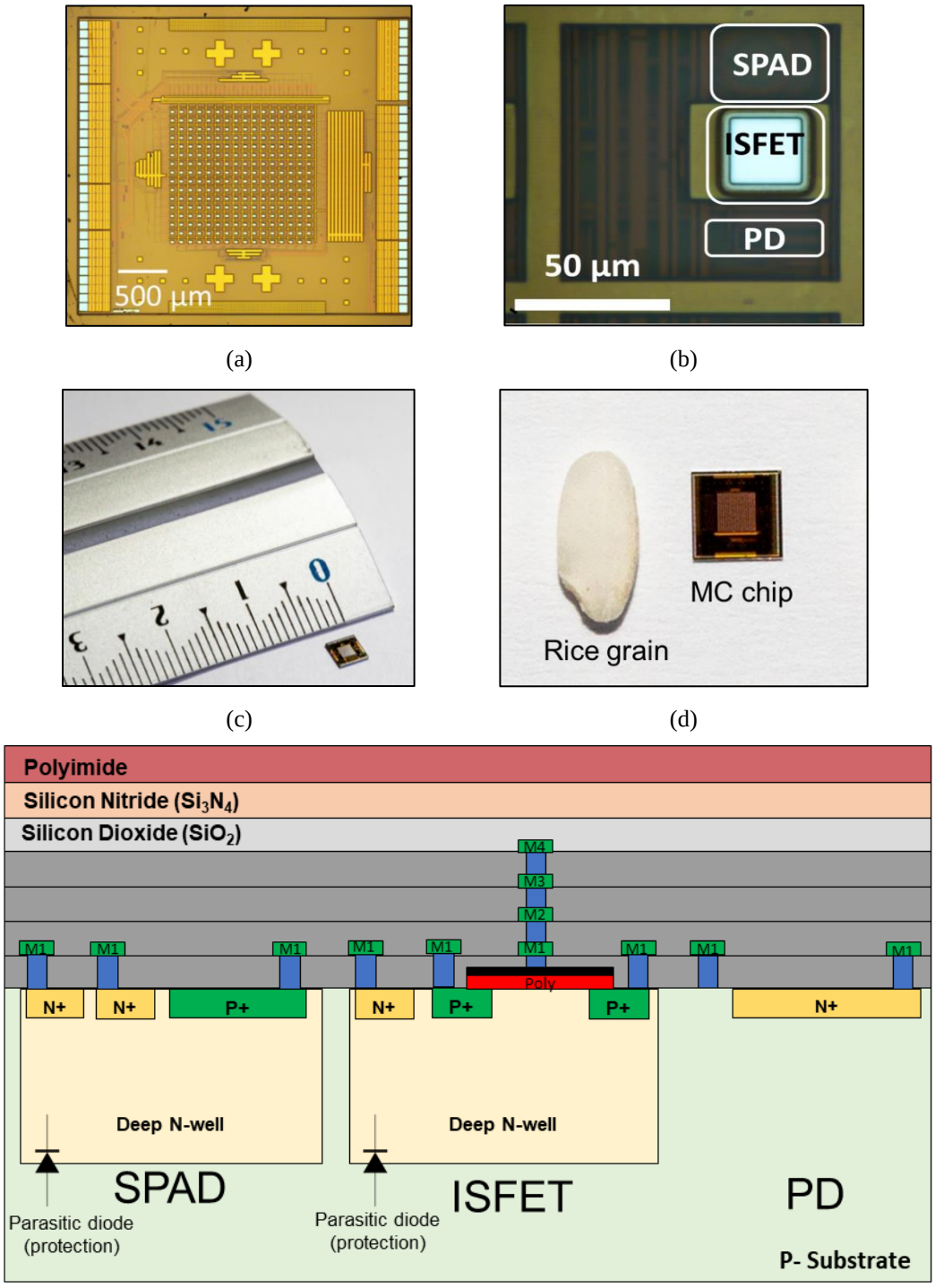

Figure 3.4 (a) Micrograph of the CMOS chip. The multi-sensor array is located at the centre of the CMOS chip. 64 pads are equally distributed on the west and the east side of the chip. Alignment markers are located on the north and south side of the sensor array. (b) Micrograph of a single multi-sensor element of the CMOS chip. Sensors are located on the east side of the cluster. Electronic interfaces are mainly located on the west side of the cluster. (c), (d) The size of the CMOS chip compared to a ruler and a rice grain. (e) Schematic representation of the multi-sensor element fabricated with CMOS technology. Schematic is not in scale, and some components are omitted for clarity. Reproduced and modified from [85]. *PD: photodiode.*

The SPAD array of the CMOS chip has also been adopted for chemiluminescence experiments, leading to the quantification of urate [250]. The fabrication of resonant nanostructures enabled the capability of performing local surface plasmon resonance experiments [250]. The photodiode array has been used for immunoassays [216]. In [84], by fabricating micro-well on top of the active area, the photodiode array was also used to simultaneously determine with colorimetric assay choline, xanthine, sarcosine and cholesterol. Remarkably, the ISFET and the photodiode arrays have been used to perform chemical multiplexing and quantify cholesterol and glucose simultaneously without any physical separation [243].

3.2.5. The photodiodes array

In this project, only photodiodes were employed. Accordingly, this paragraph describes the aspects of the CMOS chip relevant to this work. The reasons leading to the use of photodiodes are discussed here. According to the strategy previously described, an optical sensor must be used. Thus, the use of the ISFET is excluded. Potentially, both SPAD and photodiode could have been employed for colorimetric assays. They mainly differ in their dynamic range, with the SPAD being able to detect light with lower intensity. However, in this application, the device aims to measure the variation in the transmittance of light shown onto the device with tuneable initial light intensity. It is more convenient to use high light intensity for two reasons. First, high-intensity light creates a more substantial absolute transmittance drop. Secondly, the system is more stable to environmental noise. Both factors contribute to the increase in SNR. Photodiodes also did not require large reverse bias and showed excellent reliability in a real-life scenario.

The photodiode employed in this project is a p-n junction. As shown in Figure 3.5(a), the n-layer has a polygonal shape, designed to optimise the area considering both the surrounding electronics and the design rules. The total area of the n-layer is approximately 38.4 μm^2. The n-layer was diffused directly in the p-substrate, thus creating a p-n junction.

Photodiodes are organised in a 16 x 16 array format, according to the schematic in Figure 3.5(b). The addressing of the appropriate pixel in the array is performed by using row and column addressing signals, $rsel_i$ and $csel_i$ - respectively. 16 *rsel* signals ($rsel_1, \ldots, rsel_{16}$) and 16 *csel* signals ($csel_1, \ldots, csel_{16}$) are provided by two 4x16 decoders, embedded in the CMOS chip (addressing block shown in Figure 3.5(b)). Both the decoders are operated using four digital control signals, delivered to the CMOS chip by the reader. For each couple of $rsel_i$

and $csel_i$ signals, a single pixel is uniquely addressed. Each pixel integrates one photodiode and its respective readout electronics. The proposed readout method, usually referred to as accumulation mode, is provided by three transistors, namely Q_1, Q_2 and Q_3 [71].

Here the pixel circuit behaviour will be explained. Each of the pixels and their respective voltages, as described below for one pixel, are independent. The reading cycle starts with a reset pulse ($rst = V_{dd}$), bringing the node V_D of each pixel to a charged state by charging the parasitic capacitances of transistors Q1 and Q2. When rst = 0 V, Q_1 is off, and there is a direct path from V_D to ground through the photodiode. In the presence of light, the photogenerated current flows from V_D to ground, consequently discharging the parasitic capacitances. The discharge of V_D is buffered using a source follower configuration to the column read bus (V_{out1}), when the gate Q_3 is selected for the whole row of pixels with an external addressing signal (e.g. $rsel_1$). Only one row is activated at a time, using the row select (*rsel*) addressing signal.

In this implementation, the voltage V_D is inversely proportional to the detected light intensity. Thus, with reference to Figure 3.5(c), V_{D1} represents a situation where the detected incident light was less intense than for the pixel with V_{D2}. However, to have a more intuitive reading, the GUI numerically inverts data so that low values of voltage correspond to low light intensity. This is described in detail in the section dedicated to the GUI. The time between rst = 0 V and the reading of V_{out1} is generally referred to as integration time. Integration time must avoid the full discharge of V_D. In this implementation, the reset signal is a global signal but the readout is designed to give a rolling shutter output, as described in the next paragraph.

The output of the array does not use the bus signals (V_{out1}, …, V_{out16}) directly. An additional buffer stage was added in order to isolate the internal pixel circuits, raise the offset voltage of the output and dedicate only one output pad to connect to external circuitry. The output voltage (e.g. V_{out1}) of the pixel is buffered to the row read line, using a PMOS source follower configuration, composed by transistors Q_4, Q_5, Q_6. There is one PMOS source follower block for every array column. Only one column is activated at a time, using the column select (*csel*) addressing signals. One current source (Q_7) is used for all column select source followers. When a row and column select signals are enabled, a buffer path is forged to the output of the array, allowing for all the pixels to use the same output node sequentially. The output of the sensor array is then digitised using a 12-bit ADC embedded into the reader.

A comprehensive description of the CMOS chip can be found in [250], [253].

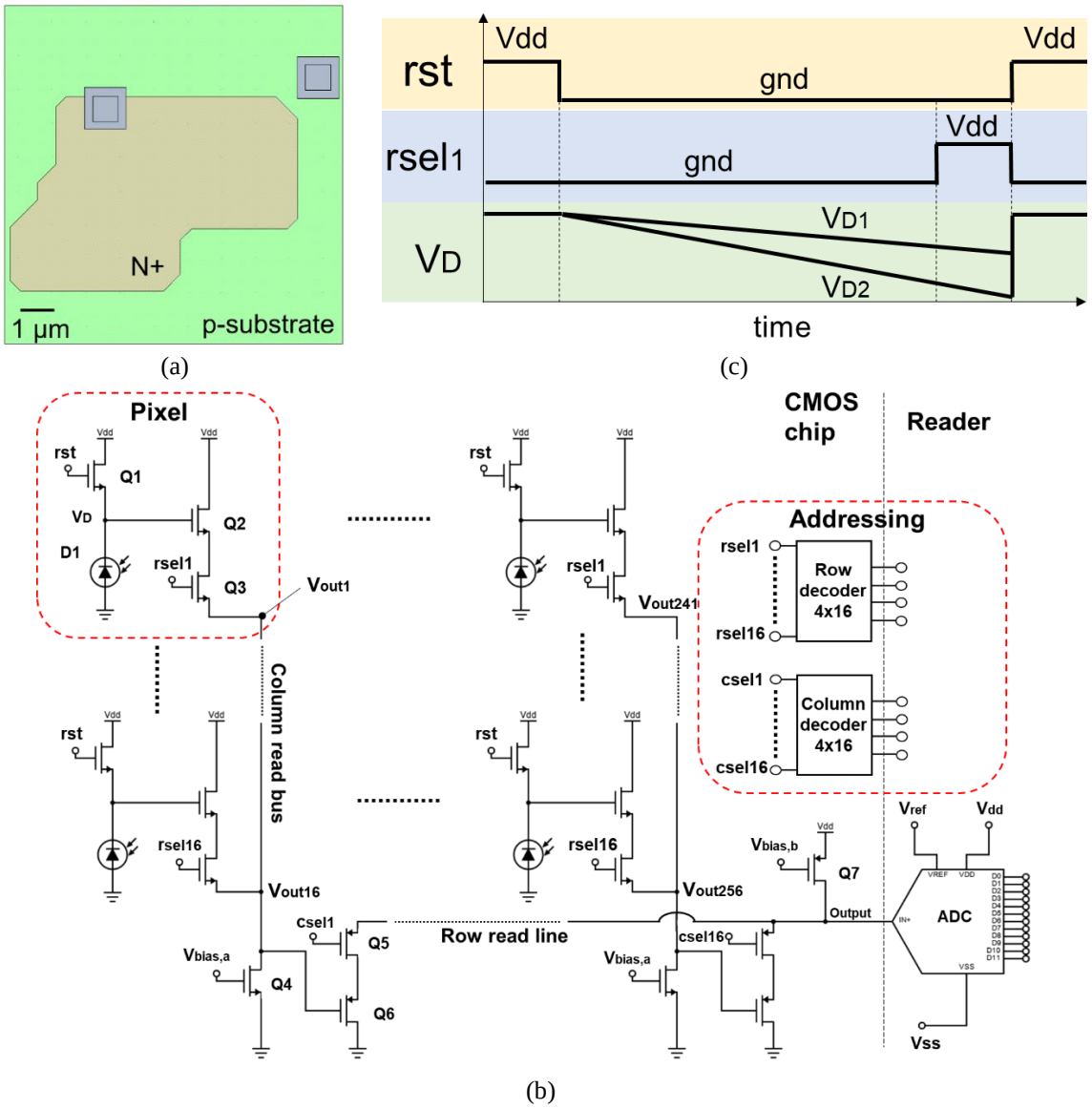

1719 *Figure 3.5 (a) Layout of the active area of the photodiode. (b) Schematic of the 16x16*
1720 *photodiode sensor array. (c) Time diagram for the operation of a single pixel.*

1721

1722 3.3. The Reader

1723 The reader is composed of a PCB (designed by Dr Claudio Accarino) and a microcontroller
1724 board. The PCB measured a compact 8.5x7.5 cm. It allowed connecting the cartridge in a
1725 very user-friendly way by employing a ZIF socket. The PCB was also used for voltage
1726 supply interface, testing and calibration. The PCB performed all the signal conditioning
1727 needed to interface the microcontroller board. The microcontroller board was dedicated to
1728 the addressing of the array, data digitisation and data transmission to the GUI. The USB link
1729 also provided power for the chip and the Mbed processor.

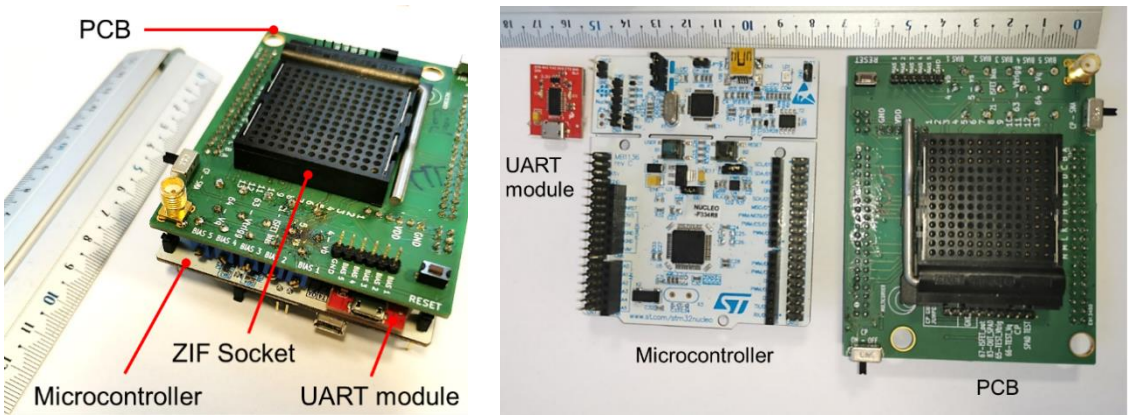

(a) (b)

Figure 3.6 (a) View of the reader in the final configuration, with individual components stacked together. (b) Components of the reader (UART module, Microcontroller board and PCB) shown individually.

The ST Nucleo F334R8 board, programmed with custom firmware [254], was selected because with a total of 51 general-purpose input-output (GPIO) ports was capable of accommodating all the required interconnections in an affordable (about £10) and user-friendly way. It integrates a 32-bit ARM Cortex-M4 microcontroller unit working at a maximum frequency of 72 MHz, which can be programmed with the on-board debugger [255]. The board also has a 64kb flash memory and a 12kb static random-access memory. Among all the capabilities of the board, the onboard 12-bit analogue-to-digital converter (ADC) was used for data digitisation. The PCB and the microcontroller board were stacked together, as shown in Figure 3.6(a). The communication between reader and GUI was achieved through the universal asynchronous receiver/transmitter (UART) communication. UART is a widespread standard for serial interfaces. However, the maximum baud rate supported by the microcontroller board is 115200. To increase the communication rate, an external module, the FT231X module by Sparkfun electronics, was plugged into the PCB. The use of the external UART module enabled a higher baud rate of 921600. The PCB board, the UART module and the microcontroller board are individually shown in Figure 3.6(b). The microcontroller supports the use of custom firmware, which was developed on the 'mbed' online compiler using C++[256]. The full C++ code is reported in Appendix B.

The firmware begins with an initialisation phase. During this phase, a first-in-first-out register is initialised for the UART communication. The register is shared by both the transmitter (the UART module in this case) and the receiver (the GUI). The transmitter sequentially writes the register. In parallel, the receiver can asynchronously access the

register and read binary values sent from the transmitter. During initialisation, GPIOs are also defined. Specifically, eight pins are used for chip addressing, four of which are dedicated to row selection, whereas the remaining four are for column addressing. One analogue input is dedicated to data digitisation. After initialisation, a loop is adopted for continuous data acquisition.

Data reading consists of three steps: reset, integration and reading. In the first step, addressing is disabled, and a reset pulse with a 500 µs width is delivered to all the photodiodes. The integration time, here set at 20 ms, is a waiting time accordingly to the adopted approach, previously described. The integration time has been selected to be much higher than the reading time and to provide a frame rate comparable to standard imaging techniques, usually providing about 30 frames per second (fps).

After the integration, a starting frame sequence is first sent to inform the GUI that a frame data is about to start. The starting sequence is a double zero encrypted with 32-bits in total. It must be pointed out that it was experimentally verified that the digitised output of the sensors never reached a perfect zero. Subsequently, the first row is addressed by the four digital output pins. The first column address is also delivered to the cartridge: a single pixel is then identified. A waiting time of 5 µs is adopted to make sure all the electronic transient effects are discharged. The analogue output of the sensor is then read with the embedded 12-bits ADC of the board. Digitised data is converted into a 16-bits value and sent to the GUI. The conversion is necessary since UART communication works using bytes. Once data is sent, a new column address is delivered to the cartridge, and further reading is performed. When all the columns have been read, a new row address is provided. The process is iterated till all the array has been scanned.

As mentioned in the previous paragraph, pixels in the same column share the same output line. Thus, from a data integrity viewpoint, it is safer to read different columns sequentially. From a data transfer viewpoint, an entire frame contains 4128 bits (516 bytes). This includes 32 bits (4 bytes) for the start frame sequence and 4096 bits (512 bytes) of data, where each pixel is sent with a 16-bits binary code (2 bytes). Frames are continually sent on the GUI. So, the necessity of the starting frame sequence is here demonstrated. Representation of data packing is provided in Figure 3.7(a).

From a timing viewpoint, the time needed from the reader to read and send an entire frame is 21.78 ms. The total time is composed of 500 µs for reset, 20 ms for the integration, and 1.28 ms for the frame reading.

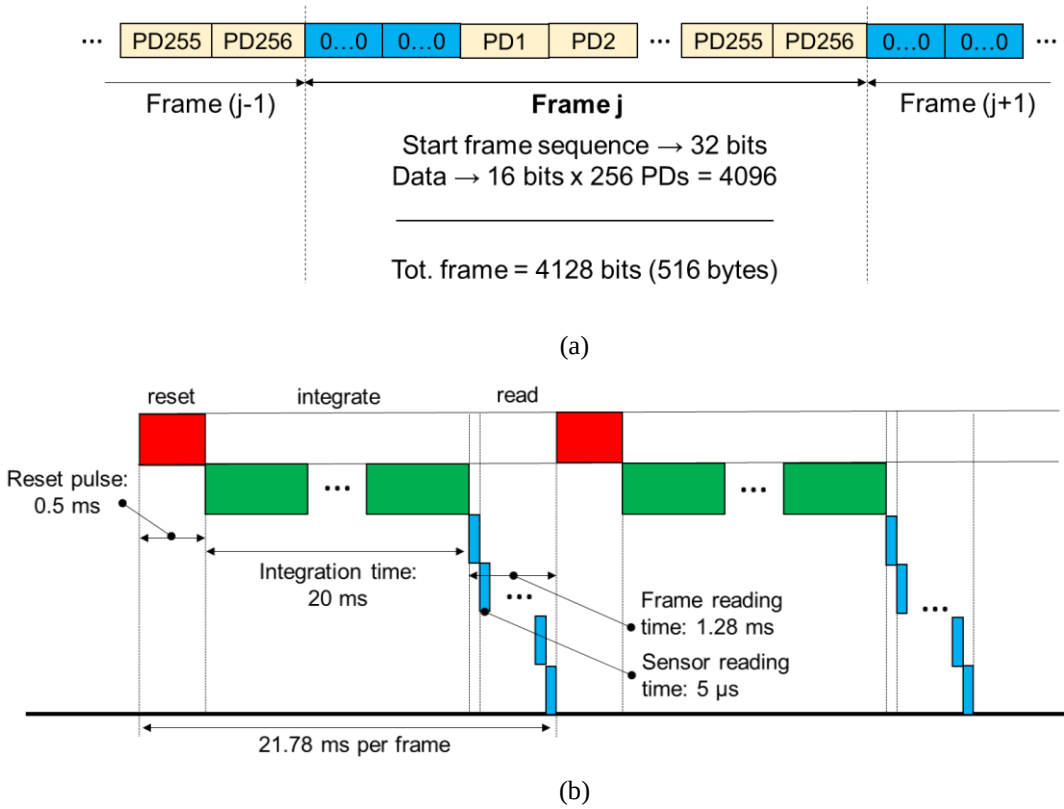

Figure 3.7 (a) Representation of data packing for serial transmission. (b) Timing diagram.

The time needed for the reading of a single pixel was approximately 5 µs. A timing diagram of data reading is provided in Figure 3.7(b). Altogether, the reader sends about 185,760 bits (23.2 kbytes) per second. This means that the approximate size of a 5-minute data recording is approximately 55,728,000 bits (6.9 Mbytes).

3.4. The Graphical User Interface (GUI)

The GUI interface is a software developed using the Matlab-based graphical user interface development tool. It was exported as a standalone application and can run on any portable device running a Microsoft Windows operating system. In this work, a PC (Dell Optiflex 7050), a laptop (HP EliteBook 830 G5) and a tablet (HP Pavillion x2) have all been successfully employed to host the GUI. A simplified android version of the GUI, currently available on the Google App Store, was developed by Bence Nagy but has not been used in this work.

The GUI connected to the reader by USB link. The USB link provided the 5V power supply to the microcontroller.

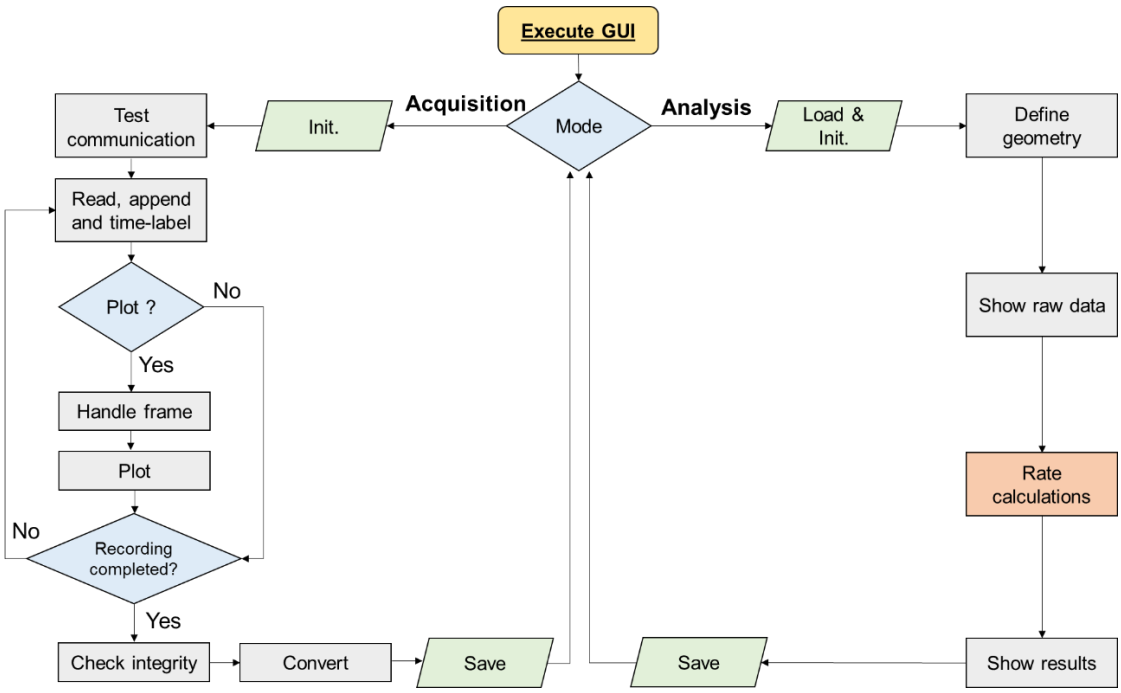

Figure 3.8 Flow chart of the GUI operation.

In turn, the reader provided the 3.3 V required for the cartridge to work through a linear voltage regulator. The GUI received binary data from the reader, and it was employed for data collection, visualisation, processing, and analysis. A flow chart of the primary operations performed by the GUI is reported in Figure 3.8. The GUI worked in two different modalities: data-acquisition mode and data-analysis mode. When working in data acquisition mode, the GUI was used in conjunction with the reader and the cartridge to collect, represent and save data. This is the modality employed for monitoring colorimetric reactions. The data analysis mode was instead used to process data once the experiment was completed. Both processing branches are described in the next sections.

3.4.1. Data acquisition

When working in data acquisition mode, the GUI executes the operation on the left-hand side of the flow chart reported in Figure 3.8. A demonstrative screen-print of the GUI working in data-acquisition mode is presented in Figure 3.9. Before running the test, the user can modify default parameters such as communication port, test duration time, and the frame per second to be represented (panel (1) in Figure 3.9). The communication port mainly depends on the physical USB port, where the reader has been plugged in. The test duration time is the time interval in which the GUI saves data.

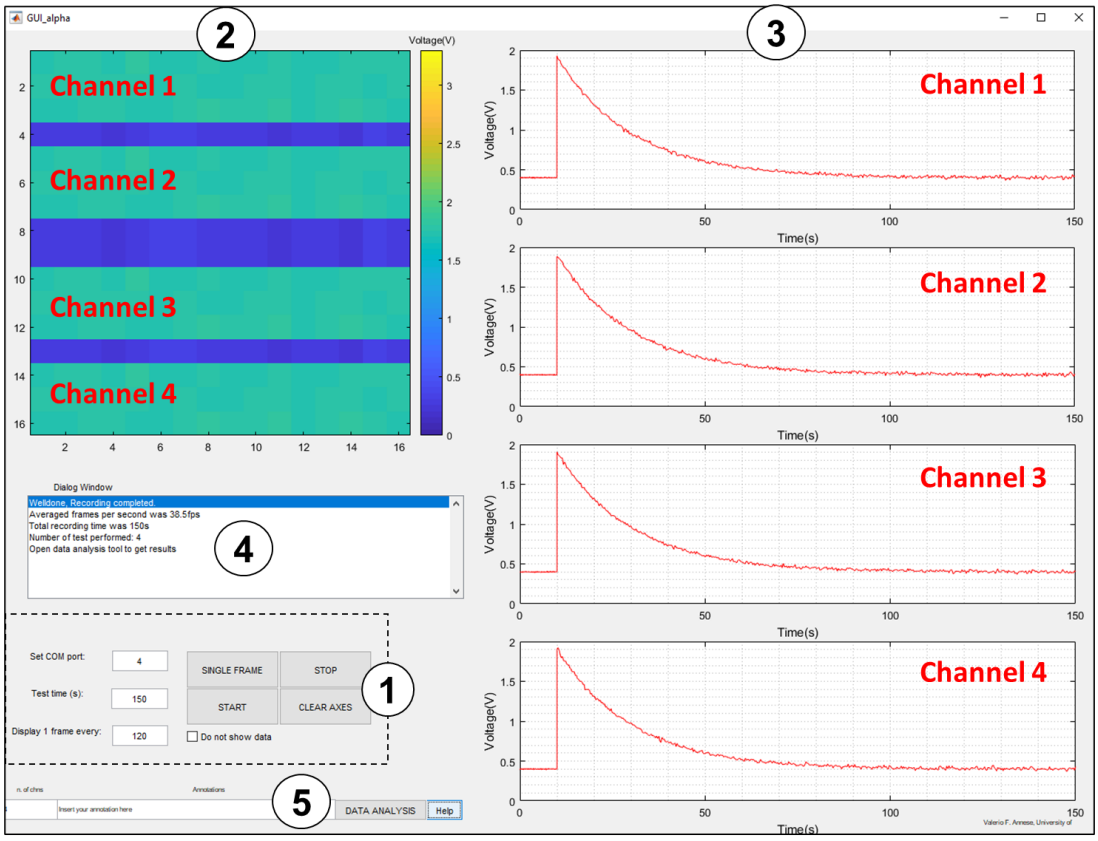

Figure 3.9 GUI in data-acquisition mode. 1) Control panel; 2) Frame visualisation; 3) Single-pixel representation; 4) Dialog window; 5) Go to data analysis.

In this section, it is also possible to decide how many frames to represent per second. The biological reaction is very slow so it might not be necessary to visualise in real-time each recorded frame. Data representation takes time and resources so overplotting should be minimised. Experiments showed that reducing the number of frames shown in real-time increased the recorded frames per second. In other words, the system is faster when no or minimal data is presented in real-time. The user expresses the will to start the test by clicking on ‘start’. Immediately, the user is prompted with a window where he can graphically select four different pixels to be shown in real-time - section (3) in Figure 3.9. After the selection, the GUI automatically records for a fixed time-period data coming from the cartridge. The user is meant to insert the sample in the cartridge at this stage. Data recording can be stopped at any time by selecting ‘stop’. For each recorded frame, a time-label is saved. While recording, real-time data is shown. Referring to Figure 3.9, the entire frame is shown in section (2), and single-pixel data is instead shown in section (3).

Once the recording is completed, data is handled for a more convenient subsequent processing. First, frames are identified and isolated. The entire recorded data is scanned for

the presence of double zeros, the starting frame sequence. Data between the two starting sequences are saved as single frames. Frames with an unexpected number of data, due to any communication error, are discarded together with their time label. Frames are organised in a 2D matrix with dimensions 256xM, where M is the number of frames in the recording. Thus, each row of the 2D matrix represent data coming from a single pixel over time. Time labels are also compressed into 1xM vectors. After frame handling, data needs to be converted into the original photodiode voltage value. The software interprets incoming single bytes as decimal values. Thus, first, the incoming decimal value is converted back to binary with 8-bits precision. This represents the most significant byte (MSB) of the reading. The subsequent decimal value, which represents the least significant byte (LSB), is also converted into a binary string with the same precision and appended to the MSB. The so created 16-bits string is now converted into decimal, providing a value in the range 0 - 2^{16}=65536. Data is also flipped for a more intuitive reading, so that a high output corresponding to high light intensity. Afterwards, the numerical decimal values are converted into a voltage value by employing the following formula:

$$V_{out}\,[V] = \frac{V_{out}\,[dec] \cdot V_{dd}}{2^N - 1} \tag{3.3}$$

Where V_{dd} is the voltage range of the ADC used (3.3 V in this case), and N the number of bits used to digitise the analogue signal (16 in this case).

At the end of the process, the recording is composed of a 256xM matrix containing the value in the range 0 – 3.3 V and a 1xM vector containing time labels in seconds, with M being the number of frames in the recording. The process concludes with data storage, eventually onto a cloud-shared folder when TCP/IP communication is available.

The GUI is meant to work in a real-time scenario and, for this reason, must be able to detect failures and ‘fail safely’. For this aim, if any communication error occurs (for example the cartridge is disconnected while the GUI is recording), an error is reported to the user, and only data collected till the error occurs is saved. Data integrity checks, consisting in verifying that each frame has the expected number of elements with numerical values included in the expected range, are also in place.

Collected data is now ready to be processed using the GUI in the data analysis mode. To switch to this modality, the user can press the ‘data analysis’ button (panel (5) in Figure 3.9). Otherwise, the system is ready for a new recording. An extract containing an essential section of the Matlab code used for the acquisition of data is reported in Appendix C.

3.4.2. Data analysis

When working in data analysis mode, the GUI executes the operation on the right-hand side of the flow chart reported in Figure 3.8. A demonstrative screen-print of the GUI working in data-analysis mode is presented in Figure 3.10. The present tool was developed for use by several researchers within the MST group and, for this reason, it allows customisation of a wide range of settings. First, the user loads the dataset to be analysed (panel (1) in Figure 3.10). Then, the user specifies how many reaction zones are present on the cartridge and defines their geometry by clicking on the dedicated button and following the guided procedure. In this project, each microfluidic channel is a reaction zone. By clicking the start button, raw data is averaged in the selected microchannels and plotted as panel (2) in Figure 3.10. At this stage, the user can analyse the data within the microchannel chosen with the user panel (3) always in Figure 3.10, which will be referred to throughout the following text. By clicking the 'process' button in (3), the user initiates a process leading to the calculation of the initial rate of the reaction. Results are then graphically shown in (4) and numerically reported in (5). Results can be saved through a dedicated button in panel (6).

The process leading to the estimation of the initial reaction rate from raw data is described in Figure 3.11 and can be divided into three sub-routines, namely data preparation, noise reduction and rate calculation.

In the first processing step, data is prepared for the analysis. The process makes sure data is converted into a voltage value; the number and geometry of pixels included in the channel to be processed are defined. Also, the starting point of the reaction is defined and validated by the user. Usually, this is visible from raw data due to the sudden transmittance variation induced by the sample introduction onto the platform, as shown in the next chapter. Data is cropped to 5 minutes (300 s) segment starting from the starting point of the reaction, even if data is recorded for longer than that. At this stage, eventual unresponsive pixels and pixels presenting strong artefacts (e.g. air bubble) are excluded after visual inspection. At the end of this process, the data which has been handled is composed of an NxL matrix containing the value in the range 0–3.3 V and a 1xM vector containing time labels in seconds and a 1xL vector. N is the number of pixels contained in the microfluidic channel after visual inspection, L is the number of frames in the 300 s recording.

In the second stage, data analysis aims to reduce expected noise. The primary noise sources in CMOS sensor arrays are temporal noise and fixed pattern noise (FPN) [80].

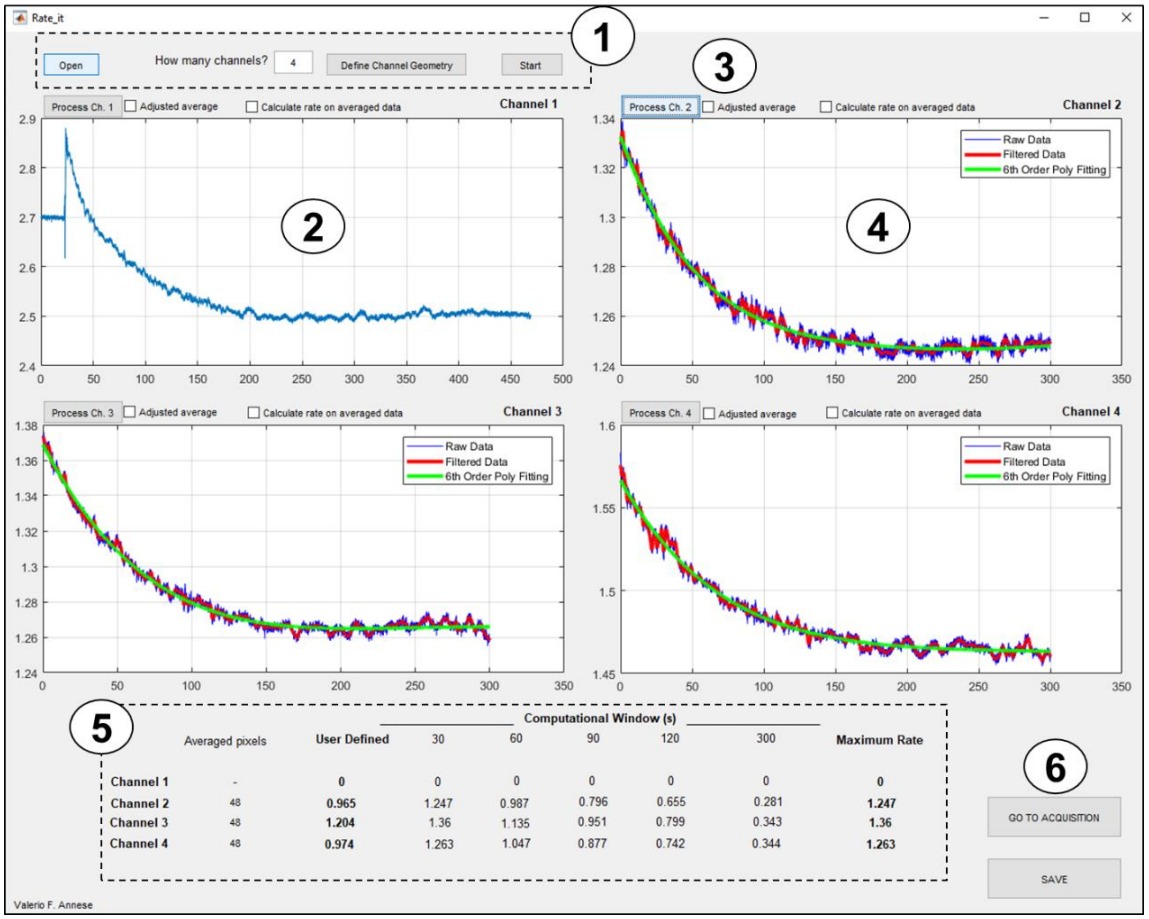

Figure 3.10 GUI in data-analysis mode. 1) Control panel; 2) Raw data visualisation; 3) Start processing button for single-channel; 4) Processed data visualisation; 5) Rates (mVs^{-1}); 6) Save and go to data-acquisition mode.

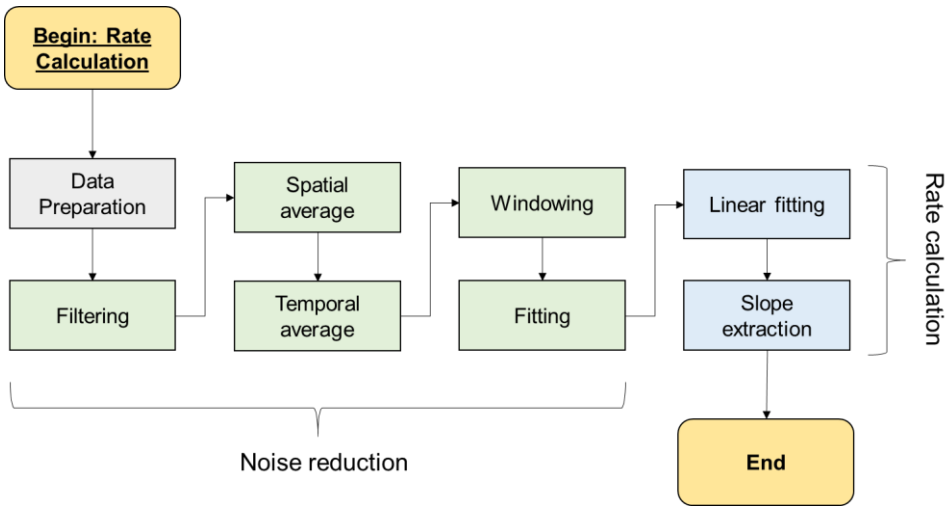

Figure 3.11. Flow chart of the process adopted for the estimation of the initial reaction rate from the raw data.

Temporal noise is a combination of pixel noise components (thermal, shot and flicker), addressing circuit noise, ADC noise. FPN is the variation of the output among pixels when the same input is applied. Data is filtered with an 8^{th} order low pass filter to reduce the standard deviation of temporal noise. The biological reaction is usually slow, as demonstrated in the simulation proposed in the initial section of this chapter. So, a low normalised cut-off frequency, namely 0.1, is selected. Precaution is taken to avoid any signal distortion at the borders. Next, data is averaged in time (usually 1-second information). However, temporal averaging does not affect the FPN. The spatial average reduces the standard deviation of the FPN over the entire channel. Pixels offset before the spatial average is compensated by aligning the starting point of the reaction to the same reference. Over the assumption that both the noise of a single sensor and of the entire array has a Gaussian distribution, the averaging process reduces the standard deviation of a factor $\sqrt{(N)}$, where N is the number of population in the average [242]. The time vector is similarly averaged. So, at the end of the process, two 1x300 vectors are created containing respectively averaged data from the channel and time. At this stage, the vector containing data is segmented using five different time windows, namely 0–30s, 0–60s, 0–90s, 0–120s, 0–300s. The user can introduce an additional time window by custom selection. Consequently, these lead to six different vectors containing voltage data with variable length. Those signals can be here converted into transmittance and absorbance to undergo the same following processing. Data from each vector is fitted using the following double exponential model:

$$y = a \cdot e^{b \cdot x} + c \cdot e^{d \cdot x} \tag{3.4}$$

Where the four numerical parameters a, b, c, and d have been optimised using Matlab-based tools for the minimisation of the root mean square error (RMSE). The proposed model experimentally showed to be the most suitable method for data fitting. Figure 3.12 shows an example of data fitting from experimental data.

In the third stage of signal processing, the initial reaction rate is estimated from the fitted signals. Reactions rates are calculated by linearisation of the fitted signals in time windows. The extracted initial reaction rate is the highest rate calculated onto all the versions of the windowed signal. The decomposition of the signal in different time windows allows the automatic calculation of the reaction. It is not known apriori which window is the best for the calculation of the reaction rate. Thus, the algorithm tries several fixed windows and selects the optimal one based on the maximisation of the reaction rate.

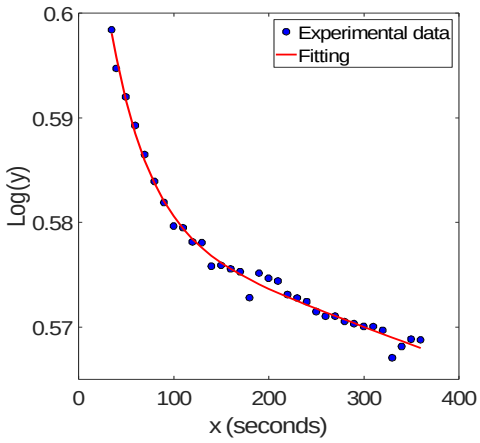

Figure 3.12 Example of data fitting according to Equation (3.4)*. Data from LAA assay in diluted serum (LAA concentration: 1mM). The blue markers indicate experimental data points. The red line represents the double exponential fitting.*

When using the method on voltage, transmittance and absorbance data, the algorithm provides rate information in mV/s, %/s, a.u./s, respectively. A per minute-rate can also be supplied by multiplying for a factor of 60. When using a device with variable geometry, it is convenient to convert the rate in μMs^{-1} by using the following formula:

$$P(t) = \frac{A(t)}{\varepsilon\, h} = \frac{\log_{10}\frac{1}{T(t)}}{\varepsilon\, h} = \frac{\log_{10}\frac{V(0)}{V(t)}}{\varepsilon\, h} \qquad (3.5)$$

Where P(t) is the concentration of the product, A(t) is the absorbance, ε is the extinction coefficient of the light-absorbing species, h is the microchannel height, T(t) is the transmittance, and V(t) is the sensor output in voltage. This representation is convenient because normalised to any variation due to the extinction coefficient and the optical length. Whatever the measurement units adopted for the rate representation, the initial concentration of the substrate can be estimated by using the Michaelis-Menten model or by using a previously calculated calibration curve. An extract containing the essential sections of the Matlab code used for the data analysis is reported in Appendix D.

3.5. Connectivity

The connectivity diagram of the platform is shown in Figure 3.13. It should be noted that the CMOS chip integrates other sensors besides the one used for this project. However, this section only reports the connections required for this project.

The CMOS chip connects to the ceramic package by 18 wire bonds. In turn, the ceramic package connects to the PCB through a ZIF socket. The same 18 connections are thus routed to the PCB. The PCB connects to the microcontroller through 16 bits. The PCB is also connected to the UART/USB module thorough 6 additional pins. The UART/USB module connects to the portable electronic device via USB. The GUI, running on the portable electronic device, handles and saves data.

Table 3.4 provides a description of the functionalities of the connections.

Table 3.4 Connection list of the platform.

	Nº of Pins	**Type**	**Function**
CMOS chip from/to Package (wire bonds)	6	Power	Biasing and reference voltages
	2	Power	ground
	1	Analogue	Photodiode data
	1	Analogue	Photodiode reset
	4	Digital	Column addressing
	4	Digital	Row addressing
	18	**Total**	
Package from/to PCB	6	Power	Biasing and reference voltages
	2	Power	ground
	1	Analogue	Photodiode data
	1	Analogue	Photodiode reset
	4	Digital	Column addressing
	4	Digital	Row addressing
	18	**Total**	
PCB from/to Controller	4	Power	Biasing
	2	Power	ground
	1	Analogue	Photodiode data
	1	Analogue	Photodiode reset
	4	Digital	Column addressing
	4	Digital	Row addressing
	1	Digital	Transmit (TX)
	1	Digital	Receive (RX)
	18	**Total**	
PCB from/to USB/UART module	1	Power	Biasing
	1	Power	Ground
	1	Digital	Transmit (TX)
	1	Digital	Receive (RX)
	1	Digital	Data Terminal Ready Control
	1	Digital	Clear To Send Control
	6	**Total**	

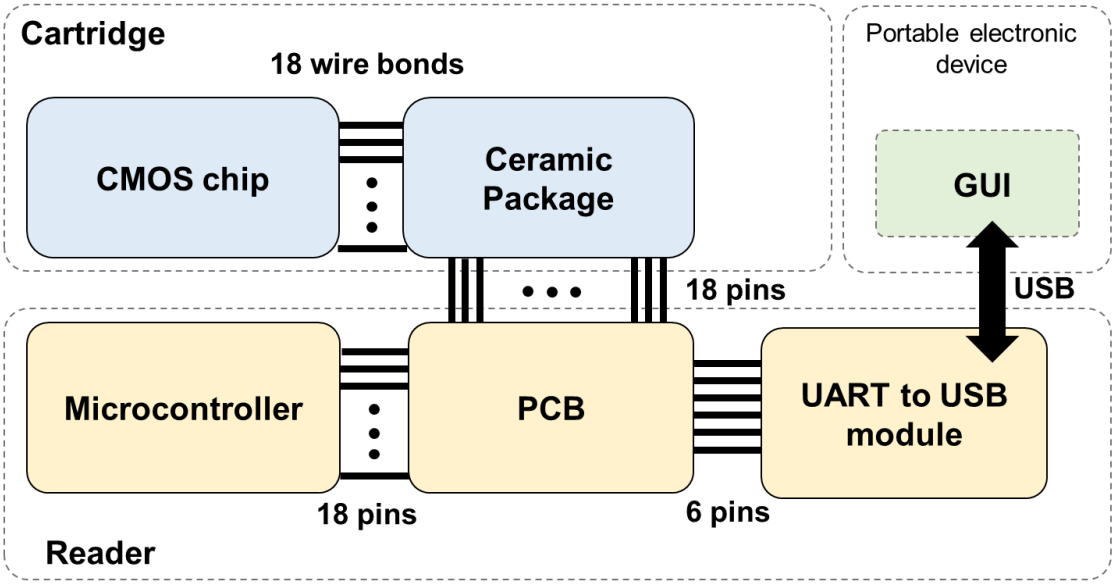

Figure 3.13 Connectivity diagram of the platform.

3.6. Graphical User Interface Benchmark

3.6.1. Data acquisition mode

The GUI in data acquisition mode was tested using a laptop as the portable electronic device (HP Elitebook 840). The sampling time for data acquisition was analysed over twenty independent measurements, each with a 5-minute duration. The probability density function of the sampling time was obtained by calculating the derivative of the time vectors, counting the recurrence into defined bins, and dividing by the total number of samples (around 260k in this analysis). The obtained probability density function is reported in Figure 3.14(a). The average and standard deviation of the sampling time was 27.4±9.7 ms. When converted into frame per seconds (fps), the average fps was 36.5±9.5 fps. However, the probability density function seems composed of two different components which might be approximated with Gaussian distributions. The right Gaussian behaviour was attributed to the additional time required for graphic representation of the samples. Signal integrity was analysed to detect any systematic source of noise in the platform. The spectra of the data from different independent recordings with a fixed optical power were analysed. Figure 3.14(b) shows one spectrum of an entire recording from one randomly selected pixel. Harmonics at 4, 8 and 12 Hz appeared to be systematically introduced in the system.

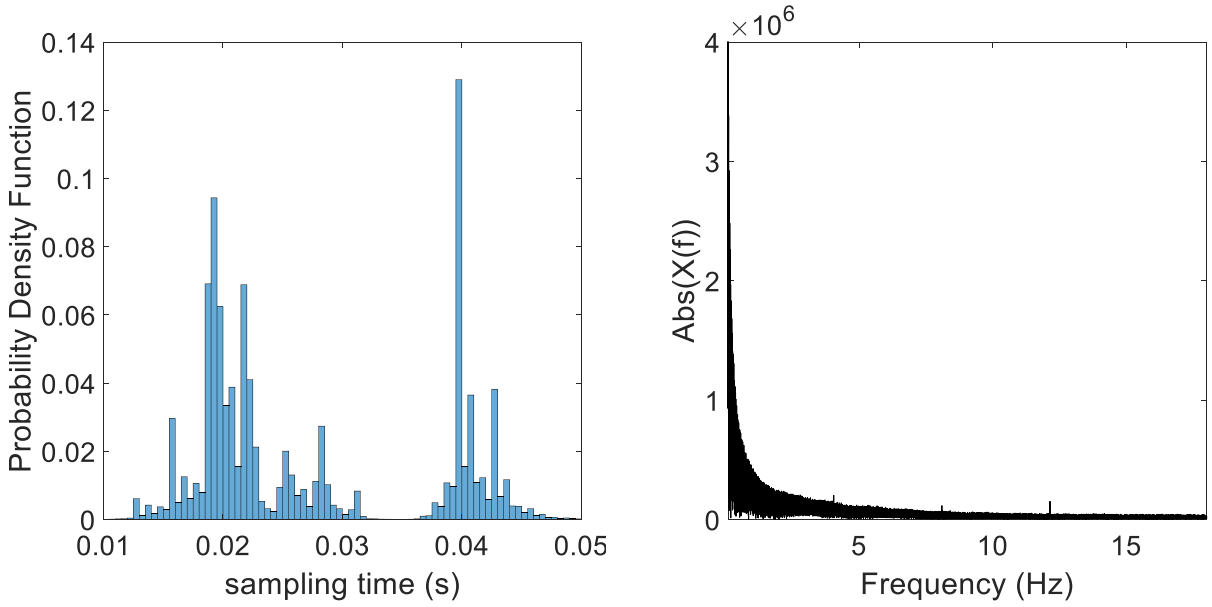

(a) (b)

Figure 3.14 (a) Probability density function of the sampling time. The analysis was obtained from 20 different measurements, each with a 5-minute duration. The total number of samples was around 260k. (b) Spectrum of the recordings.

3.6.2. Data processing mode

The GUI in data analysis mode was also tested. The signal processing algorithm was tested on computer-generated signals with the same characteristics as the expected experimental ones. The synthetic recording simulated a reaction with a constant reaction rate. The synthetic dataset had 256 pixels, a 5-minute and sampled at 36.5 fps. The presence of microfluidic channels and the spike in the signal output due to sample introduction was also emulated. White Gaussian noise was added to the synthetic signals to mimic a real-life scenario. A synthetic dataset was obtained by sweeping the reaction rate and the SNR. To simplify the study, the reaction rate was kept constant for each synthetic signal. Figure 3.15(a) shows a set of synthetic signals with different SNR levels. The developed algorithm was used to estimate the reaction rate throughout the dataset. The results were then compared with the true rate. Figure 3.15(b) goes through all the main processing steps leading to the final reaction rate estimation for a single microchannel, as already described in Chapter 3. Data from all the available pixels in the channel were filtered and averaged. An additional time averaging step was employed to average all the samples within a one-second time window, reducing the fps to 1. The resulting curve was used to produce a double exponential fitted curve.

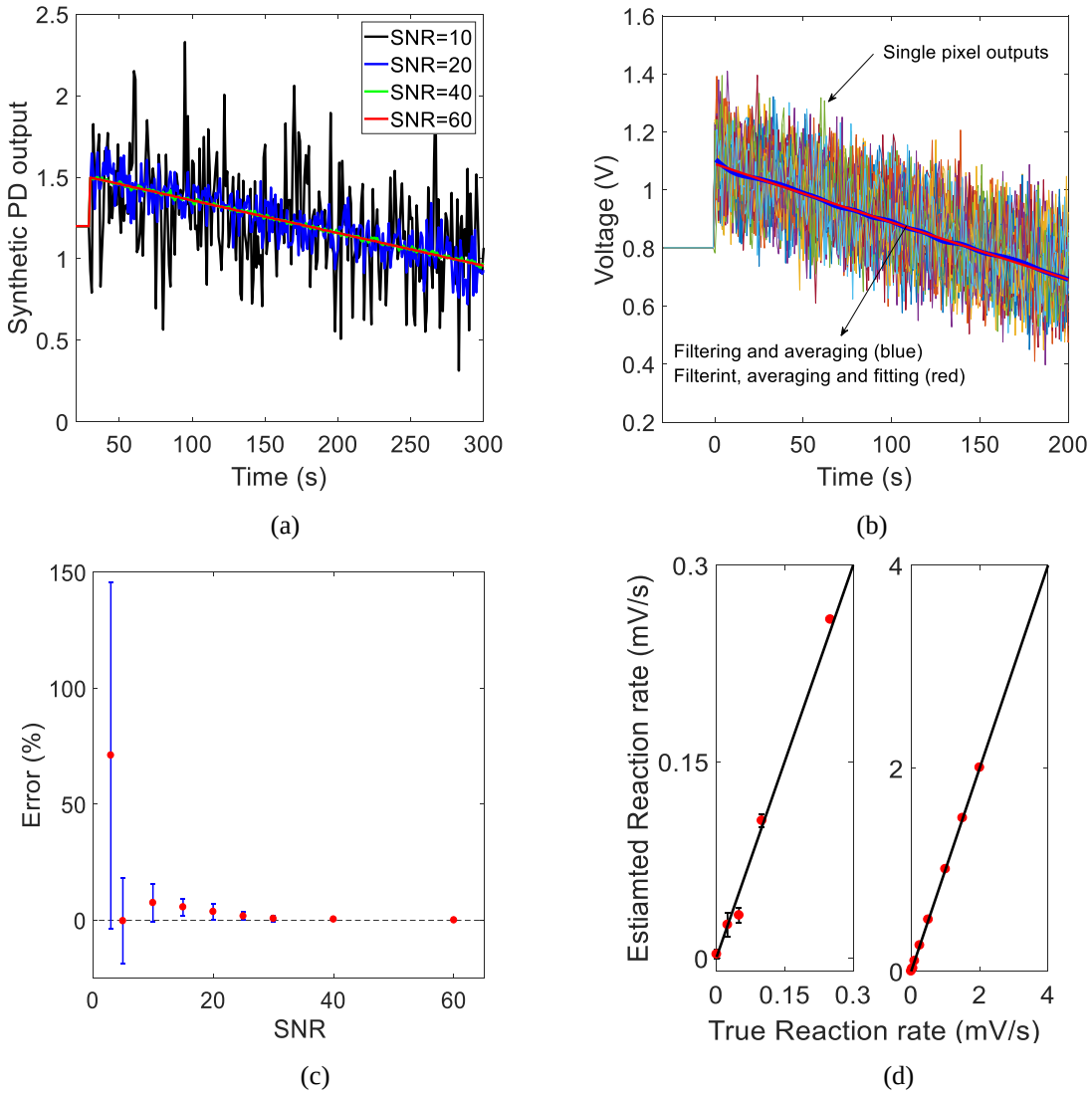

Figure 3.15 (a) Testing synthetic signals with different level of SNR. Constant reaction rate: 2 mVs^{-1}. (b) Data from 48 synthetic pixels was used (SNR=20). Data was first filtered and averaged from the reaction starting point (blue line). Data was then fit to a double exponential model (red curve) used for rate, transmittance, and absorbance evaluation. (c) Relative error of the reaction rate determination with different levels of noise. Testing signals had a fixed rate of 2 mVs^{-1} but different additive noise levels. (d) Estimated reaction rate vs. true reaction rate with reaction rate sweeping in the expected region from 0.001 mVs^{-1} to 4 mVs^{-1}. Noise was kept constant to SNR = 30.

The resulting curve was finally used to calculate rates, absorbance, and transmittance. Figure 3.15(c) quantifies the effect of the noise magnitude when calculating the reaction rate. The estimation of the reaction rate by the algorithm showed a negligible error when the SNR is higher than 30. The performance of the algorithm gradually degraded when the SNR was decreased. The degradation of the performance was verified by increased values of both error and standard deviation. The performance of the algorithm was no longer acceptable with

SNR ≤ 3. Figure 3.15(d) shows the reliability of the algorithm in the evaluation of different reaction rates with SNR = 30. The algorithm showed excellent capability in reconstructing the reaction rate, even for reaction rate as small as 0.001 mVs^{-1}. The performance of the reconstruction algorithm was not affected by the speed of the reaction, when the level of noise was in the acceptable range.

3.7. Summary of the Chapter

- The platform is composed of three units: the cartridge, the reader, and the GUI.
- The cartridge is composed of three sub-units: the CMOS chip, the microfluidics and the bioreagents.
- The CMOS chip, developed within the Multicorder project from the MST group, University of Glasgow, integrates a 16x16 array of multi-sensing elements which comprise photodiodes. The integration of the CMOS chip with microfluidics and bioreceptors is discussed in the next chapters.
- The platform was designed for the quantification of four potential metabolic biomarkers for PCa (LAA, glutamate, choline and sarcosine) and two potential metabolic biomarkers for ischemic stroke (lactate and creatinine) using a colorimetric approach. Reagents were selected accordingly.
- The reader, composed of a custom PCB and a microcontroller board, was used for sensor addressing and data digitisation. The cartridge slots into the reader thought a dedicated user-friendly socket.
- The GUI, a custom software running on a portable electronic device such as a laptop, is dedicated for data acquisition and processing. Data processing focused on estimating the initial rate of the reaction, which is related to the concentration of the target analyte by the Michaelis-Menten model.
- Reader and GUI were tested. The average fps was 36.5±9.5 fps, with variations due to real-time graphic representation settings. The algorithm performing the rate estimations was also tested using a synthetical dataset with different SNRs. The algorithm could reconstruct the synthetic reaction rate with a negligible error when SNR ≥ 30. The reduction of the SNR degraded the performance of the algorithm. Noise levels producing SNR ≤ 3 were considered unacceptable.

Chapter 4: Microfluidic System

4.1. Introduction

The integration of microfluidics and ICs is a major challenge for point-of-care devices [257], [258]. In this work, microfluidics is required to address the specification of multi-analyte testing (see Table 2.11). The microfluidics integration with the CMOS chip is required to be monolithic to address the versatility requirement. Specifically, although they were not used in this work, the CMOS chip also integrates an ISFET array, which requires to be directly exposed to the solution to be analysed. Therefore, microfluidics is required to be integrated in such a way that the sensor array is in contact with the sample. Monolithic integration is also required for application aiming to detect a weak signal [259]. The integration eliminates any superfluous signal path, which can additionally deteriorate the signal quality and introduce additional noise [259]. Monolithic integration also reduces parasitic capacities and minimises the footprint associated with sensing [259].

The present chapter illustrates the design, manufacturing, and characterisation of the microfluidic system. The chapter begins discussing the relevant state of the art on microfluidics manufacturing and integration. The design of the passive microfluidic system is then illustrated through prototypal fabrication and simulations. Subsequently, the fabrication of the microfluidic system and the CMOS chip is described. Analysis and characterisation of the manufactured cartridge conclude the chapter. Table 4.1 illustrates the contribution to each activity discussed in this chapter.

Table 4.1 Table of contributions for the activity presented in this chapter.

Task / Activity presented in Chapter 4	Main investigators
Microfluidics design and modelling	**- Valerio F. Annese**
Integration of capillary microfluidics on the CMOS chip	**- Valerio F. Annese**
Packaging for multiplexed wet assays	**- Valerio F. Annese**
Characterisation of the microfluidic structures	**- Valerio F. Annese**
Spectral characterisation of the photodiode array	**- Valerio F. Annese** - Dr Mohammed Al-Rahawani[1] - Dr Christos Giankulovitch[1]
Characterisation of the cartridge	**- Valerio F. Annese**
Characterisation of sample flow in the microfluidic system	**- Valerio F. Annese**
Affiliation at the time of completion of the activity: [1]*Microsystem Technology Group, James Watt School of Engineering, University of Glasgow.*	

4.2. Microfluidic Fabrication Techniques

The most commonly used techniques for microfluidics fabrication can be grouped into two categories: direct fabrication and moulding [206], [260] (see Figure 4.1). Further methods have been employed for the fabrication of microfluidics devices but not included in this discussion. Additional reading in [260], [261] is suggested for a more detailed review.

Direct fabrication. Direct fabrication groups all the method used to manufacture microfluidics directly on top of the substrate. There are two main techniques used for direct fabrication, namely micromachining and printing.

Surface micromachining refers to all the techniques allowing to fabricate microscale and nanoscale structures by sequential deposition and removal of structural layers on a substrate. Photolithography is probably the most commonly used method for micromachined microfluidics [262]. Other lithographic technique, such as e-beam lithography, are also commonly used [262]. Micromachined devices fabricated with the lithographic method are generally referred to as surface micromachined. The use of photoresist is widespread for surface micromachined devices [262]. SU-8 is probably the most commonly used photoresist for surface micromachined microfluidic devices [260]. SU-8 is a common negative photoresist performing high resolution, durability and capacity for high aspect ratio structures [260]. Micromachined microfluidics device can also be fabricated using etching techniques. This category of devices is usually referred to as bulk micromachined [257], [263]. This fabrication usually involves etching steps aiming to remove material from a bulk substrate, such as a silicon wafer [263].

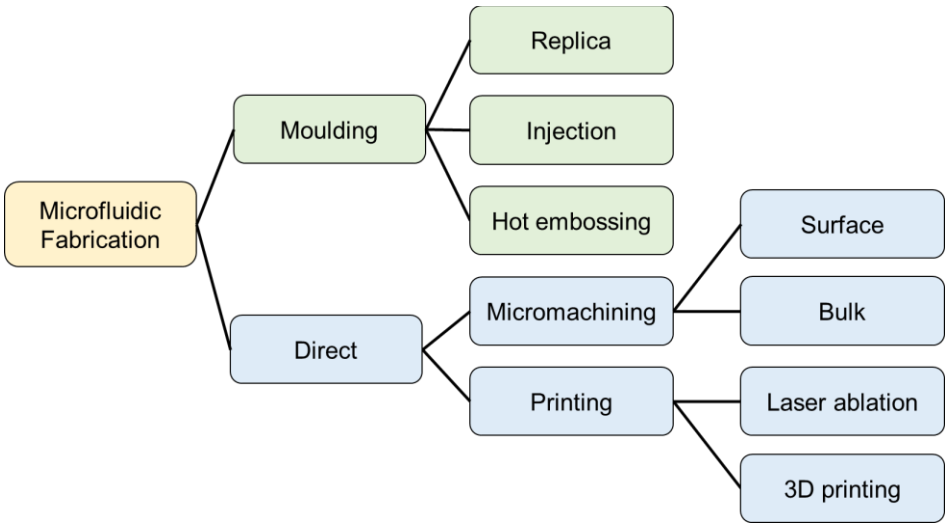

Figure 4.1 Main methods used for the manufacturing of microfluidic systems.

Several materials can be used as substrates, including silicon [262], glass slides [262], polymers for micromachined devices [264]. The resolution of micromachined microfluidics depends on the technique used for its fabrication [260], [262], [263]. The fabrication of microfluidic structure with photolithography is typically in the order of a few micrometres. However, micromachined structures suffer the need for cleanroom facilities. Materials and methods employed for the fabrication of these devices are sometimes costly and time-consuming.

Printed microfluidics refers to all the techniques allowing the direct deposition or removal of material from a substrate. Popular writing techniques include laser ablation and 3D printing [260]. Laser ablation is used for the direct remotion of material from the substrate. Microfluidics devices fabricated by stacking independently cut layers bonded together are generally referret to as laminated devices [260]. A wide range of material has been used as a substrate for direct fabrication, including paper (for chromatography strips) [199], glass slides, polymers (e.g. PMMA, polycarbonate) and tapes [260]. In this category, the depth of the microfluidic channel can be tuned by controlled the thicknesses of the layers. The layers composing the laminated structure are typically bonded by thermal or adhesive bonding. Laminated devices offer several advantages, including rapid and straightforward process steps, no need for cleanroom facilities, low-cost, versatility and scalability [260]. The main disadvantages of this technique are the difficulty in aligning the individual layers and the lower resolution when compared to alternative methods [260]. Laser-cut laminated microfluidic devices typically offer a resolution of tens of micrometres [260]. Recently 3D printed microfluidic devices are also getting progressively popular thanks to their low-cost and rapid fabrication times [265]. Printing also usually does not require cleanroom facilities.

Moulding fabrication. Moulding fabrication refers to all the method that can be used to manufacture microfluidics by mean of a mould. The mould can be fabricated in many ways, including all the methods illustrated for direct fabrication [260]. The resolution of the device usually depends on the technique adopted for mould fabrication [260]. Arguably, photolithography is the most commonly used method for mould fabrication. [260].

Moulded devices can be further divided into three categories: replica moulding, injection moulding and hot embossing [260]. They all have an initial stage of mould manufacturing [260]. Microfluidic devices fabricated by replica moulding employ a liquid polymer to be poured into the mould and subsequentially cured. The cured polymer is then peeled from the mould and bonded onto a glass slide or a substrate [260]. This process is also generally

referred to as soft lithography [260]. Among the polymers employed for the fabrication of replica moulded devices, Polydimethylsiloxane (PDMS) is probably the most popular [260]. PDMS is a polymer structure with the repeating monomer units of $SiO(CH_3)_2$. It exhibits some advantages with respect to other materials used for microfluidic (e.g. PMMA, Polycaprolactone) [257]. PDMS is transparent from 240 nm to 1100 nm, elastic, permeable to oxygen and easy to use and to manipulate. When freshly plasma-oxidised, it can be sealed to itself and other materials without any adhesive layer. Under the exposure to oxygen plasma, the methyl groups $Si\text{-}CH_3$ on PDMS surfaces are attacked by reactive oxygen radicals and substituted by unstable silanol groups Si-OH which can permanently attach to the ionic group on different plasma-oxidised substrates [266]. This property enables PDMS bonding directly on the target substrate without any intermediate adhesive layer. PDMS functionalisation techniques are also robust and well-known [214], [257], [267]–[273].

Injection moulded microfluidic devices are fabricated by injecting a melted thermoplastic (liquid form) into the mould [260]. Usually two halves of the mould are used to create a cavity [260]. Once the thermoplastic is cooled, the cast is removed from the mould [260]. Similarly, in microfluidic devices fabricated using hot embossing moulding, a thermoplastic film is shaped onto the mould by applying pressure and heat [260].

Moulded microfluidic devices share similar limitations to direct writing methods. Expensive and time-consuming methods might be required for the fabrication of the mould. However, moulding is more suitable for large scale production. The mould can be reused many times. Furthermore, the mould can also produce more than one pattern in the same processing steps. These advantages yield to time and costs reduction when producing a high number of devices. Evidence of this is shown by large scale use of moulding processing in commercial devices [260]. Direct writing techniques are instead typically used for prototyping or small scale production [260].

The platform developed in this work is meant to be affordable and suitable for large scale production. Accordingly, a moulding process was adopted. A comparison between three widely adopted fabrication techniques for microfluidic systems (i.e. photolithography, printing and moulding) is shown in Table 4.2.

Table 4.2 Comparison between widely adopted fabrication techniques for microfluidic systems.

	Photolithography	Printing	Moulding
Resolution	µm	tens of µm	Down to µm scale (depending on the technique used for the fabrication of the mould)
Time to manufacture	- From hours to days - Several fabrications steps - Cleanroom facility needed	- From minutes to hours - Largely automatised - One device is fabricated at one time - No cleanroom facility needed	- Minutes[1] - Several devices are fabricated at one time - Can be automatised - No cleanroom facility needed[1]
Adaptability	- Wide range of substrates and structural materials - Channels have a rectangular cross-section	- Wide range of substrates and structural materials - 3D structures - Highly customisable	- Wide range of substrates and structural materials - Network topology depends on the technique used for the fabrication of the mould
Cost per device	High	Low	Low[2]
Suitable for large scale production	No (expensive and slow process)	No (slow process, lower resolution)	Yes

[1] After mould fabrication
[2] When manufacturing a large number of devices

4.3. Microfluidic integration with CMOS technology

Integrated platforms are significantly complicated to implement [259]. Generally, printed devices are very difficult to monolithically integrate due to alignment problems [260][263]. Recently, printing techniques have been used to print structural materials, such as SU-8, on top of a CMOS device to achieve monolithic integration [274]. For instance, authors in [274] demonstrated the integration of a CMOS device with microfluidics through direct writing. In this work, an organic ink is firstly deposited on top of the CMOS chip [274]. Subsequently, an optically clear epoxy resin is used to encapsulate the ink filaments and the CMOS device [274]. Finally, the ink filaments are extracted by applying heat and pressure, leaving epoxy-based microchannels on top of the CMOS chip [274].

Micromachined devices have higher integration capability compared to printing methods [263]. A CMOS chip can be employed as a substrate and monolithically integrate the fluidics on top of the device [263]. In [275], for instance, the authors demonstrate a CMOS compatible microfluidic technology by integrating a microfluidic network on top of optical biosensor devices. In [275], the microfluidics is integrated by using SU-8 in a

photolithography process. A polymer slab is finally bonded onto the SU-8 microstructure to enclose the microchannel [275].

Integration of microfluidic networks fabricated with moulding techniques has also been reported in the literature. Authors in [276], for instance, adopt soft lithography to integrate a CMOS chip and microfluidic in a flexible package.

There are mainly three challenges to be addressed when integrating CMOS chip with microfluidics: size compatibility, process compatibility and economic considerations [203].

Size compatibility. The CMOS chip price is proportional to its area, so designers usually try to minimise the area [277]. Although fluidic channels have a compatible size with CMOS elements, fluidic input/output (I/O) ports need to be large enough (in the order of hundreds of micrometres) to allow practical operation. Increasing the area of CMOS to accommodate fluidic I/O in the design phase is possible. However, this typically requires an additional area which yields to an increased cost of the chip. The increase of the cost cannot be acceptable with the respect to the affordability requirement. Furthermore, when the photoresist is applied by spin-coating on a millimetric area, surface tension creates an unwanted thicker 'edge bead' around the perimeter of the IC [259]. On millimetre-scale ICs, the bead can occupy the majority of the area and can pose a significant problem [259].

Size compatibility can be addressed by planarization [203]. Planarization allows integrating the CMOS chip into a larger substrate. Typically, fluidic I/O are incorporated onto the larger substrate rather than onto the CMOS chip [203]. This technique has the potential to avoid increasing the area of the CMOS chip for microfluidic constraints which, in turn, would increase the cost of the CMOS chip. Notably, authors in [278]–[280] employ planarization before integrating the microfluidic network on top of the CMOS platform.

Process compatibility. This includes the necessity of a set of processes which demand new practical solutions [203]. Chip packaging is probably the most prominent complication to be overcome [203]. CMOS chips are usually connected to a chip package to be operated, and flip-chip bonding and wire-bonding are probably the two most reliable techniques for metallic interconnections [203]. Interconnects also require insulation and encapsulation [203]. Unlike traditional electronic packaging, fluidic packaging has not been standardised by industry [259]. Thus, the approach to accommodate fluidics on CMOS is either to modify a pre-existing standard package or develop a custom package [259]. If wire-bonding is used for packaging, the fluidic network must avoid the bond-pads [259]. Consequently, the area the microfluidics network can occupy is largely decreased, and the geometry also

constrained. Passivation of the wire-bonds can also be challenging in these conditions [259]. Remarkably, authors overcome the problem of wire bonds and metal interconnects by using liquid metal interconnects [276]. Thus, in [276] microfluidics ensures both sample handling and electrical connections. However, the approach has practical limitations and not easily repeatable. Alternative techniques have also been adopted in literature, such as screen-printing and additive manufacturing [203].

Material selection also poses a challenge to be addressed. Employed materials must be inert during the biological reaction and must not interfere [259]. The development of a reliable sterilisation and cleaning method is also essential [259]. The use of materials such as PDMS and SU-8, which deteriorates over 200^{o}C, reduces the maximum temperature to which the platform can be exposed [259]. Furthermore, the wettability of materials needs also to be considered for the optimal flow and reduction of the evaporation [259]. Further complications about process compatibility also come from the topology of the IC, the alignment and functionalisation [203], [259].

Economic considerations. Microfluidics integration requires additional fabrication steps. However, CMOS-based microfluidic systems can be justified only when the production cost of the integrated system is low [203]. Consequently, this excludes several solutions which are not economically viable.

Monolithic integration with CMOS has the potential to minimise the crosstalk between adjacent channels for multi-analyte measurements [259]. However, it is worth noting that although microfluidics can be fabricated on top of CMOS chips, sensors are still separated by the microfluidic channels due to the presence of passivation layers (see Figure 4.2). The separation between a microchannel and sensor is typically in the order of 10µm. Therefore, for optical measurements (i.e. colorimetric detection) photons transmitted through the microfluidic channels need to pass through several material interfaces before reaching the sensor. Transmitted photons can experience reflection, diffraction, and resonance effects before reaching the sensor. These unwanted optical effects can be a source of noise and contribute to crosstalk between adjacent sensors. Adequate separation between different channels might be effective in reducing the crosstalk. Table 4.3 discusses some of the integration works reported in the literature, underlining materials and techniques employed. [257], [261], [281] are suggested for an extensive review on the field.

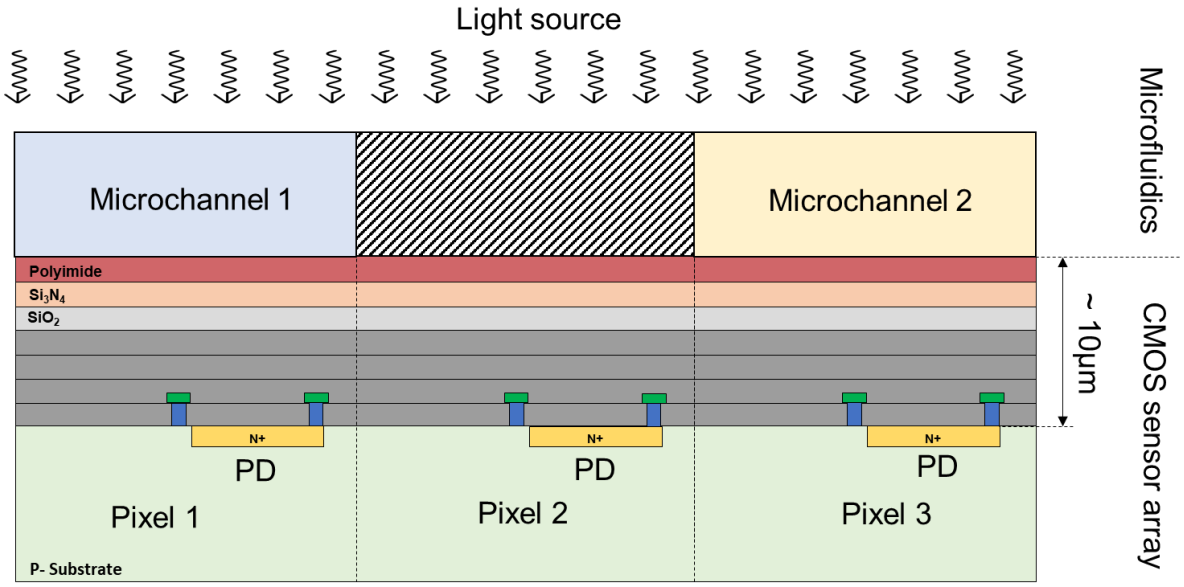

Figure 4.2 Diagram illustrating the separation between CMOS-based optical sensors and microfluidic channels for colorimetric detection. Transmitted photons pass through several layers of materials before reaching the sensor. This can cause unwanted optical effects, leading to sensor-to-sensor crosstalk.

Table 4.3 Integration of ICs with microfluidics.

Target Substrate	Channels	Intermediate layer	Distance [1]	Material	Technique	Ref.
CMOS chip	n.d.	Yes (ONO)	300 µm	SU-8, glass	Micromachining (planarization, photolithography)	[278]
IC and flexible PCB	n.d.	Yes (PDMS)	120 µm	glass	Micromachining (laser engrave)	[282]
CMOS and flexible PCB	4	Yes (Polyimide)	85 µm	PDMS	Replica moulding and adhesive bonding	[283]
CMOS chip	n.d.	Yes (photoresist)	1.8 µm	PMMA	Micromachining (planarization, laser engrave)	[279]
IC chip	1	No	0	PDMS	Replica moulding and plasma bonding	[284]
CMOS chip	1	No	0	Epoxy	Direct writing	[274]
CMOS chip	n.d.	No	0	SU-8	Micromachining (photolithography) and plasma bonding	[275]
CMOS chip	1	No	0	SU-8, PDMS	Micromachining (planarization, photolithography) and plasma bonding	[280]
CMOS chip	n.d.	No	0	PDMS	Replica moulding and encapsulation	[276]

[1] Distance between the sample and the external passivation layer of the IC.

4.4. Microfluidics Design

The process leading to the fabrication of microfluidic system can be divided into three stages: (i) design considerations, (ii) preliminary active microfluidics development and (iii) passive microfluidics development. The manufacturinghas been subjected to a trial-and-error process for continuous optimisation and different stages of design, development, and testing.

4.4.1. Design considerations

For the integration of microfluidics with the CMOS sensor array, several design specifications were considered.

Distance to the sensor array. The microfluidics was required to be in direct contact with the sensor to avoid any additional signal path which can decrease the SNR. As anticipated in the introduction, this design strategy was chosen for two reasons: monolithic integration addresses the versatility requirement of the platform and eliminates any superfluous signal path, which can introduce additional noise [259].

Manufacture technique. Soft lithography and micromachining were selected as employable technique. This choice was made mainly for three reasons: (i) availability of the bare chip to be processed, (ii) access to the cleanroom facility of the James Watt Nanofabrication Centre (JWNC) at the University of Glasgow, (iii) availability of well-established procedure for microfluidics fabrication in the literature. The selection of the manufacturing technique implicitly also contains the selection of the material to be employed, such as Polydimethylsiloxane (PDMS) and photoresists.

Number of fluidic channels. The optimal number of channels was four, so that all the metabolomics marker identified for PCa can be simultaneously measured. The maximum number of microchannels which can realistically be manufactured is 16, with each column of the sensor array hosting a single microfluidic channel. Identical microchannel geometry was also required.

Geometry. According to the selected manufacture technique, microchannels were developed with a rectangular section. Thus, designing parameters were microchannel width w, height h and length L. The active area exposed to the liquid is to be maximised to extract as much significant data as possible from the chip. However, the contact area between fluidic

walls and chip also needs to be optimised to ensure proper adhesion. The maximisation of both active and contact areas are thus opposite design requirements.

Fluidic inputs and outputs (I/Os). Ideally, the microfluidic network should have only one fluidic input and multiple fluidic outputs. For preliminary active microfluidics, I/Os were in the form of a hole where a needle was inserted. For passive microfluidics, a single sample input was required. Fluidic outputs for the passive microfluidics were in the form of an aperture/ventilation.

Constraints. The chip required to be wire-bonded onto a chip package. The fluidics had to avoid areas dedicated to wires. Pads are 100 µm wide and located on the west and east sides of the chip. A tolerance gap of 200 µm was needed to ensure proper wire-bonding of the CMOS chip. The location of the pad limited the orientation of the microchannel that had to have its length L parallel to the north-south direction. Additionally, the wire-bonds required encapsulation to ensure electrical insulation and mechanical strength.

Eventually, the process for the fabrication and integration of microfluidics on the CMOS chip had to consider real-life scenario constraints, including economic and usability considerations.

4.4.2. Preliminary active microfluidics

The initial active microfluidics development aimed to (i) verify the suitability of the selected manufacture techniques; (ii) determine critical dimensions for the development of the passive microfluidics; (iii) develop knowledge and practical experience needed for the development of passive microfluidics.

Twenty-four different networks with several channels ranging from 1 to 6 were designed with software Tanner L-Edit from Mentor Graphics, and fabricated using soft-lithography (see Figure 4.3). Networks had different microchannel width and different I/O configurations. A custom figure of merit (FoM) was identified for comparing various networks. The FoM was defined as the mathematical average between normalised active area (A_{act}), normalised contact area (A_{con}) and normalised liquid volume per channel (V_{chn}), according to the following equation:

$$\mathrm{FoM} = \frac{1}{3}\left(A_{act} + A_{con} + V_{chn}\right) \tag{4.1}$$

A_{act} represents the area exposed to the liquid sample normalised by the total active area; A_{act} represents the area covered by microfluidic walls therefore not exposed to the liquid sample

normalised by the total active area; V_{chn} represent the volume of the channel normalised to the maximum achievable volume (i.e. the volume of a single channel covering the entire active area).

The fabrication of the PDMS active microfluidics was performed at the JWNC. It employed a photolithographic process for the manufacturing of a mould and soft lithography for the manufacture of the PDMS structure. Figure 4.3(a)-(d) presents the full set of designs for 2 and 4 channels networks. Figure 4.3(e) shows that by reducing the number of channels, the FoM gradually reduces meaning that bonding strength and employed sensing area are both reduced. The measurements of the moulds by contact profilometer (Veeco Dektak) and optical profiler confirmed that:

- Channels were successfully patterned on the silicon wafer.
- The achievable depth of the microchannels was approximately 130 µm when using a single layer of SU-8 onto a silicon wafer.
- The profile of the mould was smooth and flat, particularly crucial for high bonding strength.

For testing the flow in the microfluidic structures, PDMS structures were bonded to glass and silicon substrates. Testing structure bonded onto the glass substrate are reported in Figure 4.4. The flow in the whole set of designs was tested using coloured dyes to emulate the presence of samples. The entire collection of designs was successfully bonded to the substrate. The flow was forced into the channels with a syringe pump and a 300 µm needle. The whole set of designs performed physical separation of the flow without any detectable leakage.

After testing on the glass slide, the PDMS structures were then flip-chip bonded onto the CMOS chip after exposure to oxygen plasma. PDMS active microfluidic structures bonded onto the CMOS are reported in Figure 4.5.

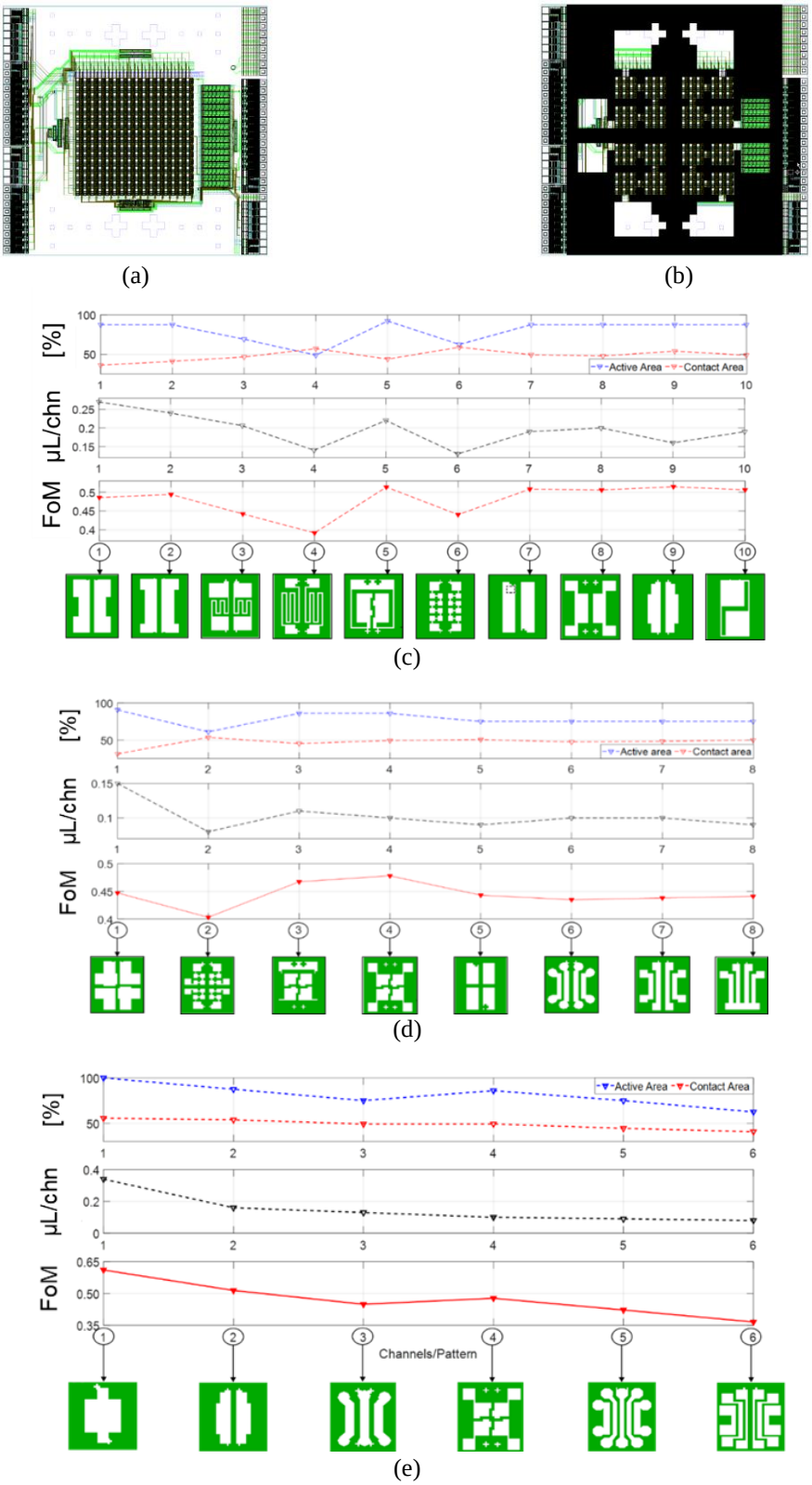

Figure 4.3 Design of an active microfluidic network by using the (a) CMOS CHIP layout and (b) overlapping it with the fluidics 2nd four-channel layout (b) Comparison of all the 2-channel active microfluidic networks designed and fabricated. (c) Comparison of all the 4-channel active microfluidic networks designed and fabricated. (d) Comparison of the active area, contact area, volume/channel and FoM for different active networks.

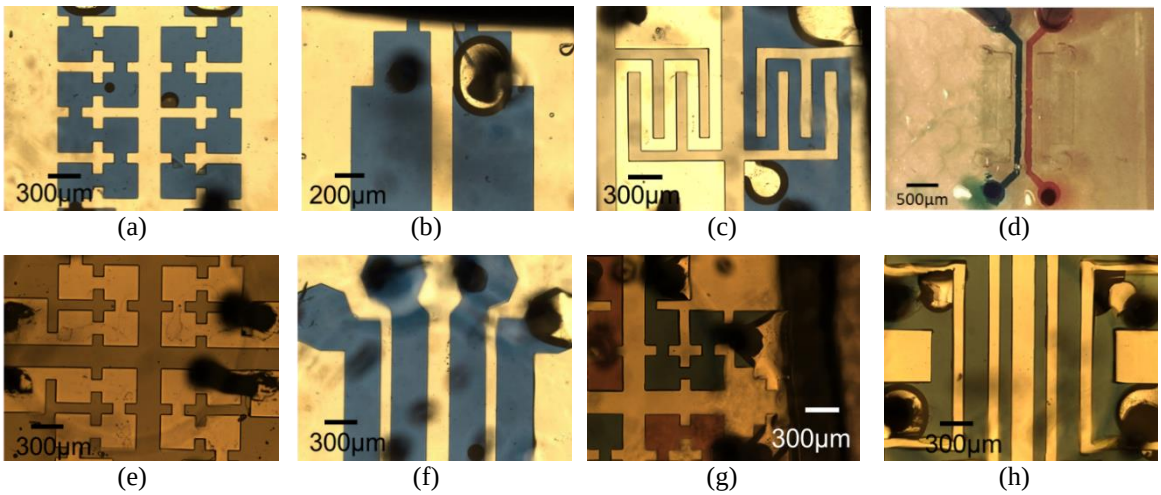

Figure 4.4 Experimental results on solution confinement in PDMS active microchannels, tested with blue and red dye. (a) 2 microchannels with microwells. (b) 2 straight microchannels. (c) The 2-microchannel design was capable of confining solution in only one channel. (d) Two parallel microchannels with 100 µm fluidic wall were enough to confine two different solutions with no apparent leakage. (e) 4-channel active microfluidic network. (f) 4-channel active microfluidic network with straight channels filled with testing dye. (g) 4-channel active microfluidic network was capable of confining different solutions. (h) 6-channel active microfluidic network with straight channels filled with testing dye.

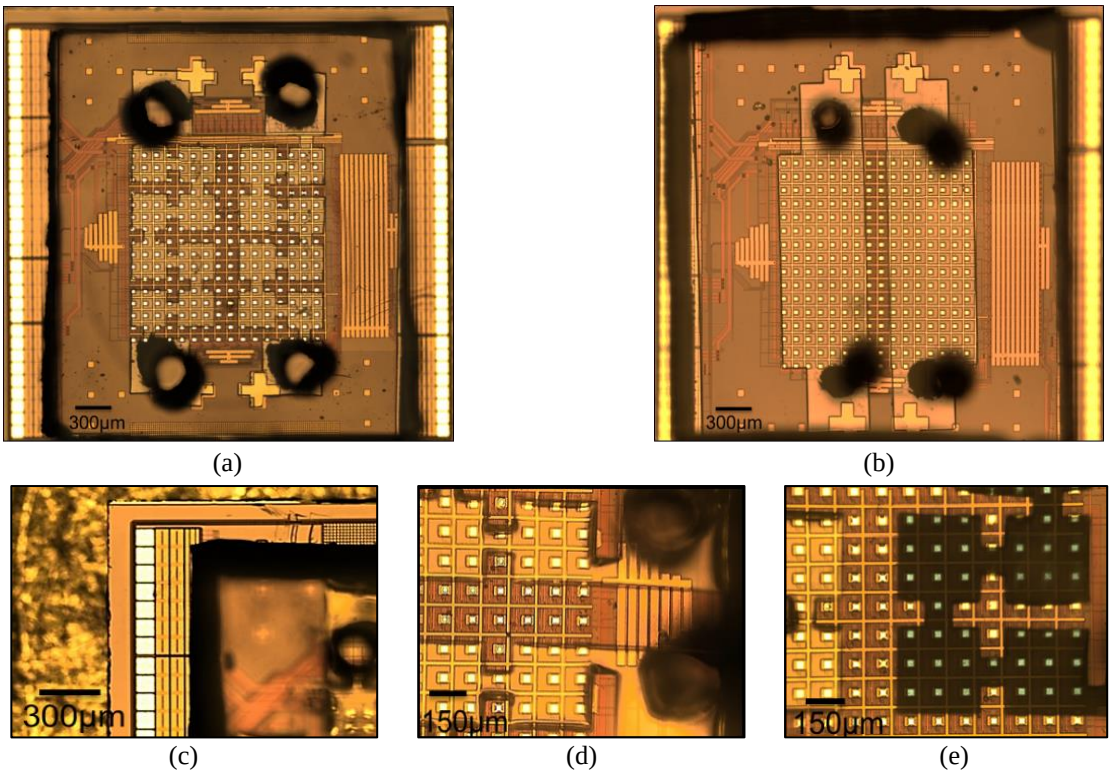

Figure 4.5. (a), (b) Active microfluidic network with two microfluidic channels bonded onto the CMOS chip. (c) Bonding pads are left exposed. (d) Detail of the fluidic I/O. (e) The liquid was confined in the microfluidic channel also when bonded onto the CMOS chip.

The preliminary active microfluidics development and testing allowed to gather information relevant to the manufacture of the passive microstructure. Specifically:

- Photolithography and soft lithography were able to produce microstructures with dimension suitable for the application.
- 100 µm wide walls could provide physical separation of two parallel channels. The absence of crosstalk was preliminarily demonstrated by visual inspection when flowing two different dyes into two adjacent channels.
- Active fluidic I/Os was not a viable solution. I/O management for the 4-channels network was difficult, for the 6-channels network was very challenging, due to their high density. Additionally, a syringe pump was required, which is not ideal in a real-life scenario. Another issue with external pumping also was the formation of air bubbles.
- No capillary action was detected when the sample was introduced using vertical via holes. However, the capillary effect was observed when I/Os were on the side of the structure (the same plane of the substrate).
- Microfluidics could have been extended on the north and south side of the CMOS chip using a planarization step.

4.4.3. Passive Microfluidics

Although active fluidic was successful in confining multiple solutions on the CMOS chip, the use of syringes and pumps was not adequate for the application when considering real-life constraints. It was then necessary to adapt the active microfluidics to work passively.
The main problem related to fluidic I/O management was the compatibility with the wire-bonds encapsulation. The encapsulation step was necessary for the proper functioning of the device. However, despite numerous approaches, the epoxy resin used in the encapsulation step kept leaking into the passive fluidics because of its capillary effect. After several attempts, it was decided to change the approach entirely and, instead, take advantage of this effect. Therefore, epoxy resin was used as structural material moulded by the PDMS microstructure. Besides being compatible with the chip packaging, the functionalisation of the epoxy resin also enables planarization without adding any processing step. The detailed procedure for the fabrication of passive microfluidics is reported in Paragraph 4.5.

The maximisation of the capillary effect was achieved by optimising dimensions and materials employed. Passive fluidics design was mainly based on theoretical equations, already discussed in the chapter, and reported here again for convenience:

$$\Delta p = \gamma\left(\frac{\cos\theta_b+\cos\theta_t}{h}+\frac{2\cos\theta_s}{w}\right) = R_h\, Q = \frac{12\eta L}{\left\{1-0.63\left(\frac{h}{w}\right)\right\}h^3 w}\, Q \quad (4.2)$$

$$l(t) = h\sqrt{\frac{\Delta p}{6\eta L}\left(1-0.63\frac{h}{w}\right)t} \quad (4.3)$$

Where Δp is the pressure gradient, Θ denotes the contact angle of the different materials employed, γ the surface tension, h and w denote the height and the width of the channel, R_h is the hydraulic resistance (kg/m^4s), Q is the flow rate (m^3/s), η is the dynamic viscosity of the fluid, L is the total length of the channel, l(t) defines the position of the advancing meniscus in the channel.

Equations (4.2) and (4.3) highlight that there are three main aspects to be evaluated, namely (i) liquid properties, (ii) geometry of the network, (iii) materials adopted.

Liquid properties. The two main parameters of interest are dynamic viscosity (η) and surface tension (γ) of the liquid sample. The platform is meant to work with blood or processed blood, such as plasma or serum. Blood and derived human samples have different fluidic characteristics. Fluidic characteristics relevant to the present work have been summarised in Table 4.4

Geometry of the microchannel. When designing a single straight microchannel with rectangular cross-section, there are mainly three parameters to be considered, i.e. width w, height h, and length L of the channel. The minimum width w of the channel can be set to correspond to the pixel size of the CMOS chip: 100 µm. The maximum channel width depends on how many channels are laid on the top of the sensor array. According to the proposed application where multiple metabolites are meant to be measured simultaneously, a fluidic network containing four identical channels is adequate for this work. In this case, the maximum width for a microfluidic channel was 300 µm. Minimum width of w = 100 µm was dedicated to fluidics wall on the sensing area. According to the Beer-Lambert law, it is essential to maximise the height h of the microchannel. But increasing h yields to a reduction of the capillary pressure, as reported in Equation (4.2). h is also linked to w since a structure with high aspect ratio could easily collapse. A target height between 100 µm and 300 µm was thus chosen to keep the height to width ratio (h/w) below 3. As previously mentioned, the area of the CMOS chip is 3.6x3.4 mm, and the pads are 100 µm wide and located on the

west and east sides of the chip. A tolerance gap of 200 µm was adopted in accordance with the tolerances of the wire-bonding equipment used. Thus, the maximum width of the entire microfluidic network was set to 2.9 mm. The minimum length L of the microchannel is the length of the active area, i.e. 1.6 mm. Thanks to planarization techniques, the length of the microchannel can be increased (in the north and south side of the chip). A great extension of the length of the channel, however, is undesirable since it would cause an increase in fluidic resistance and a decrease of the flow rate in turn. The length of the microchannel was thus set to 4 mm. The microchannel covered the CMOS chip completely (3.4 mm) with 0.3 mm tolerance on each side for convenient handling of the sample.

Materials. Aiming to maximise the capillary pressure reported in Equation (4.2), hydrophobic and hydrophilic materials can both be employed, as long as their contact angle is as far as possible from 90°. A custom setup for contact angle measurements was utilised for estimating the wettability of untreated PDMS, PVA-modified PDMS according to the recipe in [285], epoxy resin and the CMOS chip. Measured and assumed contact angles values used for the simulations are reported in Table 4.4. Appendix E describes the procedure for contact angle measurements.

Simulations. Designing equations, fluid properties, geometric constraints and wettability properties of the adopted materials have been used to simulate the behaviour of fluidic structures and to verify capillary action. Simulations analysed the behaviour of the microstructure when using different specimens (i.e. water, serum, plasma, blood), and when modifying its width, height, and top contact angle. The custom Matlab model developed to simulate the capillary effect in a single channel with a rectangular section together with a more detailed description of the results is reported in Appendix F. Simulations indicated that a microfluidic channel manufactured with w = 300 µm, h = 300 µm, L = 4 mm, θ_b = 78.2°, θ_s = 98.4°, and θ_t = 32.5° minimised the time required for the liquid to cover the sensing area entirely. In these conditions, the estimated time required for water, serum, plasma, and blood to reach and cover the sensing area are 1.7s, 10.6s, 18.1s, and 23.3s, respectively. Figure 4.6 provides a comparison of flowing simulations for different liquids into the optimised structure.

Table 4.4 Simulation parameters.

Fluid Properties		
Liquid	Dynamic Viscosity (η) [mPa/s]	Surface tension (γ) [N/m]
Water	0.84 [286]	0.073 [286]
Serum	1.4 [287]	0.050 [288]
Plasma	1.7 [287]	0.045 [288]
Whole Blood	2.4 [287]	0.056 [289]
Geometry constraints		
Variable	Min	Max
w	100 µm	300 µm (4-channel network)
h	↓ to increase Δp	↑ to increase absorbance
L	1.6 mm (active area)	none
Materials		
Material	Static water contact angle	Behaviour
PDMS (θ_t)	100° - 110°[285] 107° (measured)	Slightly hydrophobic
Plasma treated PDMS (θ_t)	< 10° (temporarily) [285]	Super hydrophilic
PVA-coated PDMS (θ_t)	20° - 40° (permanent) [285] 32.5° (measured)	Hydrophilic
Epoxy resin (θ_s)	75°-100° [290] 98.4° (measured)	Slightly hydrophobic/hydrophilic
CMOS Chip (θ_b)	78.2° (measured)	Slightly hydrophilic

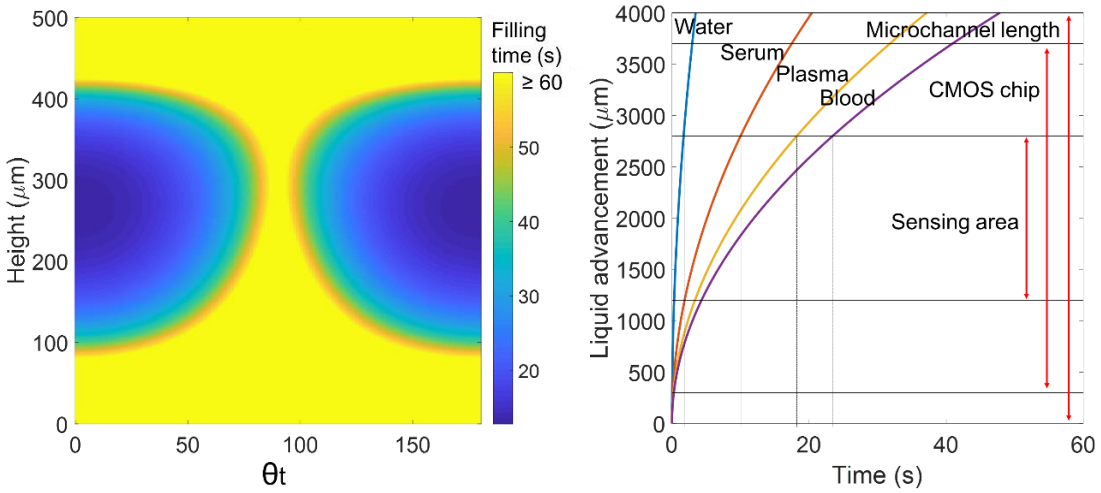

(a) (b)

Figure 4.6 (a) Time required for the sample to cover the sensing area (i.e. filling time) against microchannel height and top contact angle, assuming blood flow. Other simulation parameters: w = 300 µm, θs = 98.4°, θb = 78.2°, L = 4 mm. (b) Simulations of water, serum, plasma, and blood flowing into the optimised microstructure.

Fluidic Input/output. Having identified the optimised geometry, fluidic I/Os were defined. Experimental studies on the active microfluidics demonstrated that capillary effect was observed only when the fluidic I/Os of the network were on the same plane of the microchannel. No capillary action was observed when fluidic I/Os were fabricated in the

form of holes running perpendicularly to the plane of the microchannel. Fluidic I/Os were located on the north and south side of the chip, on the epoxy planarized area and designed as microwells, to which microchannels were connected. Besides the numerically optimised microchannels, several passive microfluidic patterns were designed and fabricated with channels ranging from 2 to 16 and different configurations for fluidic I/O. The design of the passive patterns was also performed using the Tanner L-EDIT tool from Mentor Graphics. Among all produced patterns, the most successful designs are the ones reported in Figure 4.7. It must be highlighted that the length L of the microchannel corresponds to the length of the PVA-modified PDMS slab to be bonded onto the epoxy structure. The designs reported in Figure 4.7(a) and (b) have a single common input and a common output. Differently, the design in Figure 4.7(c) has independent fluidic I/O. The designed photomask for passive microfluidics, shown in Figure 4.7(d), included a multitude of patterns to be manufactured altogether onto a 4 inches silicon wafer.

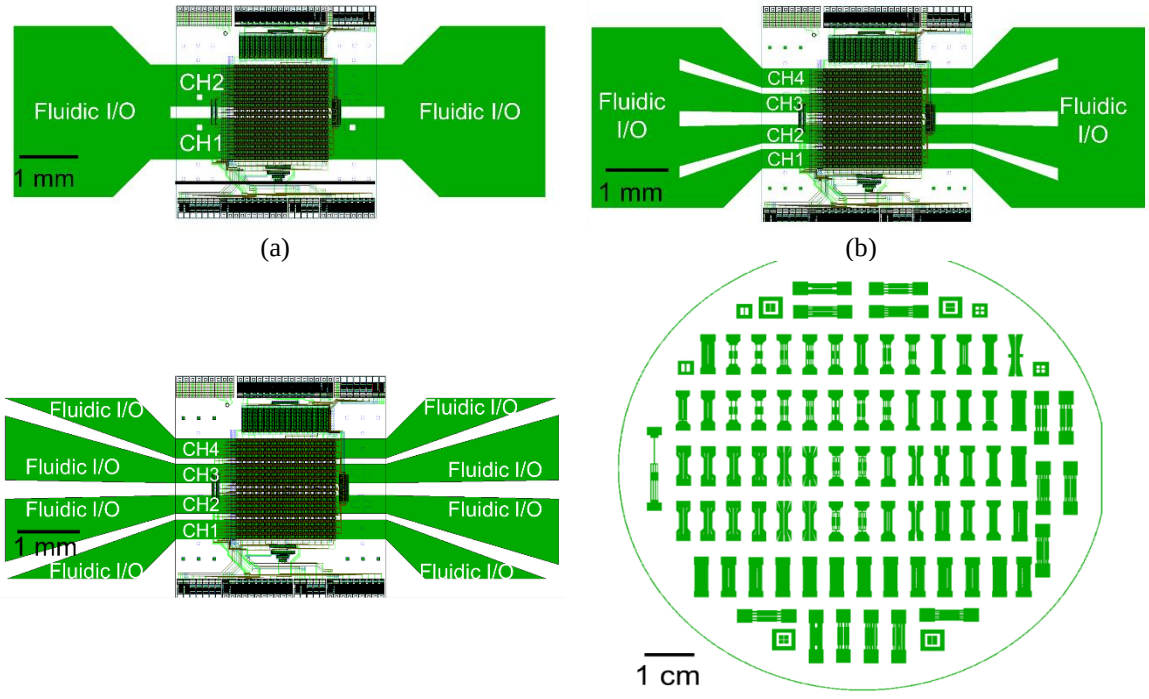

Figure 4.7. Designs of (a) passive 2-channel network, and (b), (c) passive 4-channel networks. (d) The photomask designed for the fabrication of passive microfluidics included many patterns with different configurations.

4.5. Microfluidics Fabrication

The development of the microfluidics on top of the CMOS chip was achieved with the combination of replica and injection moulding. The integration was carried out through the following processing stages: (i) SU-8 mould fabrication, (ii) PDMS mould fabrication, (iii) wire-bonding, (iv) epoxy encapsulation, and (v) channel enclosure.

First, a PDMS microstructure was fabricated from a SU-8 mould through replica moulding. The PDMS microstructure was then temporarily bonded onto the CMOS chip. CMOS chip and PDMS structure were subsequently bonded onto the chip package, and the CMOS chip was wire bonded. Next, the wire-bonded microstructure was encapsulated with black biomedical epoxy. The liquid epoxy, on the one hand, encapsulated the wire-bonds, and, on the other hand, filled the microchannels provided by the PDMS microstructure. Once cured, the PDMS microstructure was removed, leaving the epoxy microchannels exposed. Epoxy microchannels were sealed with a planar slab of PVA-coated PDMS.

The recipe was modified over time to increase the height of the microfluidic channel. In early attempts, a single SU-8 layer was spun onto the silicon wafer, resulting in a microchannel with an approximate expected height of 130 µm [291]. A double SU-8 layer was therefore adopted to bring the expected microchannel height to 260 µm [291]. Throughout the present work, it is clearly stated if the recipe employed a single or double SU-8 layer. The main process steps leading to the integration of the microfluidics on-chip are discussed in the next sub-sections and summarised in Figure 4.8.

SU-8 mould fabrication. The fabrication of the SU-8 mould was performed using a photolithographic process in the JWNC, University of Glasgow. A silicon wafer was cleaned with standard procedures, soaking it while sonicated in the following succession of solvents: isopropyl alcohol (IPA), acetone, and finally deionised (DI) water for rinsing. A 10-minute dehydration step at 90^{o}C in a convection oven under standard atmosphere followed, and immediately before spinning the sample was oxidised under oxygen plasma for 2 minutes in an ET340 PlasmaFab oxygen barrel asher with an RF power of 120W. Plasma exposure just before spinning was effective in providing a more uniform photoresist coat. The photoresist adopted in this work is the negative resist SU-8 3050. For a negative photoresist, the area of the photoresist exposed to UV light becomes insoluble to the developer. The selected is widely used for MEMS fabrication and is suitable for applications in which high film thickness is needed [291].

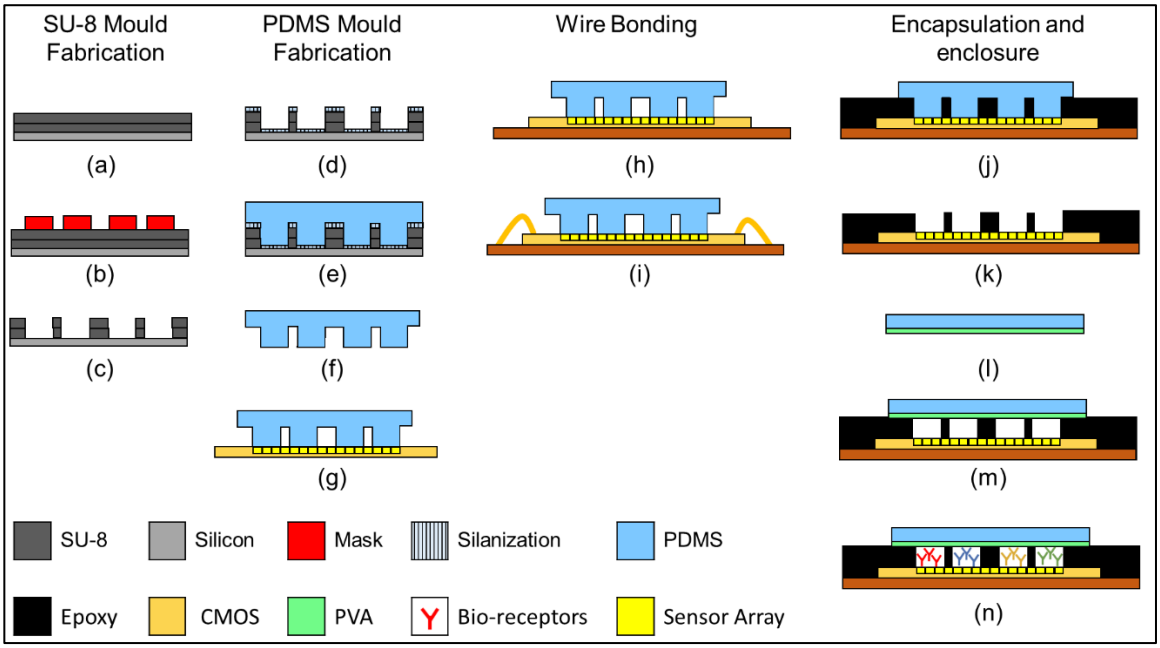

Figure 4.8 (a) Spin-coating of SU-8 3050 onto a silicon wafer. (b) Photolithography process. (c) Development and final SU-8 microstructure. (d) Silanisation of the surface of the mould. (e) Cast of PDMS onto the mould. (f) Curing of PDMS and removal of the mould. (g) Temporary bond of the PDMS microstructure onto the CMOS chip. (h) Permanent mounting of the chip on the chip package. (i) Wire-bonding of the chip. (j) Fabrication of epoxy channels through injection moulding, with epoxy also encapsulating the wire bonds. (k) Removal of the PDMS microstructure. (l) PVA-coating of a PDMS slab. (m) Bonding of the PVA-coated PDMS slab onto the epoxy microstructure. (n) Loading of the bioreceptors into the microchannels.

SU-8 3050 was spin-coated on the wafer for 30s at 1000 rpm and sequentially baked for 1min at 65°C, 90min at 90°C and 1min at 65°C on a vacuum hotplate. A second SU-8 3050 was spin-coated and baked with the same recipe on the top of the first SU-8 layer. The second layer aims to increase the total height of the SU-8 film. A slower spin speed (e.g. 500 rpm) resulted in an unacceptably non-uniform surface, and therefore this option was excluded. Subsequently, the substrate with the double SU-8 layer was exposed twice to UV using a Karl Suss MA6 photolithography mask aligner for 70s each time. A 15s wait time between the two exposures was used to avoid overheating of the photoresist. The sample and the photomask were in hard contact. After the exposure, the sample was baked for 2min at 65°C, 10min at 90°C and 2min at 65°C on a vacuum hotplate. Following exposure, the pattern was developed using EC solvent (development time 28 min) and rinsed with IPA. The mould fabrication is concluded by hard baking the wafer for 30min at180°C in a convection oven under standard atmosphere.

PDMS mould fabrication. The SU-8 mould was silanised by exposure for 30 mins to Trichloro (1H,1H,2H,2H-perfluorooctyl) silane into a vacuum chamber. The silanisation process aided with the subsequent removal of PDMS from the mould itself. The wafer was subsequently placed into a petri dish, and 25 g of a mixture of PDMS and curing agent (1:14 weight ratio) was poured onto the mould and degassed for 1 hour into a vacuum chamber to remove air bubbles. The process continued with PDMS curing by baking the sample for 2h at 70^{o}C. When cured, the PDMS was released from the SU-8 mould, placed on a clean substrate, and cut with a sharp knife. The PDMS mould was then temporarily bonded to the CMOS chip using a flip-chip bonder.

Flip-chip bonding was performed in the cleanroom facility of the JWNC using the 'flip-chip placement system model 850' by Semiconductor Equipment Corporation. For flip-chip bonding, the CMOS chip was placed on the movable stage of the tool and held in place by a vacuum system. The PDMS mould was flipped and secured by a vacuum system to the tip of the bonder, located above the stage. A movable camera, together with a beam splitter, situated between the stage and the tip, provided the user with an overlapped picture of both the substrates to be bonded. Light intensity, focus and other optical parameters were tuned to improve the quality of the provided image. The stage was moved in the x, y and z directions to align the CMOS chip with the PDMS mould. The alignment marks on both the chip and the PDMS microstructure enabled alignment with a tolerance of tens of µm that is negligible for this work. Once the alignment was achieved, the camera was removed, and the tip was brought in contact with the stage. The bonding strength was increased by heating both the stage and the tip for 10min at 90^{o}C under a constant pressure of 5 psi. Subsequently, the vacuum systems were disabled, and the tip raised, leaving the chip and the flipped mould structure bonded together. The PDMS was not exposed to any plasma, and there was no adhesive coating on the CMOS chip. Thus, the bonding was only temporary, and the PDMS mould could be easily peeled off from the chip. The use of PDMS in a weight ratio of 1:14 with the curing agent showed better adherence to the CMOS chip with respect to the more commonly used 1:10 ratio [292].

Wire bonding and packaging. The CMOS chip with the PDMS microstructure was bonded to a ceramic pin grid array (CPGA) package with 120 pins purchased from Europractice [293]. This was achieved by using the EPO-TEK H74 epoxy from Epoxy Technology Inc [294]. The overall size of the selected CPGA package was 3.3x3.3 cm, with an 8.3×8.3 mm cavity accommodating the structure to be wire-bonded.

Wire bonding was performed in the cleanroom facility of Glasgow Laboratory for Advanced Detector Development (School of Physics and Astronomy, University of Glasgow) using the Hesse and Knipps Bondjet 710). The detailed procedure for wire bonding and packing has been reported in Appendix G.

Epoxy microfluidics. The microchannels fabrication was performed using injection moulding. Initially, a mixture of black epoxy resin (302-3M 1LB by Epoxy Technology Inc.) and curing agent (weight ratio 1: 45) was flown into the PDMS microstructure [295]. Epoxy was also used for the encapsulation of the wire bonds. It provided both mechanical strength and electrical insulation to the device. The epoxy resin was then cured for 48 hours at room temperature. After curing, the PDMS structure was removed from the CMOS chip. As previously mentioned, the geometry of the wire bonding diagram allowed taking advantage of the absence of wire bonds at the north and south side by extending the microchannels in those directions. Once cured, the epoxy planarized the surface and created more available space for sample handling and delivery. For PVA-coating and channel enclosure, a plain slab of PDMS was cut with a sharp knife (5mm x 3mm), cleaned and exposed to oxygen plasma for 1min at 80 W in an ET340 PlasmaFab oxygen barrel asher. After the plasma oxidation, PDMS was immersed in the PVA solution (1 wt%) [285]. The PVA-modified PDMS slab can be permanently bonded to the epoxy microstructure by plasma activation. For the PDMS permanent bond, both PDMS and epoxy microchannel were exposed to O2 plasma at 80W for 45s and baked after being brought in contact for 15 min at 90^{o}C. A figure of the cartridge at this stage is reported in Figure 4.9.

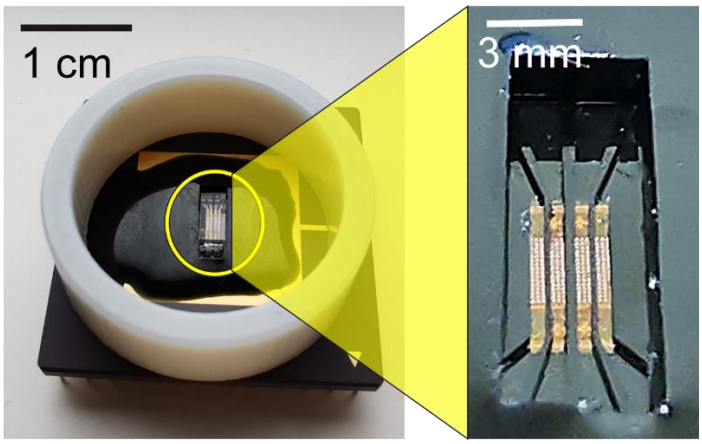

Figure 4.9 Cartridge with four microchannels on top of the CMOS chip (left) and close-up of the cartridge (right). The top PDMS lid on the right figure was removed.

4.6. Microchannel Functionalisation

As introduced in Chapter 2, there are many ways of coupling a biorecognition element together with a sensor for biosensing purposes. In this work, two different approaches were adopted, namely off-chip mixing and lyophilisation. Off-chip mixing was utilised for multiple independent assays on the same metabolite. Lyophilisation was used for multiplexed assays. The reasons leading to this approach are discussed here.

Off-chip mixing means that the bioreagents in the liquid state are mixed with the sample immediately before performing the test. Thus, both sample and bioreagents are introduced in the system at the same time. This approach is commonly used in both experimental and commercial POC devices currently available [296]. There are two major drawbacks for this method: firstly, off-chip processing is acceptable for in-laboratory based POC devices, but should be minimised for in-home POC platforms; secondly, since the passive microfluidics network has only one fluidic input, the same mixture flows in all the identical channels. Thus, this method is suitable for simultaneously repeated measurements but does not support analyte multiplexing.

Both limitations can be overcome with lyophilisation. Among the different techniques available for receptors integration, lyophilisation has been selected because it is versatile, well-demonstrated and potentially suitable for mass production. Freeze-drying can improve the stability of the biological sample over temperature, pH and time. When freeze-dried inside the microfluidic channels, the bioreceptor is confined, trapped in a solid and dry state into the microstructure. The reagents are then re-hydrated by the sample itself once introduced. In this project, enzymatic solutions were deposited into the microchannel. The deposition was performed by pipetting (when the dimension of the microchannel was large enough) or by drop-on-demand inkjet printing using the Jetlab II by Microfab. The sample was then lyophilised using the Lyotrap by LTE scientific. The procedure mentioned above has been performed on both open and enclosed channels, i.e. both before and after the PDMS bonding to enclose the channels. Quicker freeze-drying was recorded when the reagents were loaded before the enclosure of the channels. However, since the chip was routinely re-used, the bio-reactive solutions were also introduced after the channel enclosure using syringes. Freeze drying of reagents in enclosed channels proved to be just as effective as the same process on open channels since the same set of results was produced on both cases. Bioreceptors lyophilisation overcomes the limitation of off-chip mixing. Reagents are

already available on-chip. Thus, no additional sample pre-processing step is needed. Additionally, a different reaction mix can be deposited/inserted into the different microchannel, and multiplexed assays can be simultaneously performed. However, there was a drawback of lyophilisation: the CMOS chip became unresponsive after 3 – 4 freeze-drying cycles, probably because of the thermal and mechanical shock. This is not a problem for a CMOS-based disposable cartridge. However, in this project, the number of chips and resources were limited, and it was not possible to use such a large amount of CMOS chips. Thus, as initially mentioned, off-chip mixing was adopted for multiple independent assays on the same metabolite. Lyophilisation was instead used for multiplexed assays. A detailed description of the printing and lyophilisation of bioreceptor is provided in Chapter 5.

4.7. Fabrication Results

Figure 4.10 demonstrates the main manufacturing steps of the cartridge. A set of SU-8 patterns were fabricated altogether on a silicon wafer, as shown in Figure 4.10(a). The height of the microchannel was related to the SU-8 layer thickness. The SU-8 microstructures were used as a mould for the fabrication of PDMS microstructures. PDMS microstructures were then temporarily bonded on top of the CMOS chip. The misalignment of the flip-chip bonding process, evaluated over three different samples, was estimated to be, on average, less than 50 µm on both the axis, an example is shown in Figure 4.10(e). The misalignment did not appear to be systematic and therefore could not be compensated. However, the precision of the method adopted was suitable for the feature size of interest and did not affect the proper functioning of the device. Consequently, epoxy resin was flown into the PDMS structure, which was subsequently removed, leaving the epoxy microstructure on the CMOS chip, forming the microchannels as originally fabricated on the SU-8 resist layer. As shown in Figure 4.10(f) and (g), the adopted manufacturing method allowed to effectively fabricate a relatively planar microstructure surface and provided an additional off-chip area for fluidic inputs and outputs, forming a uniform rigid structure that encapsulated the CMOS chip. The final step was to cover microchannels with a flat PDMS lid, cut to measure, and create microfluidic channels on-chip.

Figure 4.11(a) quantifies the flatness degree for the planarized surface. Measurements were performed in the cleanroom facility of the JWNC, University of Glasgow, using the Contour GT-X 3D Optical Profiler by Bruker. The top PDMS lid of the microfluidic channels had

been removed to accommodate the optical measurement. The epoxy surface area converged with the CMOS chip with an average slope of 0.007 µm/µm. The slight incline of the epoxy surface region is negligible when compared to the CMOS chip surface, shown in Figure 4.11 (a) and (b). The inhomogeneous surface of the chip is derived from the CMOS manufacturing of different layers by the foundry. The surface profile of the chip is particularly uneven on the active area, where the device's top metal layer density is higher. Another factor that contributes to the uneven surface is that this chip also exhibits openings on the passivation/polymer layer above the ISFETs. The inhomogeneities of the surface of the chip led to peaks of the height of 13 µm.

Figure 4.11(c) shows the result from a surface measurement of a cartridge using the aforementioned optical equipment. Four identical microfluidic channels traversed the CMOS chip from the north to the south side, crossing the sensing area of the chip. Apart from creating channels, the casted epoxy was also used to form lateral walls that encapsulate pads and wire-bonds, providing both mechanical strength and resistance to aqueous environments. As expected, the top of the epoxy walls appeared smooth and flat, especially when compared to the CMOS chip surface. The smoothness and flatness of the epoxy walls were fundamental for achieving a robust bonding strength with the PDMS top lid.

A section of the cartridge of interest is reported in Figure 4.11 (d). The heights and widths of the manufactured microchannels were, on average, 291.95±6.44 µm and 300.87±0.86 µm, respectively. The profile of a single microfluidic wall is shown in Figure 4.11(e). The trench had a deep slope of approximately 929 µm/µm. The length of the channel was, on average, 4.0±0.1 mm. The manufactured patterns showed features that were expected, and the resulting microfluidic channels were compliant to the design specifications. In addition to the analysed microfluidic design, further patterns and recipes were manufactured. On this note, it is also relevant to report the height of microfluidic channels achieved using a single layer of SU-8. Expectedly, the height of the microchannels reached with only one SU-8 layer was lower. More precisely, the average height of 137.14±3.1 µm was measured. Figure 4.11 (f) reports the section of a microfluidic network composed of two channels with reduced height. For this pattern, the width of the microchannels was, on average, 693.65±3.3 µm.

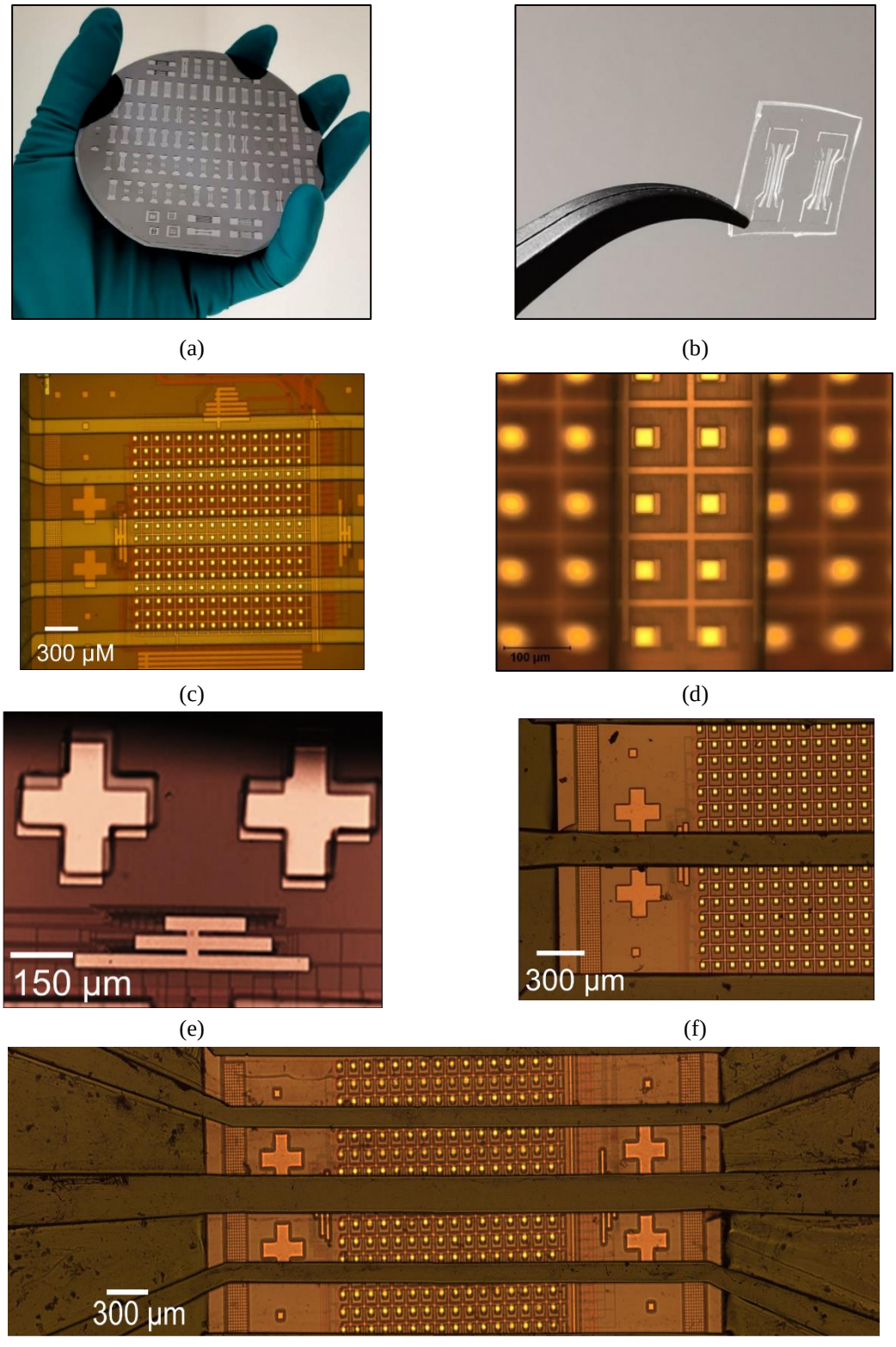

Figure 4.10 (a) Silicon wafer patterned with SU-8 microstructures. (b) Two identical PDMS microstructure for microchannel fabrication. (c) PDMS microstructure was temporarily placed onto the CMOS. (d) Close-up of the PDMS microstructure on-chip. (e) PDMS and CMOS chip misalignment. (f) A 2-microchannel microfluidic network on chip (top PDMS lid removed). (g) A 4-microchannel microfluidic system on chip (top PDMS lid removed). Multiple micrographs have been merged to produce this figure.

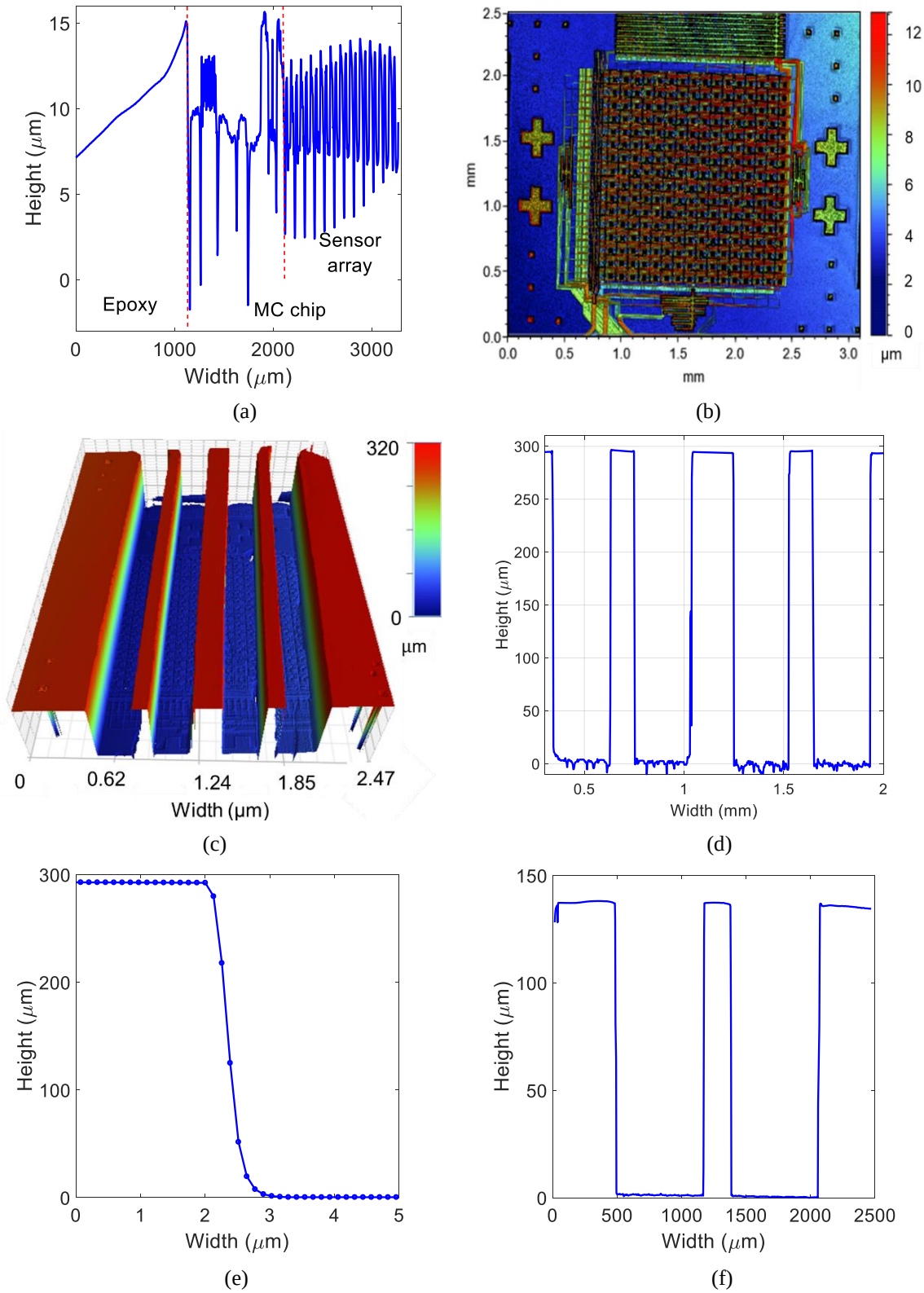

Figure 4.11 (a) Surface analysis of the flat epoxy area encapsulating the CMOS chip. (b) Surface measurement of the CMOS chip with an optical profiler. (c) Optical profile of a 4-microchannel pattern fabricated on the chip. (d) Cross-section of a 4-microchannel pattern fabricated on-chip. (e) Close up of a microfluidic wall measured using optical profiling. (f) Cross-section of a 2-microchannel pattern made on-chip using an alternative recipe involving only one SU-8 layer.

Mechanical strength of the microfluidic structure was quantified using two methods, namely shear testing and pull testing. Shear testing was carried using the DAGE 4000HS bond tester in the cleanroom facility of the Glasgow Laboratory for Advanced Detector Development (School of Physics and Astronomy, University of Glasgow) with the help of the staff. Testing was performed on seven dummy structures (PDMS structure bonded to a 3.4x3.4 mm silicon substrate with a 500 nm coating of silicon nitride to emulate the surface characteristic of the CMOS chip). An increasing lateral force was applied to the PDMS top lid using a piston while the structure was held still. Consequently, the PDMS structure was stressed, deformed, and then peeled off from the substrate (the test was destructive). The maximum shear force that the structures tolerated before permanently getting damaged was evaluated by analysing the force diagram.

Results are reported in Figure 4.12(a). The shear test showed that the bonding could tolerate a maximum lateral force of 576±190.2 g (applied on a surface circa 2.9x2 mm wide). However, the surface of the CMOS chip is not as flat as one of the testing devices, so it is expected that the final device can tolerate a lower shear force.

Pull tests were performed over two cartridges. The tested cartridges had been extensively used for other biological experiments before the pull testing. Thus, the bonding strength might have deteriorated. Pull testing was carried out in the electronics testing laboratory, Rankine Building University of Glasgow. The cartridges under test were glued onto a custom weight holder. The weights in the holder were progressively increased. For each newly introduced weight, the cartridge was lifted for 10 seconds by the PDMS block with tweezers. The total lifted weight was recorder before lifting using a precision scale. For both samples, PDMS damage started when applying a force around 70 g. Results for the pull testing are reported in Figure 4.12(b).

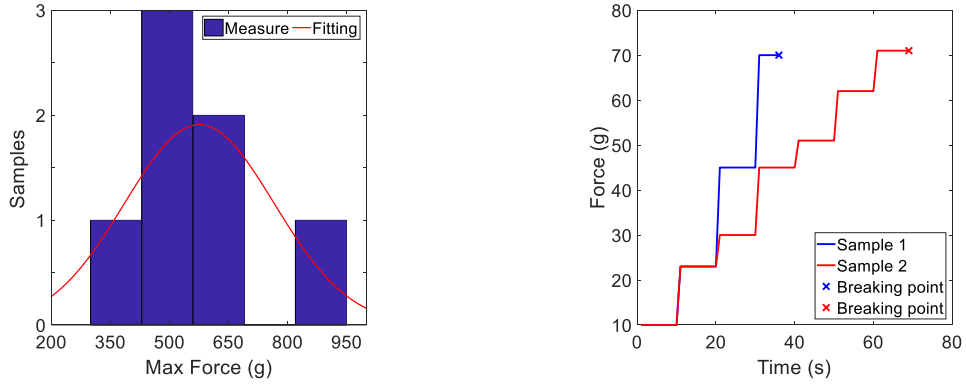

(a) (b)

Figure 4.12 (a) Results of the shear testing. (b) Results of the pull testing.

4.8. Spectral Analysis

Preliminary optical testing was performed using the micro-spectrometer ffTA-1 from Foster and Freeman. Spectrophotometric analysis was performed on three aspects of the platform, namely the colorimetric reagents, the material used for microfluidic and the type of human specimen to be tested with the platform. Dedicated test samples were fabricated to study the perform transmission mode analysis. The test devices were manufactured with the same materials and methods presented in the previous chapter, but a glass slide was used as a substrate instead of the CMOS chip. The height of the test microchannels was, on average, 137 µm. For all the measurements, the analyses were performed for wavelengths in the range of 400 – 1000 nm with 1 nm step. The calibration was performed using measurements on an empty channel and in dark conditions. For each reported spectrum, three measurements were recorded and averaged.

The analysis of the colorimetric agents aimed to quantify the extension coefficients and the wavelength range according to the relevant light absorption. The extinction coefficient was measured in the microchannels using testing solutions of H_2O_2. For this analysis H_2O_2, o-dianisidine, phenol, 4AAP and HRP were purchased from Sigma Aldrich. Two different solutions with the same total H_2O_2 concentration of 1 mM were produced. For the first solution, 30 µL of 2 mM H_2O_2, 5 µL of 41 mM o-dianisidine, 10 µL of 10 U/mL of HRP and 15 µL of DI water were mixed together. For the second solution, 30 µL of 2 mM H_2O_2, 5 µL of 44.5 mM phenol, 5 µL of 10.5 mM 4AAP, 10 µL of 10 U/mL of HRP and 10 µL of DI water were mixed together. Both the solutions were incubated for 1 h at room temperature. Subsequently, they were introduced into 137 µm high microchannels, and the transmittance spectra were recorded. The transmittance spectra were then numerically converted into absorbance and, finally, into the extinction coefficients for different wavelengths using the Beer-Lambert's law. The extinction coefficient against the wavelength for both the colorimetric methods for H_2O_2 quantification are reported in Figure 4.13(a). The trend of o-dianisidine extinction coefficient shows a maximum of 6.37 $mM^{-1}cm^{-1}$ at 463 nm. The FWHM for o-dianisidine was 112 nm. The extinction coefficient when using phenol/4AAP had a similar trend, with a maximum of 9.54 $mM^{-1}cm^{-1}$ at 440 nm and FWHM of 180 nm. For both the colorimetric methods, the results agree with the scientific literature [49].

The analysis of the materials used for cartridge manufacturing aimed to quantify the related transmission losses. Figure 4.13(b) reports the spectra for untreated PDMS, PVA-coated PDMS and epoxy microfluidic walls. No liquid was introduced in the microchannel during these measurements. Untreated PDMS had a transmittance of 98.85% at 500 nm. At the same wavelength, the PVA-coated PDMS had a slightly lower transmittance of 95.29%. Epoxy walls also showed light transmittance, although with a highly reduced value. In this case, at 500 nm the light transmittance of a 137 µm microchannel was approximately 25.28%. However, such a low transmittance was acceptable since the epoxy walls only served as liquid barriers to form the microfluidic channels and no measurement was performed in those areas.

The analysis of the target human body fluids aimed to quantify the sample-specific transmission loss when introduced into a microchannel so that it can then be isolated from changes in transmission due to metabolomic reactions. Figure 4.13(c) reports the spectra of the human body fluid of interest. When the buffer, tris hydrochloride (Tris HCl), was only added in the microchannel, a small increase of transmittance for all the wavelengths of interest was measured. The increase of the transmittance is related to the reduced reflection with respect to an empty channel. Assuming perpendicular light, according to Snell's equation, the power light reflectivity R of an interface with refractive indexes n_1 and n_2 is given by [297]:

$$R = \left|\frac{n_1 - n_2}{n_1 + n_2}\right|^2 \tag{4.4}$$

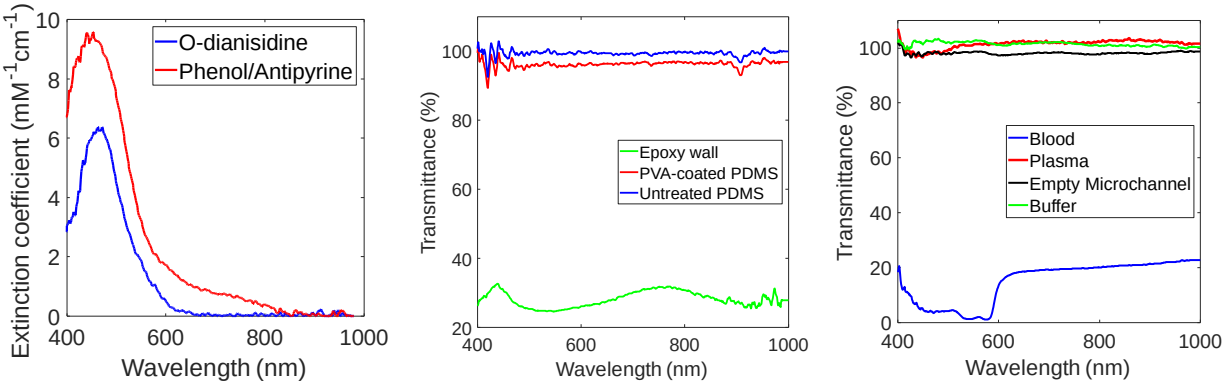

(a) (b) (c)

Figure 4.13 Measured spectra of different samples introduced into a microchannel. Spectra were measured using the micro-spectrometer ffTA-1 from Foster and Freeman. Spectra are averaged over three different measurements. Wavelength range: 400 – 1000 nm. Wavelength step: 1 nm. The spectra represent: (a) The extinction coefficients of oxidised o-dianisidine and phenol/4AAP, (b) transmittance through untreated PDMS, PVA-coated PDMS and the epoxy walls, and (c) transmittance through different media and air.

Thus, considering PDMS (n_1 = 1.4 [298]) and air ($n_2 \sim 1$), R = 0.0278. Differently, when a water-based solution is introduced (n_2 = 1.33 [299]), $R^* = 6.39 \cdot 10^{-4} < R$. The expected increase of the transmission spectrum is therefore justified.

Expectedly, the light transmission when introducing human plasma into the microchannel decreased to 97.7% at 500 nm. This reduction owes to the different optical properties of the samples. This effect is more prominent in whole human blood where light transmittance is drastically reduced to 4.2% at 500 nm as there has been no filtering of the thick nature of whole blood.

4.9. Sensor Array Characterisation

4.9.1. Photodiode spectral analysis

Spectral response of the photodiodes was characterised in collaboration with Dr Mohammed Al-Rawhani and Dr Christos Giagkoulovits, in the electronic labs of the Rankine Building, University of Glasgow. To test the spectral response of the optical devices, a monochromator (DTMS300 from Bentham) was used as the light source and it was attached to an integrating optical sphere to ensure uniform light distribution. A calibrated photodiode (DH_Si Silicon photodiode from Bentham) was fitted to one exit port to measure the light intensity.

The CMOS chip was placed at another exit port. The light source was used to measure the sensor output at different wavelengths, in the range of 350 – 1000 nm with a 5 nm step. The average power level was adjusted to avoid sensor saturation at the peak wavelength. All experiments were performed in dark conditions. Data from 25 randomly selected photodiodes in the sensor array were collected and averaged. The average voltage output was then divided by the recorded reference power to calculate the CMOS photodiode array responsivity in V/W.

Figure 4.14(a) shows the average spectral response of the photodiodes. The responsivity was normalised to its maximum, which was 0.25 V/µW at 575 nm. The responsivity graph exhibits a second peak at 620 nm. We can, therefore, assume that there was a sensor-to-sensor variability from the responsivity point-of-view. For each photodiode, we can understand the wavelength where the responsivity is maximised is in the range of 565 – 630 nm. The full width half maximum (FWHM) of the photodiode responsivity was 405 nm. When comparing the spectral response of the photodiodes with the absorbance spectrum of the H_2O_2 probe (reported in the previous section), the responsivity peak did not coincide

with the absorbance maximum. Thus, the working wavelength of the device was selected to be a trade-off of the two spectra. The optimal wavelength was calculated using a custom Matlab-based algorithm computing the variation of the platform output when varying the wavelength. The model was trained using the experimental spectra of both the photodiode responsivity and the absorbance of the H_2O_2 probes. The experimental H_2O_2 absorbance spectrum and the photodiode responsivity were fit with polynomial (6^{th} order) and a double Gaussian model, respectively. The result of the analysis is reported in Figure 4.14(b). Accordingly, the optimal working wavelength was 498 nm, and the optimal working range was 480 – 520 nm. When confronting these results with commercial LED choices by Thorlabs [64], a 490 nm LED with a 20 nm FWHM was selected. Among all the commercial LED available, this device was the most suitable in terms of optical power and required power supply (3 mW at 20 mA), wavelength range (480 – 500 nm) and package type [64].

4.9.2. Photodiode output characteristic

After the working wavelength was selected, the sensor output was characterised at the specific wavelength of 490 nm using the selected LED. For this characterisation, a cartridge with four microfluidic channels was used. The platform characterisation was performed in dark conditions.

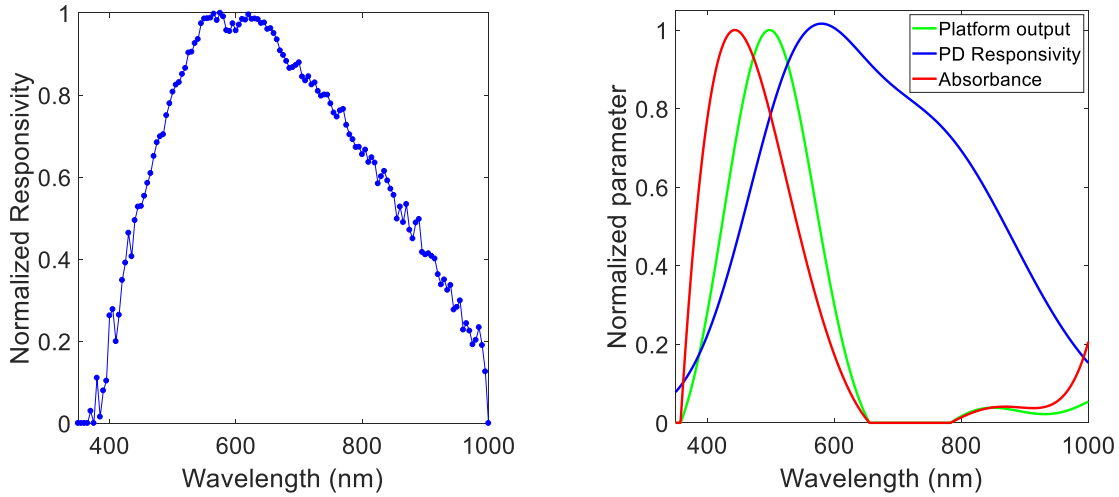

(a) (b)

Figure 4.14 (a) Average spectral response from 25 randomly selected pixels in the sensor array. The responsivity was normalised to its maximum. (b) The estimated best response of the platform (green) taking into account photodiode responsivity (blue) and absorbance spectrum of the H_2O_2 probe (red). The optimal wavelength was in the range 480 – 520 nm with a peak at 498nm.

The 490 nm LED from Thorlabs was used as the light source. An optical lens was used (AC254-035-A-ML BBAR Coating f = 35mm lens from Thorlabs) to provide collimated light. The current supply to the LED was swept across its range. The light intensity was first measured with the cartridge in each of its four microchannels. The reference light intensity was also measured with a power meter (1936-R power meter with silicon photodetector 818-SL/DB, Newport) and expressed as irradiance in μWcm^{-2} [300]. The area of the reference photodetector was 1 cm^2. The average outputs of pixels enclosed in the microchannels and the ones covered by fluidic walls versus the power recorded by the benchtop equipment are reported in Figure 4.15. The outputs of the microchannels were obtained by averaging the enclosed pixels in time (1000 frames) and space (48 pixels per channel). The output of the active area covered by microfluidic structures was obtained by averaging both in time (1000 frames) and in space (64 pixels in total) the output of the sensors covered by the epoxy walls. Reference readings from the power meter were obtained as average over 1000 samples. The output signals from the microchannels were almost identical. Considering that a 12-bit ADC was used for data digitisation on a dynamic range of 3.3V, data from each pixel had a resolution of 0.0504 mV.

In dark conditions, the average output signal reported for the microchannels was 498.97 ± 22 mV. LOD and LOQ, according to the IUPAC definition [58], were 571.57mV and 718.97 mV – respectively. When converted into irradiance using the characteristic, they correspond to 0.39 μWcm^{-2} and 1.9 μWcm^{-2}, in the same order. From 1.9 μWcm^{-2} to 11.5 μWcm^{-2}, the platform showed a linear response. Sensor output signals started saturating at around 15.6 μWcm^{-2}. Average responsivity values in the linear range were 0.116, 0.116, 0.118 and 0.119 $V\mu W^{-1}$, from channel 1 to channel 4 respectively. Pixels covered by fluidic walls showed less sensitivity to light. There are many factors which can create small fluctuations in the output of the microchannels. These include device-to-device variability, fabrication impurities, noise and variability in the read-out and biasing circuitry. Since the platform was used for rate estimation of enzymatic reactions, sensors drift in dark and condition of constant illumination of 9 μWcm^{-2} were also estimated over 5 minutes measurements. Average drifts over triplicates measures within the microchannels were 0.0014 ± 0.001 mVs^{-1} and 0.0009 ± 0.001 mVs^{-1}, respectively.

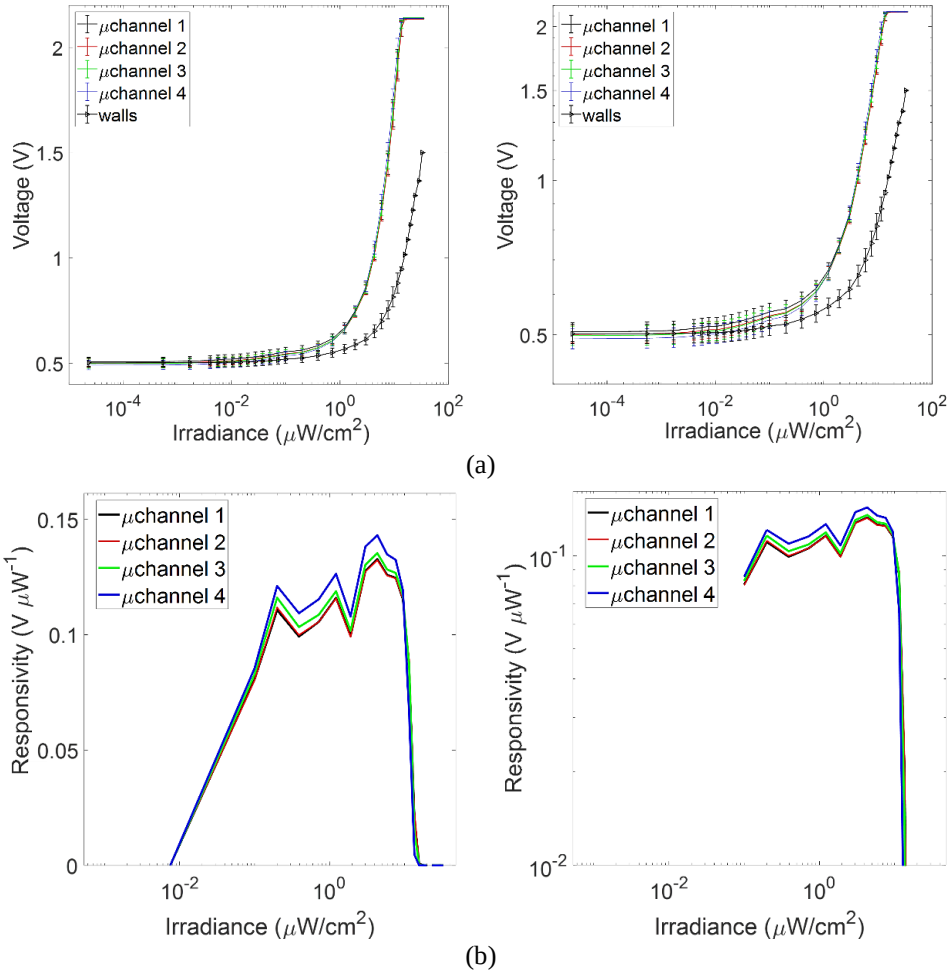

Figure 4.15 (a) Sensor output (V) vs irradiance (μWcm^{-2}) at 490nm. Voltage is shown in linear (left) and logarithmic scale (right). Irradiance is shown in logarithmic scale. The outputs from pixels enclosed in each microchannel were averaged over time (1000 frames) and space (48 pixels). The outputs from pixels covered by epoxy microstructure – 'walls'– were similarly averaged over time and space (64 pixels). (b) Responsivity of the microchannel vs irradiance at 490nm. Responsivity is shown with linear (left) and logarithmic scale (right). Irradiance is shown in logarithmic scale.

4.9.3. Sensor array characterisation

The improvements of the signal quality when using multiple sensors and oversampling are quantified. In this study, the sensor array was illuminated with a constant optical intensity of 9 μWcm^{-2} at 490 nm. To study the behaviour of standard deviation when increasing the number of averaged pixels, pixels in a single frame were randomised, and sub-groups of the array were averaged.

Figure 4.16(a) demonstrates that the standard deviation of the measurement is reduced by a factor of 1/√N when averaging N different pixels. This analysis is particularly critical when considering that the microfluidic channel encloses several pixels. Increasing the number of

microfluidic channels decreases the number of pixels enclosed in each microstructure. Therefore, it can be assumed that increasing the amount of the microfluidic channels and, accordingly, the number of metabolites to be simultaneously tested, degrades the performance of the platform. For the implemented 4-channel network, each microchannel encloses 48 pixels. This corresponds to an average reduction of the standard deviation of the measurement by a factor 6.93.

Similarly, the trend of the standard deviation when oversampling on the same sensor was analysed (time averaging). Figure 4.16(b) shows that the standard deviation reduction can also be achieved by averaging multiple measurements from the same sensor. By comparing Figure 4.16(a) and Figure 4.16(b), it is possible to conclude that the standard deviation related to space averaging is higher than the one obtained with temporal averaging. However, time averaging was particularly useful in eliminating high-frequency noise.

The combined effect of time and space averaging is analysed in Figure 4.16(c). Here, the array was divided into sub-groups and their time and space samples were randomised altogether. Then, the random space-time samples were averaged. The graph demonstrates that the reduction of the standard deviation is verified regardless of the nature of the sample population. Also, averaging allows the output to converge to its final stable value. In this case, the convergence of both standard deviation and mean value was achieved by averaging more than 500 samples. Additional averaging does not further increase the performance of the system.

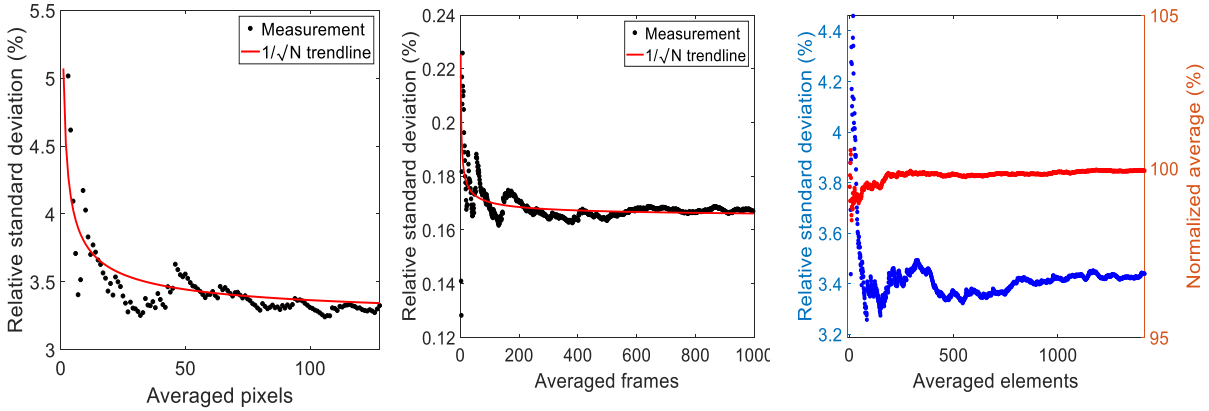

Figure 4.16 (a) Relative standard deviation decreases with a 1/√N trend when averaging different pixels. (b) Relative standard deviation also decreases likewise when averaging different frames (average over time). (c) Averaging in both space and time is effective in reducing the standard deviation and reaching a convergence to a stable value.

4.10. Capillary Flow Characterisation

Capillary flow was experimentally verified on test samples and on the cartridge using visual inspection. Figure 4.17 reports a proof-of-concept image, composed of a sequence of micrographs. In these experiments, recorded with a microscope, the capillary effect when introducing water into a microchannel can be observed. After its introduction, water travelled from the south to the north side of the device, completely covering the sensing area. In this experiment, water covered the sensing area of the CMOS chip in less than 3 seconds. The sample flow stopped once the microchannel was filled. Another key information the figure shows is that the microstructure was successful in containing the liquid only in the microchannel, and there was no evident leakage of introduced samples in adjacent channels. The flow rate of the introduced sample was quantified using the sensor array. The frames per second rate (approximately 36.5 fps) ensured a temporal resolution of 27.4 ms, suitable for the expected flow rate of the sample. It has already been demonstrated that the introduction of a liquid sample into the microstructure creates a detectable increase in the light transmittance. Raw data reported in Figure 4.18(a) corroborate that the photodiodes embedded in the sensor array were capable of detecting the arrival of the advancing meniscus. In particular, the photodiodes recorded a voltage spike and a sudden increase of transmittance once covered with the inserted liquid. The spike was very pronounced (~ 1.2 V) and clearly detectable. Pixels enclosed into microchannel and aligned in the perpendicular direction with respect to the flow responded with simultaneous voltage spikes, as shown in Figure 4.18(b). This demonstrated that the meniscus advanced with a linear front inside the microstructure. Pixels enclosed into the microchannel and aligned in the parallel direction with respect to the flow, responded with sequential spikes, effectively recording the advancement of the meniscus. Figure 4.18(c) shows an example of 16 pixels sequentially sensing the arrival of the introduced sample. When the pixels inside the microchannel were averaged, a single signal with 16 spikes was typically obtained, as shown in Figure 4.18(d) Despite the less pronounced voltage spike, it allowed the quantification of the flow rate from a single signal. In the data-analysis phase, the mentioned signal was used to verify the correct filling of the microstructure. The above-mentioned data demonstrated that the sensor array could detect the liquid flowing on the sensing area. This capability has been used to quantify the filling time of the device, i.e. the time required for the sample to completely cover the sensing area. In the design stage, several simulations were presented to show the parameter

optimisation and estimate the expected performance of the device. Ultimately, a conservative approach was adopted, and the system was designed to provide a filling time of maximum 30s when using whole blood as a fluid of interest. By using the aforementioned approach, the flow rate, and the filling time of diluted serum (1:10), diluted plasma (1:1) and whole blood were quantified over triplicates. Serum and plasma were purchased from Sigma Aldrich while whole blood was purchased from Cambridge Bioscience. Plasma and serum were diluted in DI water. A cartridge embedding four microfluidic channels with height and width of approximately 290 µm and 300 µm, respectively, were employed. For diluted serum, the time required for the sample to reach the first and the last pixel (filling time) of the array were 2.48±0.06 s and 4.58±0.129 s. The same figures increased to 2.44±0.009 s and 7.67±0.005 s, respectively, for diluted plasma (1:1).

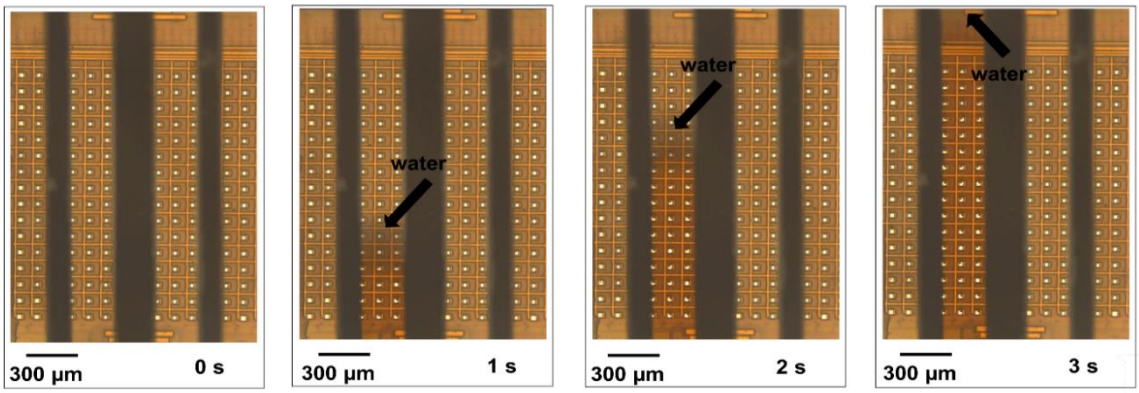

Figure 4.17 Water flowing into a microchannel fabricated on chip. The sample covered completely the sensing area of the CMOS chip in approximately 3 seconds. The micrographs also show a leakage-free flow.

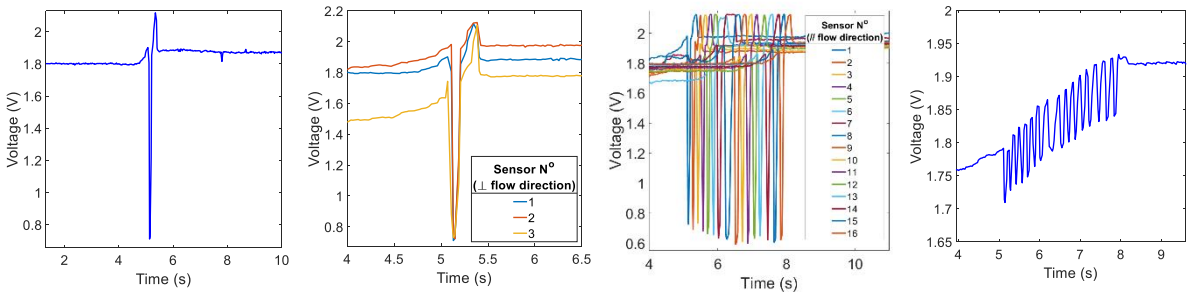

(a) (b) (c) (d)

Figure 4.18 Raw data from the sensor array when a sample (water) was introduced into a microchannel (h~290 µm). (a) Voltage spike induced by the arrival of the meniscus onto a photodiode. (b) Advancing meniscus covering sensors aligned in the perpendicular direction of the flow simultaneously. (c) Advancing meniscus covering sensors aligned in the parallel direction of the flow sequentially. (d) When averaging the pixels of a microchannel, the advancement of the meniscus over the sensing area produced sequential spikes.

Expectedly, the flow was slower when using whole blood. Precisely, in this case, the time required for the blood to reach the first and the last pixel of the array were 13.05±5.20 s and 28.23±11.77 s. The standard deviation of the flow was also higher when using blood, suggesting that the results are less repeatable when using this specimen. Experimental data were compared with the simulation model used for the design of the device. Simulations were repeated with adjusted parameters, including microchannels geometry and contact angles. Physical properties of the diluted specimens were assumed using linear regression. Experimental data, together with simulations, are represented in Figure 4.19(a). For all the analysed specimens, the correlation between experimental and simulated data was high ($R^2 > 0.98$). However, the model seemed to be affected by a small bias of 3.36 s against the experimental data. The bias was calculated as the average over the absolute measurement error, as per definition.The flow in parallel microchannels was also analysed and reported in Figure 4.19(b). Regardless of the nature of the sample introduced in the microstructure, the flow in the channel was virtually identical. Identical channels were another design specification which was therefore met.

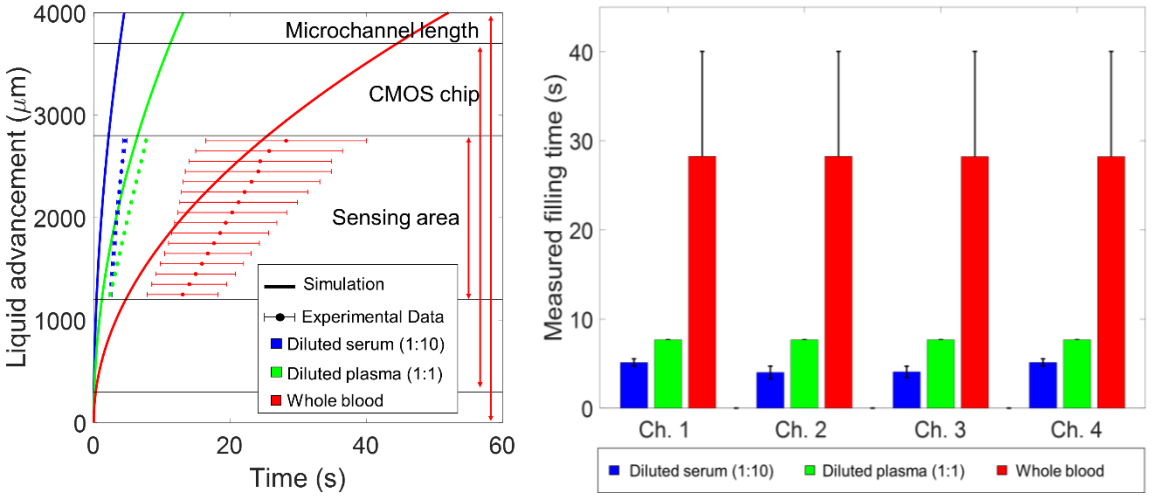

(a) (b)

Figure 4.19 The advancement of the meniscus in a four-microchannel cartridge (height ~ 290μm) was recorded with the sensor array for diluted serum (1:10) diluted plasma (1:1) and whole blood. Data is reported as the average ± standard deviation over three replicates and over all the microchannels. (a) Data compared to simulations. Simulations were adjusted using measured values of with, height, length, and contact angles. Sample parameters for diluted samples were assumed using a linear regression. As per design, all the introduced liquids completely covered the sensor array in less than 30s on average. (b) For all the introduced samples, microchannels had an identical filling time.

4.11. Summary of the Chapter

- A passive microfluidics network was integrated on top of the sensing area with no intermediate layer using a combination of soft lithography and injection moulding.
- Bioreceptors were introduced in the fluidics by off-chip mixing or preloaded using lyophilisation.
- The fabrication procedure was suitable for planarization, with a slope of 0.007 µm/µm, which was negligible when compared to the roughness of the CMOS chip. The heights and widths of the microchannels were, on average, 291.95±6.44 µm and 300.87±0.86 µm, respectively. Mechanical strength of the structure was also evaluated trough shear and pull testing (maximum lateral force: 576±190.2 gr; maximum pulling force: 70gr).
- Optical spectral testing showed that o-dianisidine and phenol/4AAP are both suitable H_2O_2 probes with experimental extinction coefficients of 6.37 mM^{-1} cm^{-1} at 463 nm (FWHM: 112 nm) and 9.545 mM^{-1} cm^{-1} at 440 nm (FWHM: 180 nm).
- The photodiodes have a maximum responsivity at 575 nm (FWHM: 405nm).
- The optimized working wavelength, considering H_2O_2 probes properties, sensors responsivity and commercially available LEDs was 490 nm.
- The sensors at 490 nm had a linear response with optical intensity in the range 1.9 - 11.5 µWcm^{-2}, showing a responsivity of 0.117±0.001 VμW^{-1}. Averaging photodiodes within the same microchannel and averaging oversampled reading from the same photodiode were effective in the reduction of the noise: the standard deviation of the measurement was reduced by a factor of $1/\sqrt{N}$ by averaging N different measurements.
- The capillary flow of different samples (i.e. diluted serum, diluted plasma and whole blood) was also tested. Visual inspection also demonstrated that the microfluidic was successful in providing passive flow and confining the liquid sample. As per the design, all the samples covered the active area within 30 seconds after their introduction in the fluidic input without any externally applied pressure. The time required for whole blood to completely cover the sensing area was 28.23±11.77s (worst-case scenario).

Chapter 5: Metabolomics-on-CMOS

5.1. Introduction

The present chapter focuses on biological experiments for the quantification of the six metabolites of interest: LAA, glutamate, choline and sarcosine for PCa and lactate and creatinine for ischemic stroke. Metabolites are first quantified in diluted human serum samples. Subsequently, multiplexed testing is demonstrated in different configurations. Procedures for reagents immobilisation are also illustrated. Proof-of-concept experiments with whole blood conclude this chapter. Table 5.1 illustrates the contribution to each activity discussed in this chapter.

5.2. Experimental Setup

The setup for the biological experiments henceforward used is described here. A schematic of the experimental setup is shown in Figure 5.1. All the optomechanical components were purchased from Thorlabs. The reader of the platform was secured to an optical aluminium breadboard using two screws with the ZIF socket facing up.

Table 5.1 Table of contributions for the activity presented in this chapter.

Task / Activity presented in Chapter 5	Main investigators
Development of the experimental setup	**- Valerio F. Annese**
Assay formulations	- Well established in the literature
Assay optimisations for this platform	**- Valerio F. Annese**
Characterisation of the platform when measuring PCa-related metabolites in diluted serum	**- Valerio F. Annese**
Characterisation of the platform when measuring ischemic stroke-related metabolites in diluted serum	**- Valerio F. Annese**
Quantification of the test duration	**- Valerio F. Annese**
Reagents printing for microchannel functionalisation	**- Valerio F. Annese**
Reagents lyophilisation for microchannel functionalisation	**- Valerio F. Annese**
Quantification of the reagents shelf-life after lyophilisation	**- Valerio F. Annese**
Multiplexed assays in human plasma (1 metabolite + control)	**- Valerio F. Annese**
Multiplexed assays with paper microfluidics (2 metabolites)	- Dr Chunxiao Hu[1] (designed the work and performed experiments) - Dr Srinivas Velugotla[1] (developed the paper strips) **- Valerio F. Annese** (developed and applied functionalisation method of the paper strips)
Whole blood experiments	**- Valerio F. Annese**
Affiliation at the time of completion of the activity: [1]*Microsystem Technology Group, James Watt School of Engineering, University of Glasgow.*	

The size of the optical breadboard was 15 x10 x1.2 cm. Exposed microcontroller pins were electrically isolated with rubber tape. A cartridge, whose geometry and characteristics are specified for each set of experiments, was inserted into the ZIF socket. Accordingly, the sensing area of the CMOS chip was parallel to the optical breadboard and facing up.

An optical post with an approximated height of 30 cm was vertically fixed to the same optical breadboard. Two T-junction connectors were mounted onto the vertical post, and two new transversal optical posts were fitted into the setup. The top transversal optical post accommodated a LED holder. A 3mW LED working at 490 nm (FWHM 20 nm) was mounted inside the holder and orientated with the emitting junction facing straight down towards the reader. The light source was power supplied by an external power supply (HP E3631A). The lower transversal optical post accommodated a lens holder, where an achromatic collimating lens (AC254-035-A-ML BBAR Coating f = 35 mm) was mounted. The height and the orientation of the two optical posts were adjusted so that the active area of the chip could receive perpendicular collimated light. The setup mounted onto the optical breadboard was enclosed into a cardboard box, externally coated with a blackout cloth made of nylon and polyurethane. The coating was essential to ensure that the experiments were performed in a dark environment. Only a small aperture was left open to accommodate connection wires and undertake on-chip sample delivery. The enclosing box was internally coated with aluminium, to reduce any eventual environmental electrical interference. The reader inside the enclosed dark environment was connected to an external laptop (HP EliteBook i7-8650u 16 GB) through a USB cable. A ferrite adapter was used to reduce any eventual interference noise affecting data travelling through the USB cable. The Matlab-based user interface was running on the laptop. During the work, the GUI evolved in several different versions. However, the modifications were mainly graphical, therefore did not substantially affect the format of the recorded data. The USB link also provided power supply to the reader (5V). Data was recorded with an average frame rate of 36.5 fps and a resolution of 12-bit. Typically, the duration of a single experiment was 5 minutes (approximately 11000 frames).

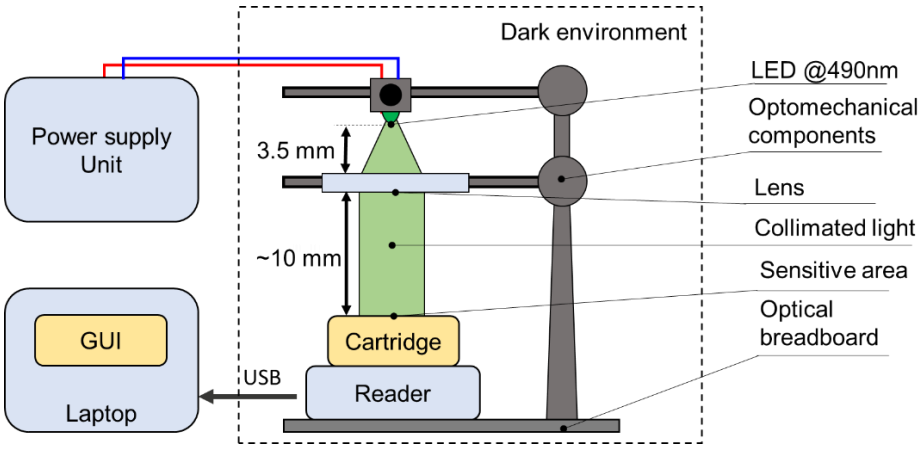

Figure 5.1 Experimental setup for biological experiments.

5.3. Metabolomics-on-CMOS in Diluted Serum

The capability of the platform in quantifying the target metabolites was first assessed in diluted serum. Human serum was modified with known concentrations of metabolites of interest to determine the calibration curves of the platform.

5.3.1. Materials and Methods

Assay formulation. All the chemicals were purchased from Sigma Aldrich. Dehydrated human serum was also obtained from Sigma Aldrich and reconstituted with DI water following the recommended protocol. The reconstituted human serum was further diluted with additional DI water for a volume ratio of 1:10. All the reagents were prepared using 0.1 mM Tris HCl buffer (pH 8). Modified serum samples were freshly prepared before each test. Biochemical protocols for the preparation of reagents used for diluted serum experiments are detailed in Appendix H.

The formulations of the assays were optimised using a trial-and-error approach. The optimisation aimed to create a detectable colour change in the physiological range of the target metabolite within a few minutes. The procedure was first performed off-chip. Fine-tuning was subsequentially performed on-chip. The assay formulation led to the determination of desired concentrations for enzymes and reagents. Expectedly, by increasing the level of the enzymes in the formulation, the reactions had a higher reaction rate. Similarly, the colour change of the solution was more accentuated by increasing the concentration of the substrate in the testing solution. Figure 5.2 shows demonstrative

solutions for the LAA assay. The colour change of the reagents increased when increasing the level of the substrate in the test. Similar results were obtained off-chip before running the assay on-chip. Assay formulations for metabolites sensing in diluted human serum are summarised in Table 5.2 (for PCa) and Table 5.3 (for ischemic stroke).

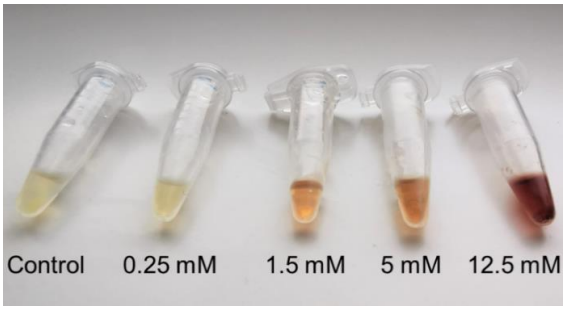

Figure 5.2 Demonstration of the colour changes due to different concentrations of the substrate (LAA assay). The picture was taken 30min after the assay was started.

Table 5.2 Assay formulations for PCa-related metabolites sensed in diluted human serum using the developed platform.

	LAA	Glutamate	Choline	Sarcosine
Cartridge	Four parallel and identical microchannels (h ~ 137 µm)			
Microchannel volume	0.158 µL			
Light source	LED @ 490nm (3 mW, FWHM = 20 nm)			
Total Volume	50 µL			
Sample Volume	25 µL			
Reagent mix volume	25 µL			
Reagent buffer	0.1 Tris HCl			
1st reaction stage	LAAOx (10µL, 4U/mL)	GlOx (10µL, 4U/mL)	ChOx (10µL, 150U/mL)	SaOx (10µL, 200U/mL)
2nd reaction stage	10µL HRP 65.5U/ml 5µL o-dianisidine 41mM		10µL HRP 300U/ml 5µL o-dianisidine 41mM	
Negative control	1st reaction stage was substituted with 10µL of DI water			

Table 5.3 Assay formulations for ischemic stroke-related metabolites sensing in diluted human serum using the developed platform.

	Lactate	**Creatinine**
Cartridge	Two parallel and identical microchannels (h ~ 137 µm)	
Microchannel volume	0.316 µL	
Light source	LED @ 490nm (3 mW, FWHM = 20 nm)	
Total Volume	60 µL	60 µL
Sample Volume	30 µL	24 µL
Reagent mix volume	30 µL	36 µL
Reagent buffer	10 mM PBS	
1st reaction stage	LaOx (10µL, 4U/mL)	CNN (6µL, 200U/mL) CTN (6µL, 200U/mL) SaOx (6µL, 150U/mL)
2nd reaction stage	10 µL HRP 150U/ml 5µL 4-Aminoantipyrine 10.5 mM 5µL Phenol 44.5 mM	6µL HRP 150U/ml 6µL 4-Aminoantipyrine 10.5 mM 6µL Phenol 44.5 mM
Negative control	1st reaction stage was substituted with 10µL of DI water	CNN was substituted with 6µL of DI water

Procedure. Experiments were conducted at room temperature in the laboratories of the MST group, Rankine Building, University of Glasgow. Metabolites were tested individually. Reagents were off-chip mixed with the sample and immediately introduced into the cartridge within a few seconds. Sample introduction was achieved by pipetting the total testing volume onto the fluidic input. The sample flowed into the microstructure and over the sensing area by capillary effect. A schematic representation of the adopted protocol is shown in Figure 5.3. Cartridges with four microchannels were used for PCa-related metabolites. Cartridges with two microchannels were used for PCa-related ones. In both cases, the height of the microchannel was, on average, 137.14±1.1 µm.

Data handling. For each concentration, the assay was performed in triplicates, herein referred to as biological replicates. Since each cartridge had multiple microchannels, each biological replicate had several readings, herein indicated as technical replicates. After data collection, measurements were offline processed using the developed GUI. Technical replicates with unexpected behaviour were excluded. Examples of readings with unexpected were:

- Readings where the rate of the reaction accelerated over time.
- Readings where transmittance increased over time.
- Readings where the noise level was excessive with respect to the standard measures.
- Measurements affected by air bubbles or other strong artefacts.
- Readings affected by microfluidics failure, including underfilling of the microstructure.
- Measurements considered outliers.

Data from technical replicates were independently analysed using the developed GUI, and the results were averaged. Thus, for each biological replicate, only one result was obtained. The result for each concentration was obtained as the average and standard deviation over the biological replicates.

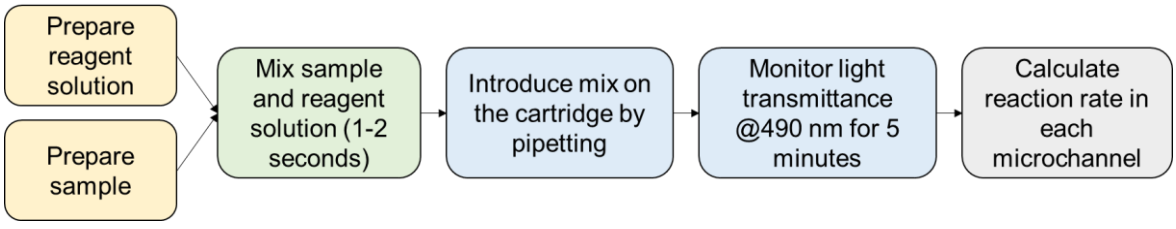

Figure 5.3 Protocol adopted for metabolomics experiments in diluted serum.

Cartridge reuse. Cartridges were cleaned and re-used. Ten cartridges were used for PCa-related experiments. Three cartridges were employed for ischemic stroke experiments. A cleaning procedure after each measurement was adopted to avoid cross-contamination. The cleaning recipe involved subsequent rinse in DI water, IPA, ethanol, and nitrogen blow-dry. Cleaning the cartridge with more aggressive solvents, such as piranha, was attempted. However, it was avoided because the solvent also etched the epoxy microchannels. Cross-contamination minimisation was also achieved by optimising the testing sequence. For each metabolite, a negative control (control measurement) was first recorded. Then, the colorimetric estimation was performed in triplicates.

5.3.2. PCa Metabolites

Calibration curves for LAA, glutamate, choline and sarcosine in diluted human serum are reported in Figure 5.4. The complete characterisation of the platform for the analytes of interest is discussed in Table 5.4. An example of raw data for LAA and sarcosine, the tests with respectively the highest and lowest physiological ranges, are shown in Figure 5.5. Typically, increased concentrations of the substrate created increased transmittance drop, measured by a reduction of the voltage output of the photodiodes. Transmittance drop was nonlinear and is in line with the Michaelis-Menten model. Other metabolites showed analogue behaviours.

Kinetics constants (K_m) were estimated by fitting data to the Michaelis-Menten model. K_m results for all the metabolites were comparable with the values reported in the literature [49]. The discrepancies are related to the different materials, methods, and conditions of the tests. For all the metabolites, the fitting of the experimental data with the Michaelis-Menten model was satisfactory with R^2 values ≥ 0.98.

A subset of the collected data (low concentrations) was also fitted using a linear model. Herein, linear range is defined as the range of measurement reporting $R^2 \geq 0.90$ when a linear fit is performed. Linear ranges were covering the physiological ones. The sensitivity of the assays was increased when the physiological range of the target analyte decreased. This was expected and reflected the choice of enzyme concentrations in the formulation of the tests described previously. Relative standard deviations of the measurement in the linear range were in between 12.7% and 19.8%.

LOD and LOQ were quantified using the respective control. LOD and LOQ expressed in mVs^{-1} were then converted in µM by using the estimated Michaelis-Menten for each

metabolite. Thus, LOD for LAA, glutamate, choline and sarcosine were 69.01 µM, 6.86 µM, 3 µM and 0.26 µM, respectively. Similarly, LOQ values for the metabolites in the same order were 218.3 µM, 12.04 µM, 4.22 µM, 2.13 µM. LOD and LOQ results demonstrated the suitability of the platform for the measurements in the target range in diluted human serum.

Table 5.4 Platform Characterisation in diluted human serum for PCa-related metabolites. V_m, c and K_m are calculated using the Michaelis-Menten model. Metrics have been defined in Table 2.3.

	LAA	**Glutamate**	**Choline**	**Sarcosine**
Physiological Range	1.7 – 4.6 mM	40 – 150 µM	10 – 40 µM	0 – 20 µM
Test Range	0 – 12.5 mM	0 - 800 µM	0 – 500 µM	0 – 500 µM
Relation with PCa	↑	↑	↑	↑
Model	$y = \frac{V_m \cdot x}{K_m + x} + c$			
V_m (mVs^{-1}) (95% coefficient bounds)	4.70 (3.68, 5.71)	4.60 (3.61, 5.59)	3.219 (2.62, 3.82)	2.874 (2.297, 3.45)
c (mVs^{-1}) (95% coefficient bounds)	0.016 (-0.027, 0.058)	-0.014 (-0.115, 0.088)	-0.029 (-0.166, 0.108)	0.012 (-0.123, 0.146)
K_m (µM) (95% coefficient bounds)	18610 (12280, 24940)	715.1 (411.9, 1018)	197 (95.77, 298.1)	172.9 (70.45, 275.4)
SSE	0.010	0.0284	0.049	0.059
RMSE	0.034	0.064	0.091	0.099
R^2	0.997	0.995	0.992	0.989
Linear Model	$Y = S \cdot x + C$			
Linear Range[1]	0 – 3.5 mM	0 – 300 µM	0 – 100 µM	0 - 100 µM
Analytical Sensitivity (S) ($mVs^{-1}mM^{-1}$) (95% coefficient bounds)	0.226 (0.210, 0.243)	4.72 (4.15, 5.30)	11.79 (8.77, 14.82)	11.72 (11.0, 12.44)
C (mVs^{-1}) (95% coefficient bounds)	0.02 (-0.009, 0.049)	0.003 (-0.317, 0.324)	$7.8 \cdot 10^{-4}$ (-0.143, 0.143)	0.034 (0.003, 0.065)
SSE (linear)	0.004	0.023	0.034	0.003
RMSE (linear)	0.023	0.062	0.093	0.025
R^2 (linear)	0.993	0.985	0.967	0.997
Precision[2]	17.8%	12.7 %	13.4%	19.8%
LOD (mVs^{-1})	0.033	0.030	0.019	0.017
LOQ (mVs^{-1})	0.070	0.063	0.039	0.047
LOD (µM)[3]	69.01	6.86	3.00	0.26
LOQ (µM)[3]	218.3	12.04	4.22	2.13
Resolution (µM)[4]	24.52	1.03	0.48	0.4

[1] Linear range is defined as the measurement range were the linear model had $R^2 > 0.9$.
[2] Calculated as the average of the relative standard deviation of the measurements in the linear range.
[3] Converted from mVs^{-1} to µM using the Michaelis-Menten model.
[4] Calculated as the ratio between the standard deviation of the control measurements and the sensitivity in the linear range [58].

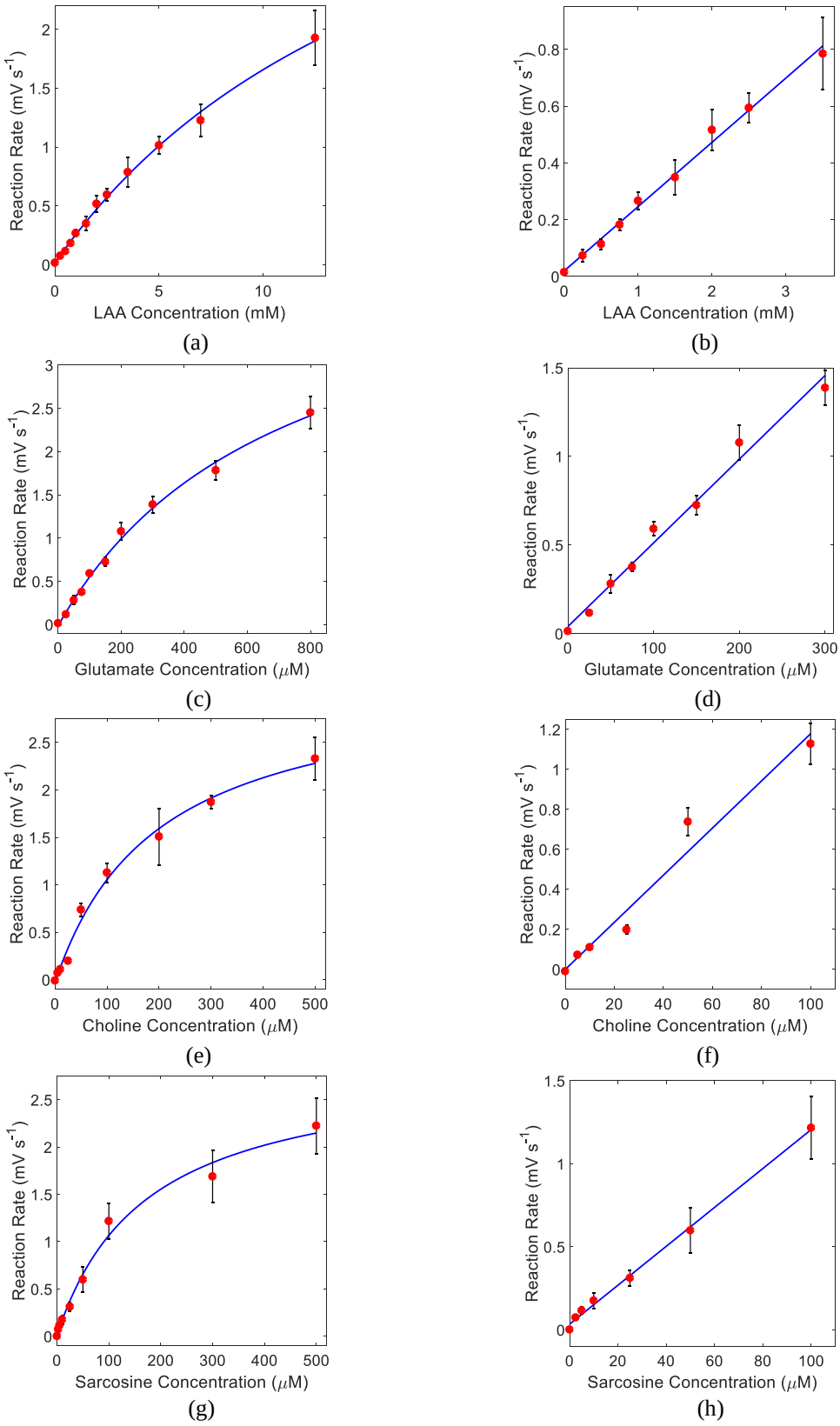

Figure 5.4 Calibration curves obtained by fitting data with Michaelis-Menten in the extended range (left) and with a linear model (right) for (a)(b) LAA, (c)(d) glutamate, (e)(f) choline and (g)(h) sarcosine in diluted human serum. Concentrations refer to the total reaction volume.

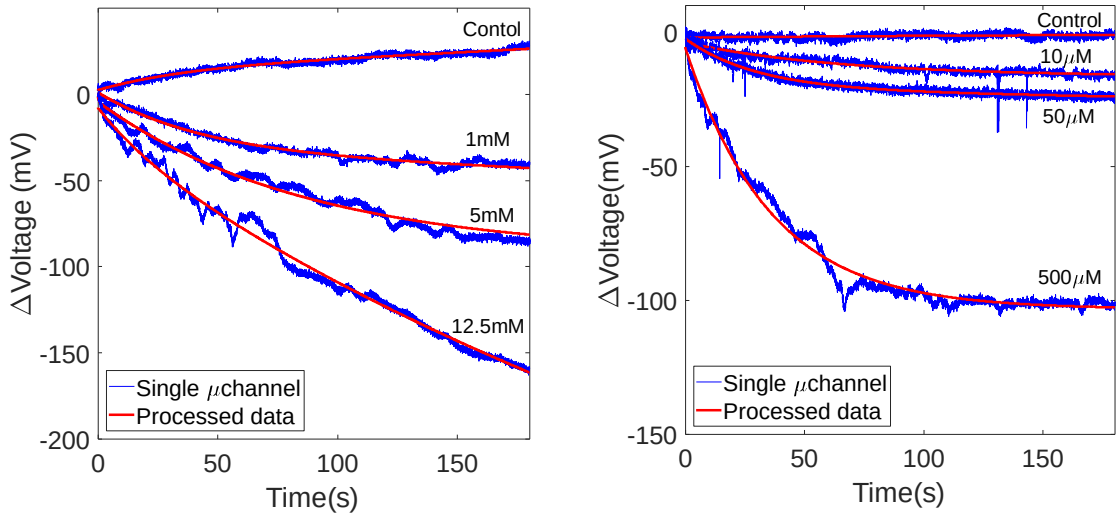

Figure 5.5 Averaged raw data from single microchannel (blue) and processed data (red) for LAA (a) and sarcosine (b).

5.3.3. Ischemic Stroke Metabolites

Calibration curves for lactate and creatinine in diluted human serum are shown in Figure 5.6 while the complete characterisation of the platform for the analytes of interest is reported in Table 5.5. Like the analysis performed for PCa-related metabolites, Kinetics constants were estimated by data fitting to the Michaelis-Menten model. Also for lactate and creatinine, K_m results are comparable with the values reported in the literature [49]. For both the metabolites, the fit with the Michaelis-Menten model was satisfactory with R^2 values ≥ 0.96. Also in this case, a subset of data points with lower concentrations was fitted using a linear model.

As shown in Table 5.5, the linear range for lactate was smaller than the physiological one. This suggests the need for sample dilution when testing lactate. The linear range for creatinine was suitable for determination in the physiological range. The average standard deviations of the measurement in the linear range for lactate and creatinine were 17.5% and 25.1%, respectively. LOD and LOQ were also quantified using the respective control measurements. The LOD for expressed in µM for lactate and creatinine were 31.85 µM and 5.21 µM, respectively. The LOQ for both the metabolites were 64.38 µM and 36.55 µM. The performance of the platform in the quantification of lactate and creatinine indicates that it is suitable for the determination of the two metabolites in the physiological range.

Table 5.5 Platform Characterisation in diluted human serum for ischemic stroke related metabolites. V_m, c and k_m are calculated using the Michaelis-Menten model. Metrics have been defined in Table 2.3.

	Lactate	**Creatinine**
Physiological Range	0.3 – 2.0 mM	100 – 150 µM
Test Range	0 – 3 mM	0 –2 mM
Relation with ischemic stroke	↑	↑
Model	$y = \frac{V_m \cdot x}{K_m + x} + c$	
V_m (mV s^{-1}) (95% coefficient bounds)	3.99 (2.90, 5.08)	1.263 (0.818, 1.708)
c (mV s^{-1}) (95% coefficient bounds)	-0.177 (-0.954, 0.601)	0.010 (-0.086, 0.106)
K_m (µM) (95% coefficient bounds)	362 (260, 751)	1085 (807, 2089)
SSE	0.360	0.0069
RMSE	0.300	0.042
R^2	0.967	0.998
Linear Model	Y = S · x + C	
Linear Range[1]	0 – 0.5 mM	0 – 0.5 mM
Analytical Sensitivity (S) (mV s^{-1} mM^{-1}) (95% coefficient bounds)	5.175 (2.738, 7.612)	0.803 (0.143, 1.462)
C (mV s^{-1}) (95% coefficient bounds)	-0.023 (-0.690, 0.644)	0.028 (-0.152, 0.209)
SSE (linear)	0.090	0.007
RMSE (linear)	0.212	0.057
R^2 (linear)	0.977	0.932
Precision [2]	17.5%	25.1%
LOD (mV s^{-1})	0.146	0.016
LOQ (mV s^{-1})	0.425	0.051
LOD (µM)[3]	31.85	5.21
LOQ (µM)[3]	64.38	36.55
Resolution (µM)[4]	7.92	39.76

[1] Linear range is defined as the measurement range were the linear model had $R^2 > 0.9$.
[2] Calculated as the average of the relative standard deviation of the measurements in the linear range.
[3] Converted from mV s^{-1} to µM using the Michaelis-Menten model.
[4] Ratio between the standard deviation of the control measurements and the sensitivity in the linear range [58].

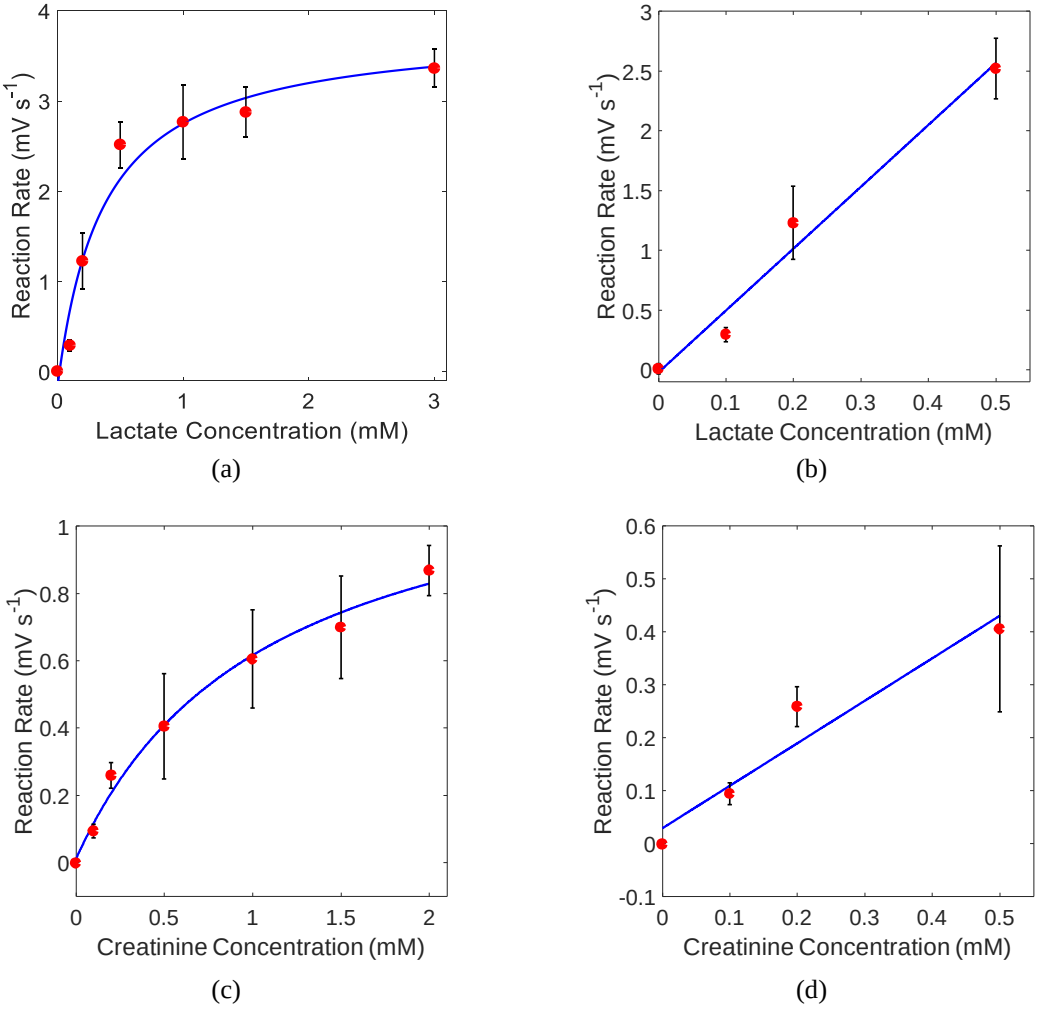

Figure 5.6 Calibration curves obtained by fitting data with Michaelis-Menten in the extended range (left) and with a linear model (right) for (a)(b) lactate and (c)(d) creatinine.

5.3.4. Discussion

The biological experiments in diluted serum showed that the platform is suitable for the quantification of LAA, glutamate, choline, sarcosine, lactate, and creatinine with physiological concentrations. Experimental data were in agreement with the Michaelis-Menten model. All the metabolites, except for lactate, showed a linear response within the expected physiological concentration levels. For lactate, it is suggested the use of diluted body fluid to take advantage of the linear response of the platform.

The precision of the measurements, calucalted as the average standard deviations, was in the range 12.7 % - 25.1%, that is comparable to the precision of the glucose meters currently on the market [237]. LODs and LOQs were lower than the expected physiological levels. Additionally, for the selected applications, increased levels of analytes are expected.

Therefore, the LOD and LOQ values do not impose any limitation on the selected applications.

The analytical sensitivity of the platform was variable in relation to the metabolite under test. Analytical sensitivity ranged from was 0.226 – 11.79 $mVs^{-1}mM^{-1}$. A correlation was identified between the analytical sensitivity and the concentrations of the enzymes used for the assays. Assays formulated with a higher level of enzymatic solutions were more sensitive towards the lower concentration of the substrate and had a higher sensitivity. However, creatinine sensitivity was low despite the high concentrations of the enzymatic solution. In this specific case, it is worth underlining that the first reaction stage leading to H_2O_2 was made up of three different enzymatic reactions. Thus, this assay is not easily comparable to all the other ones. Creatinine assay was, in fact, expectedly slower than the other tests, where only one enzymatic reaction led to H_2O_2. Despite the decreased sensitivity, creatinine testing demonstrated that the platform could also support more complicated enzymatic systems and that the suggested metabolites could be considered as a proof-of-concept of the platform.

Regarding the versatility of the platform, it is should be emphasised that the same hardware with no modification was used for the measurements of six different metabolites linked to different diseases. This was achieved by minimal modification of the assay formation only. Aguably, the platform might be suitable for the quantification of substrates where a respective oxidase enzyme exists and a similar chemistry can be deployed. This might include the use of up to 350 oxidase enzymes and respective substrate reported in the enzyme database BRENDA [49]. Additional substrates could also be quantified using a series of multi-step reaction leading to the production of H_2O_2 (e.g. creatinine assay).

There were some limitations to these experiments. Firstly, the sample composition was simplified. From a microfluidic point of view, the diluted serum (1:10) ensured a quick and reliable filling of the microcavities. Also, the sample was modified with a pure and freshly introduced substrate. The high dilution ratio of the serum simplified the composition of the sample by decreasing the concentration of both endogenous substrate and interfering substance. This scenario simplifies in many ways, the functioning of the platform in a real-life environment. A thicker whole plasma or blood sample has a much slower flow rate, and the filling of the microchannel is, therefore, less repeatable, as experimentally demonstrated in the previous chapter. Undiluted samples also contain impurities which degrade the signal to noise ratio of the recorded signal, consequently affecting the test result. From an organic point of view, an undiluted sample also contains thousands of additional molecules which

can potentially interfere with the developed assay. Experiments with clinically source undiluted human plasma are illustrated in the next chapter.

5.3.5. Test Duration

Some considerations can be done about the time that the platform requires to estimate the reaction rate. Only the initial reaction rate is important for the estimation of the substrate level. Thus, recording only the first part of the reaction is enough. This raises the question about the minimum time required for the platform to estimate the reaction rate. Experimentally, it was observed that tests with higher substrate concentrations required a shorter test duration. This was expected because the high substrate concentration created a rapid transmittance drop and a short recording was enough to determine the initial reaction rate. On the contrary, tests with lower substrate concentrations required a longer test duration to provide a reliable result. This was also expected since the additional data collected due to the increased time duration allowed a better estimation of the reaction rate. However, in a real-life scenario the substrate concentration is not known.

To answer this question, additional data processing was performed. All the biological experiments recorded had a duration of 5 minutes. Three recordings from the glutamate dataset were used for this analysis. Conservatively, glutamate test with a substrate concentration of 50 µM was selected. The duration test of the recordings was gradually reduced by 1 second. Recording truncation was purely numerical. For each single shortened fragment of data, the reaction rate was calculated and normalised against the reaction rate obtained with the 5 minutes test. The results of the analysis are proposed in Figure 5.7(a). It shows that when using only 60 seconds of data from the reaction starting point, the algorithm was able to calculate the reaction rate with an error < 1% with respect to the full-length duration. The error then stabilised to zero for test length longer than 60 seconds. Thus, one minute can be considered as the minimum test duration required to the platform for the substrate quantification. For a conservative approach, one additional minute can be added to the previous amount as a tolerance factor.

Arguably, evaporation can potentially pose a problem when handling liquid in the microliter scale. This raises the question of whether the drying of the sample in the microchannel is quick enough to interfere with the assay. To address the question, microchannels were filled with water, and sensor data were collected until the full evaporation of the sample. Experiments were performed at room temperature. Results are reported in Figure 5.7(b). For

all the three channels analysed, no evaporation effect was observed in the first 27 minutes. Subsequently, evaporation effects were evident and profoundly affected the signal.

Precisely, during the evaporation of the sample, the trend of the average signal of the microchannel resembled the voltage spikes observed when the channel was filling. This showed that the sample inside the microchannel was progressively evaporating, from the more external pixels to the internal ones. After approximately 1 hour, the water sample was evaporated entirely. This is a crucial figure for reagents loading into the microchannels, where drying methods have been employed. Therefore, despite the volume of the sample, the confinement of the liquid into the microstructure sensibly increased its evaporation time. In summary, we can therefore conclude that a two-minute test duration is adequate for the quantification of the metabolites of interest. A test with such duration can be considered unaffected by the process of the evaporation of the sample, which started to be evident only after 27 minutes.

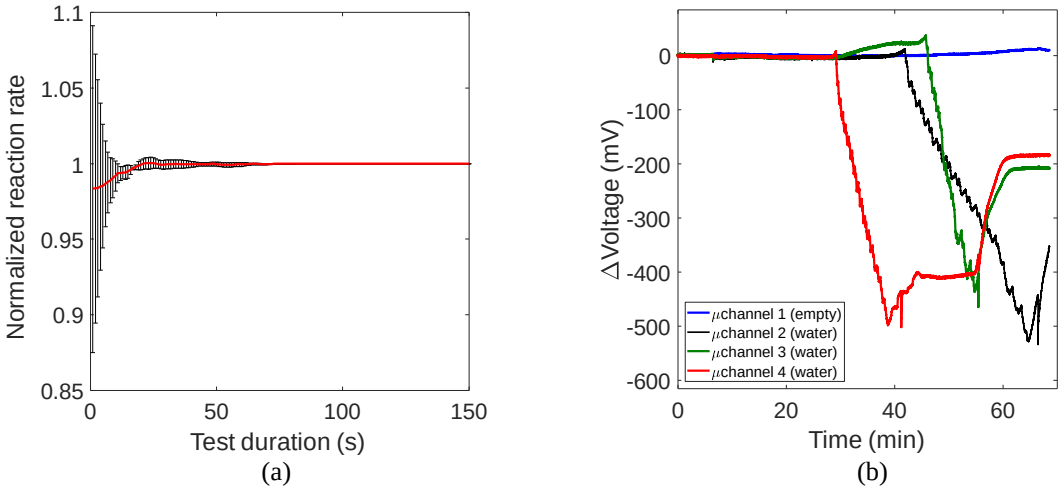

Figure 5.7 (a) Normalised reaction rate calculated for different test durations. Test duration was numerically reduced, and the reaction rate iteratively recalculated. Rate is normalised to the rate calculated when using the full-length data (5 minutes). (b) Effects of water evaporation on the platform. Evaporation effects start to be relevant after 27 minutes. The test, whose duration was 5 minutes, can be considered unaffected by evaporation effects.

5.4. Microchannel Functionalisation

For multiplexed assays, biological reagents need to be preloaded into the different microchannels with each channel acting as an individual reaction zone. The present section also focuses on the procedures for reagents lyophilisation, is a well-established and versatile procedure commonly used in the biotechnology industry for the production and storage of commercial products or reagents. The entrapment of the bioreagents was achieved by two processing steps: (i) deposition and (ii) freeze-drying.

5.4.1. Deposition and Regents Printing

Bioreagents deposition was mostly achieved by manual pipetting in the microchannel by micropipetting under the microscope. However, this method is not suitable for mass-production. Thus, a scalable approach for the functionalisation of the platform is illustrated here. In the following experimental study, the suitability of the printing techniques for the deposition of bioreagents on the chip is demonstrated. This was achieved by quantifying printing performance when using materials commonly employed in enzyme-based solutions. The Jetlab® II piezoelectric drop-on-demand inkjet printer was used in this experimental study. The printer was connected by serial ports (RS232 and 2xUSB 2.0) to a desktop computer (Advantech PPC-157T, Window 7 Pro, 32bit, Intel® Core Duo Processor, 2.00GHz, 1GB RAM). By scaling down the orifice size to few micrometres (70 µm used in this experimental study), the process of drop ejection becomes very dependent on the operating conditions, and the jetting parameters need to be empirically tuned [301]. Here, jetting parameters were optimised according to a ‘trial and error’ process based on literature references and experimental evidence [301], [302]. The Jetlab II has eleven jetting parameters to be tuned, including stimulation wave shape, amplitude and frequency, backpressure of the print head, the temperature of the print head. The optimal jetting parameters allowed having picolitre droplets with no satellites, almost no solid angle, speed lower than 2m/s (to avoid splash) and high repeatability over time. However, for a specific ink, the set of parameters could not be unique [301], [302]. Parameter optimisation and analysis of the printed droplets was achieved using custom Matlab algorithms performing automatic drop recognition and image-processing tools. The radius of each drop, deformation and position were quantified. Since the printed droplets were not perfect circles for physical reasons, ‘drop radius’ is used to refer to as the radius of a circle approximating

the printed drop. The deformation of the drop is the ratio between the effective area of the drop and the area of the perfect circle. The automatic drop recognition was performed using the Hough circle transform [302], a widely used technique for facial recognition in image processing [303].

The experimental study using 14 different inks and 10 different substrates showed that the printing performance depends on the materials employed in the process. The quantification of the printing performance in terms of drop deformation and radius broadening using different inks on silicon and using DI water on various substrates are presented in Figure 5.8(a) and (b), respectively. Assuming that the effects of inks and substrates are independent, a numerical interpolation shown in Figure 5.8(c) highlights the printing performance for all the different combinations of ink and substrate. Demonstrative pictures are shown in Figure 5.9. Printing performance was also quantified on Polyimide, the outer layer of high-voltage 0.35 CMOS technology. Specifically, the use of a solution made by PBS buffer and Glycerol 20% on polyimide showed a radius broadening of 1.96. By delivering several piezo stimulations, it was possible to print a desired amount of ink. However, the evaporation of the printed droplets was observed to be rapid. Figure 5.10(a) shows the reduction in the radius of the droplets over time while printing with different volume of a solution of PBS/glycerol 20% printed on silicon. The experimental analysis demonstrated that in the first 10 minutes after printing, part of the printed drop spontaneously evaporates (Figure 5.10 (b)). Expectedly, the evaporation process was dependant on the type of ink used and the environmental condition.

After having demonstrated that bio-printing is capable of depositing patterns with a size comparable to the CMOS chip, two different enzymatic solutions (cholesterol oxidase and glucose oxidase) were successfully deposited on the top of a CMOS chip. Post fabricated microstructure on the CMOS chip also helped improve the printing process performance. Figure 5.11 reports some optical microscope images of printed patterns on different substrates with and without microchannels. Figure 5.11(a) shows a picture of the Jetlab II inkjet printer used in this study. Figure 5.11(b) illustrates the shape and the volume of the ejected droplets. Figure 5.11(c) demonstrates that it is possible to print into a microfluidic channel 200 μm wide. Figure 5.11(d)-(g) demonstrate that the printing technique provides adequate deposition accuracy that can potentially allow the deposition of different inks into microstructures. The volume of the droplet can be controlled according to requirement. Figure 5.11(g) experimentally demonstrated that inkjet printing could be used for the direct

deposition of bio-inks on CMOS. In the pictures, glucose oxidase was printed on the CMOS chip. The printing time was less than 20 seconds. Patterning the surface of the chip can help improving accuracy.

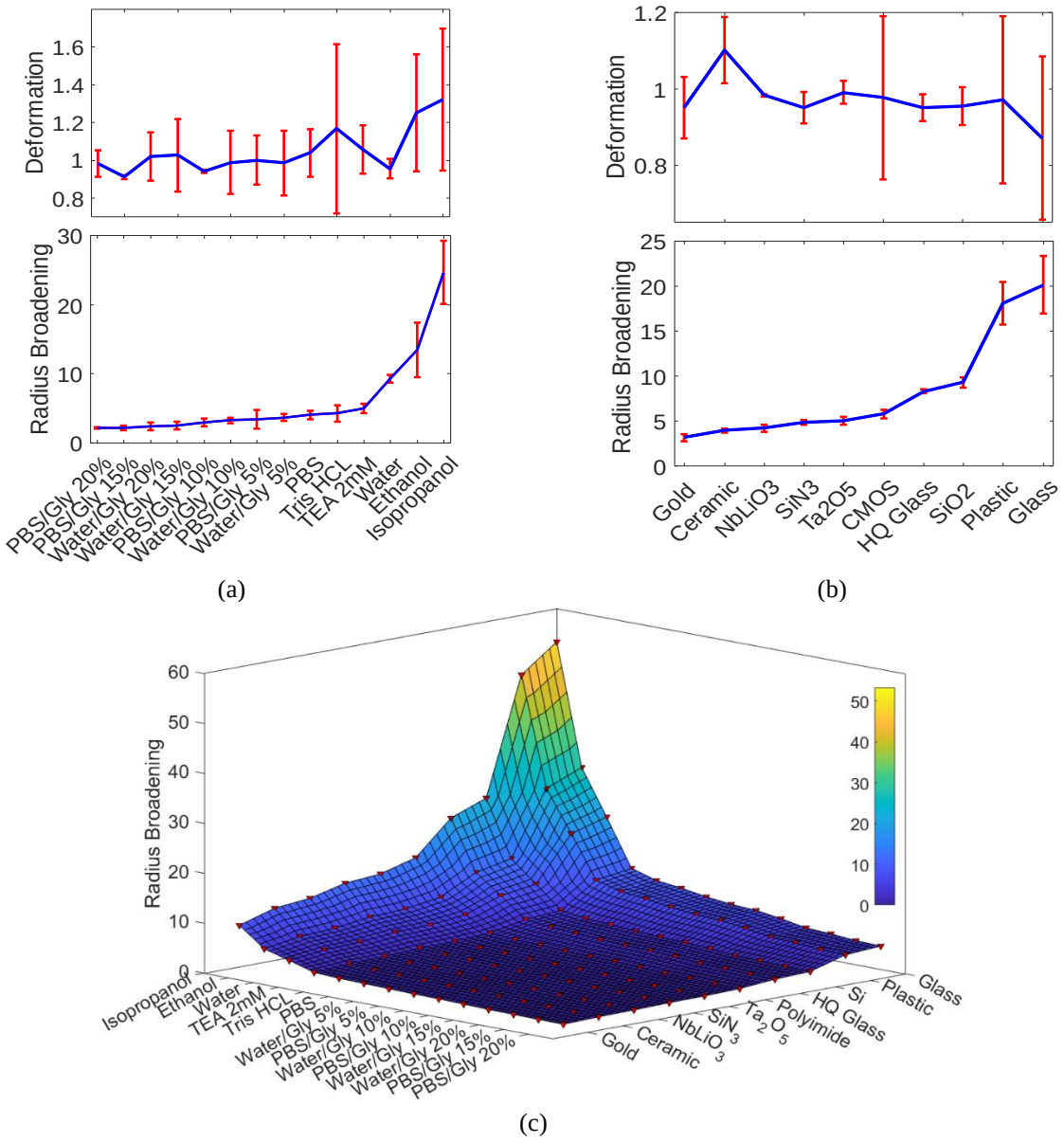

Figure 5.8 (a) Deformation (top) and radius broadening (bottom) of printed droplets using 14 different inks on a silicon substrate. (b) Deformation (top) and radius broadening (bottom) of DI water on ten different substrates, including polyimide, the outer layer of standard 0.35 CMOS technology. (c)Radius broadening numerical interpolation for 140 combinations of ink and substrate.

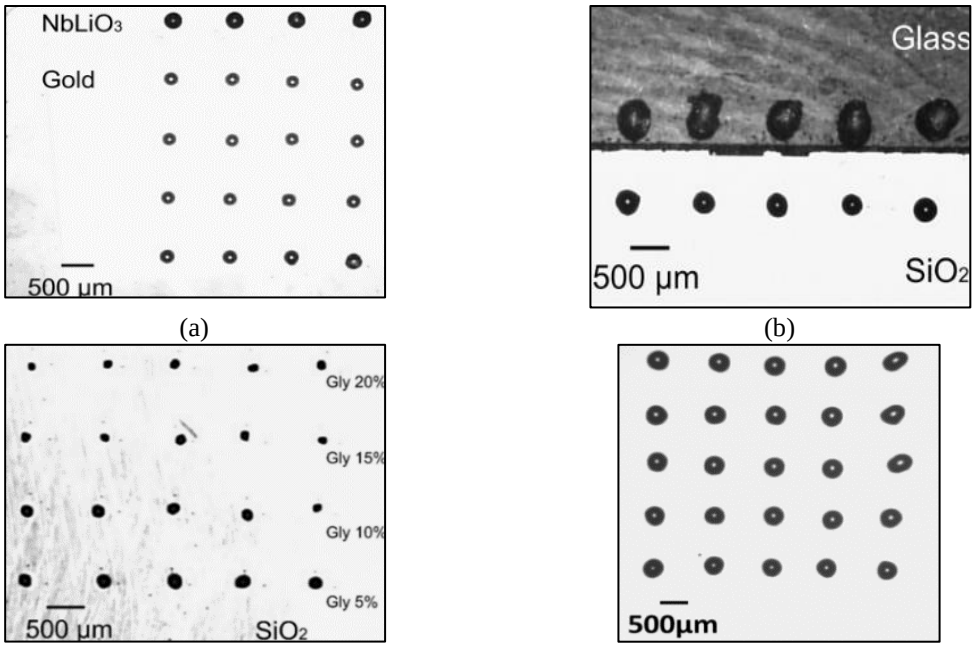

Figure 5.9 (a) DI water printed on $NbLiO_3$ and gold. (b) DI water printed on glass and SiO_2. (c) Different solutions containing glycerol on SiO_2. (d) Array of DI water droplets on silicon.

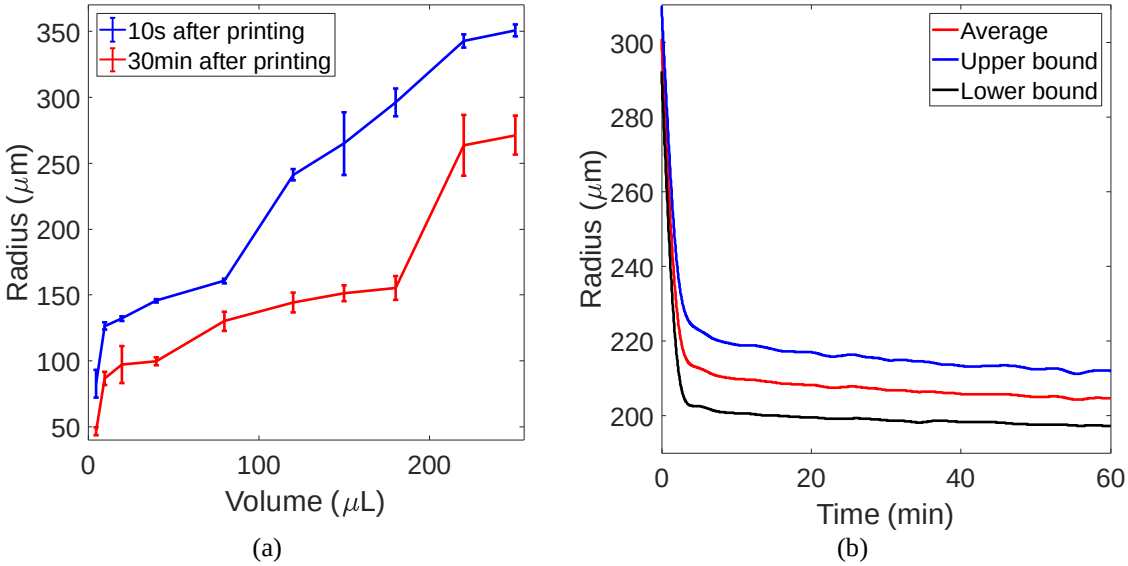

Figure 5.10 (a) Evaporation dynamics of a solution of PBS/Glycerol 20% on a silicon substrate: Volume vs Radius. (b) Short-term evaporation dynamics: radius vs. time. PBS on silicon. Droplet volume was ~180µL.

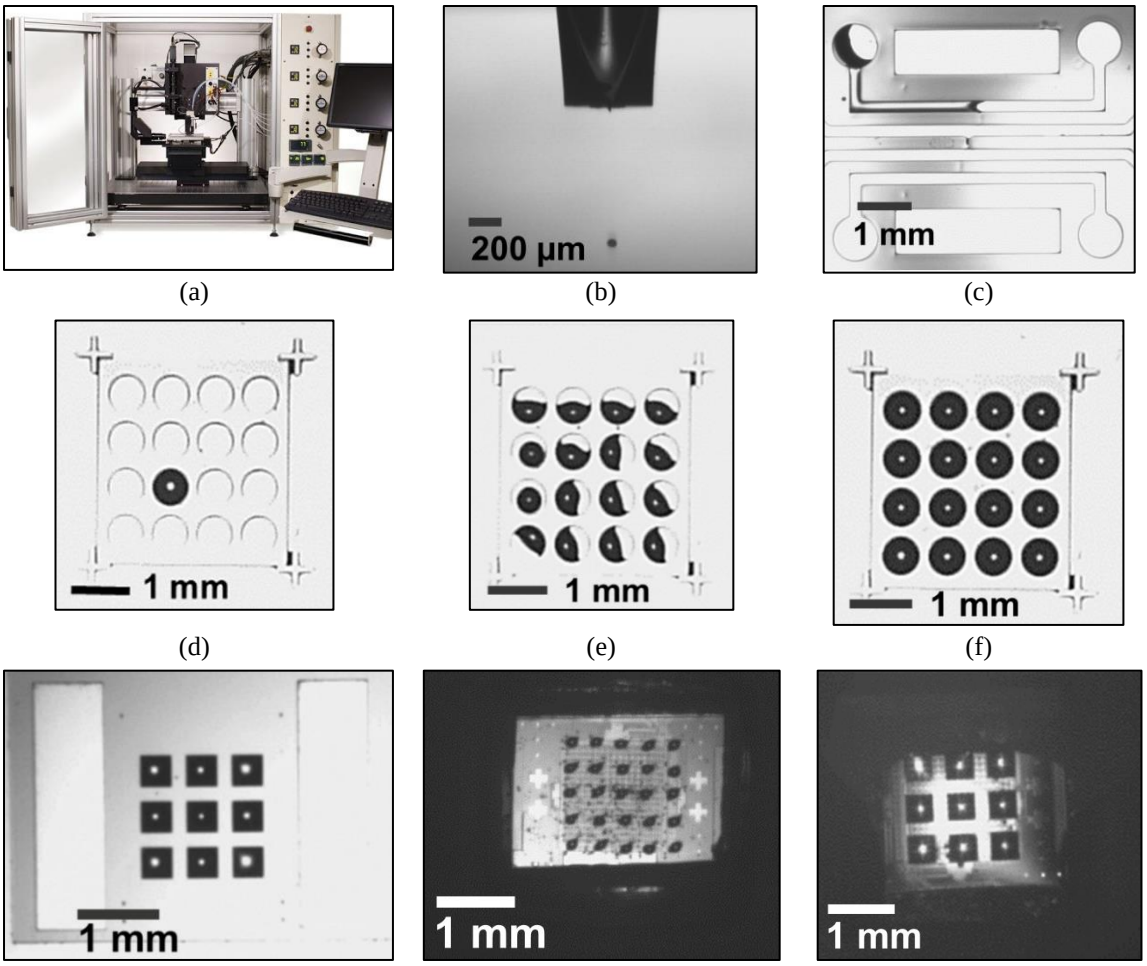

Figure 5.11 (a) Ejection of a picoliter droplet from a 70 µm print head. (b)Printing in a 200 µm wide open microchannel. (c)-(g) Printing into a SU-8 microstructure with different positions and volume. (h) Direct enzyme printing (GOX) in an array format on the Multicorder chip. (i) Multi-enzyme printing (GOX and ChOX) into a SU-8 structure fabricated on top of the Multicorder chip.

5.4.2. Freeze-drying

Lyophilisation was achieved by using a benchtop freeze-dryer - the Lyotrap by LTE Scientific in Figure 5.12(a) - with a cylindrical condenser chamber (diameter: 20 cm, depth: 35 cm). The size of the chamber allowed the parallel processing of multiple cartridges. For this model, the minimum temperature that can be reached in the chamber is -85^{o}C, which was suitable for this application where reagents are in an aqueous environment. The typical drying cycle adopted in this work is shown in Figure 5.12(b). Samples with liquid reagents to be lyophilised were loaded into the chamber at room temperature and atmospheric pressure. After the Lyotrap was loaded, the top lid of the chamber was closed, and the freezing cycle was activated. Typically, the chamber reached a temperature of -77^{o}C in

approximately 30 minutes. Once reached a stable temperature, the sample was left in the chamber for 1 hour at atmospheric pressure. In this phase, the functionalisation solution is expected to freeze rapidly. Subsequently, the chamber was pumped down to pressure typically in the range of 0.02 – 0.05 mbar. Generally, the chamber reached the target pressure in about 15 - 30 minutes. The sample was left in this condition for 24 hours. After 24 hours, the chiller of the unit was switched off, and the temperature of the chamber gradually increased. The pressure of the chamber was kept in the same range. After a further 24 hours, the temperature of the chamber was proximal to the ambient temperature. The chamber was then slowly brought to atmospheric pressure in about a few minutes through a dedicated valve. At this phase, the samples were unloaded from the unit and ready to be stored or used for testing. Temperature, pressure, and timing of the processing were empirically tuned. The temperature and pressure typically depend on the composition of the solution to be lyophilised. Timings usually depend on the volume of the solution.

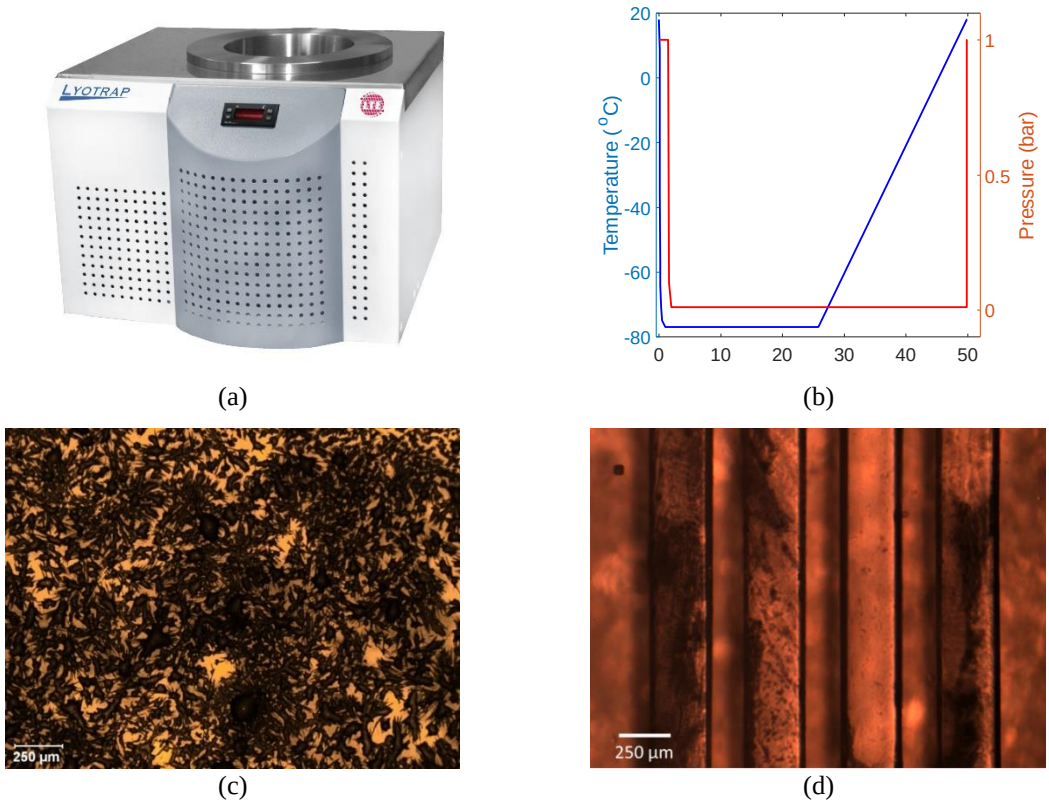

(a) (b)

(c) (d)

Figure 5.12 (a) The Lyotrap freeze-dryer from LTE Scientific. (b) Typical drying cycle used in this work. (c) Reagents required for choline oxidase lyophilised onto a petri-dish (stabiliser: 1%glcerol (w:w). (d) Reagents required for choline oxidase lyophilised into three PDMS microchannels. One channel was deliberately left unmodified to demonstrate channel-specific capabilities.

The process of lyophilisation was successful for reagents deposited on both glass substrates (e.g. petri dish and well plates) and into microfluidics structures. Figure 5.12(c) shows the result of the lyophilisation process into a 385-well plate using reagents for choline assay (i.e. ChOx, HRP and o-dianisidine). Successful lyophilisation was also obtained when the reagents were inserted into microchannels. As shown in Figure 5.12(d), different microchannels were loaded with application-specific reagents. Therefore, the process enables multiplexed testing. Reagents were also successfully freeze-dried on the chip. However, the process of lyophilisation was found to be affecting the CMOS chip, which usually became unresponsive after undergoing this process multiple times. This is not an issue for an application where the CMOS chip is meant to be disposable.

5.4.3. Reagents stability

The stability of the reagents over a period of time after the lyophilisation was experimentally assessed using for the choline reagents as a case study.

Materials and methods. The activity of the reagents was evaluated by the micro-spectrometer ffTA-1 from Foster and Freeman using a 384-wells clear plate. Experiments were performed in triplicates, and the results of this study are summarised in Figure 5.13. First, the initial reaction rate was estimated using reagents in solution (Figure 5.13(a)). The reaction rate was measured by mixing 50 µL of a test solution containing 1 mM of choline in 0.1 Tris HCl (pH 8) and 50 µL of a reacting solution composed of 20 µL of ChOx (150 U/mL), 20 µL of HRP (300 U/mL) and 10 µL of 41 mM o-dianisidine. Subsequently, 50µL of reacting solutions were freeze-dried into different wells of the 384-wells plate using the Lyotrap by LTE scientific. There is evidence in the scientific literature that cryoprotectant substances (stabilisers) can increase the stability over time of the lyophilised substances [304]. Thus, the reacting solutions were freeze-dried with and without potential stabiliser solutions (see Figure 5.13). Four different types of stabiliser solution combinations were used: (i) the addition of glycerol with 1% and (ii) 2% w:w ratio, (iii) and (iv) the addition of the commercial stabilizers STKES by SunChemicals, in two different formulations. The composition of the commercial stabiliser was not known, due to copyright reason. However, no interference with the colorimetric reaction was expected, according to the company guidelines.

After the lyophilisation, the stability of the reagent was tested using a solution by mixing 50µL of a test solution containing 1mM of choline in 0.1 Tris HCl (pH 8) and additional

50µL of the buffer. The reagents were tested within 2 hours after the completion of the lyophilisation process (storage condition: A) and after seven days storage at 20°C into a vacuum-sealed plastic bag under dark conditions (storage condition: B).

Results. For all the formulations and conditions, the freeze-drying process was observed to affecting the activity of the reagents. By observing the results in condition 'A', it can be assumed that the lyophilisation process created an inherent loss of the activity of the reagent. Among all the formulations, the one with no addictive retained most of the activity when tested in storage condition A. However, the loss of activity due to the lyophilisation process can be compensated by increasing the enzymatic units and the concentration of the reagents to be freeze-dried. The stability of the lyophilised reagents over time is expressed by storage condition B. After seven days of storage, the formulation with no addictive reported the most significant drop in activity: -76.8%. The formulation containing glycerol improved the stability, with approximately a -67% drop for both the conditions. The stability was further enhanced using the commercial stabiliser kit, with an average decrease in the activity of -29% in 7 days. Reagents stored with no vacuum-sealed bag (i.e. exposed to open-air) reported inconsistent results due to partial rehydration, due to ambient humidity. Therefore, storage under vacuum condition is recommended.

Discussion. Based on this data, reagent stability can be estimated in different storage conditions using the standard model for accelerated ageing (American Society for Testing and Materials, standard F1980-02) [305]. The standard for accelerated ageing is based on the Arrhenius' law. Typically, reducing the storage temperature of 10°C increases the shelf life of a multiplication factor Q_{10}. Q_{10} is set to 2 for most of the applications [305]. The shelf-life is defined as the time required for a property to be lower than a certain threshold [305]. For enzymatic stability, such as in this case, we can define the shelf-life of the reagents as the storage time producing an enzyme activity decrease more than 10%. The shelf-life estimations of the lyophilised reagents for choline assay in different storage conditions are summarised in Table 5.6. In summary, the use of stabiliser for the lyophilisation process has the potential to increase the shelf-life of the reagents. The best-case-scenario obtained in this work is a shelf-life of more than 2 months when freeze-drying the reagents with the commercial stabiliser STKES by SunChemicals and storing the sample at -20°C. It is expected that the shelf-life of the lyophilised reagents for all the other assays are like the one estimated for choline.

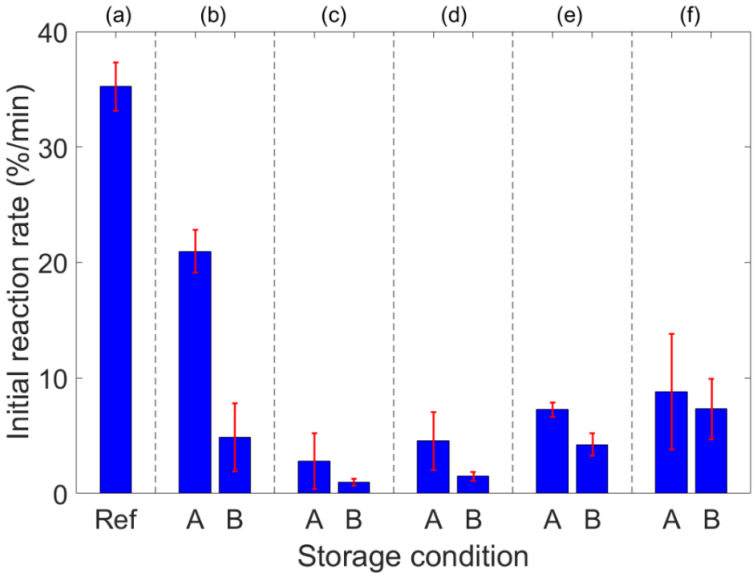

Figure 5.13 Assessment of the stability of the reagent after freeze-drying for choline. Storage condition: Ref = reference (no lyophilisation); A: freeze-dried reagents tested within 2 hours after the completion of the process. B: freeze-dried reagents tested after 7 days of storage at 20°C in a vacuum-sealed plastic bag and in dark conditions. (a) Reaction in solution. Reagents were freeze-dried with (b) no addictive, (c) with 1%, (d) 2% glycerol, (e),(f) with two different formulations of the commercial stabiliser STKES by SunChemicals.

Table 5.6. The shelf life of the lyophilised reagents for choline assay.

	Shelf life (reduction of 10% of reaction rate) in days				
Storage temperature (°C)	No addictive	1% glycerol	2% glycerol	Commercial stabilizer (1)	Commercial stabiliser (2)
20*	0.92	1.08	1.04	1.7	4.21
10**	1.83	2.17	2.08	3.41	8.42
0**	3.67	4.33	4.16	6.83	16.83
-10**	7.33	8.67	8.33	13.67	33.67
-20**	14.66	17.33	16.67	27.33	67.33
* Shelf-life calculation based on the data ** Shelf-life estimation using accelerated ageing model [305]					

5.5. Multiplexed Assays

5.5.1. Multiplexed Assays in Human Plasma

The capability of the platform working with preloaded reagents in the dry state was verified with glutamate assay and controls performed simoultaneosuly in human plasma.

Materials and methods. A cartridge with four microchannels (h ~ 290 µm) was functionalised with three channels dedicated to glutamate assay and one channel left for the negative control. Accordingly, two solutions were prepared for the microchannel functionalisation: a control solution and a glutamate assay solution. The former solution was used to functionalise microchannel dedicated to negative control testing. The latter was used to functionalise microchannels allocated for metabolite assays. 1 µL of the solution was deposited in the respective microchannel. The protocol for solution preparation is reported in Appendix I.The deposition was obtained both by pipetting and printing. Same results were obtained, regardless of the deposition method. After the deposition, solutions were lyophilised. No stabiliser was used during the lyophilisation process. Cartridges were used for experiments immediately after the completion of the lyophilisation process. Cleaning procedures and setup of the experiment were identical to the one previously described. Human plasma was purchased from Sigma Aldrich and reconstituted following the manufacturer instructions. It is expected that human plasma had an endogenous concentration of glutamate. The sample was then spiked with additional known concentrations of glutamate. A volume of 20 µL of the sample was introduced into the cartridge with no further dilution. Experiments were performed in triplicates. A schematic representation of the adopted protocol is shown in Figure 5.14.

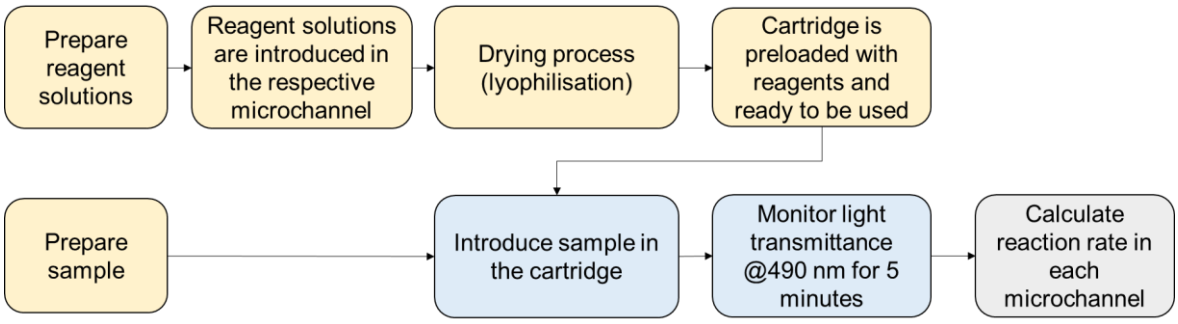

Figure 5.14 Protocol adopted for multiplexed assays in human plasma.

Results. Results of the experiments are presented in Figure 5.15. Expectedly, channels allocated for control measurements provided a minimum measurable signal, with an average rate of 0.031±0.03 mVs^{-1}. However, for the channels functionalised with the solution containing GlOx, the rate of the reaction, using the same unmodified plasma sample, increased of more than 10 folds to 0.394±0.188 mVs^{-1}. Accordingly, rates increased further when the plasma sample was spiked with 150 µM and 300 µM, respectively. Excluding the measurements on the unmodified plasma sample, data points had high linearity ($R^2 = 0.977$). The linearity justified the estimation of the endogenous concentration of the unmodified sample using the auto-controlled approach, adopting the two spiked samples as positive controls. Thus, the glutamate level was estimated to 108.4 µM. Under this assumption, a calibration curve was obtained using a linear model and shown in Figure 5.16(a). The sensitivity of the platform (slope of the linear model) in these experiments was 3.3 $mVs^{-1}mM^{-1}$. Averaged and filtered data and signal after curve fitting are shown in Figure 5.16(b).

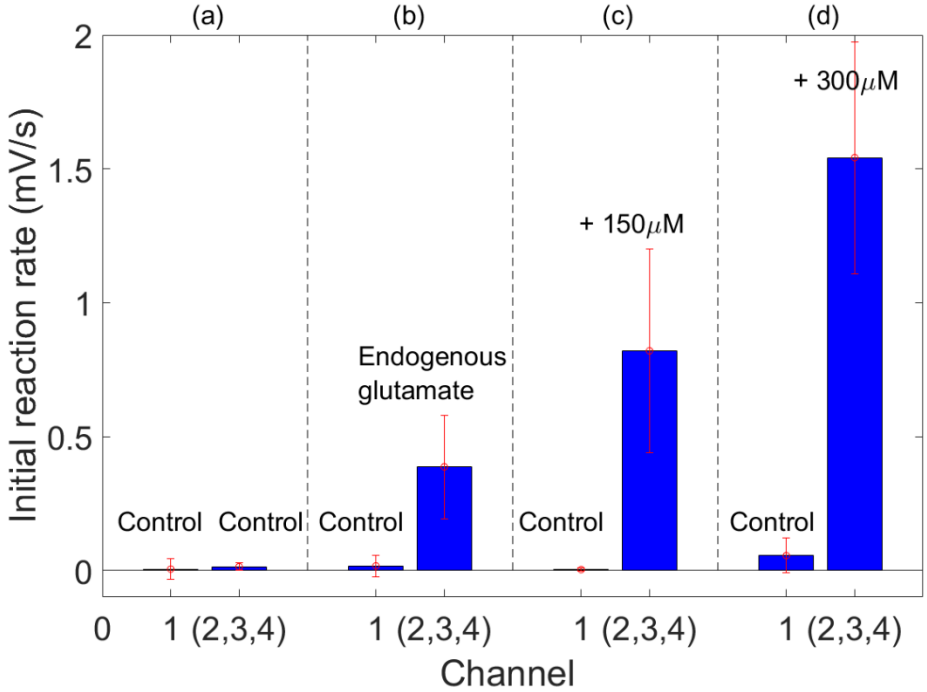

Figure 5.15 Glutamate experiments in undiluted human plasma with preloaded dry reagents. (a) All channels were functionalised for control measurements. The introduced sample was unmodified plasma. (b)-(d) Channel 1 was functionalised for control measurement, the remaining for glutamate assay. The introduced sample was (b)Unmodified plasma; (c) plasma spiked with 150 µM of glutamate; (d) plasma spiked with 300 µM of glutamate.

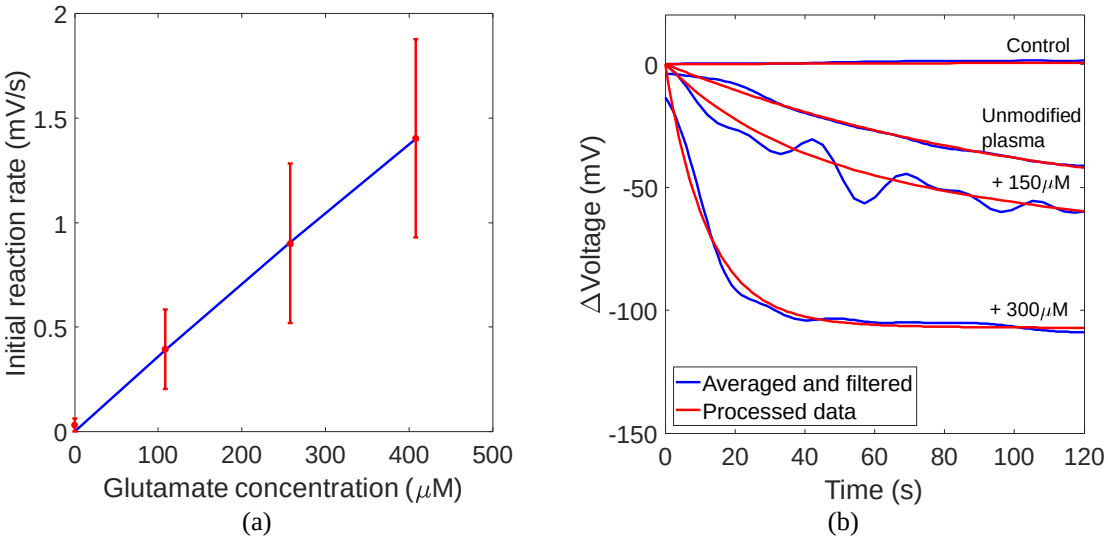

Figure 5.16 (a) Calibration curve of glutamate assay with preloaded reagents. (b) Average and filtered data (blue) and processed data (red) for different samples.

Discussion. It is not possible to directly compare the rates calculated from the lyophilised reconstituted reagents on-chip with the rates obtained from wet assays for several reasons explained below:

- Microchannels were functionalised with a different number of units with respect to the units used in wet experiments.
- During the drying process activity loss is expected.
- Plasma introduced in the platform had no further dilution.
- The process of rehydration of the reagents could produce systematic modification on the light absorbance drop.

Although a direct comparison is not suitable, there have been several positive outcomes of this work. This set of experiments is the first of the multiplexed assays performed on the CMOS chip, with 1 channel always dedicated to the control measurement and the others performing the actual measurements. An optical inspection confirmed that channels were successful in confining the liquid, and no leakage was observed. Nevertheless, crosstalk between two adjacent channels is still possible. This is due to optical effects of reflection and dispersion taking place in the platform since there are multiple optical interfaces: air-PDMS, PDMS-sample, sample-passivation layers, passivation layers-doped region. Thus, a crosstalk quantification can be computed using the following approach [45]:

$$\text{Crosstalk}_{\%} = \frac{\sum_{i=1}^{N} \frac{|r_{c,i} - \mu_c|}{|r_{t,i} - \mu_c|}}{N} \cdot 100 \qquad (5.1)$$

Where $r_{c,i}$ is the generic rate in the control channel when the adjacent channel is performing a metabolite assay, $r_{t,i}$ is the generic rate in the assay channel when the adjacent channel is performing a control measurement, μ_c is the average rate in the control channel when the adjacent channel is performing a control measurement, N is the number of averaged experiments. Accordingly, average channel-to-channel crosstalk of 2.59±0.8 % was quantified in these set of tests.

From a fluidic point of view, optical inspection showed that the layer of powdered reagents within the microchannels promoted a reliable and stable flow.

In conclusion, these experiments exhibited that this platform could perform simultaneous assays for glutamate and related control, using on-chip preloaded reagents. However, the loss of activity of the reagent was observed due to the functionalisation process, and the additional noise introduced by the reagents' rehydration has the potential to degrade the performance of the platform.

5.5.2. Paper Microfluidics: An Alternative Approach

On-chip multiplexed assays have also been demonstrated by using an alternative method based on paper-microfluidics. This work has been carried out in collaboration with Dr Chunxiao Hu and Dr Srinivas Velugotla [306]. Dr Chunxiao Hu and Dr Srinivas Velugotla designed the concept idea and developed prototypal paper microfluidics. I have completed the paper-microfluidic manufacturing by appropriate functionalisation. Dr Chunxiao Hu performed biological experiments. I also offered technical support to all the phases of the processing. The reader and GUI, as developed in this PhD research project, were also employed. A detailed report of this work has been published [306]. In this section, an overview of the work is presented to demonstrate the versatility of the platform.

The paper-strip based platform is schematically represented in Figure 5.17(a). Functionalised paper microchannels were placed on top of the active area of the CMOS chip. Once the sample was introduced on the fluidic input, it flowed through the paper substrate due to capillary effect and split into three microchannels were the colorimetric reaction was triggered. The platform was designed for the simultaneous colorimetric determination of glucose and lactate on cellulose, which is partially permeable to visible light. A CMOS chip was glued to a chip carrier and wire bonded. No microfluidics was fabricated on top of the CMOS. Reader and GUI were unchanged.

Materials and methods. A paper-microfluidics strip to be placed on top of the sensing area was separately fabricated. A Grade 1 Cellulose Chromatography Paper (thickness: 0.18 mm; water linear flow rate: 130 mm/30 mins) was purchased from GE Healthcare Life Sciences to be used as the substrate for the paper microfluidics. The paper microfluidics was fabricated using laser micromachining (CO_2 laser cutting machine by Laser Micromachining Ltd.). Laser micromachining had a few advantages than other commonly used techniques, including wax printing and photolithography. It required only a single step of fabrication with no need of cleanroom facilities. It was a flexible process with good reproducibility, high throughput, and low cost. The paper strip, as shown in Figure 5.17(b) had a size of 30 × 2.8 mm. It was composed of (i) sample pad (ii) detection zone and (iii) absorbent pad. The sample pad (length: 5 mm) was used for sample loading. The detection zone (2 × 2 mm) had approximately the same size of the active area of the CMOS chip. The absorbent pad (length: 4 mm) was in place to absorbed overflowed liquid. Three microfluidic channels were fabricated. Lateral channels were 380 μm wide. The central channel, which was used for negative control measurements, had a width of 300 μm. Two 280 μm wide gaps between the channels prevented crosstalk.

Two different solution inks containing reagents for the lactate assay and glucose assay were printed on the specific paper microfluidic channels using the Jetlab II printer (see Appendix J for protocol). The freeze drier (Lyotrap by LTE Scientific) was used to store freeze-dried paper strips right after the enzyme printing. No noticeable signal drop was observed after two weeks of storage in the fridge at 4 ºC.

To increase mechanical strength, reduce sample evaporation and reduce contamination, the paper strip was sandwiched in two transparent acrylic films (3MTM 9969 Diagnostic Microfluidic Adhesive Transfer Medical Tape), as shown in Figure 5.17(c). A laser micromachined aperture in the top acrylic film was used for exposing the sample pad. The acrylic films provided excellent support to the bare paper strip so that it could be easily folded to accommodate the chip surface. Preliminary experiments were performed to prove that the acrylic film had no discernible effect on the biological reaction. The paper strip was kept in place on top of the CMOS chip by magnet bases.

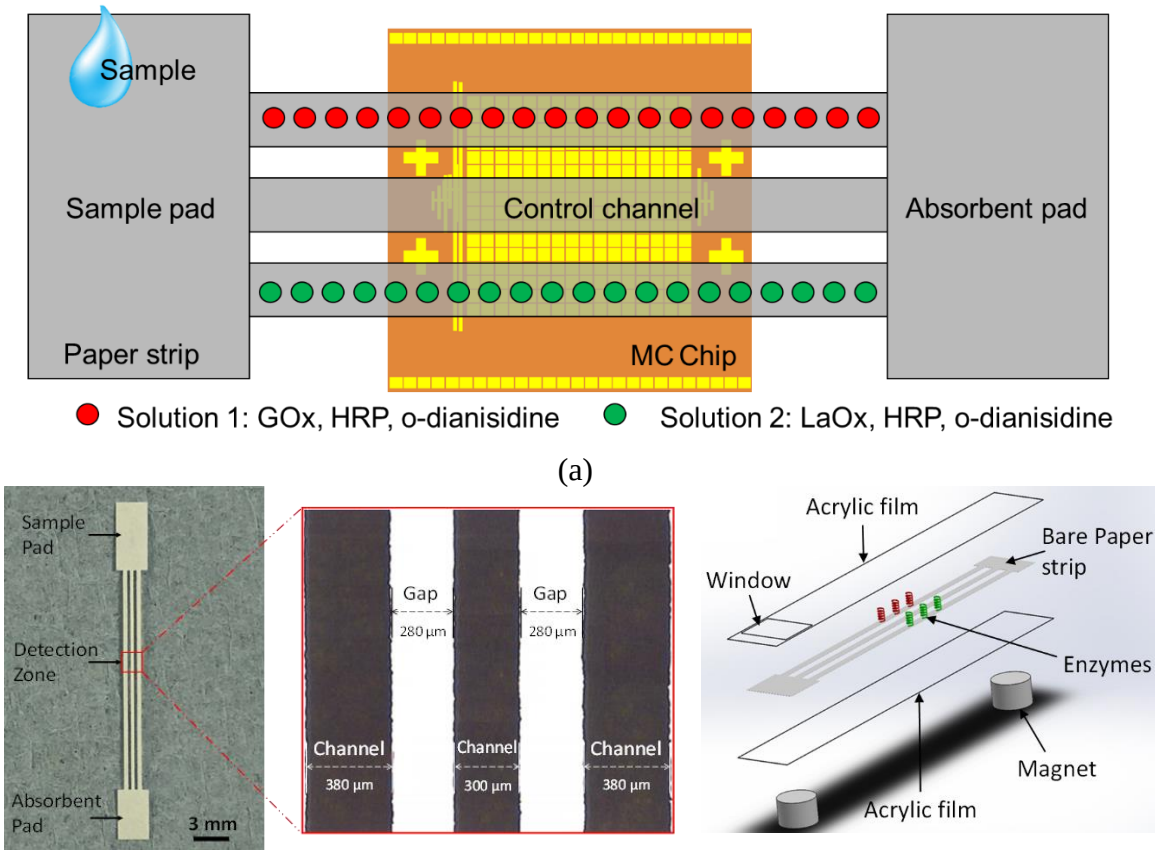

Figure 5.17 (a) Schematic of the paper strip based platform. (b) Fabricated paper strip and size of the paper microchannels. (c) Encapsulation of the paper strip into acrylic films [306].

Results. Analyte solutions containing glucose and lactate were measured in a buffer solution simultaneously with the photodiode array. The total volume of the solution was 6 µL, which was large enough to wet the channels in a relatively short time, but not too large to cause an overflow. A preliminary analysis showed that no obvious crosstalk was observed [306]. In total, three concentrations of lactate (0.5, 1, 2 mM) and glucose (2.78, 5.55, 11.1 mM) were measured. Lateral channels were dedicated to the quantification of lactate and glucose, where a signal decrease was observed. The central channel was used as a control channel where no signal drop was observed.

All the three microfluidic channels were wet simultaneously, which gave a good comparison of the reactions occurring on the three individual channels. Both enzymatic reactions produced a colour change from clear to brownish, which absorbed the green LED light, therefore decreasing the amount of light getting to the photodiode and therefore decreasing the voltage signal. A new paper-strip was used for each measurement. No washing step of

the chip was required due to the encapsulation of the paper strip. The change in photodiode voltage for different channels is plotted Figure 5.18. Initial reaction rates were calculated, and calibration curves were obtained [306]. The Michaelis constant K_m values were estimated and found to be 33±13 mM for glucose-glucose oxidase and 1655±527 µM for lactate-lactate oxidase, respectively. The LOD was 520 µM for glucose and 110 µM for lactate. Detailed results have been published in [306].

Discussion. There are three main advantages of using paper strips rather than on-chip integrated microfluidics. Firstly, paper strips can be easily disposed of and incinerated. Secondly, the use of paper strip implies the re-use of the CMOS chip leading to a lower cost per test. Thirdly, an inherent capability of the passive flow of the paper strip dramatically simplifies the platform.

This approach has some limiations. The alignment of the paper strip to the sensing area is, in fact, crucial and needs to be supported by an additional mechanical structure in a real-life scenario. Also, the paper strips can accommodate a limited number of microfluidic channels because laser patterning has a lower resolution than photolithography. Thirdly, the sample is not directly integrated onto the sensing area, which can potentially reduce the sensitivity towards low concentrations of the substrate. In conclusion, the versatility of the platform allows its use in different configurations which can satisfy different application-specific requirements.

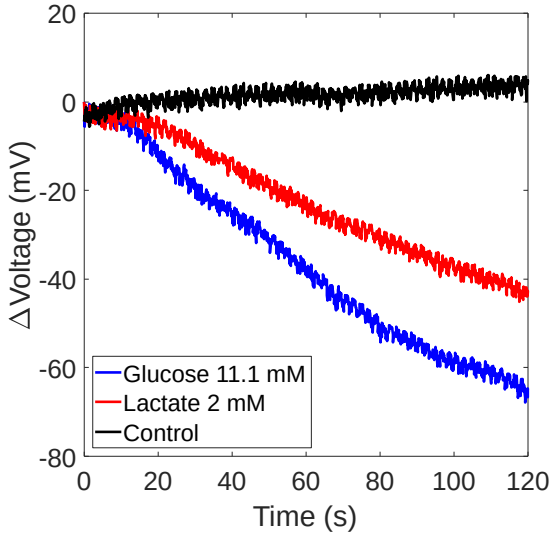

Figure 5.18 Real-time recording of the reactions detected by the three paper channels. Data shown is the average over the channel. Lateral channels were functionalised for glucose and lactate assays. Central channels were used for blank measurements (control).

5.6. Whole Blood Experiments

In a real-life scenario, sample processing steps need to be minimised or eliminated. This rise the question if the developed platform is suitable for metabolite quantification with no or integrated sample processing. The use of whole blood in optical measurements it is challenging because of the reduction in the light transmission. The spectrum reported in Figure 5.19 shows the light transmittance of whole human blood inserted in a microfluidic channel (h ~ 290µm) obtained using a micro-spectrometer (ffTA-1 from Foster and Freeman).

The light absorbance is also particularly high in the range of wavelength where the platform operates. The light transmission of the whole blood is around 4% at 490 nm. However, a sharp increase in the transmission is observed for wavelength higher than 600 nm, with a 20% transmittance at 800 nm. Besides the low light transmission, the whole blood is also viscous and contains many impurities. It is therefore expected a further decrease in the SNR for experiments performed in whole blood. To assess the possibility of the use of whole blood on the platform, two different strategies have been implemented: (i) direct assay in the whole blood and (ii) on-chip blood filtration.

Direct assay on whole blood. Preliminary experimental studies demonstrated that the change in absorbance was detectable also in whole blood as the sample, with no pre-processing. One sample of human blood was purchased from Cambridge bioscience.

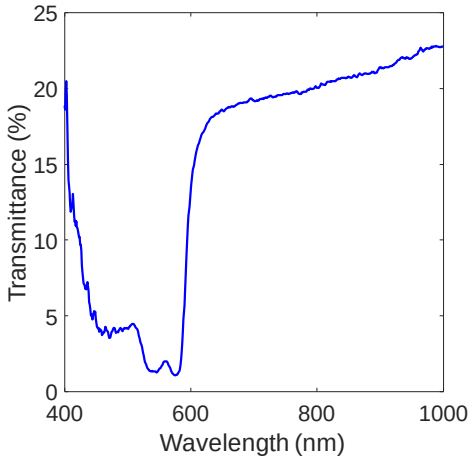

Figure 5.19 Light transmittance spectrum for whole blood in a microfluidic channel with h ~ 290µm. The curve is an average over three measurements.

Half of the sample was centrifuged, and plasma was extracted. Both plasma and blood from the same sample were spiked with an additional LAA concentration of 3.75 mM. The resulting samples were tested using the same protocol adopted for the experiments with diluted serum. For the testing in whole blood, the light intensity of the LED was increased to keep the working point in the same range as previous experiments.

Despite the low transmittance, an increase in absorbance was also observed when blood was used as the sample under test, as shown in Figure 5.20(a). When comparing the rate of the reaction in blood and plasma from the same sample, a higher initial rate was observed when using blood. It is not completely clear the reasons leading to increased rate from this preliminary study. Probably, the process of centrifugations filters out compounds that are catalysing the reaction. Also, whole blood might contain a higher concentration of free oxygen, which also takes part in the colorimetric reaction. However, when considering the system noise, the presence of unprocessed blood degraded the quality of the signal (see Figure 5.20(b)). High-frequency noise was introduced when using unprocessed blood, with peak-to-peak spikes reaching 200 mV. The high-frequency noise was probably related to the presence of agglomerates of molecules free to move on the top of the sensors. In conclusion, direct assay on whole blood was possible, but additional work is needed to reduce or minimise the noise introduced by the impurities in the sample.

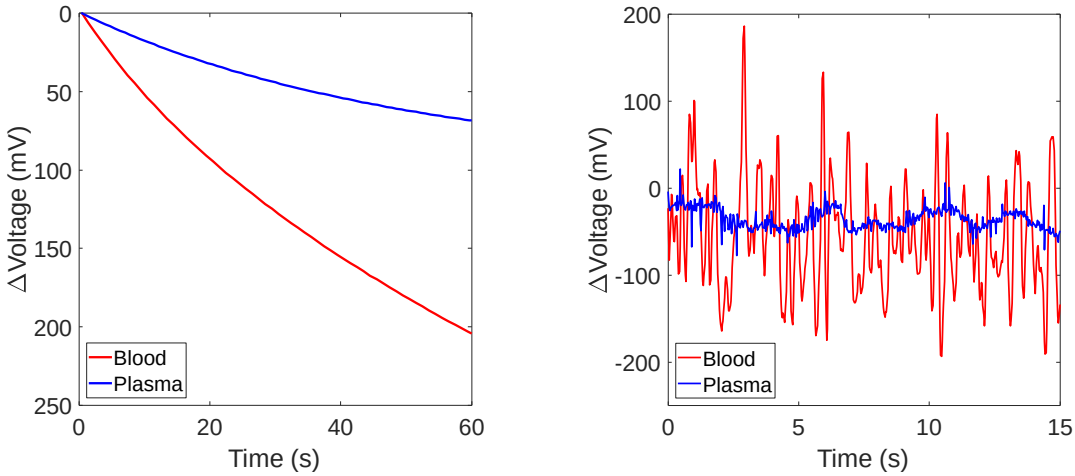

(a) (b)

Figure 5.20 (a) Processed output for LAA assay in blood and plasma. Both blood and plasma were modified with 3.75mM of LAA. (b) Unprocessed data from a single-pixel selected into a microchannel. LAA assay in blood and plasma, both modified with 3.75mM. The noise level when testing LAA in the blood was substantially higher than when testing LAA in plasma.

On-chip blood filtration. Integration of a blood filter for on-chip sample preparation has the potential to increase the practical use of the platform. Integrating commercially available passive blood filters with custom microfluidics platform has already been reported in the scientific literature [307], [308]. Thus, several passive commercial blood filters were purchased and tested for their integration with the cartridge. Glass fibre blood separator LF1, MF1, VF2 and GF/DVA were purchased from GE Healthcare. The Vivid™ plasma separation membrane was also obtained from PALL Corporations. Blood filtration devices were tested using whole blood commercially sourced from Cambridge Bioscience. The blood sample was not subjected to any freezing step since freezing modifies the shape and the properties of red cells. All the commercially sourced filters use porous materials (with variable porous size) to trap red cells during the passive flow of the sample. Among the filters commercially sourced, the glass fibre blood separator LF1 was adopted because it provided more reliable results according to the target sample volume (10 – 20 µL). The LF1 blood separator has a thickness of 247 µm, wicking rate of 35.6 s/4cm, and water absorption of 25.3 mg/cm^2. Thus, the LF1 glass fibre blood separator was shaped using a laser cutter (CO_2 laser cutting machine by Laser Micromachining Ltd). A circular pad with a 1 cm diameter was used as a sample pad. From the sample pad, a straight 3 mm wide glass fibre strip was used to converge the plasma flow in the preferred direction. The strip was also patterned with laser-cut perforation to physically reduce the absorbance of the substrate and facilitate the flow for plasma.

Figure 5.21(a) demonstrates the process of blood filtration on the laser-cut device. 15 µL of blood inserted on the sample pad and plasma was extracted in the glass fibre strip after a few seconds by capillary action. The passive filter was then integrated with a cartridge - see Figure 5.21(b). For its integration, part of the epoxy on the side of the CMOS chip was removed to create a slot for the insertion of the glass fibre filter. The blood filter was then slotted in the cavity in immediate contact with the microfluidic channels - Figure 5.21(c). The strategy was successful, and plasma entered the microfluidic channels after separation. However, the process was not easily repeatable with many underfilling or no-filling of the microchannels recorded. After inspection using a microscope, it was clear that the interface between the blood filter and the microchannel is crucial since the plasma was reluctant to leave the blood filter. In summary, the strategy of integrating the blood filter with the developed cartridge was promising, but the results were difficult to replicate and very unreliable, suggesting the need for optimisation.

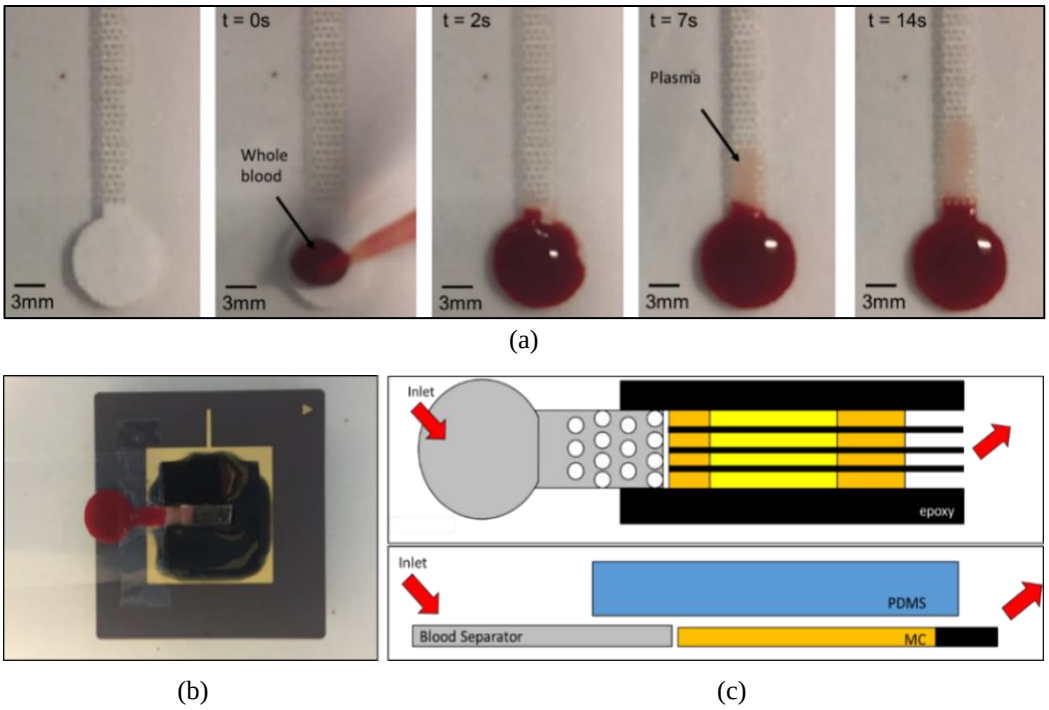

(a)

(b) (c)

Figure 5.21 (a) Passive blood filtration using the GE glass fibre filter. (b) Integration of the filter into the cartridge. (c) Strategy for the integration of the filter.

5.7. Summary of the Chapter

- The platform was successful in quantifying six target metabolites, namely LAA, glutamate, choline, sarcosine, lactate, and creatinine, in diluted human serum (ratio 1:10). Table 5.7 summarised the main findings.
- Inkjet printing has the potential to be used for the deposition of enzymatic solutions on top of the CMOS and microstructures for the immobilisation of reagents.
- Lyophilisation was successful in trapping reagents in the solid-state within the microchannel. The process also increased the shelf-life of the reagents, estimated to be more than 60 days for choline-related chemicals when freeze-dried and stored at -20^{o}C in a vacuum-sealed package.
- The capability of the platform working with preloaded reagents in the dry state was verified with glutamate assay in modified human plasma. For all the measurement, one channel was used for control measurement, demonstrating that the platform can run different assays at the same time. The crosstalk between adjacent channel was quantified to be 2.59%.

- An alternative approach based on paper microfluidics was also demonstrated to be capable of performing three measurements at the same time, i.e. glutamate, negative control, and lactate.
- Preliminary testing demonstrated that the platform could be used for metabolomics assays using whole blood by both using it without any processing and by integrating a commercial passive blood filter into the cartridge.

Table 5.7 Summary of on-chip metabolites quantification in diluted serum.

	LAA	**Glutamate**	**Choline**	**Sarcosine**	**Lactate**	**Creatinine**
Cartridge type	4 microchannels on CMOS				2 microchannels on CMOS	
Microchannel height	h ~ 137.14 µm					
Sample volume	25 µL				30 µL	24 µL
Application	PCa				Ischemic stroke	
Physiological Range	1.7 - 4.6 mM	40 - 150 µM	10 - 40 µM	0 - 20 µM	0.3 - 2.0 mM	100 - 150 µM
Test Range	0 - 12.5 mM	0 - 800 µM	0 - 500 µM	0 - 500 µM	0 - 3 mM	0 - 2 mM
Linear Range	0 - 3.5 mM	0 - 300 µM	0 - 100 µM	0 - 100 µM	0 - 0.5 mM	0 - 0.5 mM
Linearity (R^2)	0.993	0.985	0.967	0.997	0.977	0.932
K_m (µM)	18610	715.1	197	172.9	362	1085
Analytical Sensitivity ($mVs^{-1}mM^{-1}$)	0.226	4.72	11.79	11.72	5.175	0.803
LOD (µM)	69.01	6.86	3.00	0.26	31.85	5.21
LOQ (µM)	218.3	12.04	4.22	2.13	64.38	36.55
Resolution (µM)	24.52	1.03	0.48	0.4	7.92	39.76

Chapter 6: Clinical Evaluation

6.1. Introduction

A clinical evaluation of the platform was performed for both prostate cancer and ischemic stroke. Multiplexed assays were also demonstrated with clinically source human plasma samples. Table 6.1 illustrates the contribution to each activity discussed in this chapter.

The objective of this evaluation was to determine the analytical accuracy of the device with respect to the state of the art using clinically sourced samples. This was achieved by comparing results obtained using this platform with results obtained using standard measuring methods. Lactate is already a well-established biomarker for ischemic stroke, so the diagnostic accuracy of this metabolite is not under analysis. However, the diagnostic accuracy of the proposed metabolomic biomarkers for prostate cancer is unknown. As such, the secondary objective was to provide a scientific evaluation linking the candidate metabolic biomarkers to prostate cancer.

6.2. Platform Optimisation for Clinical Evaluation

Transitioning from diluted samples to undiluted biological required significant modifications of the platform. The main problem encountered was the drastically reduced colour change when using o-dianisidine in undiluted samples. The possible explanation to this phenomenon was the interference with other substances in the undiluted sample, whose concentrations were negligible when heavily diluted. Specifically, the degradation of performance was attributed to a specific enzyme naturally present in the blood: catalase.

Table 6.1 Table of contributions for the activity presented in this chapter.

Task / Activity presented in Chapter 6	Main investigators
Optimisation for clinical evaluation	**- Valerio F. Annese**
Clinical evaluation with PCa samples	**- Valerio F. Annese**
Clinical evaluation with ischemic stroke samples	**- Valerio F. Annese**
Multiplexed assays with PCa samples	**- Valerio F. Annese**

Blood is structured to be very stable and integrates several substances to preserve its stability, including catalase an enzyme which catalyses the decomposition of free hydrogen peroxide to water and oxygen [49]. Catalase also has one of the highest turnover numbers among all the enzymes and, therefore, it is one of the most efficient catalysts [49]. Therefore, it was hypothesised that catalase was interfering with the designed assays by decomposing hydrogen peroxide faster than the colorimetric probe. The introduction of a catalase inhibitor was initially considered. Among the inhibitors, hydroxylamine was selected, and preliminary tests were carried out. Nevertheless, hydroxylamine also appeared to undesirably reduce the activity of HRP. Preliminary experiments showed that assays using phenol/4AAP instead of o-dianisidine were working correctly. This corroborated the hypothesis of catalase interaction, as both phenol and 4AAP are also catalase inhibitors [49]. Regarding the fluid properties, undiluted samples contained impurities which led to a decreased SNR. This was expected because of larger particles free to move on top of optical sensors. In addition, higher fluidic density due to undiluted solutions led to higher filling times.

In order to mitigate the above-mentioned challenges, the platform was modified as follows:

- All experiments were performed using phenol/4AAP as H_2O_2 probe in substitution to o-dianisidine. Formulations were modified accordingly.
- HRP concentration was increased to compensate for potential activity loss due to interferences.
- Channels with increased height (h ~ 290 µm) were employed to speed-up the liquid flow and provide more substantial transmittance drop.

6.3. Research Ethics and Data Protection

Samples were clinically sourced under ethical approved. For cancer samples, the ethical approval was issued by the West of Scotland Research Ethics Service with reference number 10/S0704/18. For ischemic stroke samples, the ethical approval was issued by the West of Scotland Research Ethics Service with reference number 17/WS/0252. Ethical approval letters are reported in Appendix K. Samples were anonymised and randomised within the relative group, in accordance with the General Data Protection Regulation. No personal data which could have undermined the anonymity of the sample was requested or recorded. Numeric IDs were assigned to the samples.

6.4. Prostate Cancer Clinical Evaluation

The POC testing for PCa diagnosis was performed in three stages: calibration, validation, and clinical evaluation. In the first stage, calibration curves were obtained using a single human plasma sample modified with a known concentration of metabolites of interest. Validation was performed by two methods: (i) by testing human plasma samples modified with different and unknown levels of analytes of interest (blind validation) and (ii) by comparing readings from the platform with commercial methods. Clinical evaluation for PCa was performed on ten samples from healthy men and sixteen samples from people affected by PCa.

6.4.1. Materials and Methods

Reagents. All chemicals required for the assays were purchased from Sigma Aldrich unless otherwise specified. Plasma samples for calibration and blind validation were purchased from Sigma Aldrich. Ambient temperature and humidity were recorded during the clinical testing using the Texas Instrument Module HDC 1080EVM. Assay formulations were optimised using a trial-and-error approach. Table 6.2 summarises the main aspects of the assay formulations for PCa-related metabolites in clinical samples.

Non-PCa group. Ten healthy human plasma samples were commercially sourced from Cambridge Bioscience. Healthy plasma samples are herein referred to as 'non-PCa' and constituted the control group. Non-PCa donors were adult males, with diversified ethnicity and an average age of 34±10 years. Healthy samples were randomly assigned a numeric ID from 1 to 10.

Table 6.2 Assay formulations.

	LAA	**Glutamate**	**Choline**	**Sarcosine**
Cartridge	4 parallel and identical microchannel (h ~ 290 µm)			
Microchannel volume	0.348 µL			
Light source	LED @ 490nm (3 mW, FWHM = 20 nm)			
Total Volume	60 µL			
Sample Volume	30 µL			
Reagent mix volume	30 µL			
Reagent buffer	DI water			
1st reaction stage	LAAOx (10µL, 10U/mL)	GlOx (10µL, 4U/mL)	ChOx (10µL, 150U/mL)	SaOx (10µL, 200U/mL)
2nd reaction stage	10µL HRP 300U/ml 5µL Phenol 44.5mM 5µL 4AAP 10.5mM			
Negative control	1st reaction stage is substituted wit~10µL of DI water			
Positive control	The sample is spiked with a known concentration of the analyte of interest			

PCa group. Sixteen human plasma samples from people diagnosed with PCa were sourced from the Beatson Cancer Institute, Glasgow, UK, under ethical approval, with the collaboration with Dr Robert Jones and Prof Jeff Evans. Donors were selected to be adults who had already been diagnosed with PCa. Cancer samples constituted the cancer or PCa group. PCa samples were randomly assigned a numeric ID from 11 to 26. Protocols for sample collection are reported in Appendix L.

Procedure. The setup used for clinical testing was the same as the one used for experiments in diluted serum. Reagents were mixed with the sample off-chip and immediately introduced into the cartridge within a couple of seconds. Metabolites were tested individually using the cartridge with four microchannels. The concentrations of the target metabolites in plasma samples were not known when the experiments were performed. A schematic representation of the adopted protocol is shown in Figure 6.1.

Control measurements. Positive and negative controls were performed. Negative control refers to the measurement designed for the quantification of non-specific activity. In this case, a reaction was initiated between the sample, HRP and colour-changing reagents without substrate-specific enzyme. Thus, a negative control considers the colour change, which is not related to the reaction with the specimen under test (non-specific activity). Non-specific activity is expected due to the intrinsic complexity of the undiluted sample.

Positive control indicates the measures designed to create a detectable signal. For this purpose, the formulation of the positive control includes the addition of a known quantity of analyte under test. The presence of positive controls aims to verify that the assay was working as intended.

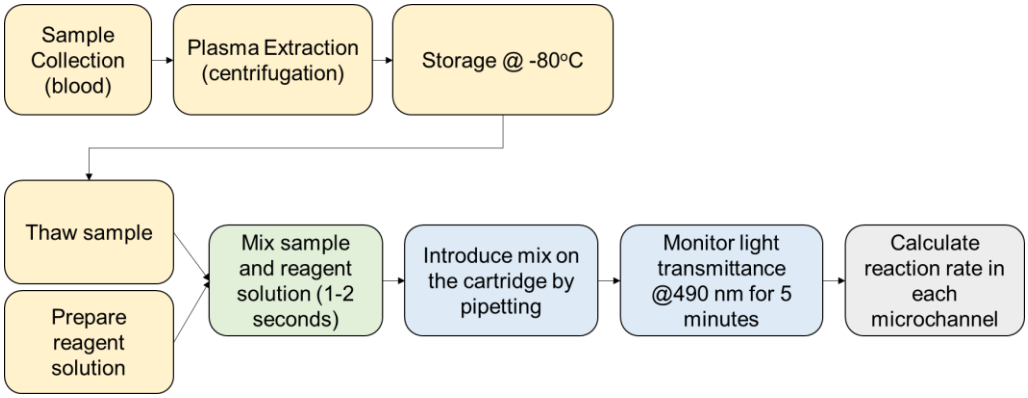

Figure 6.1 Protocol adopted for clinical evaluation of the platform.

Cartridge reuse. Cartridges were cleaned and re-used. Approximately twenty cartridges have been used for this set of experiments. Cleaning procedure after every measurement was adopted to avoid cross-contamination. Like the experiments performed in diluted serum, the cleaning recipe involved subsequent rinse in DI water, IPA, ethanol, and nitrogen blow-dry. For the clinical evaluation only, an additional rinsing step with diluted piranha solution was used (1:10). Cross-contamination was kept to a minimum by optimising the testing sequence. For an individual metabolite, the negative control was first recorded. Then, the colorimetric estimation was performed in triplicates, and finally, the measurements for two positive controls were carried out.

Data handling. Tests were performed in triplicates (biological replicates). Since a four-microchannel cartridge was used, each biological replicate had four readings (technical replicates). Data was processed according to the same methods used for diluted serum experiments.

Substrate quantification. The substrate quantification was carried out using two different methods. The first method was based on the Michaelis-Menten model and therefore herein referred to as 'model-based estimation'. For this estimation method, Michaelis-Menten kinetics parameters extracted during the calibration stage were used to estimate the concentration of the analyte of interest according to Michaelis-Menten model - see Eq. (2.4). The second method was based on sample-specific control measurements and therefore herein referred to as 'auto-controlled estimation'. In this estimation method, controls were used to create a sample-specific calibration. The sample-specific calibration involved the determination of (i) baseline and (ii) analytical sensitivity for each sample. The negative control was used as a baseline. Let us use r_n and r_t to indicate the initial reaction rates resulting from the negative control and from the actual test, respectively. It was, therefore, possible to provide an adjusted initial reaction rate r_t* as follows:

$$r_t^* = r_t - r_n \tag{6.1}$$

The sensitivity was estimated using two different positive controls. Herein, positive control A and B refer to controls where an additional known substrate concentration [A] and [B], respectively, were added to the undiluted sample. The positive controls A and B provided the resulting rates r_a and r_b, respectively. Thus, the additional concentration [A] and [B] and the rates r_a and r_b provided the sample-specific sensitivity of the apparatus according to the following formula:

$$S = \frac{r_b - r_a}{[B] - [A]} \text{ with } [B] > [A] \text{ and } r_b > r_a \quad (6.2)$$

A and B were selected so that r_a and r_b were in the linear range of the apparatus. [A] and [B] were chosen by using the calibration curves. The concentration of the analyte under test [T] was then estimated using linear regression, as follows:

$$[T] = \frac{r_t^*}{S} \quad (6.3)$$

Analogously, the sensitivity might also be calculated using the following variants:

$$S' = \frac{r_b - r_t}{[B] - [T]};\ S'' = \frac{r_a - r_t}{[B] - [T]} \quad (6.4)$$

Typically, S, S' and S'' had a similar numerical value. Their average was used for the substrate quantification using the auto-controlled method.

6.4.2. Calibration

A human plasma sample purchased from Sigma Aldrich was modified by adding known quantities of analytes of interest. Additional concentration did not consider the unknown endogenous level of the substrate of interest in the sample. The endogenous concentration was estimated by linearization using the first two points of the characteristic. Thus, calibration curves report the total concentration of the substrate in the volume under test. Calibration curves for LAA, glutamate, choline and sarcosine in human serum are reported in Figure 6.2. The complete characterisation of the platform for the analytes of interest is reported in Table 6.3.

Kinetics constants were estimated by data fitting to the Michaelis-Menten model. K_m values obtained from the curve for all the metabolites were in line with the values reported in the literature [49]. For all the metabolites, fittings to the curve using the Michaelis-Menten model were satisfactory with R^2 values ≥ 0.97. As in the previous chapter, a subset of the collected data was also fitted using a linear model. Linear ranges for the measured metabolites were covering the physiological concentration ranges. Average standard deviations of the measurement in the linear range were in the span 16% - 20%.

LOD and LOQ were also quantified over six control biological replicates. Thus, the average reaction rate was 0.005±0.0027 mVs^{-1}. Consequently, LOD and LOQ were 0.014 mVs^{-1} and 0.032 mVs^{-1}, respectively. LOD and LOQ expressed in mVs^{-1} were then converted in µM by using the estimated Michaelis-Menten for each metabolite. Thus, LOD for LAA, glutamate,

choline and sarcosine were 11.1 µM, 1.4 µM, 1.7 µM and 1.4 µM, respectively. Similarly, LOQ values for the metabolites in the same order were 25.5 µM, 3.3 µM, 3.9 µM, 3.5 µM. LOD and LOQ results demonstrated the suitability of the platform for the measurements in the target range.

Table 6.3 Platform characterisation in human plasma for PCa metabolites. Metrics have been defined in Table 2.3.

	LAA	**Glutamate**	**Choline**	**Sarcosine**
Physiological Range	1.7 – 4.6 mM	40 – 150 µM	10 – 40 µM	0 – 20 µM
Test Range	0 – 5.4 mM	0 - 1500 µM	0 – 600 µM	0 – 600 µM
Relation with PCa	↑	↑	↑	↑
Model	$y = \frac{V_m \cdot x}{k_m + x} + c$			
V_m (mV s^{-1}) (95% coefficient bounds)	3.63 (2.62, 4.63)	5.28 (3.46, 7.10)	11.34 (-2.24, 24.93)	11.03 (6.97, 15.10)
c (mV s^{-1}) (95% coefficient bounds)	-0.032 (-0.280, 0.216)	-0.087 (-0.607, 0.433)	0.082 (-0.172, 0.336)	0.027 (-0.060, 0.115)
K_m (µM) (95% coefficient bounds)	2866 (890, 4842)	529.7 (1.06, 1058)	1382 (-991.1, 3755)	1209 (551.2, 1867)
SSE	0.022	0.283	0.142	0.020
RMSE	0.086	0.266	0.169	0.062
R^2	0.994	0.979	0.985	0.998
Linear Model	Y = S · x + C			
Linear Range*[1]	0 - 1500	0 – 320 µM	0 – 120 µM	0 - 120 µM
Analytitcal Sensitivity (S) ($mVs^{-1}mM^{-1}$) (95% coefficient bounds)	0.83 (0.824, 0.830)	6.06 (4.08, 8.04)	9.98 (6.46, 13.5)	7.84 (5.65, 10.03)
C (mV s^{-1}) (95% coefficient bounds)	0.020 (0.017, 0.023)	0.003 (-0.317, 0.324)	0.019 (-0.177, 0.215)	0.050 (-0.059, 0.159)
SSE (linear)	$1.5 \cdot 10^{-06}$	0.076	0.054	0.019
RMSE (linear)	$8.6 \cdot 10^{-04}$	0.159	0.116	0.070
R^2 (linear)	1.000	0.969	0.939	0.961
Precision (linear range)[2]	18.3%	17.2 %	16.4%	19.2%
Negative control (mV s^{-1}) [3]	0.005 ± 0.0027			
LOD (mV s^{-1})	0.014			
LOQ (mV s^{-1})	0.032			
LOD (µM)[4]	11.1	1.4	1.7	1.4
LOQ (µM)[4]	25.5	3.3	3.9	3.5
Resolution (µM)[5]	3.25	0.45	0.27	0.35

[1] Linear range is defined as the measurement range were the linear model had $R^2 > 0.9$.
[2] Calculated as the average of the relative standard deviation of the measurements in the linear range.
[3] Average over 24 measurements.
[4] Converted from mV s^{-1} to µM using the Michaelis-Menten model.
[5] Calculated as the ratio between the standard deviation of the control measurements and the sensitivity in the linear range [58].

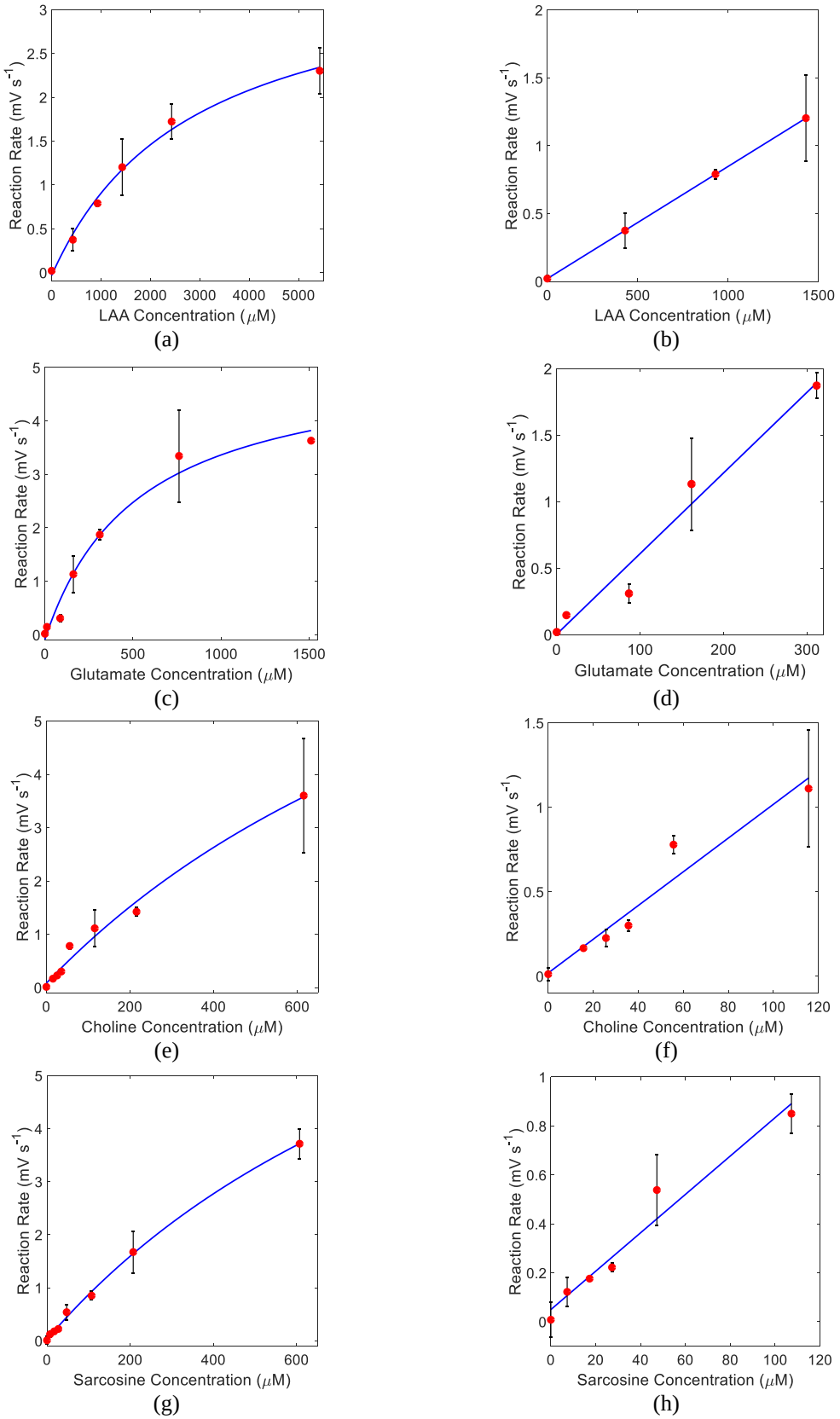

Figure 6.2 Calibration curves obtained by fitting data with Michaelis-Menten in the extended range (left) and with a linear model (right) for (a)(b) LAA, (c)(d) glutamate, (e)(f) choline and (g)(h) sarcosine in human plasma. Concentrations refer to the total reaction volume.

6.4.3. Blind validation

Method. A further human plasma sample was purchased from Sigma Aldrich, aliquoted and modified with additional amounts of analytes of interest. Modified plasma samples were produced by a different member of the MST group, which disclosed the additional concentrations only after the testing was completed. Thus, the modified concentration levels were unknown while performing the assays. For each blind sample and metabolite, measurements were performed in triplicates. Negative control and two positive controls (A and B) were also measured. Controls were repeated in triplicates. The additional concentrations for positive controls A for LAA, glutamate, choline and sarcosine were 500 µM, 100 µM, 100 µM, 100 µM, respectively. The additional concentration for the positive control B was [B] = 2[A]. The unknown quantity of additional metabolite was calculated by performing an additional measurement on the unmodified sample.

Results. Results are reported in Figure 6.3 and Table 6.4. Relative errors were calculated as per definition illustrated in Chapter 2, Paragraph 2.2.5. LAA levels estimated with the auto-controlled approach had an average relative error of 10%. Data had a high correlation (R^2 = 0.96) with the ideal response, and no relevant bias was observed. A 22.6% error was recorded when estimating the same quantities with the approach based on the Michaelis-Menten model. The correlation was R^2 = 0.96, and a small bias compared to the physiological range (620 µM) was observed.

Glutamate levels calculated with the auto-controlled method had an average relative error of 15.8%. The correlation with the ideal response and the bias of the estimation was R^2 = 0.92 and 8.63 µM, respectively. When performing the same determination adopting the model-based approach, average error, correlation, and bias were 59.6%, R^2 = 0.87 and -113.9 µM, respectively.

Table 6.4 Characterisation of the blind tests results.

	LAA	**Glutamate**	**Choline**	**Sarcosine**
Auto-controlled estimation method				
Average relative error	10.0%	15.8%	18.2%	8.6%
Correlation coefficient (R^2)	0.96	0.92	0.98	0.96
Bias of the estimation*	0.22 mM	8.63 µM	17.91 µM	- 3.65 µM
Model-based estimation method (Michaelis-Menten)				
Average relative error	22.6 %	59.6%	73.9%	81.4%
Correlation coefficient	0.96	0.87	0.98	0.96
Bias of the estimation*	0.62 mM	- 113.9 µM	-73.61 µM	-82.6 µM
* Calculated as the average of the absolute error.				

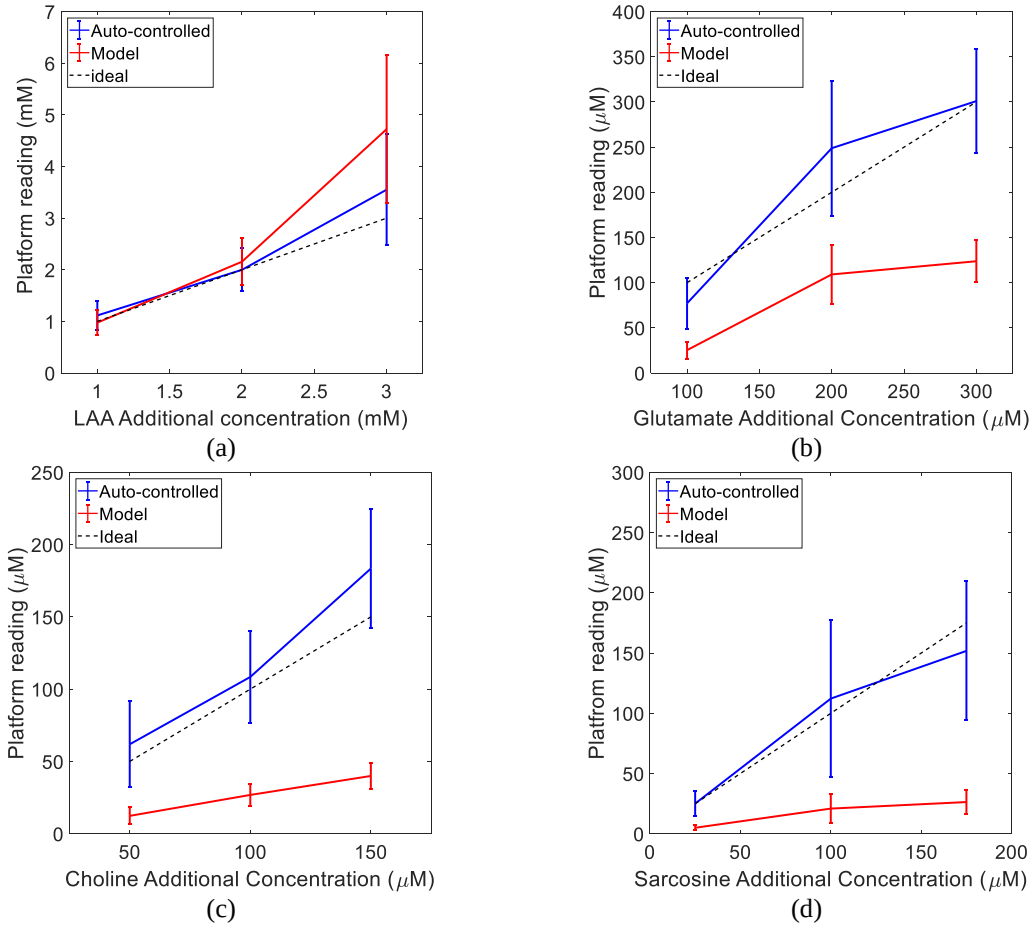

Figure 6.3 Blind validation results when estimating the concentration of the substrate using the model-based method (red) and the auto-controlled approach (blue) for (a) LAA, (b) glutamate, (c) choline and (d) sarcosine.

For choline, average error, correlation, and bias when using the auto-controlled method were 18.2%, R^2 = 0.98 and 17.91 µM, respectively. When the model-based method was used, the average error increased to 73.9%. The correlation remained very high (R^2 = 0.98) and the bias observed was -73.61 µM.

For sarcosine, average error, correlation, and bias when using the auto-controlled method were 8.6%, R^2 = 0.96 and -3.65 µM, respectively. The same quantities were 81.45%, 0.96 and -82.6 µM when the model based on the Michaelis-Menten equation was used. Comparing the two adopted models for substrate quantification, the auto-controlled method was more successful in estimating the unknown concentration of analytes for all the performed assays.

Discussion. For LAA, estimation with the auto-controlled and the model-based methods are very similar in the linear range. The model-based approach seems to start failing only for higher concentrations of LAA. Low sample-to-sample variability was observed for the LAA

assay. For glutamate, choline and sarcosine determination, the model-based approach provides results with a high correlation with the ideal response. However, they systematically provide lower values. Arguably, the sample-to-sample variation was high. Specifically, these experiments demonstrate that the calibration curve obtained from one human sample might be not satisfactory for a different one. Probably, this is related to the composition of the human specimen, which may or may not include molecules interfering with the developed assay in several concentrations. This is a common problem for POC diagnostics that many variables and specimens can affect the result. On the contrary, for all the performed assays, the auto-controlled method provided more reliable results with estimation errors which are comparable to the glucose meter devices on the market. The increased reliability of the measurement was achieved by using all the controls to calibrate the platform on the specific sample. Consequently, the auto-control can compensate for several variables, including sample-to-sample variation, cartridge-to-cartridge variation, environmental conditions, and ambient interferences. Drawbacks of this approach include the need for additional reagents, additional sample volume and further data processing to be performed. On this basis, the auto-controlled approach was the adopted approach for clinical evaluation.

6.4.4. Clinical evaluation

Method. Samples from non-PCa and PCa group were tested for the four metabolites of interest for PCa diagnosis. The concentration of the metabolites of interest was unknown during the experiments. The non-PCa group was tested before the PCa group. Within the group, metabolites were measured in the following order: LAA, glutamate, choline, sarcosine. For each sample and metabolite, the negative control was first assessed. Then, the three biological repeats of the assay were performed. Finally, positive controls A and B were performed. The additional concentrations for positive controls A for LAA, glutamate, choline and sarcosine were [A] = 500μM, 100μM, 100μM, 100μM, respectively. The additional concentration for the positive control B was [B] = 2[A]. To save sample volume, the total volume of the reaction was reduced from 60μL to 40μL. The amount of the samples and reagents were proportionally reduced by one third. Thus, the total sample volume used for each biological replicate was 20 μL. The auto-controlled method was adopted for the quantification of the analytes. All the errors are expressed as one standard deviation.

Results. Results from the clinical evaluation for both non-PCa and PCa groups are reported in Table 6.5. For LAA, the average over the entire dataset, herein referred to as grand average, was 2421±952 µM. LAA levels were in the range 1213 - 5421 µM for the entire dataset. Non-PCa samples had an LAA average concentration of 1984±527 µM, in the range from 1213-3167 µM. PCa samples had, on average, an increased level of LAA. The LAA average level in the PCa group was 2694±1052 µM. The range of the measurements in the PCa group was 1503-5410 µM. Results obtained were in expected physiological ranges for both non-PCa and PCa groups. The ratio between average LAA in the PCa group and the non-PCa group was 1.36. The observed average increase in the PCa group was +35.8 %. When performing a one-tail t-test with homoscedastic variance, a value of $p = 0.03$ was observed: the increase in the LAA concentration in the PCa group had statistically significant variation.

The grand average glutamate level was 53.7±26.4 µM, with measured values ranging from 6.3 µM to 149.5 µM. The average non-PCa glutamate level was 40.2±11.2 µM, in the range 21.9-67.1 µM. PCa samples had, on average, an increased concentration of glutamate. The average PCa glutamate concentration was 62.2±29.5 µM. Measurements in the PCa group were in the range of 6.3-149.5 µM. Results were compatible with physiological ranges. The ratio between average glutamate in the PCa group and the non-PCa group was 1.55. The observed average increase in the PCa group was +54.8 %. The glutamate concentration in the PCa group had a statistically significant increase ($p = 0.02$).

For choline, the grand average of the entire dataset was 11.7±7.0 µM, and the measurements were in the range 2.3-36.9 µM. The average non-PCa choline level was 9.0±4.1 µM. The range of the non-PCa choline measurements was 2.3-15.4 µM. PCa samples had increased concentration of choline, with an average of 13.4±7.9 µM. PCa results for choline were in the range of 4.7-36.9 µM. The ratio between average choline in the PCa group and the non-PCa group was 1.49. The observed average increase in the PCa group was +49.2 %. The t-test, performed assuming one tail distribution and homoscedastic variance, demonstrated the statistically significant difference in the average of the two groups ($p = 0.06$).

For sarcosine, clinical evaluation reported a grand average of 10.6±6.0 µM and a range of 1.7- 27.2 µM. The average non-PCa sarcosine level was 11.5±4.3 µM, and measurements were in the range 5.1-18.8 µM. PCa samples had decreased concentration of sarcosine, with an average of 10.0±6.8 µM. The range of sarcosine in the PCa group was 1.7-27.2 µM. Results were compatible with physiological ranges. The ratio between average choline in the

PCa group and the non-PCa group was 0.87. The observed average decrease in the PCa group was -13.5 %. The t-test, performed assuming one tail distribution and homoscedastic variance, demonstrated that this variation was not statistically significant ($p = 0.27$).

Results are presented in Figure 6.4(a) where data has been normalised to the grand average of the analyte under test. Figure 6.4(b) shows the difference in the statistics of the two groups for the metabolomics panel. LAA, glutamate and choline showed a statistically relevant increase in their concentration in the PCa group. Among them, glutamate and choline had, respectively, the lowest and the highest p-value. Differently, sarcosine concentration in the PCa group was decreased with respect to the control group but differences were not considered statistically relevant.

Figure 6.5 suggests that, when used together, metabolites can potentially identify cancerous conditions. Concentrations of LAA, glutamate and choline seem to be capable of dividing the two groups in cartesian space. For example, Figure 6.5(b) demonstrate that, for this population, it is possible to separate the PCa group from the non-PCa group. Cross-correlation of the profile of the metabolites is also reported in the figure. There is no relevant cross-correlation among different metabolites (highest recorded cross-correlation was between LAA and glutamate in the non-PCa group: $R = 0.38$). The study suggests that there is merit in using the dataset for training a classification model. The research also indicates that, for this population, LAA, glutamate and choline could be considered metabolic biomarkers for PCa. On the contrary, for this population, sarcosine could not be regarded as a metabolic biomarker for PCa.

4105 *Table 6.5 Clinical evaluation results on control (non-PCa) and cancer (PCa) groups.*

Group	Sample ID	LAA		Glutamate		Choline		Sarcosine	
		Avg. µM	Std. %	Avg. µM	Std. %	Avg. µM	Std. %	Avg. µM	Std. %
non-PCa	1	1961	16.2	42.5	16.9	15.4	11.5	15.1	23.5
	2	2493	9.5	67.1	44.7	8.7	34.0	7.5	9.8
	3	1972	29.4	30.7	28.5	2.3 (<LOQ)	78.7	7.0	21.8
	4	3167	10.4	34.2	8.8	10.2	39.9	18.8	38.1
	5	1983	20.8	39.5	14.5	14.8	54.5	7.4	32.2
	6	2187	5.4	47.1	32.0	11.3	36.0	5.1	44.6
	7	1780	15.5	37.6	53.0	3.2 (<LOQ)	32.0	12.4	63.5
	8	1213	13.1	21.9	4.1	9.4	17.5	12.2	45.6
	9	1390	14.4	40.8	8.7	8.4	86.9	13.2	39.5
	10	1693	6.7	40.1	45.0	6.1	9.7	16.4	43.3
PCa	11	1736	13.0	75.6	34.9	4.7	10.5	7.7	20.2
	12	2837	6.2	6.3	25.9	19.4	77.2	12.7	33.8
	13	4152	10.2	61.7	91.9	14.3	59.0	22.2	24.1
	14	5410	14.4	62.5	54.2	9.0	18.5	13.6	63.4
	15	4109	5.7	48.7	32.3	16.3	23.6	< 1.4	100.0
	16	3495	15.4	149.5	20.2	12.7	64.8	9.6	16.7
	17	2872	11.7	33.4	17.9	17.2	100.0	5.3	68.5
	18	2528	16.2	33.5	2.3	10.5	72.8	10.2	78.5
	19	1851	18.9	60.3	87.1	8.7	69.5	27.2	63.0
	20	2479	15.2	46.3	13.5	23.5	58.2	< 1.4	100.0
	21	1940	15.3	84.5	47.3	36.9	58.0	4.0	72.4
	22	1789	20.6	73.8	82.8	7.3	35.5	8.0	6.9
	23	2292	13.1	59.4	77.9	9.7	50.2	12.8	41.6
	24	1503	1.0	75.0	13.8	10.2	33.7	11.3	100.0
	25	1947	6.3	68.2	48.3	7.5	39.2	9.6	25.3
	26	2162	6.7	56.0	38.6	6.1	38.8	< 1.4	100.0
Overall results									
Grand average (µM)		2421		53.7		11.7		10.6	
Grand median (µM)		2072		47.9		10.0		9.9	
Grand std. dev. (µM)		952		26.4		7.0		6.0	
Range (µM)		1213 – 5421		6.3 – 149.5		2.3 – 36.9		1.7 – 27.2	
Avg.envir. Temp. (°C)		27.3 ± 1.0		26.4 ± 1.3		26.3 ± 0.9		25.9 ± 1.2	
Avg.envir hum. (%)		52.6 ± 5.0		49.5 ± 7.8		44.4 ± 9.0		42.2 ± 10.5	
Cross-correlation Matrix (R values)		$\begin{pmatrix} 1.00 & 0.17 & 0.17 & 0.05 \\ 0.17 & 1.00 & 0.08 & -0.08 \\ 0.17 & 0.08 & 1.00 & -0.27 \\ 0.05 & -0.08 & -0.27 & 1.00 \end{pmatrix}$							
non-PCa group									
non-Pca average (µM)		1984		40.2		10.0		11.5	
non-Pca median (µM)		1966		39.8		9.0		12.3	
non-Pca std (µM)		527		11.2		4.1		4.3	
Range (µM)		1213 - 3167		21.9 – 67.1		2.3 – 15.4		5.1 – 18.8	
Cross-correlation Matrix (R values)		$\begin{pmatrix} 1.00 & 0.38 & 0.17 & 0.09 \\ 0.38 & 1.00 & 0.18 & -0.32 \\ 0.17 & 0.18 & 1.00 & 0.02 \\ 0.09 & -0.32 & 0.02 & 1.00 \end{pmatrix}$							
PCa group									
Pca average (µM)		2694		62.2		13.4		10.0	
Pca median (µM)		2386		61.0		10.4		9.7	
Pca std. dev. (µM)		1052		29.5		7.9		6.9	
Range (µM)		1503 - 5410		6.3 – 149.5		4.7 - 36.9		1.7 – 27.2	
Cross-correlation Matrix (R values)		$\begin{pmatrix} 1.00 & -0.02 & 0.05 & 0.11 \\ -0.02 & 1.00 & -0.08 & 0.01 \\ 0.05 & -0.08 & 1.00 & -0.30 \\ 0.11 & 0.01 & -0.30 & 1.00 \end{pmatrix}$							
Univariate analysis									
Pca/non-Pca (average)		1.36		1.55		1.34		0.87	
Pca/non-Pca (median)		1.21		1.53		1.15		0.79	
t-test (p value)		0.03		0.02		0.06		0.27	

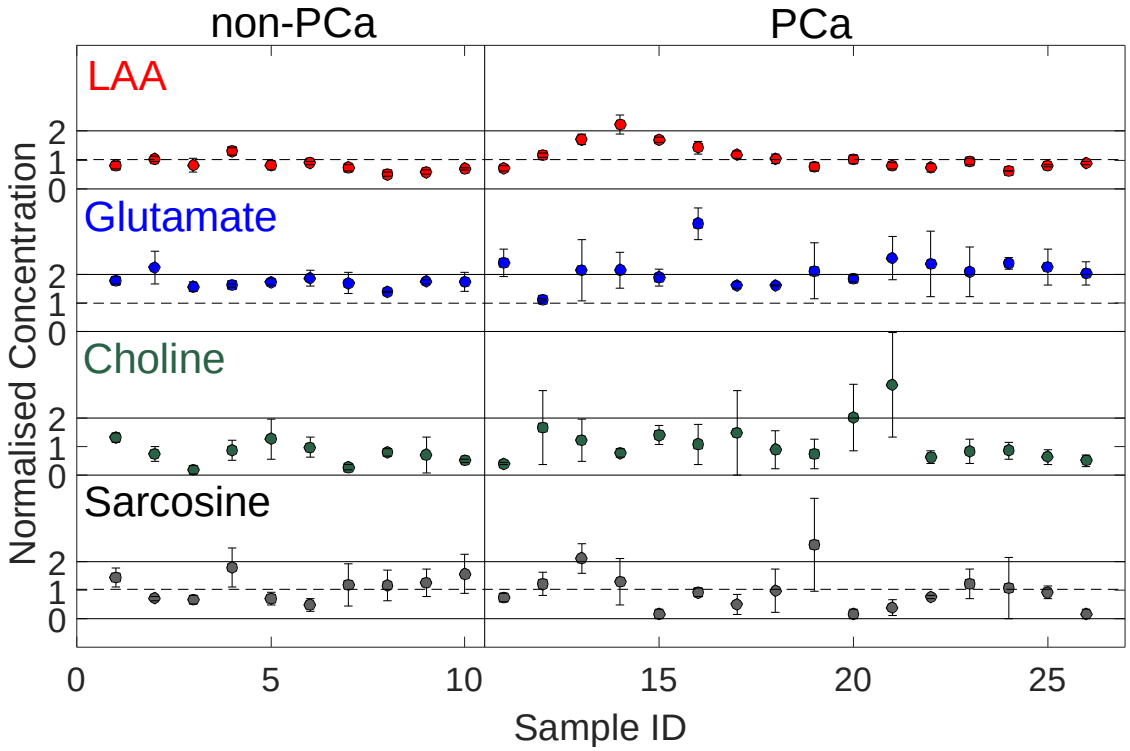

(a)

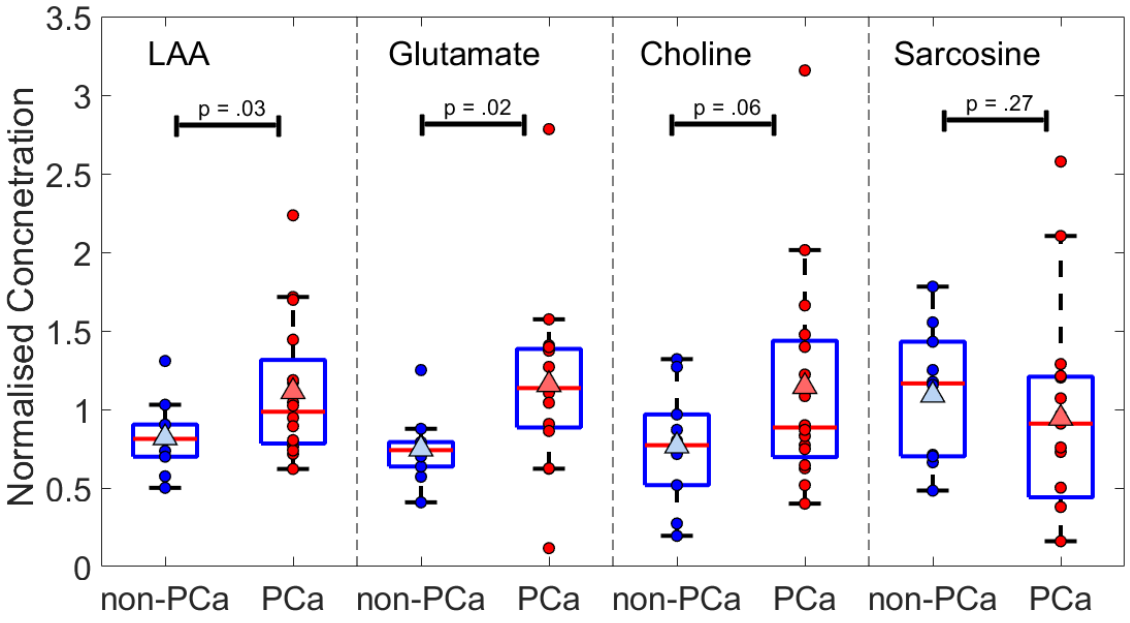

(b)

Figure 6.4 (a) Metabolites quantification in non-PCa (samples 1-10) and PCa group (samples 11-26). The concentration of the metabolic biomarkers was normalised to the grand average. From top to bottom, LAA (red), glutamate (blue), choline (green), sarcosine (black) data. (b) Box plots for the non-PCa group vs the PCa group. Blue and red markers indicate non-PCa and PCa measurements, respectively. Triangular markers indicate the average of the group. Concentrations of LAA, glutamate and choline are statistically increased in PCa group. No statistically significant difference was observed for sarcosine.

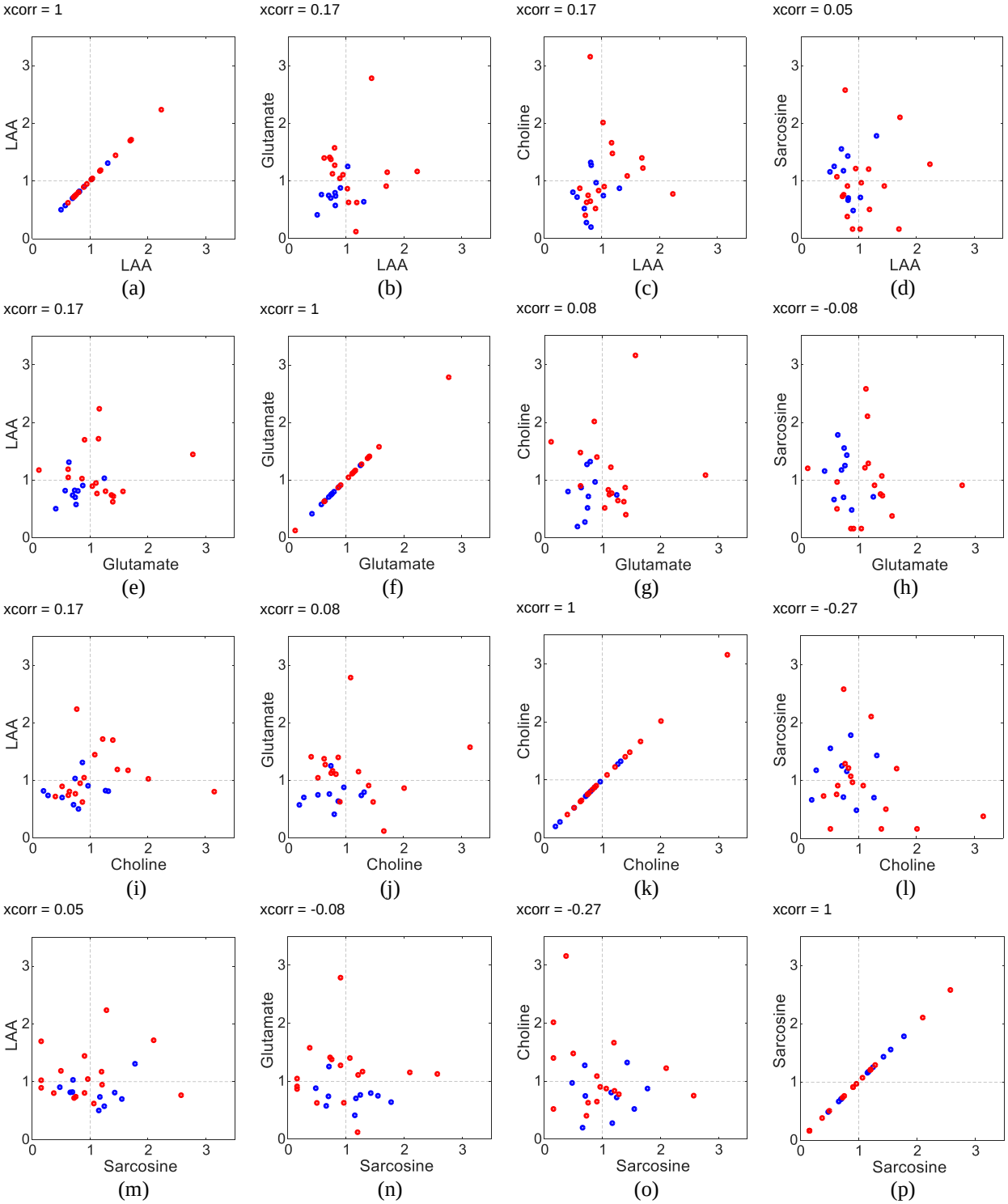

Figure 6.5 (a)-(p) Scatter plots for all the metabolite combinations. Concentrations are normalised to the respective grand average. Blue markers: non-PCa samples. Red markers: PCa samples. Cross-correlation values are referred to the overall dataset.

6.4.5. Validation against standard methods

Method. LAA, glutamate, choline, and sarcosine concentrations in the non-PCa group were independently analysed by Dr Liam Heaney, Lecturer in Bioanalytical Science, School of Sport, Exercise and Health Sciences, Loughborough University. Plasma samples were shipped under a specific material transfer agreement. All the metabolites were tested using commercially available fluorescent plate-based assays following manufacturer instructions (product codes: ab65347, ab138883, ab219944, ab65338, Abcam, Cambridge, UK). Choline was also analysed by ultra-performance liquid chromatography-tandem mass spectrometry (UPLC-MS/MS) using an Acquity liquid chromatography coupled to a Quattro Ultima triple quadrupole mass spectrometer (Waters, Wilmslow, UK).

Results. Results are shown in Figure 6.6. For each sample, metabolite and testing method, concentrations were normalised to the group average. All four metabolites had comparable results with commercial methods. For this population, the average relative errors of the platform when quantifying LAA, glutamate, choline and sarcosine with respect to the reference method were 18.5%, 13.81%, 21.37% and 44.4%, respectively. Choline comparison, shown in Figure 6.6(e), is particularly interesting because data from the developed platform showed higher correlation with MS-MS measurements (R=0.8) rather than with data obtained with the commercial fluorescent kit (R=0.5). It is well-known that MS-MS provides more accurate results than commercial assay kits. MS-MS analysis for all the metabolites was not possible due to limited resources. However, data suggests that measurements with the platform might be more accurate than the commercial kit.

Discussion. There are some factors that might have affected the comparison and should be highlighted. Samples tested in the third-party laboratory went through an additional long-distance shipping process which might have affected the concentration of the metabolites. Also, one set of calibration parameters were used for each metabolite using the third-party method. Concentrations measured with the developed platform were instead estimated using sample-specific calibration parameters. Furthermore, adopted methods used different working principles. Authors in [90] warn that serum metabolites measured with different approaches might have discrepancies due to chemical interferences and therefore exact match is not expected.

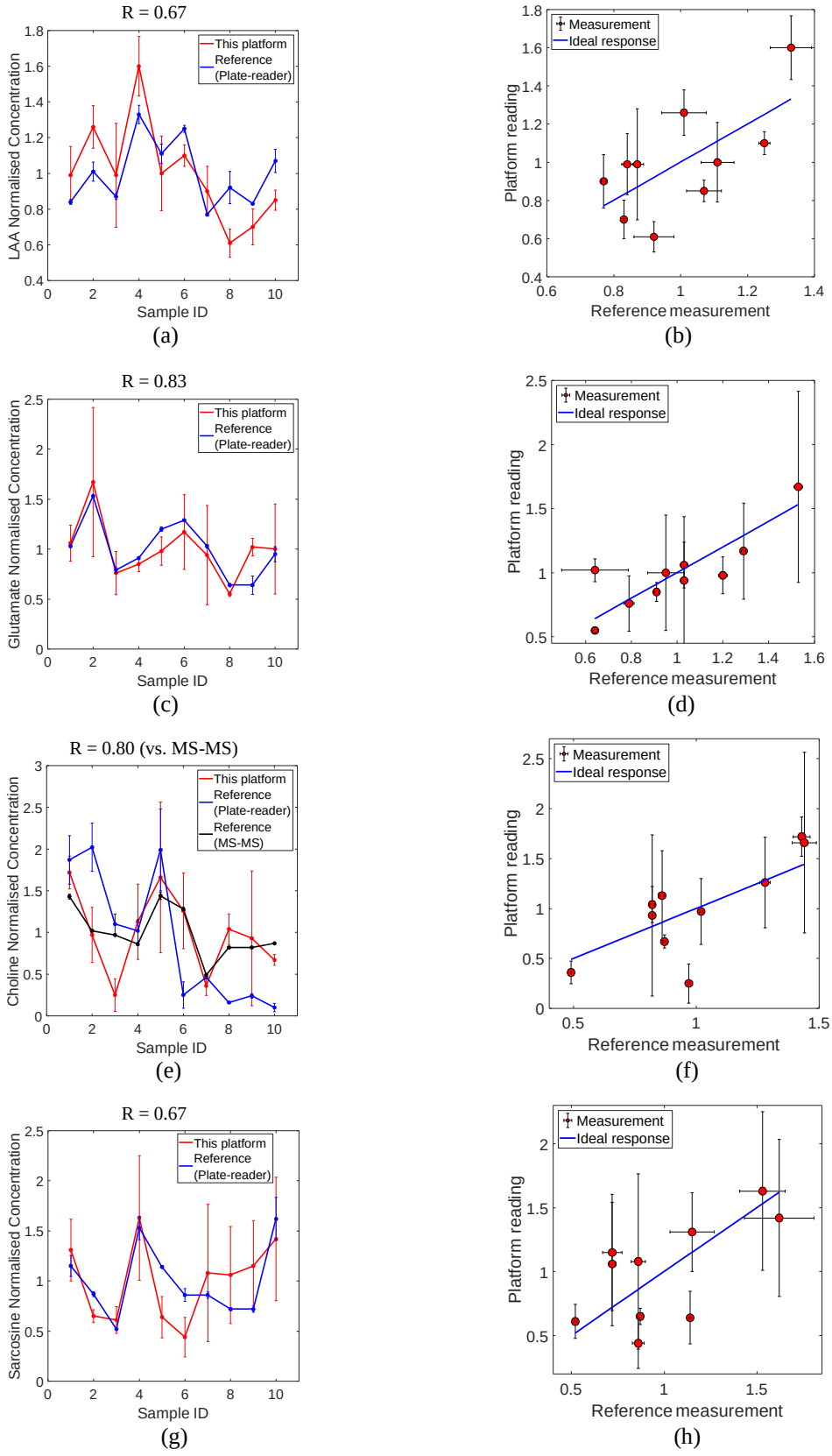

Figure 6.6 Normalised metabolite levels measured with this platform compared with commercial standard methods for (a),(b) LAA, (c)(d), glutamate, (e)(f) choline (levels were measured with fluorescent assay kit used with a benchtop plate reader - solid blue line - and MS-MS - solid black line) and (g)(h) sarcosine.

6.4.6. Classification

Clinical sensitivity, specificity and accuracy of the platform was quantified by applying several well-known classification algorithms to the dataset. The comparison of different classification algorithms was performed using a customised Matlab-based script. Matlab built-in functions for creating classification models have been used. It was experimentally verified that sarcosine data was not relevant for data classification, and therefore it was excluded from this analysis.

Metrics. The following metrics have been adopted:

- Test outcome is positive/negative if the sample is classified as belonging to the PCa/control group.
- True positives/negatives (TP/TN) are samples correctly classified.
- False positives (FP) are negative samples wrongly classified as positive.
- False negatives (FN) are positive samples wrongly classified as negative.
- Diagnostic (or clinical) sensitivity (Sn), also referred to as true positive rate (TPR), is the portion of positive samples correctly classified as positives (see Figure 1.1) [17] [18].
- Diagnostic (or clinical) specificity (Sp), also referred to as true negative rate (TNR), is the portion of negative samples correctly classified as negatives (see Figure 1.1) [17] [18].
- Diagnostic (or clinical) accuracy (Acc.) of the classification is the sum of true positive and negatives dived by the entire population (see Figure 1.1) [17].
- The area under the curve (AUC) is the area under the receiver operating characteristic curve (ROC). ROC is a curve created by plotting sensitivity against specificity at various threshold settings [17], [309]. The scientific community usually adopts the AUC for comparing different classification algorithm [309].

Methods. Normalised data of LAA, glutamate and choline were used to train several well-established classification algorithms. Models were trained using a k-fold cross-validation approach, which was used to overfitting. In k-fold validation, the dataset was divided into k sub-groups. The algorithm was then trained using (k-1) sub-groups. The remaining sub-group was used for validation. The division in sub-group was random. To avoid variation due to the random process of partitioning the dataset, the process was re-iterated for 500 repetitions where the k sub-groups were randomly re-defined. Considering the population size, a k value of 5 was selected.

The classifiers were also trained on data processed with the Principal Component Analysis (PCA). PCA is a statistical analysis for dimension reduction. It decomposes a dataset with N dimension into a new dataset, with the same number of uncorrelated dimensions, called components [310]. The components are orthogonal and successively maximise variance [310]. The method has been widely used and described in the literature [310]. PCA analysis is reported in Figure 6.7. The scores of the PCA analysis are reported in Appendix M.

Algorithms from four different classification classes were adopted:

- *Decision trees*. Decision tree-based algorithms define several flow-chart-like decisions to reach an outcome. They can have different degrees of complexity and many structures have been proposed in the literature [311]. The more sophisticated algorithm here adopted is the random forest algorithm, which groups several decision trees were features are randomly selected.
- *Discriminant analysis*. Algorithm using discriminant analysis develops a discriminant function to distinguish between the classes of interest in the feature space [312].
- *Support Vector Machines (SVMs)*. SVMs derive the hyperplane that maximises the distance between the closest negative and the positives [313]. The points defining the borders of the hyperplane are called support vectors. Support vector points are then fitted using a kernel function for mathematically define the hyperplane [313]. In this work, four different kernel functions have been used, namely linear, quadratic, cubic and Gaussian. A detailed theoretical description of the method is reported in [313].

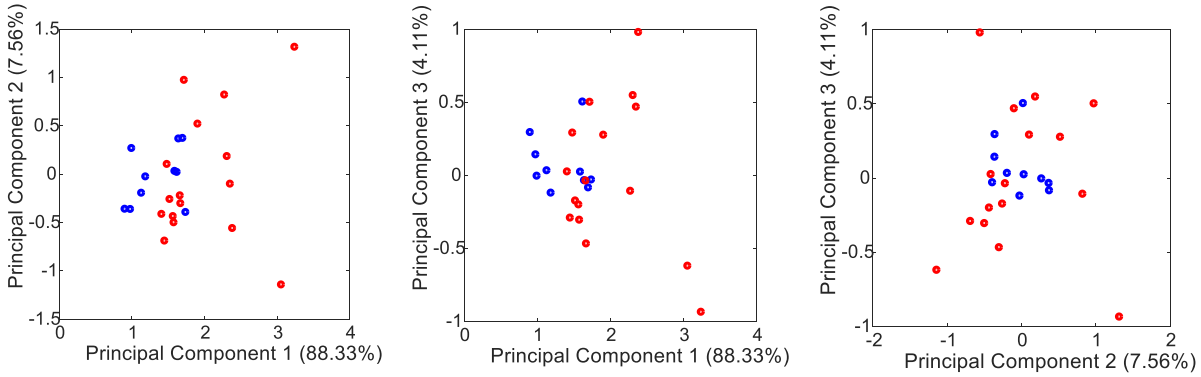

(a) (b) (c)

Figure 6.7 (a),(b),(c) Scatter plots for all the combination of the PCA scores. Blue markers: non-PCa scores. Red markers: PCa scores.

- *k-nearest neighbours (KNN)*. KNN algorithms use a set of k nearest points in the feature space to determine the class of the sample under test using a likelihood approach [314]. This class of algorithms can be considered as a voting system based on the closer points in the feature space [314]. There are many parameters which can be modified to improve the performance of the decision. The main parameters to be considered are the number k of nearest point and the type of distance to be used (e.g. Euclidean, correlation, etc.). The k nearest point can also be weighted when performing the distance [315]. Additional theoretical knowledge about KNN algorithms can be found in the literature [314], [315].

Other classifiers and training methods are available. However, it was beyond the scope of this work to identify the ultimate method for classifying the population. Thus, only the most used algorithms have been trained and validated.

Results. Results from all the classifiers are reported in Table 6.6. All the classification metrics are here reported as the average over 500 iterations. Diagnostic sensitivity and specificity were calculated in the point of the ROC curve which was the closest to the ideal condition (Sn=Sp=1) [309]. Generally, training the model with the scores of the PCA analysis only improved the results for discriminant analysis algorithms.

The classification algorithm with the highest AUC was the weighted KNN algorithm, with an AUC of 0.862. Weighted KNN also showed the highest accuracy: 0.84. The approach which showed the highest sensitivity was the Gaussian SVM. In this case, sensitivity was 0.90. The method performing the highest specificity was the medium KNN algorithm trained on PCA scores. In this case, the specificity was 0.83.

The AUC was here used for selecting the algorithm with the best performance, according to standard procedures [309]. Hence, the weighted KNN algorithm was selected as the optimal method among the adopted for data classification. Therefore, additional information is here provided for the developed weighted KNN algorithm.

The model was trained using ten neighbours' samples and evaluating the distance by the Euclidean definition. The set of weights followed a squared inverse model. When cross-validating data with the trained KNN, true positive and the true negative were, on average, 13.97 and 7.38, respectively. False positive and false negative were, on average, 2.62 and 2.03. Sensitivity and specificity for this model, as reported in the table, were 0.84 and 0.78, respectively. The ROC curve for the KNN model is reported in Figure 6.8.

Table 6.6 Diagnostic evaluation of the platform using classification and k-fold validation for different methods. Bold values highlight the best value obtained within the classification group. Values marked with '' are the best value among all the adopted classification methods.*

Method	PCA disabled				PCA enabled			
	AUC	**Acc.**	**Sn**	**Sp**	**AUC**	**Acc.**	**Sn**	**Sp**
	Decision trees							
Fine Tree	0.73	0.80	0.86	0.71	0.73	0.70	0.79	0.54
Medium Tree	0.74	0.80	0.86	**0.72**	0.73	0.71	0.80	0.55
Coarse tree	0.73	0.80	0.86	0.71	0.73	0.70	0.79	0.55
Boosted tree	0.79	0.81	0.88	0.70	0.79	0.72	0.76	0.66
Random Forest	**0.79**	**0.81**	**0.88**	0.70	0.79	0.72	0.75	0.68
	Discriminant analysis algorithms							
Linear	0.76	0.67	0.76	0.53	**0.76**	0.67	0.76	0.53
Quadratic	0.75	0.76	0.78	0.73	0.76	**0.76**	0.78	**0.73**
Logistic Regression	0.75	0.70	0.81	0.53	0.76	0.71	**0.82**	0.54
	SVMs							
Linear	0.78	0.75	0.87	0.54	0.77	0.73	0.86	0.53
Quadratic	0.77	0.74	0.72	0.77	0.81	0.75	0.73	**0.79**
Cubic	0.74	0.71	0.71	0.73	0.72	0.69	0.65	0.76
Gaussian	0.82	**0.81**	**0.90***	0.66	**0.84**	0.79	0.86	0.69
	KNN algorithms							
Fine	0.78	0.79	0.83	0.73	0.75	0.75	0.77	0.72
Medium	0.73	0.68	0.66	0.70	0.77	0.69	0.60	**0.83***
Coarse	0.53	0.62	0.25	0.80	0.53	0.62	0.25	0.80
Cubic	0.77	0.70	0.69	0.73	0.74	0.68	0.61	0.78
Weighted	**0.86***	**0.84***	**0.84**	0.78	0.83	0.81	0.84	0.77
*Maximum value among all the adopted methods								

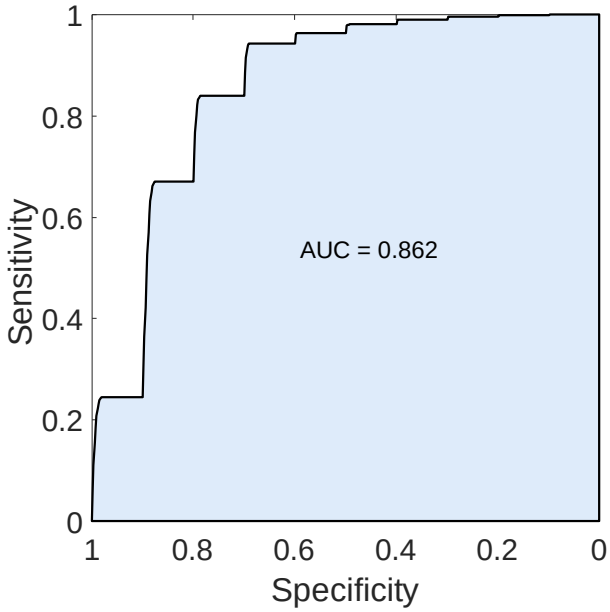

Figure 6.8 ROC curve for the weighted KNN algorithm.

6.4.7. Discussion

The clinical study arises a multitude of discussion points. The first consideration to be highlighted is that there is merit in using multiple metabolites to create a model for the discrimination of PCa. However, the selected metabolites must show a correlation with the disease. Sarcosine in plasma did not show relevant correlation with PCa and it was therefore concluded that plasma sarcosine was not a metabolic biomarker in this population, corroborating the reports in the literature [180]. Differently, LAA, glutamate and choline showed significant correlations and were used as features to train a classification model. The best classification model here obtained from the AUC viewpoint, was a model based on a weighted KNN algorithm. However, there are many other classification approaches which might be adopted for this dataset potentially providing improved performance. It is also worth stressing that the classification was performed assuming a k-fold validation approach, and different results might be achieved with varying values of k. More optimistic results were obtained when no validation was performed. However, model training with no validation might be affected by overfitting and might not reliable and, as a result, have not been reported here.

Data was also independently analysed by Dr Ronan Daly, data analysis manager at Glasgow Polyomics, University of Glasgow. Glasgow Polyomics confirmed the superfluity of sarcosine data in the classification and the unnecessity of preliminary PCA analysis and verified that there is merit in the selected metabolic biomarkers. Glasgow Polyomics suggested the use of a random forest classification algorithm trained using the R packages 'randomForest' and 'caret' [316]. The algorithm was set to use 500 trees and try up to three metabolites at each split. The model was validated using a *leave-p-out* cross-validation procedure [317], [318]. The resulting cross-validated AUC was 0.8. The ROC showed the optimal operational point at a sensitivity of 0.93 and a specificity of 0.70. Glasgow Polyomics also suggested an alternative model based on glutamate measurements only, which could optimise the sensitivity given a specificity of approximately 0.85.

It is interesting to compare the diagnostic capability of the selected metabolites with the current standard, i.e. PSA testing. Due to ethical reasons, it was not possible to access PSA data over the studied population. However, PSA testing has been widely characterised in terms of sensitivity and specificity [18]. In clinical practice, PSA sensitivity and specificity are 0.32 and 0.87, respectively, for a PSA threshold of 3.1 ng/mL. Sensitivity and specificity can be tuned by modifying the PSA cut-off [18], [319]. However, the clinical PSA cut-off is

optimised to maximise specificity. This choice is related to the fact that, in order to diagnose the highest number of tumours, a relevant number of false positives is acceptable since, in these cases, further tests will be in place to confirm or confute the PSA test. Differently, people having a false negative result might not immediately undergo further testing, resulting in the progression of the disease.

Based on these considerations, the working point of the classifier can be selected to maintain the same specificity level of PSA. Figure 6.9 shows a comparison of the potential working points for the classifier of interest, together with the PSA ROC curve obtained from [18].

The random forest model based on glutamate only has the potential to increase the sensitivity of the diagnosis to 0.63 while maintaining the specificity at 0.87. The random forest model based on all the metabolic profiles works just as good as PSA testing with a specificity level of 0.87. However, this model has the potential to increase the sensitivity to 0.94 when reducing the specificity to 0.68. The weighted KNN algorithm has comparable performance to the random forest (glutamate only) with specificity 0.86 and sensitivity of 0.64. This model also has a working point comparable to the random forest – all metabolites, with specificity and sensitivity of 0.68 and 0.95. A trade-off between the two points can also be selected, with specificity of 0.78 and specificity of 0.81.

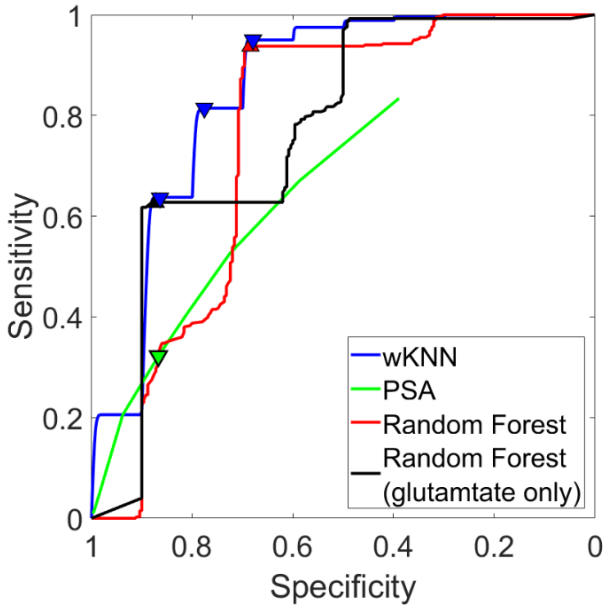

Figure 6.9. Comparison of different ROC curves. Weighted KNN ROC, trained and validated using a k-fold validation approach within this PhD research work, is shown in blue. Random forest algorithms using all the metabolites ana glutamate only, trained and validated by Glasgow Polyomics, are shown in red and black, respectively. PSA ROC obtained from [18] *is shown in green.*

The weighted KNN algorithm contained both the optimised working points from the random forest algorithms and therefore it was selected as the final choice in this analysis. Within this algorithm, the working point (0.86, 0.64) is suggested for a real-life scenario. This working point improves the performance of the current clinical standard by doubling the sensitivity when maintaining the same specificity.

It might be argued that medications might have affected the concentration of the metabolites. It was experimentally verified that, for this population,the treatment did not influence the concentration of the metabolites under test. To do this, the PCa group was divided in sub-groups, according to the ongoing treatment. No statistically relevant correlation was identified in the subgroups.

The proposed metabolic biomarker panel was based on literature review and discussion with PCa clinician experts. However, the metabolic panel can be potentially improved by including additional or different metabolites. Regardless, it is out of the scope of this work to identify the best metabolic panel for PCa, which remains an open medical question. Differently, this study aimed to stress that such a platform can assay the metabolites with accuracy suitable for the determination of pathological conditions. These findings are particularly promising if both diagnostic approaches based on PSA and metabolomics are combined.

In summary, the results from the PCa clinical evaluation reported promising development after comparison with the current clinical standard. However, certain limitations of the study may not allow generalising the findings at this stage. Considering the finite set of metabolite biomarkers, the platform demonstrated its potential for the quantification of multiple metabolites with accuracy suitable for diagnostically relevant information.

6.5. Ischemic Stroke Clinical Evaluation

A clinical evaluation to perform lactate assay on-chip for ischemic stroke stratification was performed on ten plasma samples from patients which had been affected by an ischaemic stroke event. Target analytes were lactate and creatinine. However, the volume of the clinical sample obtained was not enough for performing both the assays. Thus, only lactate determination was performed. Results from the clinical evaluation were compared with the results obtained from conventional gold standard measurements used in the National Health Service (NHS) laboratories.

6.5.1. Materials and Methods

Reagents. Reagents were purchased from Sigma Aldrich. Formulations were optimised using a trial-and-error approach. To save sample volume and avoid platform saturation, stroke samples were diluted with DI water (ratio 1:4). Calibrators were also used in diluted form. Dilution factors were numerically compensated in the data-analysis stage. Environmental temperature and humidity were also monitored. Table 6.7 summarises the formulations for ischemic stroke clinical evaluation.

Clinical samples. Ten samples of human plasma from people diagnosed with ischemic stroke were sourced from the Queen Elizabeth University Hospital, Glasgow, UK, under ethical approval, thanks to the collaboration with Dr Samadhan B. Patil, lecturer in medical engineering at the University of York, and Prof Jessie Dawson, professor of stroke medicine and consultant stroke physician at the Queen Elizabeth Hospital, Glasgow. Donors were adults recently diagnosed ischemic stroke. The approximate available volume, for each sample, was 100 µL. A numeric sample IDs from 1 to 10 was randomly assigned to each sample. Calibration samples (calibrators) were sourced from the Institute of Cardiovascular and Medical Sciences, University of Glasgow. Calibrators were used in diluted form. The protocol for sample collection is reported in Appendix L.

Procedure. The setup used for lactate clinical evaluation was the same as the one used for cancer clinical evaluation. Similarly, reagents were mixed with the sample off-chip and immediately introduced into the cartridge in a few seconds. Metabolites were tested individually, using cartridges with four microchannels. The adopted protocol is the same as the one illustrated for PCa and previously shown in Figure 6.1.

Table 6.7 Assay formulation for ischemic stroke clinical evaluation.

	Lactate
Cartridge	4 parallel and identical microchannel (h ~ 290 µm)
Microchannel volume	0.348 µL
Light source	LED @ 490nm (3 mW, FWHM = 20 nm)
Total Volume	60 µL
Sample Volume	6 µL
DI water	24 µL
Reagent mix volume	30 µL
Reagent buffer	DI water
1st reaction stage	10µL LaOx 10 U/ml
2nd reaction stage	10µL HRP 300U/ml 5µL Phenol 44.5mM 5µL 4AAP 10.5mM
Negative control	1st reaction stage was substituted with 10µL of DI water
Positive control	The sample was spiked with a known concentration of analyte of interest

Data handling. Each measurement had four independent repeats. Measurements were performed in biological triplicates, each composed of four technical replicates.

Cartridge reuse. Cartridges were cleaned and re-used using the same procedure used during cancer clinical evaluation. Two cartridges were used for this experiment.

Substrate quantification. Lactate is routinely measured in the clinical environment. Thus, a similar clinical protocol was adopted in this project, which can be divided into two stages: calibration and testing. In the clinical environment, calibration is performed every day. The calibration procedures consist of testing two commercial calibration solutions with known concentrations of lactate, x_1 and x_2. Let us refer with y_1 and y_2 to the output of the equipment when testing the calibrators. The points on a Cartesian coordinates system (x_1, y_1) and (x_2, y_2) identify a calibration line, which is usually obtained by a linear fit of the calibrator outputs. After calibration, samples were tested in triplicates. Substrate concentration was determined by comparing the output with the calibration curve.

6.5.2. Calibration

Method. Calibration was performed using two commercial calibrator solutions. The concentrations of lactate in the calibrators were 440 µM and 2070 µM. Calibrators were also used in diluted form.

Results. Table 6.8 summarises the results of the calibration stage. Figure 6.10(a) shows data from a microchannel for both the calibration solutions. The average initial reaction rates over the biological triplicates were used to determine a linear calibration curve. The 2-points calibration curve is presented in Figure 6.10(b). The concentration reported in the calibration curve is the lactate level after dilution. Dilution impact was subsequently compensated using the appropriate dilution factor. The calibration curve showed a sensitivity of 6.302 $mVs^{-1}mM^{-1}$ and a baseline of 0.1484 mVs^{-1}. Results are summarised in Figure 6.10. The values obtained for LOD and LOQ during the PCa clinical evaluation can be assumed to be valid also for lactate evaluation. This is a conservative assumption since experiments in diluted samples are more likely to provide lower LOD and LOQ. LOD and LOQ were adjusted according to the dilution factor and therefore refer to the undiluted sample. LOD and LOQ were 206.0 µM and 229.0 µM, respectively.

Table 6.8 Platform Characterisation in human plasma for ischemic stroke metabolites. Metrics have been defined in Table 2.3.

	Lactate
Physiological Range	300 - 2000
Relation with stroke	↑
Linear Model	$Y = S \cdot x + C$
Dilution factor	8
Analytical Sensitivity (S) ($mV\ s^{-1}\ mM^{-1}$)	6.302
C ($mV\ s^{-1}$)	0.1484
Negative control ($mV\ s^{-1}$) [1]	0.005 ± 0.0027
LOD ($mV\ s^{-1}$)	0.014
LOQ ($mV\ s^{-1}$)	0.032
LOD (µM) [2]	206.0 µM
LOQ (µM) [2]	229.0 µM
Resolution (µM)[3]	3.44 µM

[1] From the PCa measurements. The composition of the control measurement remains the same.
[2] Converted using the linear model presented in this table. LOD and LOQ were adjusted according to the dilution factor therefore refer to the undiluted sample.
[3] Calculated as the ratio between the standard deviation of the control measurements and the sensitivity in the linear range [58]. The resolution was adjusted according to the dilution factor therefore refers to the undiluted sample.

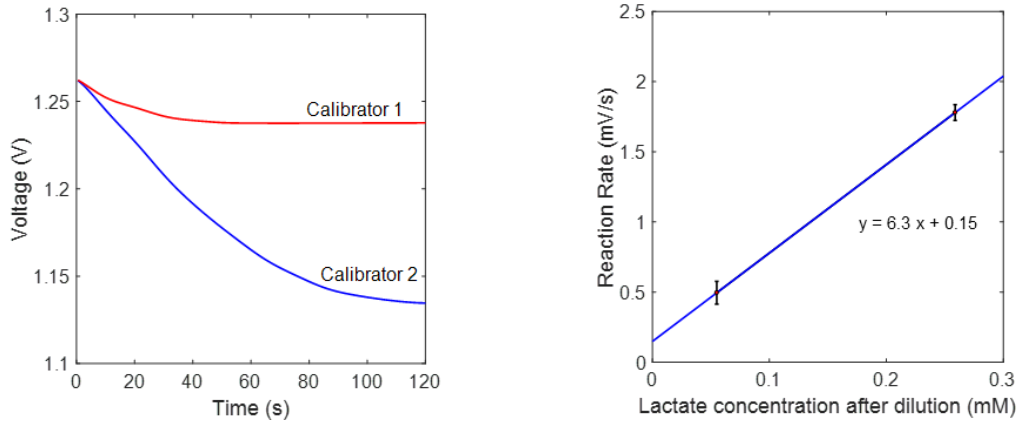

(a) (b)

Figure 6.10 Calibration data. (a) Output signals from single microchannels for calibrator 1 and calibrator 2. (b) Linear calibration curve resulting from the 2-points calibration procedure.

6.5.3. Clinical evaluation

Method. Lactate plasma level of the ischemic stroke samples was assessed using the developed platform. Lactate plasma levels in the samples were known during the experiments.

Results. Results are shown in Table 6.9. Concentrations were in the range of 0.40 – 2.52 mM. The average standard deviation of the measurements was 11.15%. Data normalised to the average is represented in Figure 6.11.

Table 6.9 Clinical evaluation results on ischemic stroke group.

Group	Sample ID	Lactate	
		Avg. mM	Std. %
Stroke	1	1.86	7.23
	2	1.73	7.69
	3	1.42	12.38
	4	1.01	10.37
	5	0.40	11.13
	6	1.36	13.27
	7	1.54	14.40
	8	1.07	17.45
	9	2.52	7.51
	10	1.11	10.07
Ischemic stroke group			
average (mM)		1.40	
median (mM)		1.39	
std. dev. (mM)		0.54	
Range (mM)		0.40 – 2.52	
Avg. environmental. Temp. (°C)		24.7 ± 0.4	
Avg. environmental humidity (%)		34.7 ± 2	

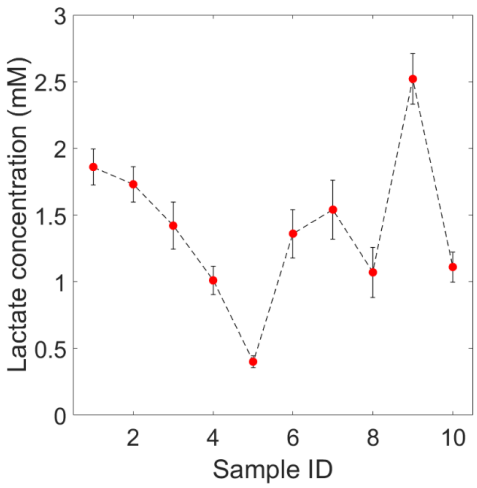

Figure 6.11 Normalised lactate concentrations for ischemic stroke samples

6.5.4. Validation against standard method

Method. Samples were independently tested in the Institute of Cardiovascular and Medical Sciences, University of Glasgow, routinely used by NHS, by trained personnel. These measurements were performed using the Cobas C 311 analyser form Roche Hitachi. The analyser was calibrated with a 2-points linear approach, using the same calibrator solutions. Both normalised datasets have been overlapped in Figure 6.12(a).

Results. The average lactate concentration determined with the gold standard measurement was 1.45 mM ± 0.39 mM. When comparing the average of the group obtained with both the methods, an average error of 50 µM was observed. The standard deviation of the measurements performed with the developed platform was 150 µM. When comparing the two datasets normalised to the respective average, a correlation coefficient R = 0.77 was observed. For this population, the average relative error of the platform when quantifying lactate with respect to the reference method was 27.8%.

A linear fitting was performed using the obtained measurement. The linear fit of the platform is compared to the ideal response in Figure 6.12(b). The correlation between the linear fitting of the platform measurements and the ideal response was $R^2 > 0.98$.

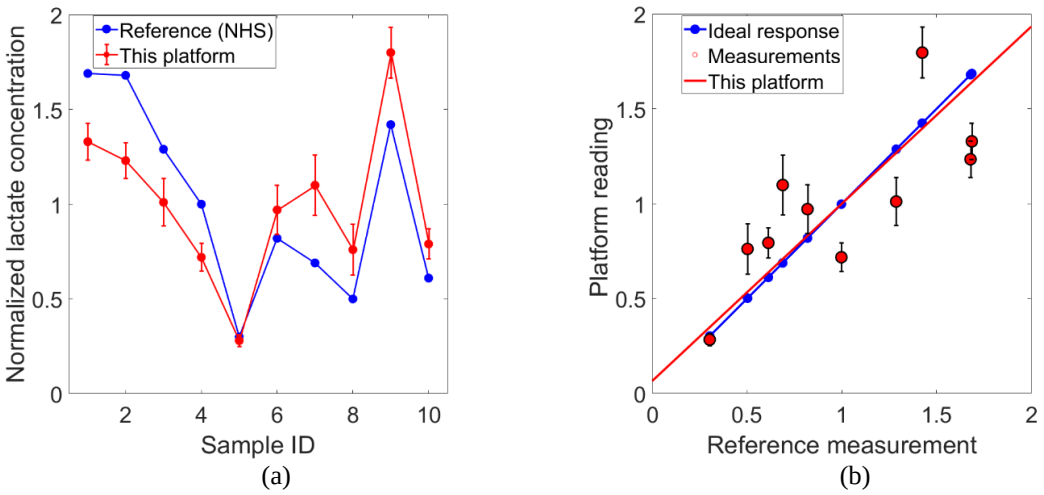

Figure 6.12 (a) Normalised gold standard measurement (blue) overlapped to the normalised measurements performed with the proposed platform (red) for lactate levels. (b) Platform response (red) compared to ideal response (blue).

6.5.5. Discussion

Clinical evaluation of ischemic stroke samples underlined the ability of the handheld setup to perform the measurements of a clinical biomarker with performance comparable to established practice. The handheld platform provided comparable values highlighting its potential for its use in resource-limited settings. The device used in the gold standard laboratory-based method (Cobas C 311 analyser from Roche Hitachi) is bulky (width: 1338 mm, depth: 855 mm, height: 1262 mm), heavy (weight: 270 kg), requires to be connected to the electric grid (230/400 Volts AC 50 Hz) and can only be operated by trained personnel [320]. Laboratory-centric systems also require patient admission into the hospital, sample collection, sample testing, result production and communication. These steps inevitably need additional time which might be not affordable in situations when the timing is crucial.

Differently, the platform has the potential to allow on-the-spot patient stratification in minutes. Thus, the precision and accuracy of the test might be de-prioritised, in favour of readiness of the result. Arguably, there are lactate meters already in the market, which could provide similar results. However, devices on the market only enable the determination of a single metabolite. This platform can be scaled for the determination of additional markers, like in the PCa clinical evaluation. Unfortunately, due to the small available volume, it was not possible to perform additional measurements for other metabolites. However, there is potential merit in using a panel of markers also for the stroke patients at the risk of other complications such as multiple organ failure. As previously mentioned, creatinine is another biomarker routinely used to monitor organ functions in ICU. Availability of data on a larger marker panel would enable comprehensive analysis of the patients at the higher risk of mortality. Clinical evaluation of ischemic stroke samples also has some of the limitations already outlined for PCa, including the lack of detailed information about the samples and the small size of the population.

6.6. Multiplexed Assay with Clinical Samples

Multiplexed assays were performed on two clinical samples from the prostate cancer study. This study aimed at demonstrating that the platform can perform simultaneous quantification of the proposed biomarker panel.

Materials and methods. Reagents were preloaded into the microchannels. Since sarcosine has been observed not to be a potential biomarker in the analysed population, it was omitted from the simultaneous assays. Instead of sarcosine, the remaining channel was used as a common negative control. The microchannels were functionalised in the following order from left to right: control, choline, glutamate, LAA. This sequence was selected to reduce any potential cross-contamination with other measurements. While the control channel was susceptible to crosstalk, LAA channel was expected to produce the highest absorbance drop. Thus, they were confined to the sides of the cartridge. Choline was expected to provide a lower absorbance drop than glutamate, so it was more suitable to be tested adjacently to the control. Four different solutions were prepared for drying into the microchannels for (i) negative control, (ii) choline assay, (iii) glutamate assay, (iv) LAA assay. The protocol for solution preparation is reported in Appendix I. 1 µL of each solution was deposited in the respective microchannel. The deposition was achieved by manual pipetting, but printing would have also been suitable. After the deposition of the solution, the cartridge was dried for 1 hour at room temperature in a vacuum chamber. Dried reagents slightly increased the light absorbance of the platform in the steady-state. Consequently, the intensity of the light produced by the LED was increased to keep the platform in its operating point.

Cartridges were used immediately after the drying step. 15 µL of clinically sourced human plasma samples were introduced into the cartridge with preloaded reagents without any further dilution step. Experiments were conducted in duplicates.

Results. Figure 6.13 demonstrates that the platform was suitable for measuring multiple metabolites simultaneously. Figure 6.13(a) and (c) show average data from each channel after processing. Figure 6.13(b) and (d) reports the average initial reaction rates calculated in each channel for the two samples under test.

As already discussed in Paragraph 5.5.1, it is not possible to directly compare the rates obtained with dried reagents with the one obtained with reagents in solution due to different working conditions. However, dried assays had high correlation with the results obtained in the clinical testing for all the metabolites and all the replicates ($R^2 > 0.91$). When comparing

rates normalised to the negative control from sample 3 (non-PCa group) with sample 15 (PCa group) for respective metabolites, rates were consistently higher for the PCa sample, corroborating data obtained during the clinical evaluation.

Discussion. The experiments demonstrated that the platform is suitable for multi-metabolite testing with preloaded reagents. Expectedly, higher variability was observed due to the reasons discussed in Paragraph 5.5.1. It is worth noticing that the estimation of the potential metabolic biomarker for PCa clinical evaluation was performed using positive and negative controls. Here, only a model-based substrate estimation can be achieved. An example of on-chip positive controls is presented in Figure 6.13(e). Channel 1 was functionalised for the negative control, as described above with the substitution of HRP 10 µL by DI water. The remaining channels were functionalised for LAA positive control using a solution obtained by mixing 6 µL of 25 mM LAA substrate, 4 µL of DI water, 10 µL of 150 U/mL HRP, 5 µL of 44.5 mM phenol and 5 µL of 10.5 mM 4AAP (total LAA concentration: 5 mM). 15 µL of human plasma was mixed off-chip with 10 µL of LAA (4 U/mL) and immediately introduced into the platform. Figure 6.13(e) demonstrates that the platform can perform positive controls to extrapolate sample-specific calibration. As expected, the lowest rate was detected for the channel functionalised for negative control. The remaining channels recorded a considerably high rate due to LAA substrate dried into the microchannels.

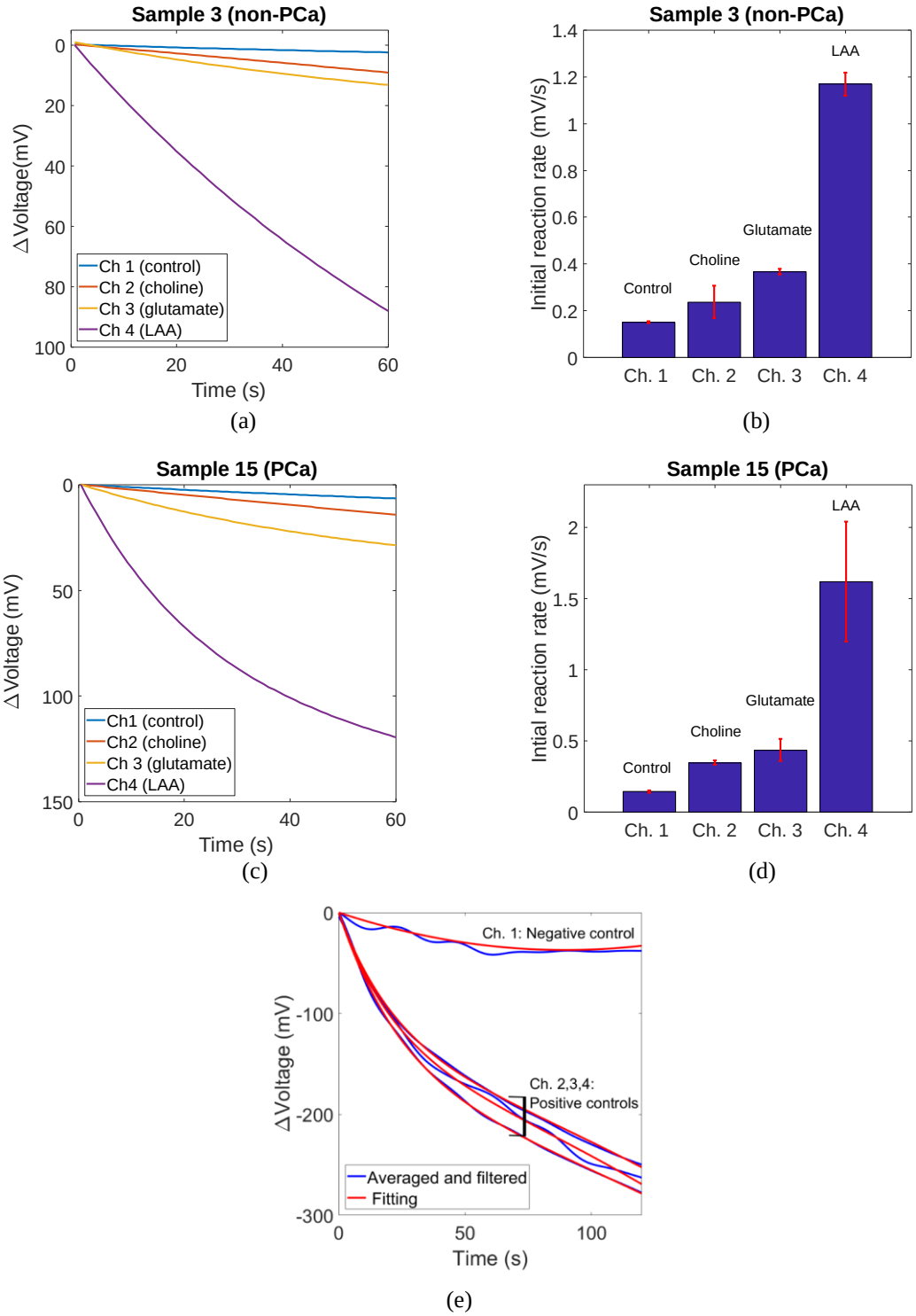

Figure 6.13 Simultaneous testing of PCa-related metabolites in clinical samples. (a) Output signals from each of the microchannel for sample 3 (non-PCa group). (b) Initial rate calculations in each of the microchannel for sample 3 (non -PCa group). (c) Output signals from each of the microchannel for sample 15 (PCa group). (d) Initial rate calculations in each of the microchannel for sample 15 (PCa group). (e) Simultaneous control measurements for LAA assay. Ch. 1 is functionalised for negative control. Ch. 3-4 are functionalised for positive control with known quantity of preloaded substrate.

6.7. Summary of the Chapter

- The platform was evaluated using clinical samples for both PCa and ischemic stroke aiming to quantify both clinical and analytical performance (see Table 6.10).
- For PCa, LAA, glutamate, choline and sarcosine were first quantified in undiluted human plasma for calibration and validation. Afterwards, the platform was used for the quantification of the metabolites panel over 10 healthy men and 16 patients affected by PCa. Measurements, which had comparable value with respect to commercially available methods, showed increased levels of LAA, glutamate and choline in the PCa group. Metabolic profiles were then used to train a weighted KNN algorithm with k-fold validation which scored AUC = 0.862. With the same specificity (around 0.86), the classifier had higher sensitivity than PSA in this population (0.64 vs 0.32). The sensitivity of the weighted KNN algorithm could also be increased to 0.95 when specificity was reduced to 0.68. Based on the PCa clinical evaluation, the platform demonstrated to potentially be capable of providing metabolic information with precision suitable to improve the current clinical standard and address the need for new and complementary diagnostic tools.
- For ischemic stroke, lactate was quantified in diluted human plasma from 10 subjects affected by an ischemic stroke. Results were compared with lactate levels measured by NHS after admission in the hospital. Measurements with the platform were in the range 0.4 – 2.52 mM and were comparable with the gold reference (R = 0.77). Gold reference measurements were acquired with bulky and expensive equipment. Based on the ischemic stroke clinical evaluation, the platform demonstrated to be potentially suitable for rapid and on-the-spot testing in acute medical events.
- Multi-metabolite testing was demonstrated using two clinical samples, respectively from the non-PCa and PCa groups. The four channels of the platform were functionalised with different reagents allowing to measure, at the same time, negative control, LAA, glutamate and choline. Output signals were consistent with measurements performed without lyophilising the reagents ($R^2 > 0.91$).

4557 *Table 6.10 Performance of the platform in clinically sourced human plasma.*

Criterion	This Platform	Reference
Diagnostic performance for prostate Cancer		
Approach	LAA, glutamate, choline 4 microchannels on CMOS Microchannel height ~ 290 µm	PSA is clinically used for PCa diagnosis and typically measured with laboratory equipment.
Sensitivity/Specificity	0.95/0.68 or[1] 0.64/0.86	0.32/0.86 [18]
Diagnostic performance for Ischemic stroke		
Approach	Lactate 4 microchannels on CMOS Microchannel height ~ 290 µm	Lactate is clinically used for ischemic stroke stratification and typically measured with laboratory equipment (e.g., Cobas C 311 analyser).
Sensitivity/Specificity	The same biomarker was used. Therefore, clinical capabilities depend on the analytical performance of the platform.	
Analytical performance		
Relative error of the measurements	LAA: 18.5%[2] Glutamate: 13.81%[2] Choline: 21.37%[3] Sarcosine: 44.4%[2] Lactate: 27.8%[4]	Glucose meters: <15% [16] Lactate meter: < 13 % [321]
LOD	LAA: 11.1 µM Glutamate: 1.4 µM Choline: 1.7 µM Sarcosine: 1.4 µM Lactate: 206.0 µM	Physiological ranges: LAA: 1.7 – 4.6 mM Glutamate: 40 – 150 µM Choline: 10 – 40 µM Sarcosine: 0 – 20 µM Lactate: 300 - 2000 µM
Resolution	LAA: 3.25 µM Glutamate: 0.45 µM Choline: 0.27 µM Sarcosine: 0.35 µM Lactate: 3.44 µM	Glucose meters: ~ 50 µM [322] Lactate meter: ~ 100 µM [323]
Sample volume	20 µL	Glucose meters: < 20 µL [16] Lactate meters: < 100 µL [324]
Test duration	2 - 5 min	Glucose meters: < 30s [16] Lactate meters: < 5 min [324]
Portability	Handheld	- Measurements for PCa and ischemic stroke are typically performed in a laboratory. - Other commercial POC devices (i.e. glucose and lactate meters) are handheld [16].
Multi-analyte capabilities	- 6 metabolites in diluted serum and 5 metabolites in human plasma were demonstrated. - 4 simultaneous assays were demonstrated. - The platform was used for 2 different applications. - The platform can supports further modalities (e.g. ISFET)	- Most of the POC devices on the market have single metabolite capabilities. - A small number of POC devices on the market have multi-metabolite capabilities (e.g. i-stat) [16].

[1] Different operating selected from the ROC can be used.
[2] Average value vs. fluorescent plate-based assays.
[3] Average value vs. ultra-performance liquid chromatography-tandem mass spectrometry.
[4] Average value vs. Cobas C 311 analyser (NHS equipment)

Chapter 7: Conclusion

7.1. Introduction

Metabolomics POC platforms have vast unexplored potential in modern society. POC testing aims at a different healthcare model which diverges from the classic laboratory-based approach and favours portable, rapid, on-the-spot, and low-cost testing.

This thesis illustrated the development of a POC platform used for the diagnosis of PCa and ischemic stroke using candidate metabolic biomarkers. The main achievements of this PhD research project are:

- The understanding of the CMOS sensor array chip designed and manufactured within the 'Multicorder project'. The chip was employed as the sensing unit in this project.
- The development of a cartridge, which integrated on the same ceramic package the CMOS chip, passive microfluidics, and biological reagents. Specifically:
  - A novel method for integrating microfluidics on the CMOS chip was conceived, developed, and tested.
  - A versatile method for bioreagents preloading, based on lyophilisation, was developed and tested on the chip.
  - A packaging procedure enabling the use of the cartridge in an aqueous environment was developed and tested.
- The development of a reader and a GUI for interfacing with the cartridge.
- The characterisation of all the units composing the POC platform: the sensor array, the microfluidics, the bioreagents, the reader and the GUI.
- The identification of two case-studies, namely PCa and ischemic stroke. Six potential metabolic biomarkers to identify these conditions were selected: LAA, glutamate, choline, sarcosine (for PCa), lactate and creatinine (for ischemic stroke).
- The development of colorimetric enzymatic assays for the on-chip quantification of the selected metabolic biomarkers.
- The characterisation of the platform for the quantification of all the six metabolites in diluted human plasma.
- The development of a scalable strategy for on-chip preloading of reagents involving the use of inkjet printing and lyophilisation.

- The demonstration of the potential use of the platform for simultaneous multi-metabolite testing achieved by preloading different reagents in different microfluidic channels on the same chip.
- The demonstration of alternative platform configurations, involving the use of paper microfluidics and on-chip sample processing.
- The clinical evaluation of the platform for PCa diagnosis on a population composed of 10 healthy samples and 16 men diagnosed with PCa.
- The clinical evaluation of the platform for ischemic stroke stratification on a population composed of 10 samples from patients affected by ischemic stroke.
- The demonstration of multi-analyte capabilities with clinically sourced human plasma.

The rest of this chapter discusses the main limitations of this research and presents some potential future works.

7.2. Limitations and Future Works

The limitations of this research project can be grouped into two categories: (i) limitations of the platform and (ii) limitations of the clinical studies. Accordingly, the research work has the potential for improvement in term of the electronic platform used as well as the biological experiments. Future works are here proposed for mitigating the effects of the limitations identified.

7.2.1. Technology limitations and future works

The limitations of the platform from a technology point of view and future works to mitigate their effects are discussed here.

CMOS chip limitations. The CMOS chip had a limited number of sensors. The geometry of the sensing platform, especially considering the position of the pads used for wire-bonds, limited the number of microchannels and the layout of the microfluidics. The CMOS chip had no embedded temperature sensor. The temperature of the sample is a relevant variable potentially affecting reagents activity. The design of a new CMOS chip integrating a larger sensor array and minimising the use of bonding pads (e.g. using serialised solutions) could be used to improve the accuracy of the measurement and/or increase the number of tests simultaneously performed on-chip. The integration of an on-chip temperature sensor to monitor the temperature of the sample within the microstructure has the potential to enable

strategies to compensate for temperature-related effects. The availability of a large area, for example by wire-bonding the CMOS chip to a PCB or the use of a different package, alongside with the planarization, can allow the implementation of more sophisticated microfluidic networks. The optimisation of the GUI, especially by developing software for all the major operative systems, would enable the sample-to-answer test with no user interaction. The use of wireless technologies, together with miniaturisation strategies, has the potential to improve the user-friendliness of the apparatus.

Assay formualtions. The formulation of the colorimetric assays did not satisfactorily investigate the use of cofactors, inhibitors, and stabiliser agents. The lyophilisation process was a disruptive process for the CMOS chip, which became unresponsive after a few processing cycles. This was a limitation for the reuse of the cartridges since the number of available chips was limited.

Additional works regarding the optimisation of the formulations and aiming to improve the shelf life of the reagents as well as the accuracy and precision of the platform are encouraged. A potential compensation strategy can, for example, employ the Arrhenius' law [325], [326]. This model could be used to estimate the loss of activity of the reagents due to storage time and condition and numerical compensation of the measured rate. The optimisation of the formulations used for colorimetric assays can be optimised to enhance stability, reliability, and sensitivity of the test. The use of cofactors and inhibitors, for instance, can be used to reduce sample-to-sample variability. The use of stabiliser agents can improve the shelf life of the reagents preloaded on the chip.

Sample pre-processing. The platform was mainly tested with processed samples. Although a feasibility study was demonstrated, further optimisation of the platform is required to reliably use unprocessed samples. A more elaborated microfluidics' network, integrating, for example, capillary pumps or gratings, can be necessary to develop a reliable strategy for on-chip blood filtration [327]. Finger-powered pumps can also be a viable solution [328]. The use of different H_2O_2 colorimetric dyes, working at a different wavelength, can also be a successful strategy for quantifying metabolites in unprocessed blood. Amplitie^{TM}, for instance, is a H_2O_2 colorimetric probe working at 650 nm and therefore should minimise the optical interference of whole blood.

Target analytes. The class of analytes which measured with the platform was limited to substrates which can be converted into H_2O_2 using specific enzymatic reactions.

Future work is also suggested to investigate other capabilities embedded onto the CMOS chip. Other researchers of the MST group are parallelly working using different integrated capabilities developed during the Multicorder project, including amperometry [45], fluorescent sensing [86], SPR [85] and pH sensing [85], [243], [251]. The combination of the findings has the potential to lead the way to multi-sensing POC platform [85]. The use of different sensing capability can also widen the class of analytes that can be quantified with the developed platform.

Affordability of the platform. In Table 2.11 maximum costs for reader and cartridge were set to £5200 and £10 – respectively – after comparison with POC platforms on the market. The reader can be manufactured at a cost largely lower than the requirement. The use of affordable off-the-shelf components and a simple custom PCB yield to an estimate price in the order of hundred pounds. However, the target cost of the cartridge was not met in this PhD work because cartridges were not produced in high-volume. This raises the question if the cartridge can meet the requirement when mass-produced.

Fabrication costs for the cartridge can be divided into 4 addends: (1) CMOS chip, (2) fluidics and packaging, (3) functionalization and (4) human work and instrumentation costs.

1. When mass-produced, the cost of CMOS technology can be dramatically reduced. Texas Instruments estimates that the cost per die for CMOS 0.35 μm technology can be as low as 2.7 £/cm^2 [329]. Considering the area of CMOS chip used in this work (12.24 mm^2), each CMOS chip would cost approximately £0.33 if mass-produced.
2. The chip could be packed onto a PCB slot (1x2 cm) rather than on a ceramic package. Such a PCB slot would cost approximately £0.1 each. For the fabrication of the fluidics, a SU-8 fabricated onto a 6-inch wafer would cost about £100. However, this would be allocating around 135 patterns which can be re-used at least 10 times. This results in £0.08 per pattern. SU-8 mould is used to fabricate a PDMS microstructure. Considering the cost of PDMS on the market (1.1 kg = £170) we estimate that each PDMS pattern would cost £0.04 per cartridge. Finally, epoxy (302-3M 1LB by Epoxy Technology Inc.) was used for the final microstructure and encapsulation. The estimated cost for epoxy is £0.1 per cartridge. In summary, the total cost for fluidics and packaging is estimated to be around £0.32 per cartridge.
3. Functionalization costs depend on the assay to be performed. The worst-case scenario is a choline assay, where 1 kU of ChOx costs £703 from Sigma. For 1 test, 1 μl of reaction solution with 200 U/ml of ChOx was used. This yield to approximately £0.2 per test. If

4 tests are run on the same cartridge, reagents for functionalisation will cost £0.8 per cartridge.

4. Human costs and equipment should include the amortization of equipment used for chip bonding, SU-8 mould fabrication and functionalisation. It is reasonable to assume a +200% cost for this addend.

In summary, the cost per cartridge when mass-produced is estimated to be £4.35. Retail price is likely to have a +100% surcharge. As such, a retail cost of £8.72 can be estimated. This figure falls within the cost required for the cartridge.

The cost of the cartridge depends on the application and could be reduced by simplifying the system. For instance, paper-strip based solutions (such as the one demonstrated in paragraph 5.5.2) can be used to reduce the cost for determined applications. However, based on the versatility requirement, the research team believed that a reduction of the functionalities of the platform was not advised at the prototypal stage. Optimisations aimed at cost reduction will be part of future works.

7.2.2. Limitations and future work of the clinical studies

The limitations of the platform concerning the biological experiments and future works to mitigate their effects are discussed here.

Population. For both clinical evaluations, the sample population was small. Relevant information on clinical samples was also missing ethical reasons.

Future works are encouraged on a larger population. Availability of data on a larger scale is necessary to potentially verify and generalise the findings. Additional details of the population, including age, ethnicity, co-morbidities, drug treatment, is necessary to understand possible interferences in the study. Larger trials with standardised protocol will be needed to confirm the validity of the platform and achieve medical approval.

Procedure. For both clinical evaluations, when metabolites were individually tested, samples were off-chip mixed with the reagent solution. Some commercial POC platforms are needing this procedure [296]. However, a pre-processing procedure should be avoided for a commercial POC platform for in-home use. Due to limited resources, cartridges were reused in this work, adopting appropriate cleaning procedures. However, the degradation of performance is possible after multiple tests. The reuse of the cartridges also increased the risk of cross-contamination. Appropriate metabolic quenching techniques (i.e. freezing) was

necessary. Plasma samples were frozen and contained anticoagulant agents. There is the possibility that sample storage and additives might have interfered with the measurements. Methods for future works need to be modified to mitigate several limitations of the clinical studies at the current state. Clinical studies should also be widened to cartridges with preloaded reagents, which would better mimic a real-life scenario. Ideally, a definitive disposable cartridge prototype embedding the technological improvement outlined above should be employed. The study should also include freshly collected samples, ideally seconds after the collection from a fingerpick.

Prostate Cancer. For PCa, the population of the studies included people with advanced disease. The advanced stage of the disease might have exacerbated the concentration of the metabolites. Also, healthy and control samples were collected from different institutions. Although protocols were in place to ensure the coherence of the study, there is the possibility that this introduced systematic errors in the groups. Furthermore, the performance of the classifier was characterised using the measured metabolic profile, which was averaged over biological triplicates.

Additional work is encouraged for improving the results achieved during clinical testing. For PCa, a more extensive clinical study also involving third parties laboratory is required to: (i) validate or modify the metabolic panel; (ii) validate the classification performance of the platform; (iii) consolidate the evidence that the developed platform can provide diagnostically relevant information. Accordingly, a more significant number of PCa samples and controls are required. Specifically, controls and PCa samples should be collected in the same clinic. Controls donors should be selected to have similar age and lifestyle than PCa samples. PCa donors should be selected in various stage of the disease. To consolidate the suitability of the platform for PCa detection, early-stage donors are particularly needed. Detailed information about PSA levels, eventual drug treatments, co-morbidities, ethnicity, are required. Validation with high-performance equipment, such as mass spectroscopy, is needed to characterise the platform performance. The robusticity of the classifier against single measurements needs to be quantified.

Ischemic stroke. For ischemic stroke, the analysed population included people after hospital admission for ischemic stroke. As for PCa clinical testing, the advanced state of the disease might have increased the metabolite levels which can potentially be different at an early stage. Also, due to limited resources, only one metabolite (i.e. lactate) was quantified in the available samples.

A larger clinical study also involving third parties laboratories is required to: (i) include additional metabolites in the panel, (ii) develop classification algorithms, (iii) consolidate the evidence that the platform can provide comparable results with NHS equipment. Consistently, a larger number of ischemic stroke samples are required. Control samples should be included too. Ischemic stroke samples should be selected in various stages of the cardiovascular event. People at high risk of developing ischemic stroke should also be analysed. Detailed information about the population would also be necessary. Validation with clinical standards, such as the Cobas C 311 analyser form Roche Hitachi, should be used to consolidate the performance of the platform. The use of additional metabolites alongside lactate and creatinine should also be analysed to develop classification procedure leading to a rapid on-the-spot patient stratification in emergency scenarios.

7.2.3. Additional potential applications

A multitude of potential users can take advantage of the developed platform in a variety of scenarios. Prospective users of the platform include the general population, healthcare (NHS) staff, insurance groups, pharmacies, drug companies, general practice (GP) surgeries, paramedics, private healthcare sector, researchers, care homes, social care, athletics bodies, online doctor, wellbeing monitoring, or online physicians.

The large variety of potential users opens countless opportunities for different metabolomics-based applications where the potential of metabolomics has been acknowledged. The use of a similar platform could be employed, for example, for the diagnosis of other cancer types, other CVDs, sepsis, kidney failure and dementia. Similarly, the platform can be used for the monitoring of chronic disease where treatment is already in place, for example, haemophilia or arthritis. Applications other than healthcare are also equally achievable. For instance, such a platform could be employed for personal wellbeing or environmental monitoring.

All the mentioned potential applications can be accommodated with minimal modification of the platform. The use of different reagents within the microfluidics chapter can target application-specific analytes. Similar chemistry and procedures (such as printing and lyophilisation) can be employed. Apart from the utilisation of different reagents, the platform would not require any substantial modification, which makes it ideal for a wide range of applications.

7.2.4. Towards a commercial device

The findings of this research partially contributed to the foundation of 'Multicorder DX limited', a University of Glasgow spin-off company [330]. Multicorder DX aims to bring technology for rapid and low-cost metabolic biomarkers quantification to the market [330]. The start-up, which to date filed three patents, is now in the process of securing new funding aiming to develop a commercial product [330]. In this frame, a working prototype of the platform was developed. The prototype is shown in Figure 7.1. Cartridges are interchangeable, disposable and can be functionalised in different ways to address various diseases. For improved storage, cartridges can be vacuum-sealed and labelled. The reader of the prototype has been reworked to facilitate the use of the device. A black box encloses both the PCB and the microcontroller board, which remain identical to the ones described in the dedicated section of Chapter 3. The box of the prototype encapsulates a light-emitting diode (LED) operating at 490 nm wavelength, and lenses for colorimetric sensing. The system is aligned so that collimated light is shone onto the active area of the cartridge. The box also encloses a top lid, which can be closed during the colorimetric assay, to exclude interference from ambient visible light when the reaction takes place. The black box enclosing the reader has been outsourced from a specialised company. The GUI works the same way as described in the dedicated section of this chapter. Only minor modifications of the layout have been performed to improve the usability onto a tablet device. The platform shown in the figure was not employed for any of the experiments reported in this thesis but was used for public and industrial engagements. It has been demonstrated in numerous events such as 'BIOCHIP: International Forum on Biochips & Biochip Solutions', Berlin 7-8.5.2019. The prototype provides a demonstration that the platform can be optimised for in-home use by non-trained users and can potentially become a commercial POC device. The presented POC device has the potential to lead the way for a new generation of diagnostic tools for low-cost, portable, rapid, and user-friendly disease-related multi-metabolite quantification.

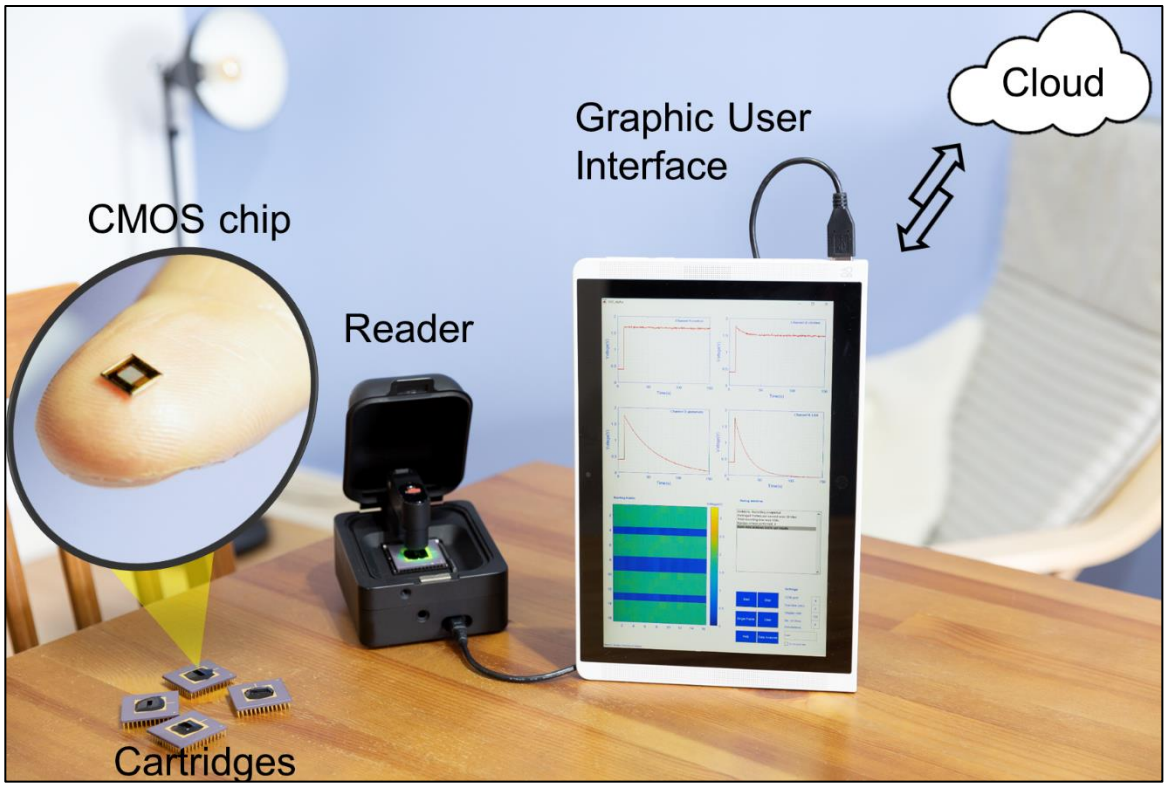

Figure 7.1 Working prototype of the platform

Appendix

A. Matlab Modelling of Colorimetric Reactions

This appendix illustrates a custom Matlab model for simulating colorimetric reactions. The model is based on the Michaelis-Menten model and Beer-Lambert's law. Model parameters have been reported in the thesis (Table 3.3). The model has been modified for performing other simulations reported in the thesis.

```
clear all
close all

Vm = 0.025;          % Value assumed from the literature in mM/s
km = 3;              % Value assumed from the literature in mM
% Initializations
N = 1000; c = zeros(1,N);  v = zeros(1,N); A = zeros(1,N); perT = zeros(1,N); d = zeros(1,N); t = linspace(0,120,N);
% Initial substrate concentrations in mM
concentrations = [0 0.01 0.02 0.03 0.04 0.05 0.075 0.1 0.125 0.15 0.2]
for z = 1:length(concentrations)
c(1) = concentrations(z);       % Initial concentration of the substrate
v(1) =  Vm*c(1)/(km+c(1));   % Initial reaction rate
d(1) = 0;                       % Initial concentration of the light absorbing species
T(1) = 100;                     % Initial transmission level
A(1) = 0;                       % Initial absornance level
ep = 7.5                        % @500nm for oxidised o-dionisidine (brown) - use L/mmol cm according to Sigma
l = 0.5;                        % optical length vector in cm

for j = 2:N
v(j) = Vm*c(j-1)/(km+c(j-1));           % Apply Michaelis-Menten
c(j) = c(1) - v(j)*t(j);                % Rate equation
d(j) = d(1) + v(j)*t(j);                % Rate equation
A(j) = ep*l*d(j);                       % Apply Beer-Lambert's law
T(j) = 1./10.^A(j);                     % Calculate transmittance
perT(j) = T(j)*100;                     % Calculate relative transmittance

if c(j) < 0 || c(j)>c(j-1)              % Break the loop when substrate concentration is zero
   c(j:N) = c(j-1).*ones(1,N-j+1);
   v(j:N) = v(j-1).*ones(1,N-j+1);
   A(j:N) = A(j-1).*ones(1,N-j+1);
   perT(j:N) = perT(j-1).*ones(1,N-j+1);
   d(j:N) = d(j-1).*ones(1,N-j+1);
   break
end

Absorbance(z,:) = A; Transmittance(z,:) = perT; % Save variables and repeat

end

clearvars -except t Vm km N c v A perT d t concentrations Absorbance Transmittance

end

% Graphic Rapresentation
figure(); plot(t,Transmittance'); axis('square'); ylim([50 105]); xlim([0.2 120]); xlabel('time (s)'); ylabel('Transmittance
(%)')
```

B. Microcontroller firmware (C++)

This appendix reports the custom C++ code implemented on the mbed board of the reader.

```
#include "mbed.h"
# include "delay.h"

PortOut PDcol(PortB, 0x0f00);          // Define 4 bits for columns addressing
PortOut PDrow(PortB, 0x00f0);          // Define 4 bits for row addressing
AnalogIn PD(PB_0);                     // Define pin for analog input
DigitalOut PDrst(PD_2);                // Define pin for reset signal
Serial pc(PC_4, PC_5);                 //Set pin for serial communication (USBTX, USBRX);

int main()
{
int i,j;
int  PDv;
pc.baud(921600);                       // Set baud rate
PDrst = 0;

while(1)
{
  PDrst = 1;                           // Reset
  PDcol.write(0);
  PDrow.write(0);
  wait(0.000500);                      // Pulse width
  PDrst = 0;
  PDv = 0;                             // Deliver starting frame sequence
  pc.putc(PDv>>8);                     // Send 32 zeros, 8 at a time
  pc.putc(PDv&0xff);
  pc.putc(PDv>>8);
  pc.putc(PDv&0xff);

  wait(0.020000);                       // Integration time

        for (i=0; i<16; i++) {

                PDrow.write(j<<4);// Address row

                for(j=0; j<16; j++) {

                        PDcol.write(j<<4);          // Address column
                        wait(0.000005);             // wait
                        PDv = PD.read_u16();        // Read and convert in 16  bits
                        pc.putc(PDv>>8);            // send first 8 bits (MSB)
                        pc.putc(PDv&0xff);          // send last 8 bits (LSB)
      }}}}
```

C. Extract of the data acquisition code (Matlab)

This appendix reports the custom Matlab code for data acquisition.

```
function pushbutton2_Callback(hObject, eventdata, handles) % RECORDING ROUTINE
% Tidy up_____________________________________________________
axes(handles.axes1); grid on; hold on; cla; axes(handles.axes2); grid on; hold on; cla;
axes(handles.axes3); grid on; hold on; cla; axes(handles.axes4); grid on; hold on; cla;
axes(handles.axes5); grid on; hold on; cla;
set(handles.text7,'String',''); set(handles.text8,'String',''); set(handles.text10,'String','');
set(handles.text9,'String','');
```

```
4928    % Start communication_____________________________________________
4929    instrreset; set(handles.togglebutton2, 'Value',0); COM =str2num(get(handles.edit2,'String'));
4930    uno = 'com'; due = num2str(COM); port = strcat(uno,due);
4931    one_frame = 516; N = 1; buff = one_frame*N;                         % in Bytes if PD@16bits
4932    MSB = (1:2:buff-2); LSB = (2:2:buff-1); clims = [5000 60000];
4933    frame = str2num(get(handles.edit1,'String'));
4934    display_rate = str2num(get(handles.edit3,'String'));                % if 1 display every display_rate
4935
4936    % Test Connection & Select pixel to display_____________________________
4937    try
4938    clu = 0; trial = 0; s = serial(port); s.InputBufferSize = 2*buff;
4939    set(s,'BaudRate',921600);
4940    fopen(s); %<----------------------------------------------------------------------% Open communication
4941    clear k SS index
4942    tic; trial = trial +1; flushinput(s);
4943    clc;
4944    k = fread(s); %<------------------------------------------------------------------  % Read data
4945    SS = movsum(k,4); index = find(SS==0); n_flags = length(index);     % Find frame start
4946            for y = 1:n_flags-1
4947            clu = (index(y+1)-index(y));
4948                    if clu == one_frame
4949                    frame_start  = index(y); frame_stop = index(y+1);
4950                    break
4951                    end
4952            end
4953            if trial == 100                                 % Try up to 100 times to get a valid frame
4954            break
4955            end
4956            toc
4957            end
4958    fclose(s) % <---------------------------------------------------------------------% Close communication
4959    % If connection is good go ahead, otherwise 'catch me' is exectured.
4960    str1 = 'Connected: Nice to meet you Multicorder Chip!';
4961    str2 = 'Choose 4 pixels to be shown during aquisition';
4962    new_str = strvcat(str1, str2);
4963    set(handles.listbox2,'String', new_str);
4964
4965    catch ME                        % An error in the communcation occurred. Display error accordingly.
4966    fclose (s); %<--------------------------------------------------------------------% Close communication
4967    str1 = 'Oooops something went wrong: I was not able to get data!';
4968    str2 = 'Check your connection/settings and try again.';
4969    new_str = strvcat(str1, str2); set(handles.listbox2,'String', new_str);
4970    pause()                         % Standby for new command
4971    end
4972
4973    % Test data handling
4974    try
4975    primo = k(frame_start+1:frame_stop-2); binarydata = dec2bin(primo,8);
4976    value = bin2dec([binarydata(MSB,:),binarydata(LSB,:)]);
4977    value = value*-1+2^16; axes(handles.axes1); cla; grid on; drawnow;
4978    mat = vec2mat(value,16);                % Plot test frame
4979    xlim([1,16]); ylim([1,16]); imagesc(mat,clims); colorbar;
4980    [colomn,row] = ginput(4)                % Select 4 pixels to be displayed
4981    colomn = round(colomn); row = round(row); clc;
4982    catch ME            % Error in data handling occurred. Display error accordingly.
4983    close (s) %<----------------------------------------------------------------------% Close communication
4984    str1 = 'Oooops something went wrong: I was not able to plot data!';
4985    str2 = 'Check your connection/settings and try again.';
4986    new_str = strvcat(str1, str2);
4987    set(handles.listbox2,'String', new_str);
4988    pause()
4989    end
4990
4991    % Data recording loop_____________________________________________________________
4992    % tidy up
```

```
4993  axes(handles.axes1); cla; colorbar('off'); set(handles.axes1,'visible','off'); set(handles.axes2,'visible','on');
4994  set(handles.axes3,'visible','on'); set(handles.axes4,'visible','on'); set(handles.axes5,'visible','on');
4995  set(handles.axes1,'visible','on'); axes(handles.axes1); grid on; hold on; cla; axes(handles.axes2); grid on; hold on; cla;
4996  axes(handles.axes3); grid on; hold on; cla; axes(handles.axes4); grid on; hold on; cla;
4997  axes(handles.axes5); grid on; hold on; cla; set(handles.text7,'BackgroundColor','white');
4998  set(handles.text7,'String',''); set(handles.text8,'BackgroundColor','white'); set(handles.text8,'String','');
4999  set(handles.text9,'BackgroundColor','white'); set(handles.text9,'String',''); set(handles.text10,'BackgroundColor','white');
5000  set(handles.text10,'String',''); drawnow
5001  % Initialisations
5002  try
5003  t = datetime('now');  Day_month_year = datestr(t); set(handles.text5,'String',Day_month_year )
5004  axes(handles.axes1); cla; grid on; xlim([1,16]); ylim([1,16]); colorbar; clear k
5005  p = NaN; pp = NaN; ppp = NaN; pppp = NaN;
5006  i_p = 1; i_pp = 1; i_ppp = 1; i_pppp = 1;
5007  time = ones(1,frame)*NaN;
5008  ch1 = 16*(row(1)-1)+colomn(1); ch2 = 16*(row(2)-1)+colomn(2); ch3 = 16*(row(3)-1)+colomn(3); ch4 = 16*(row(4)-
5009  1)+colomn(4);
5010  ad = get(handles.checkbox3, 'Value');
5011  s.InputBufferSize = buff;
5012  fopen(s); %<----------------------------------------------------------------------------% Open communication
5013  flushinput(s);
5014  set(handles.listbox2,'String', 'Recording...'); drawnow; tic;
5015          for i=1:frame-1
5016          k((i-1)*buff+1:buff*i) = fread(s);  %<--------------------------------------% Read frame
5017          time(i) = toc; %<-----------------------------------------------------------% Save time label frame
5018                  if ad == 1
5019                  P = sprintf('Progress : %2.1f/100',i/frame*100); set(handles.listbox2,'String',P); drawnow;
5020                  end
5021                  if get(handles.togglebutton2, 'Value') == 1 break; end
5022                  if (rem(i, display_rate) == 0)&&(ad==0)
5023                      if get(handles.togglebutton3, 'Value') == 1
5024                         % Clean the axes
5025                         axes(handles.axes2); cla; grid on;hold on; axes(handles.axes3); cla; grid on;hold on;
5026                         axes(handles.axes4); cla; grid on;hold on; axes(handles.axes5); cla; grid on;hold on;
5027                         axes(handles.axes1); cla; grid on; hold on; set(handles.togglebutton3, 'Value',0);
5028                      end
5029                  % Manipulate date for plotting
5030                  temp  = k(end-1027:end);
5031                  index = find(movsum(temp,2)==0);
5032                  current_frame = temp(index(1)+1:index(1)+512);
5033                  value = (current_frame(MSB).*2^8+current_frame(LSB))*-1+2^16;
5034                  mat = vec2mat(value,16); i_p = i-display_rate;
5035                  % Plot current frame
5036                  d = value(ch1); dd = value(ch2); ddd = value(ch3); dddd = value(ch4);
5037                  axes(handles.axes2); plot([i_p, i], [p,d], '.-b'); set(handles.text7,'String',d);
5038                  axes(handles.axes3); plot([i_p, i], [pp,dd], '.-r'); set(handles.text8,'String',dd);
5039                  axes(handles.axes4); plot([i_p, i], [ppp,ddd], '.-k'); set(handles.text9,'String',ddd);
5040                  axes(handles.axes5); plot([i_p, i], [pppp,dddd], '.-g'); set(handles.text10,'String',dddd);
5041                  axes(handles.axes1); imagesc(mat,clims); drawnow;
5042                  p = d; pp = dd; ppp = ddd; pppp = dddd; % Save save
5043          end
5044  end
5045  a = toc;                % Total recording time
5046  fps = i/a;  % Average frame per second
5047  fclose(s); % <---------------------------------------------------------------------% Close communication
5048  catch ME % In case of error save automatically and give error
5049     uisave;     % <-------------------------------------------------------------------% Save
5050     fclose(s); % <---------------------------------------------------------------------% Close communication
5051     str1 = 'Oooops something went during the recording!';
5052     str2 = 'You can save anyway your data (not handled).';
5053     new_str = strvcat(str1, str2);
5054     set(handles.listbox2,'String', new_str);
5055  end
5056  % Confirm recording completed
5057  str1 = 'Welldone, Recording completed!!'; str2 = 'Averaged frames per second was:';
5058  str3 = num2str(fps); str4 = 'Total recording time was (sec):';
```

```
str5 = num2str(a); new_str = strvcat(str1, str2,str3, str4,str5); set(handles.listbox2,'String', new_str);

% Data handling _____________________________________________________________
%Find flags
S = movsum(k,2); index = find(S==0); j = 1;
% Search and exclude invalid frames
for i = 1:length(index)-1
        if (index(i+1)-index(i)) == one_frame;  good_index(j) = index(i);  j = j+1; end
end
clear index; index = good_index;
% Extract frames and convert
for i = 1:length(index)-1
   frame_rec = k(index(i)+1:index(i)+512); binarydata = dec2bin(frame_rec,8);
   value = bin2dec([binarydata(MSB,:),binarydata(LSB,:)]); value = value*-1+2^16; data(:,i) = value;
   clear value frame_rec binarydata
end
% Exclude time-lables of invalid frames
good_time = time(floor(good_index(1:end-1)/514)+1);
% Plot final data
axes(handles.axes2); cla; plot(data((16*(row(1)-1)+colomn(1)),:)); axes(handles.axes3); cla; plot(data((16*(row(2)-
1)+colomn(2)),:)); axes(handles.axes4); cla; plot(data((16*(row(3)-1)+colomn(3)),:));
axes(handles.axes5); cla; plot(data((16*(row(4)-1)+colomn(4)),:));
% Save
NoC = get(handles.edit4,'String'); Notes = get(handles.edit5,'String');
clearvars -except data fps good_time k Day_month_year time NoC Notes
B = datestr(datetime('now'), 30); yyyy = B(1:4); mm = B(5:6); dd = B(7:8); hh = B (10:11); minu = B (12:13); sec = B
(14:15); div1 = '-'; div2 = '_'; titolo = horzcat([yyyy, div1, mm,div1, dd, div2, hh, div1, minu, div1, sec]);
uisave({'data', 'fps', 'good_time', 'k', 'Day_month_year', 'time','titolo','NoC','Notes'},titolo) % <---% Save
```

D. Extract of the data processing Code (Matlab)

This appendix reports the custom Matlab code for data processing.

```
% Initialisation_____________________________________________________________
Clc; clearvars -except dark eps L data Day_month_year fps good_time NoC Notes titolo; close all;
seconds = 10; dark = 0.3989; %Volts eps = 10000; %M-1cm-1 L = 0.027; %cm-1 start_after_x_seconds= 10;
Niir = 8; Fst = 0.05; Fs = fps; % Filter settings SP1 = 0;SP2 = 0;SP3 = 0;SP4 = 0;
% default structure with 4 channels
ch1 = 1:16*3; wall1 = 16*3+1:16*4; ch2 = 16*4+1:16*7; wall2 = 16*7+1:16*9; ch3 = 16*9+1:16*12; wall3 =
16*12+1:16*13; ch4 = 16*13+1:16*16;

% Pixel inspection and exclusion_____________________________________________
pix = 1:256;  data_label = [pix', data];

% Channel 1
figure(99); plot(data_label(ch1,:)'); plotedit on; title('channel 1'); xlim = [2,size(data_label,2)]; pause()
figure(99); a = get(gca,'Children'); ydata = get(a, 'YData'); close all; ch1_default = ch1; clear ch1;
for i=1:size(ydata,1)
   temp = ydata{i,1};    ch1(i) = temp(1);
end
clear ydata;

% Channel 2
figure(99); plotedit on; plot(data_label(ch2,:)'); title('channel 2'); xlim = [2,size(data_label,2)]; pause()
figure(99); a = get(gca,'Children'); ydata = get(a, 'YData'); close all; ch2_default = ch2; clear ch2;
for i=1:size(ydata,1)
   temp = ydata{i,1};     ch2(i) = temp(1);
end
clear ydata;

% Channel 3
figure(99); plot(data_label(ch3,:)'); plotedit on; title('channel 3'); xlim = [2,size(data_label,2)]; pause()
```

```
figure(99); a = get(gca,'Children'); ydata = get(a, 'YData'); close all; ch3_default = ch3; clear ch3;
for i=1:size(ydata,1)
    temp = ydata{i,1};    ch3(i) = temp(1);
end
clear ydata;

% Channel 4
figure(99); plot(data_label(ch4,:)'); plotedit on; title('channel 4'); xlim = [2,size(data_label,2)]; pause()
figure(99); a = get(gca,'Children'); ydata = get(a, 'YData'); close all; ch4_default = ch4; clear ch4;
for i=1:size(ydata,1)
    temp = ydata{i,1};    ch4(i) = temp(1);
end
clear ydata;

% Pixel map
map=zeros(1,16*16); map(ch1)=1; map(ch2)=2; map(ch3)=3; map(ch4)=4;
figure(); imagesc(vec2mat(map,16)); colormap('Jet'); title('Pixel map');
% convert and normalize
data1 = data(ch1,:)*3.3/2^16-dark; data2 = data(ch2,:)*3.3/2^16-dark;
data3 = data(ch3,:)*3.3/2^16-dark; data4 = data(ch4,:)*3.3/2^16-dark;
% Spatial average
medio1 = mean(data1); medio2 = mean(data2);medio3 = mean(data3); medio4 = mean(data4);
stand1 = std(data1'); stand2 = std(data2'); stand3 = std(data3'); stand4 = std(data4');
figure(); plot(good_time, medio1); hold on; plot(good_time, medio2); plot(good_time, medio3); plot(good_time,
medio4); legend('ch1','ch2','ch3','ch4');

% Select starting point_____________________________________________________
% Ch1
figure(); plot(medio1);hold on; plot(medio1,'or'); title('Channel 1'); zoom on; waitfor(gcf, 'CurrentCharacter',
char(13));zoom reset; zoom off; [x1,y1] = ginput(1);
% Ch2
figure(); plot(medio2);hold on; plot(medio2,'or'); title('Channel 2'); zoom on; waitfor(gcf, 'CurrentCharacter',
char(13));zoom reset; zoom off; [x2,y2] = ginput(1);
%Ch3
figure(); plot(medio3);hold on; plot(medio3,'or'); title('Channel 3'); zoom on; waitfor(gcf, 'CurrentCharacter',
char(13));zoom reset; zoom off; [x3,y3] = ginput(1);
%Ch4
figure(); plot(medio4);hold on; plot(medio4,'or'); title('Channel 4'); zoom on; waitfor(gcf, 'CurrentCharacter',
char(13));zoom reset; zoom off; [x4,y4] = ginput(1);

% Processing Ch1_____________________________________________________
% Filtering
x= round(x1); filt_this  = data1(:,x:end);
iir = designfilt('lowpassiir','FilterOrder',Niir,'HalfPowerFrequency',Fst,'SampleRate',Fs);
for j = 1:size(filt_this,1)
            data_filt(j,:) = filtfilt(iir,filt_this(j,:));
end
% Match the initial value
time = good_time(x:end)-good_time(x); off = mean(data_filt(:,1:250),2); off_mode = mean(off); adj = off - off_mode;
data_filt = data_filt - repmat(adj,1,size(data_filt,2));
SP1 = off_mode;
% Spatial average
step = floor(fps*1); medio = mean(data_filt,1);
%Crop
temp = find(time>330); try five = temp(1); catch  five = find(medio == medio(end-step)); end
% Temporal average
k = 1;
for j = 1:step:length(medio(1:five))
    mediot(k) = mean(medio(1,j:j+step)); timet(k) = mean(time(j:j+step)); k = k + 1;
end
% Calculate Rates in defined windows; do not start rate calculation from 0; start from si. This would avoid discrepances
between average and fitted data at the end point
si = min(find(timet>start_after_x_seconds));

% Process over 30 seconds
window = 30+2*start_after_x_seconds;
```

```
5187    % Curve fitting
5188    try end_pointt = find(timet>window); end_point = end_pointt(1);
5189    catch end_point = find(mediot == mediot(end)); end
5190    [xData, yData] = prepareCurveData( timet(1:end_point), mediot(1:end_point)); ft = fittype( 'exp2' );
5191    opts = fitoptions( 'Method', 'NonlinearLeastSquares' ); opts.Display = 'Off'; opts.Robust = 'LAR';
5192    [fitresult, gof] = fit( xData, yData, ft, opts ); timef_30s = timet(1:end_point); fitted_30s = feval(fitresult, xData);
5193    % Transmittance, Absorbance
5194    T_30s = fitted_30s./fitted_30s(1); A_30s = -log10(T_30s); i30 = min(find(timet>(30+si)));
5195    if isempty(i30) == 1 i30 = -si; end
5196    % Rates
5197    index = i30 ;P = polyfit(timet(si:index),mediot(si:index),1); R30 = P(1)*1000; clear P; % On average
5198    P = polyfit(timef_30s(si:index),fitted_30s(si:index)',1); F30 = P(1)*1000; clear P; % On fitting
5199    P = polyfit(timet(si:index),T_30s(si:index)',1); T30 = P(1)*1000; clear P; % On Trasmittance
5200    P = polyfit(timet(si:index),A_30s(si:index)',1); A30 = P(1)*1000; clear P; % On Absorbance
5201
5202    % Process over 60 seconds
5203    window = 60+2*start_after_x_seconds;
5204    % Curve fitting
5205    try end_pointt = find(timet>window); end_point = end_pointt(1);
5206    catch end_point = find(mediot == mediot(end)); end
5207    [xData, yData] = prepareCurveData( timet(1:end_point), mediot(1:end_point)); ft = fittype( 'exp2' );
5208    opts = fitoptions( 'Method', 'NonlinearLeastSquares' ); opts.Display = 'Off'; opts.Robust = 'LAR';
5209    [fitresult, gof] = fit( xData, yData, ft, opts ); timef_60s = timet(1:end_point); fitted_60s = feval(fitresult, xData);
5210    % Transmittance, Absorbance
5211    T_60s = fitted_60s./fitted_60s(1); A_60s = -log10(T_60s);  i60 = min(find(timet>(60+si)));
5212    if isempty(i60) == 1 i60 = -si; end
5213    index = i60; P = polyfit(timet(si:index),mediot(si:index),1); R60 = P(1)*1000; clear P; % On average
5214    P = polyfit(timef_60s(si:index),fitted_60s(si:index)',1); F60 = P(1)*1000; clear P; % On fitting
5215    P = polyfit(timet(si:index),T_60s(si:index)',1); T60 = P(1)*1000; clear P; % On Trasmittance
5216    P = polyfit(timet(si:index),A_60s(si:index)',1); A60 = P(1)*1000; clear P; % On Absorbance
5217
5218    % Process over 90 seconds
5219    window = 90+2*start_after_x_seconds;
5220    % Curve fitting
5221    try end_pointt = find(timet>window); end_point = end_pointt(1);
5222    catch end_point = find(mediot == mediot(end)); end
5223    [xData, yData] = prepareCurveData( timet(1:end_point), mediot(1:end_point)); ft = fittype( 'exp2' );
5224    opts = fitoptions( 'Method', 'NonlinearLeastSquares' ); opts.Display = 'Off'; opts.Robust = 'LAR';
5225    [fitresult, gof] = fit( xData, yData, ft, opts ); timef_90s = timet(1:end_point); fitted_90s = feval(fitresult, xData);
5226    % Transmittance, Absorbance
5227    T_90s = fitted_90s./fitted_90s(1); A_90s = -log10(T_90s); i90 = min(find(timet>(90+si)));
5228    if isempty(i90) == 1 i90 = -si; end
5229    index = i90; P = polyfit(timet(si:index),mediot(si:index),1); R90 = P(1)*1000; clear P; % On average
5230    P = polyfit(timef_90s(si:index),fitted_90s(si:index)',1); F90 = P(1)*1000; clear P; % On fitting
5231    P = polyfit(timet(si:index),T_90s(si:index)',1); T90 = P(1)*1000; clear P; % On Trasmittance
5232    P = polyfit(timet(si:index),A_90s(si:index)',1); A90 = P(1)*1000; clear P; % On Absorbance
5233
5234    % Process over 120 seconds
5235    window = 120+2*start_after_x_seconds;
5236    % Curve fitting
5237    try end_pointt = find(timet>window); end_point = end_pointt(1);
5238    catch end_point = find(mediot == mediot(end)); end
5239    [xData, yData] = prepareCurveData( timet(1:end_point), mediot(1:end_point)); ft = fittype( 'exp2' );
5240    opts = fitoptions( 'Method', 'NonlinearLeastSquares' ); opts.Display = 'Off'; opts.Robust = 'LAR';
5241    [fitresult, gof] = fit( xData, yData, ft, opts ); timef_120s = timet(1:end_point); fitted_120s = feval(fitresult, xData);
5242    % Transmittance, Absorbance
5243    T_120s = fitted_120s./fitted_120s(1); A_120s = -log10(T_120s); i120 = min(find(timet>(120+si)));
5244    if isempty(i120) == 1 i120 = -si; end
5245    index = i120; P = polyfit(timet(si:index),mediot(si:index),1); R120 = P(1)*1000; clear P; % On average
5246    P = polyfit(timef_120s(si:index),fitted_120s(si:index)',1); F120 = P(1)*1000; clear P; % On fitting
5247    P = polyfit(timet(si:index),T_120s(si:index)',1); T120 = P(1)*1000; clear P; % On Trasmittance
5248    P = polyfit(timet(si:index),A_120s(si:index)',1); A120 = P(1)*1000; clear P; % On Absorbance
5249
5250    % Process over 300 seconds
5251    window = 300+2*start_after_x_seconds;
5252    % Curve fitting
```

```
try end_pointt = find(timet>window); end_point = end_pointt(1);
catch end_point = find(mediot == mediot(end)); end
[xData, yData] = prepareCurveData( timet(1:end_point), mediot(1:end_point)); ft = fittype( 'exp2' );
opts = fitoptions( 'Method', 'NonlinearLeastSquares' ); opts.Display = 'Off'; opts.Robust = 'LAR'; [fitresult, gof] = fit(
xData, yData, ft, opts ); timef_300s = timet(1:end_point); fitted_300s = feval(fitresult, xData);
% Transmittance, Absorbance
T_300s = fitted_300s./fitted_300s(1); A_300s = -log10(T_300s); i300 = min(find(timet>(120+si)));
if isempty(i300) == 1 i300 = -si; end
index = i300; P = polyfit(timet(si:index),mediot(si:index),1); R300 = P(1)*1000; clear P; % On average
P = polyfit(timef_300s(si:index),fitted_300s(si:index)',1); F300 = P(1)*1000; clear P; % On fitting
P = polyfit(timet(si:index),T_300s(si:index)',1); T300 = P(1)*1000; clear P; % On Trasmittance
P = polyfit(timet(si:index),A_300s(si:index)',1); A300 = P(1)*1000; clear P; % On Absorbance
Rates = [SP1, R30, R60, R90, R120, R300; SP1, F30, F60, F90, F120, F300; SP1, T30, T60, T90, T120, T300; SP1, A30,
A60, A90, A120, A300];

%Graphical Representations
figure(); plot(time, filt_this,'k'); hold on; plot(timet,mediot,'b'); plot(timef_300s,fitted_300s,'g');
plot(timef_30s,fitted_30s,'r') legend('Raw pixels', 'blue - Filtered & Averaged', 'Red - Fitted 30s', 'Green - Fitted 5min')

% Save variables and clean
start1 = x;                 %Starting point
time1 = time;               %Re-scaled time axis
data_filt1 = data_filt;     %Filtered data
medio1 = medio;             %Spatial average
mediot1 = mediot;           %Spatio-temporal average
timet1 = timet;             % Re-scaled axis for spatio-temporal axis
T1 = T_300s;                % Transmittance
A1 = A_300s;                % Absorbance
Rates1=Rates;
%Line 1 in mV/s; Line 2 in mV/s using fitted data; Line 3 in %/s, Line 4 in absorbance units/s
fitted1 = fitted_300s;      % Fitted data
timef1 = timef_300s;        % Time diagram for fitted signal
clearvars -except dark eps L data Day_month_year fps good_time NoC Notes titolo ...
   x1 x2 x3 x4 data1 data2 data3 data4 SP1 SP2 SP3 SP4...
   start1 time1 timet1 data_filt1 medio1 mediot1 T1 A1 Rates1 fitted1 timef1...
   Niir Fst Fs start_after_x_seconds

% Processing Ch2_____________________________________________________________
x= round(x2); filt_this  = data2(:,x:end);
{ …} Code is here omitted, been very similar to the one reported for channel 1.
% Save variables and clean
start2 = x;                 %Starting point
time2 = time;               %Re-scaled time axis
data_filt2 = data_filt;     %Filtered data
medio2 = medio;             %Spatial average
mediot2 = mediot;           %Spatio-temporal average
timet2 = timet;             % Re-scaled axis for spatio-temporal axis
T2 = T_300s;                % Transmittance
A2 = A_300s;                % Absorbance
Rates2 = Rates;             % Rates
fitted2 = fitted_300s;      % Fitted data
timef2 = timef_300s;        % Time diagram for fitted signal
clearvars -except dark eps L data Day_month_year fps good_time NoC Notes titolo ...
   x1 x2 x3 x4 data1 data2 data3 data4 SP1 SP2 SP3 SP4...
   start1 time1 timet1 data_filt1 medio1 mediot1 T1 A1 Rates1 fitted1 timef1...
   start2 time2 timet2 data_filt2 medio2 mediot2 T2 A2 Rates2 fitted2 timef2...
   Niir Fst Fs start_after_x_seconds

% Processing Ch3_____________________________________________________________
x= round(x3); filt_this  = data3(:,x:end);
{ …} Code is here omitted, been very similar to the one reported for channel 1.
% Save variables and clean
start3 = x;                 %Starting point
time3 = time;               %Re-scaled time axis
data_filt3 = data_filt;     %Filtered data
medio3 = medio;             %Spatial average
```

```
mediot3 = mediot;              %Spatio-temporal average
timet3 = timet;                % Re-scaled axis for spatio-temporal axis
T3 = T_300s;                   % Transmittance
A3 = A_300s;                   % Absorbance
Rates3 = Rates;                %Rates
fitted3 = fitted_300s;         % Fitted data
timef3 = timef_300s;           % Time diagram for fitted signal
clearvars -except dark eps L data Day_month_year fps good_time NoC Notes titolo ...
   x1 x2 x3 x4 data1 data2 data3 data4 SP1 SP2 SP3 SP4...
   start1 time1 timet1 data_filt1 medio1 mediot1 T1 A1 Rates1 fitted1 timef1...
   start2 time2 timet2 data_filt2 medio2 mediot2 T2 A2 Rates2 fitted2 timef2...
   start3 time3 timet3 data_filt3 medio3 mediot3 T3 A3 Rates3 fitted3 timef3...
   Niir Fst Fs start_after_x_seconds

% Processing Ch4_____________________________________________________________
x= round(x4); filt_this  = data4(:,x:end);
{ …} Code is here omitted, been very similar to the one reported for channel 1.
% Save variables and clean
start4 = x;                    %Starting point
time4 = time;                  %Re-scaled time axis
data_filt4 = data_filt;        %Filtered data
medio4 = medio;                %Spatial average
mediot4 = mediot;              %Spatio-temporal average
timet4 = timet;                % Re-scaled axis for spatio-temporal axis
T4 = T_300s;                   % Transmittance
A4 = A_300s;                   % Absorbance
Rates4 = Rates;                % Rates
fitted4 = fitted_300s;         % Fitted data
timef4 = timef_300s;           % Time diagram for fitted signal
clearvars -except dark eps L data Day_month_year fps good_time NoC Notes titolo ...
   x1 x2 x3 x4 data1 data2 data3 data4 SP1 SP2 SP3 SP4...
   start1 time1 timet1 data_filt1 medio1 mediot1 T1 A1 Rates1 fitted1 timef1...
   start2 time2 timet2 data_filt2 medio2 mediot2 T2 A2 Rates2 fitted2 timef2...
   start3 time3 timet3 data_filt3 medio3 mediot3 T3 A3 Rates3 fitted3 timef3...
   start4 time4 timet4 data_filt4 medio4 mediot4 T4 A4 Rates4 fitted4 timef4...
  Niir Fst Fs start_after_x_seconds

% Show and save_____________________________________________________________
Rates = [Rates1, Rates2, Rates3, Rates4];
figure(); title('PD Output (mV)'); plot(timef1,fitted1); hold on; plot(timef2,fitted2); plot(timef3,fitted3);
plot(timef4,fitted4); figure(); title('Transmittance and Absorbance'); yyaxis left; plot(timef1,T1,'b-o'); hold on;
plot(timef2,T2,'b-v'); plot(timef3,T3,'b-s'); plot(timef4,T4,'b-p'); yyaxis right; plot(timef1,A1,'r-o'); hold on;
plot(timef2,A2,'r-v') plot(timef3,A3,'r-s'); plot(timef4,A4,'r-p'); uisave;
```

E. Contact angle measurements

The capillary pressure within a passive microfluidic channel depends on the cosine of the contact angles of the employed materials. The static contact angle θ is one of the conventional ways to measure the wettability of a material. It is defined as the angle that encompasses a liquid between two interfaces with materials in the solid and vapour phase. Figure E.1 (a)-(c) shows static contact angles for hydrophobic (θ > 90°) and hydrophilic (θ < 90°) surfaces, as well as the case of θ = 90°. Aiming to maximise the capillary pressure, hydrophobic and hydrophilic materials can both be employed, as long as their contact angle is as far as possible from 90°.

PDMS is a slightly hydrophobic material with static water contact angle ranging from 100° to 110°, but its wettability can be modified [285]. Exposure of PDMS to oxygen plasma gives the material super hydrophilic properties (θ<10°) [285]. Unfortunately, this surface modification is only temporary, and the surface recovers its hydrophobic behaviour in a few hours [285]. Polyvinyl alcohol (PVA) deposition on PDMS is another method for the surface modification of PDMS. Authors in [285] show that PVA-coated PDMS has a permanent hydrophilic behaviour with a contact angle in the range 20°- 40° [285]. The recipe reported in [285] has been replicated in this PhD research project. Epoxy resin materials have a slight hydrophobic/hydrophilic behaviour depending on the recipe [290].

A custom setup was developed to measure the contact angle of the materials employed in the fabrication and is schematically shown in Figure E.1 (d). The experimental setup consisted of a digital microscope (Dino-Lite AD4113T-I2V) mounted onto the z-axis, used to take micrographs of a 10 µL drop of water deposited onto the surface. A Matlab-based script was written to: (i) identify the droplet, (ii) fit the droplet shape with an elliptical model, (iii) identify the liquid-solid interface, (iv) calculate the tangent to the ellipse from the surface interface, and (v) compute the contact angle. The script used for the determination of the contact angle is reported below. The custom setup for contact angle measurements was utilised for estimating the wettability of untreated PDMS, PVA-modified PDMS according to the recipe in [285], epoxy resin and the CMOS chip. Figure E.1 (e)-(h) show pictures of the measurements conducted with the custom setup. It is interesting noticing that the CMOS chip has a slight hydrophilic behaviour, probably related to its irregular surface.

```
RGB = imread('Z:\Digital microscope\2019_01_10\contact angle\epoxy.jpg');
figure(1)
title('select area of interest')
imshow(RGB); drawnow; re = getrect; close(figure(1))
RGB_cut = RGB(re(2):re(2)+re(4),re(1):re(1)+re(3),1);

clear RGB; RGB = RGB_cut;

figure(1); imshow(RGB); title('Select point 1 of the substrate'); drawnow;
zoom on; waitfor(gcf, 'CurrentCharacter', char(13)); [xx1,yy1] = ginput(1); close(figure(1))

figure(1); imshow(RGB); title('Select point 2 of the substrate') ;drawnow; zoom on; waitfor(gcf, 'CurrentCharacter',
char(13)); [xx2,yy2] = ginput(1); close(figure(1))

figure(1); imshow(RGB); hold on; coefficients = polyfit([xx1, xx2], [yy1, yy2], 1); a = coefficients (1);
b = coefficients (2); xx = 1:size(RGB,2); yy = a.*xx+b; hold on; plot(xx,yy,'r','LineWidth',6)
title('Drop under test and substrate definition'); close(figure(1))

figure(1); imshow(RGB); drawnow; title('Select multiple points on the edge of the drop')
zoom on; waitfor(gcf, 'CurrentCharacter', char(13)); poly = getline; close(figure(1))

 % Ellipse fitting function from Matlab:
```

```
% https://uk.mathworks.com/matlabcentral/fileexchange/22684-ellipse-fit-direct-method
A = EllipseDirectFit(poly);% ax^2 + bxy + cy^2 +dx + ey + f = 0 algebraic solution
% Coordinates conversion function from Matlab:
%          https://uk.mathworks.com/matlabcentral/fileexchange/32105-conversion-of-conics-
parameters?focused=5192019&tab=function
[G,w] = AtoG(A);

figure(2); xCenter = G(1); yCenter = G(2); xRadius = G(3); yRadius = G(4); angle = 0;
theta = 0 : 0.01 : 2*pi; x = xRadius * cos(theta) + xCenter; y = yRadius * sin(theta) + yCenter;
imshow(RGB); drawnow; hold on; plot(x, y, 'LineWidth', 3); hold on; plot(xx,yy,'r','LineWidth',3)

 figure(3); imshow(RGB); hold on; plot(x, y, 'LineWidth', 3); hold on; title('Select intersection');
plot(xx,yy,'r','LineWidth',3); zoom on; waitfor(gcf, 'CurrentCharacter', char(13));
[px1,py1] = ginput(1);
[slope, intercept] = tangentEllipse(px1, py1, xCenter, yCenter, xRadius, yRadius, angle)
tang1 = slope.*xx+ intercept; hold on; title('Tangent Rapresentation'); plot(xx,tang1,'g','LineWidth',3)

m1 = slope; m2 = a; contact_angle_wet = abs(atand((m1-m2)/(1-m1*m2)))
contact_angle_not_wet = 180 - atand((m1-m2)/(1-m1*m2))
```

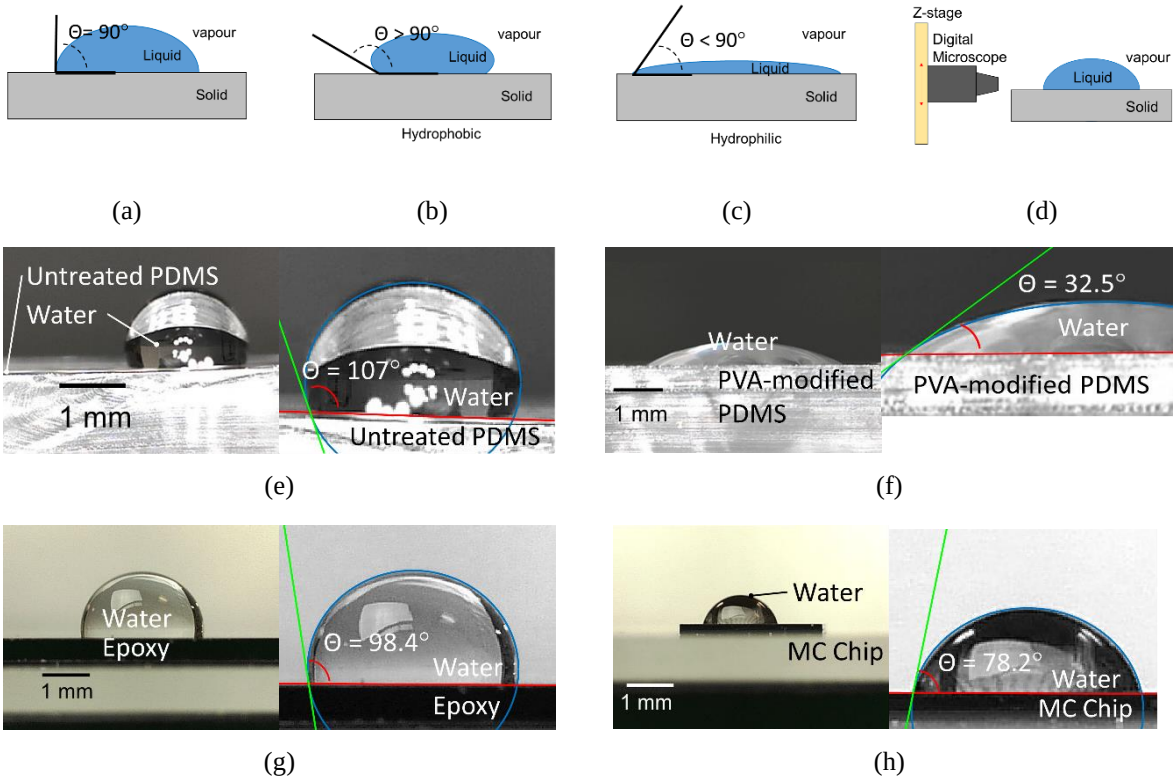

Figure E.1 (a) Contact angle definition. (b) Hydrophobic material. (c) Hydrophilic material. (d) Setup for contact angle measurements. (e) Contact angle measurement of untreated PDMS. (f) Contact angle measurement of PVA-modified PDMS. (g) Contact angle measurement of epoxy resin. (h) Contact angle measurement of the CMOS chip.

F. Matlab Modelling of a Passive Microfluidic Channel with Rectangular Section

This appendix illustrates a custom Matlab model for simulations of capillary laminar flow in a straight rectangular microfluidic channel. The model is based on theoretical equations for capillary pressure, fluidic resistance, and flow rate.

```
clear all
close all

tsim = 60;                  % Simulation time
N = 10000;                  % Simulation points
t = linspace (0,tsim, N);   % Create simulation time vector from 0 to tsim containing N samples
% Variables for graphical representation of the results
Lim1 = t*0+0.3;
Lim2 = t*0+0.3+(3.4-1.6)/2;
Lim3 = t*0+0.3+(3.4-1.6)/2+1.6;
Lim4 = t*0+4-0.3;
Lim5 = t*0+4;

% Sweeping variables
testing = [100*10^-6 150*10^-6 200*10^-6 250*10^-6 300*10^-6 350*10^-6]
testing2 = [0.073 0.050 0.045 0.056]
for g = 1:length(testing)
eta = 0.0024;               % Liquid properties (use blood) in [N][s][m]^-2
alpha =0.056;               % Liquid properties (use blood) in in [N][m]^-1
% Geometry of single channel with rectangular section
h = testing(g);             % Height of the microchannel
w = 300*10^-6;              % Width of the microchannel
Ltot = 4000*10^-6;          % Length of the microchannel

% Materials
tetab= 78.2;                % Measured contact angle material back (CMOS)
tetat= 107;                 % Measured contact angle material top (PDMS or PVA-coated PDMS)
tetas= 98.4;                % Measured contact angle material side (Epoxy)

% Calculations
R(g) = 12*eta*Ltot/((1-0.63*h/w)*h^3*w);      %Fluidic resistance [N][s][m]^-5
deltap = alpha*((abs(cosd(tetab))+abs(cosd(tetat)))/h + 2*abs(cosd(tetas))/w) % Capillary pressure [N][m]-2
chi = 12*eta/((1-0.63*h/w)*h^2);              % For convenience [N][m]-2[m]-2[s]
L(g,:) = 2*deltap/chi*sqrt(t);                % liquid advancement [m]
Q(g) = abs(deltap)/R(g);                      %Flow rate [m]^3[s]^-1
 end

% Representation of the results
figure()
for g = 1:length(testing)
plot(t,L(g,:)*10^6, 'LineWidth',3); hold on; ylabel('Liquid advancement (\mum)'); xlabel('Time (s)')
end
plot(t,Lim1*10^3,'k-', 'LineWidth',1); hold on; plot(t,Lim2*10^3,'k-', 'LineWidth',1); plot(t,Lim3*10^3, 'k-',
'LineWidth',1); plot(t,Lim4*10^3, 'k-', 'LineWidth',1); plot(t,Lim5*10^3, 'k-', 'LineWidth',1); axis('square')

figure(); yyaxis left; plot(Q,'o-','LineWidth',3); ylabel('Flow Rate (m^3 s^-^1)'); yyaxis right; plot(R,'o-',
'LineWidth',3); ylabel('Fluidic Resistance (N s m^-^5)'); axis('square')
```

In the simulation, the bottom material of the channel was assumed to be the CMOS chip, the sides consisted of epoxy resin, and the top was PDMS. The model thus considered measured contact angles of epoxy resin (θ_s = 98.4°), chip surface (θ_b = 78.2°), and untreated PDMS (θ_t = 107°) in the first instance. The Matlab-based model was first employed to simulate the behaviour of a single microchannel with several liquids. Simulation results proposed in Figure F.1(a),(b) model the behaviour of water, serum, plasma and blood flowing into a rectangular microchannel with w = 100 µm, h = 100 µm, and L = 4 mm. Water experiences an adequate capillary action, covering the entire sensing area in less than 50s. Simulated water flow rate is considerably higher than that of serum, plasma, and blood. On the other hand, filling times for serum, plasma and blood are too high for the requirements. Thus, additional optimisation is required.

A conservative approach was adopted, so the usage of whole blood was assumed for subsequent simulations. The effect of the variation of the microchannel width was investigated - see Figure F.1(c),(d). Simulations predict the behaviour of blood flowing into a rectangular microchannel with w in the range 100 – 400 µm, h = 100 µm, and L = 4 mm. Increasing the width of the microchannel increased the flow rate of the channel, consequently decreasing the filling time of the structure. Despite the lower filling time, this optimisation step alone is not enough for meeting the requirements of the capillary action. As previously mentioned, a maximum w = 300 µm can be adopted for manufacturing a 4-channel passive fluidic network. The effect of the variation of h when flowing blood was then investigated (see Figure F.1(e),(f)). Simulations studied the behaviour of blood flowing into a rectangular microchannel with w = 300 µm, h in the range 100 – 350 µm, and L = 4 mm. Increasing h led to a decrease in filling time. However, no improvement in the filling time was recorded with > 300 µm. The last parameter than was investigated was the wettability. PDMS contact angle can be modified by PVA deposition. The effect of the variation of the contact angle of the top PDMS when flowing blood in a microchannel with w = 300 µm and h = 300 µm was investigated (see Figure F.1(g),(h).). The worst condition for capillary action was θ_t = 90°. Filling time then decreases when increasing the difference $\Delta\theta$ with θ_{t0} = 90°, regardless of the hydrophilic or hydrophobic nature of the material. The fluidic resistance was not affected by the contact angle of the top PDMS lid.

The simulations highlighted that the contact angle of the top PDMS lid and the height of the microchannel are probably the most effective and convenient design parameters to be optimised – see Figure F.1 (i),(j).

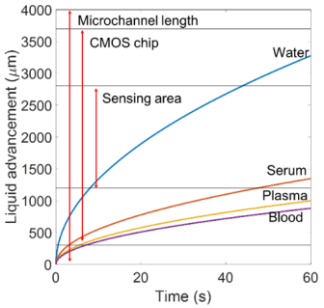

w=100 μm, h=100 μm, θs=98.4°, θt=107°, θb=78.2°, L=4 mm

(a)

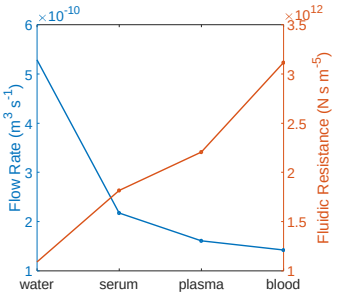

w=100 μm, h=100 μm, θs=98.4°, θt=107°, θb=78.2°, L=4 mm

(b)

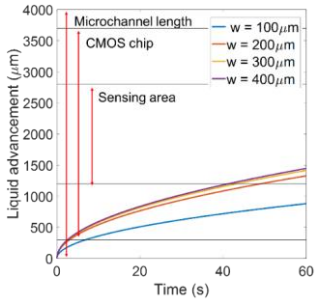

h=100 μm, θs=98.4°, θt=107°, θb=78.2°, L=4 mm

(c)

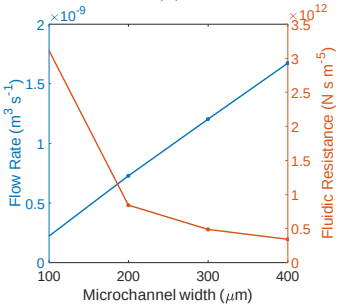

h=100 μm, θs=98.4°, θt=107°, θb=78.2°, L=4 mm

(d)

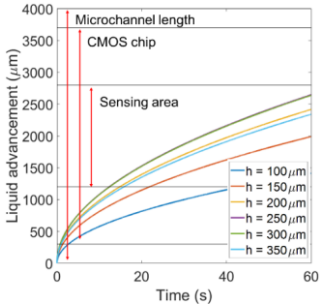

w=300 μm, θs=98.4°, θt=107°, θb=78.2°, L=4 mm

(e)

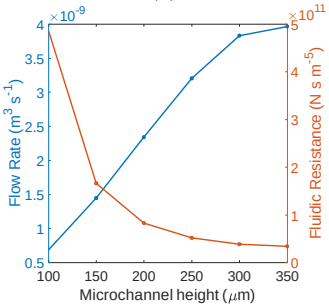

w=300 μm, θs=98.4°, θt=107°, θb=78.2°, L=4 mm

(f)

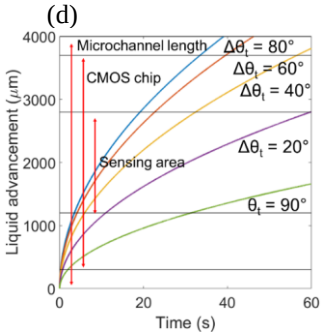

w=300 μm, h=300 μm, θs=98.4°, θb=78.2°, L=4 mm

(g)

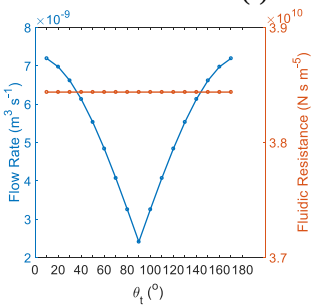

w=300 μm, h=300 μm, θs=98.4°, θb=78.2°, L=4 mm

(h)

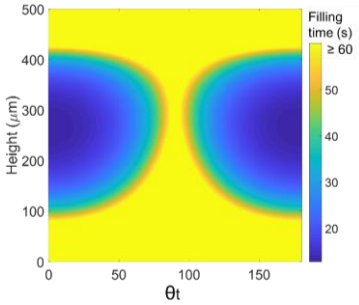

w = 300 μm, θs = 98.4°, θb = 78.2°, L = 4 mm

(i)

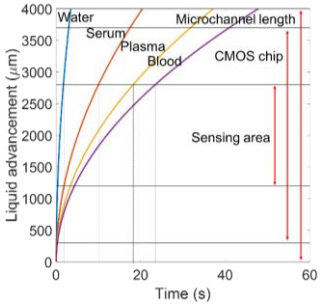

w = 300 μm, θs = 98.4°, θb = 78.2°, L = 4 mm

(j)

Figure F.1 (a) Liquid advancement vs time (vs specimens). (b) Initial flow rate and fluidic resistance vs. specimen. (c) Blood advancement vs time (vs w values). (d) Initial flow rate and fluidic resistance vs. channel width (blood). (e) Blood advancement vs time (vs h values). (f) Initial flow rate and fluidic resistance vs channel height (blood). (g) Blood advancement vs time (vs Δθt). (h) Initial flow rate and fluidic resistance vs. top contact angle (blood). (i) Time required for the sample to cover the sensing area (i.e. filling time) vs h values vs θ_t (blood). (j) Simulations of water, serum, plasma, and blood flowing into the optimised microstructure.

G. Wire Bonding and Packaging Protocol

This appendix illustrates the wire bonding and packaging protocol used for the fabrication of the cartridge described within this PhD project. Wire bonding was performed in the cleanroom facility of Glasgow Laboratory for Advanced Detector Development (School of Physics and Astronomy, University of Glasgow). The Hesse and Knipps Bondjet 710 was used for the wire bonding of the CMOS onto a ceramic chip package [331]. The CMOS chip was wire bonded onto a Ceramic Pin Grid Array (CPGA) package with 120 pins purchased from Europractice [293]. The overall size of the selected CPGA package was 3.3x3.3 cm, with an 8.3×8.3 mm cavity accommodating the structure to be wire-bonded.

The wire-bonding process consisted of three stages: preparation, programming, and bonding.

Preparation. The CMOS chip with the PDMS mould on top of it was glued in the cavity of the CPGA package using the EPO-TEK H74 epoxy from Epoxy Technology Inc [294]. The epoxy resin was mixed with the curing agent in a weight ratio 100:3. Approximately 20 µL of the prepared solution was placed in the centre of the CPGA cavity and spread, before placing the PDMS mould-topped chip onto the epoxy applying slight pressure. The epoxy was cured by baking the structure for 5 minutes at 150^{o}C.

Programming. The structure was secured in the centre of the stage of the Bondjet 710 with electrostatic discharge safe tape. The equipment was programmed to automatically perform the wire bonding, according to the wire-bonding diagram reported in Figure G.1(c). The first step in the programme was the definition of the source (CMOS chip) and destination (package) of the bonds. Then reference points, heights and all the parameters summarised in Table G.1 were set. After that, the bond paths were defined. 58 pads out of the available 64 were wire-bonded (test pads were not used). However, only 18 wire bonds are necessary for this PhD project. The other connections are needed for other functionalities of the chip not used in this work. Bond paths were defined via-software using graphical tools supported by the digital microscope. Configurations were saved and reused in similar wire-bonding jobs.

Bonding. The Bondjet 710 support different bonding modalities. Usually, the full-automatic mode has been adopted. However, whenever an error occurred, or a bond failed, it was necessary to manually re-define the position of the bond and re-bond the pad in manual mode.

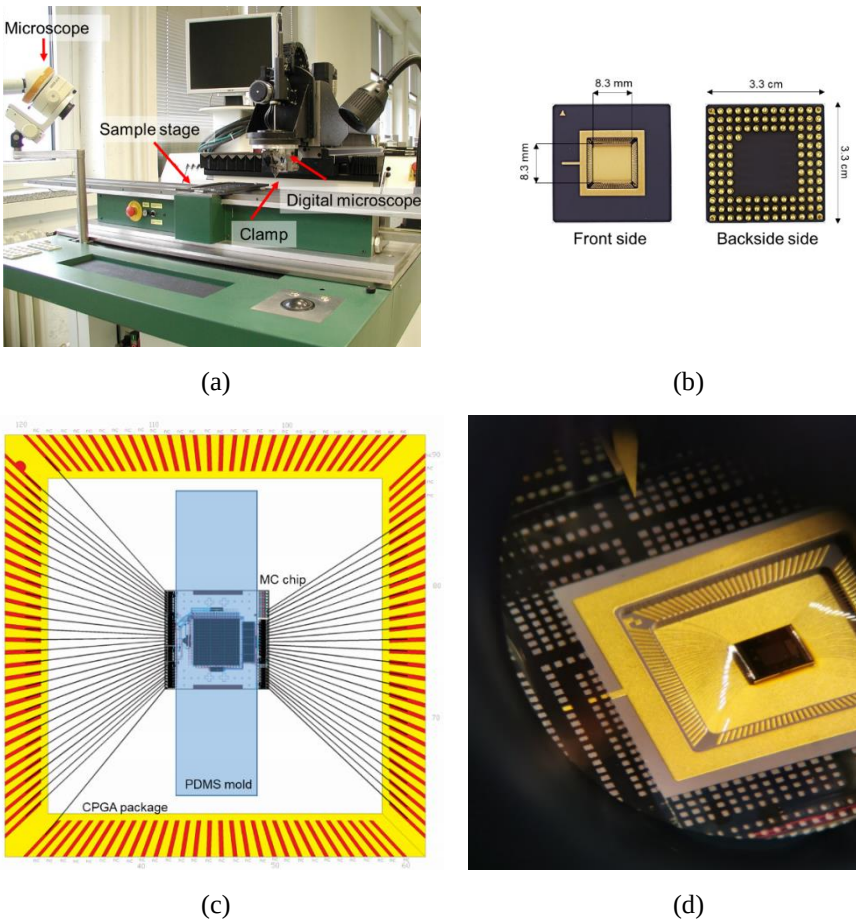

(a) (b)

(c) (d)

Figure G.1 (a) The Hesse and Knipps Bondjet 710 ultrasonic automatic wire bonder. Reproduced and modified from [332]. *(b) CPGA with 120 pins. (c) Bonding diagram. (d) Exemplative micrograph of a bonding process.*

Table G.1. Main parameters used for wire-bonding.

Parameter	**Value**
Ultrasonic power	30% (source), 20% (destination)
Bond force	24 cN (source), 20 cN (destination)
Start height	1000 µm
Loop height	250 µm
Start angle	45º
Bonding speed	20 %
Position accuracy	5 µm
Touch down area	100 µm
Safety area	80 µm (radius)
Reference Points	Source: (1) top left corner of the top left pad; (2) bottom right corner of the bottom right pad. Destination: (1) top left corner of the top left pad; (2) bottom right corner of the bottom right pad.
Bonding Height	Reset every bonding job

H. Biochemical Protocol for reagents preparation used for diluted serum experiments

This appendix illustrates the procedure adopted for the metabolomics experiments in diluted serum.

Prostate Cancer Metabolites. All the chemicals were purchased from Sigma Aldrich. Dehydrated human serum was also obtained from Sigma Aldrich and reconstituted with DI water following the recommended protocol. The reconstituted human serum was further diluted in DI water (volume ratio 1:10). All the reagents were prepared using 0.1 mM Tris HCl buffer (pH 8). For LAA assay, L-Tryptophan (grade ≥98%) and L-Arginine were used to create an LAA solution of 25 mM in buffer. The LAA solution was used to introduce a known concentration of LAA into the diluted human serum samples. For the first stage of the reaction, LAAOx (L-Amino Acid Oxidase from Crotalus adamanteus) was used to prepare a 4 U/mL enzymatic solution. LAAOx has different kinetics variable depending on the substrate under test. The average K_m for LAAOx over all the substrates is 8.5±7.4 mM [49]. For practical and economic reasons, it was not viable to prepare an LAA testing solution with all the available LAAs on the market. Thus, tryptophan and arginine have been selected because they exhibit low (4.2 mM) and high (12.5 mM) K_m, respectively [49]. Accordingly, the expected Km of LAAOx when reacting with the prepared LAA testing solution can be assumed to be 8.35 mM [49], when the two amino-acids are equally present in the solution. Therefore, this was a good approximation for a real-life scenario. For the glutamate assay, dehydrated glutamate (L-Glutamic acid monosodium salt monohydrate) was dissolved in the buffer to produce a 5 mM glutamate solution, which was used to introduce an additional known quantity of metabolite into the diluted serum samples. GlOx (L-Glutamate Oxidase from Streptomyces sp.) was prepared with a concentration of 4 U/mL to be used for the 1st reaction stage of the glutamate assay. For choline assay, dehydrated choline (Choline chloride ≥99%) was dissolved in the buffer for the preparation of a 2.5 mM solution to be used for increasing the concentration of choline in the diluted serum samples. For the 1st reaction stage of choline assay, ChOx (Choline Oxidase from Alcaligenes sp.) was dissolved in buffer with a concentration of 150 U/mL. For Sarcosine quantification, dehydrated sarcosine (sarcosine 98%) was used to prepare two different solutions in buffer with concentrations of 0.5 mM and 50 mM. Sarcosine solutions were used to introduce an additional known quantity of the metabolite into the serum samples to be tested. For the 1st stage of the assay, SaOx (Sarcosine Oxidase from Bacillus sp.) was dissolved in buffer to create a 200 U/mL enzymatic solution. For all the assays, o-dianisidine was selected for the

2nd stage of the assays. Dehydrated o-dianisidine was used to prepare a 41 mM solution in buffer. The enzyme HRP (Peroxidase from horseradish) was also used to catalyse the o-dianisidine oxidation. Dehydrated HRP was used to prepare two solutions with different concentrations of 65.5 U/mL and 300 U/mL. All the chemicals were aliquot and stored in appropriate refrigerator units in the laboratories of the MST group, Rankine Building, University of Glasgow.

Ischemic stroke metabolites. All the chemicals were purchased from Sigma Aldrich. Dehydrated human serum was also obtained from Sigma Aldrich and diluted with DI water (volume ratio of 1:10). Reagents were prepared using a 10 mM PBS (Phosphate-buffered saline) buffer (pH 7.4).

For lactate assay, lactate (Sodium L-lactate ~98%) was used to create a lactate solution of 10 mM in buffer, which was used to introduce a known concentration of the analyte into the diluted human serum samples. For the first stage of the reaction, LaOx (Lactate Oxidase from Aerococcus viridans) was used to prepare a 4 U/mL enzymatic solution.

For creatinine assay, creatinine (Creatinine anhydrous, ≥98%) was used to prepare a testing solution in buffer with 5 mM concentration. The first reaction stage of the reaction for creatinine quantification is composed of three enzymatic reactions. For the first reaction, CNN (Creatininase from Flavobacterium sp.) was used to prepare a 200 U/mL solution. For the second reaction, CTN (Creatinase from Actinobacillus sp) was used to develop a solution with enzyme concentration of 200 U/mL. For the third reaction stage, SaOx (Sarcosine Oxidase from Bacillus sp.) was dissolved in buffer to create a 150 U/mL enzymatic solution. All the chemicals were aliquot and stored in appropriate refrigerator units in the laboratories of the MST group, Rankine Building, University of Glasgow.

I. Biochemical Protocol for reagents preparation used for microchannel functionalisation

This appendix illustrates the protocol adopted for the preparation of enzymatic solutions for dry assays. Four different solutions were prepared to be dried/lyophilised into the microchannels:

1) Solution for negative control: a negative control solution was obtained by mixing 10 µL of DI water, 10 µL of 150 U/mL HRP, 5 µL of 44.5 mM phenol and 5 µL of 10.5 mM 4AAP. Instead of an enzyme solution, DI water was used to make it as a control microchannel.

2) Solution for choline assay: a solution containing all the reagents required for choline testing was obtained by mixing 10 µL of 150 U/mL ChOx, 10 µL of 150 U/mL HRP, 5 µL of 44.5 mM phenol and 5 µL of 10.5 mM 4AAP.
3) Solution for glutamate assay: a solution containing all the reagents required for glutamate testing was obtained by mixing 10 µL of 4 U/mL GlOx, 10 µL of 150 U/mL HRP, 5 µL of 44.5 mM phenol and 5 µL of 10.5 mM 4AAP.
4) Solution for LAA assay: a solution containing all the reagents required for LAA testing was obtained by mixing 10 µL of 10 U/mL LAAOx, 10 µL of 150 U/mL HRP, 5 µL of 44.5 mM phenol and 5 µL of 10.5 mM 4AAP.

For the immobilisation of these reagents into the microchannel, 1 µL of each solution was deposited in the respective microchannel according to the desired configuration. The deposition was achieved by manual pipetting. After the deposition of the solution, the cartridge was dried for 1 hour at room temperature in a vacuum chamber.

J. Enzyme printing protocol

This appendix illustrates the protocol adopted for the functionalisation of paper-strip with enzymatic solutions using a printing technique. Two different inks containing reagents for the lactate assay and glucose assay were printed on the specific paper microfluidic channels using the Jetlab II printer. Reagents were purchased from Sigma Aldrich. The adopted patterns were straight line composed of 20 spots with 0.5 mm pitch. The stimulus waveform was a negative pulse, tuned for each printing job. The total volume of each printed enzymatic solution was approximately 2.5 µL. The ink solution for glucose testing was composed as follows: 190 µL 100 mM Triethanolamine buffer at pH 8, 30 µL 600 U/mL peroxidase, 160 µL 7.89 mM o-dianisidine, and 120 µL 8 U/mL glucose oxidase. The ink solution for lactate testing was composed as follows: 210 µL 100 mM Triethanolamine buffer at pH 8, 60 µL 600 U/mL peroxidase, 120 µL 7.89 mM o-dianisidine, and 100 µL 2 U/mL lactate oxidase.

L. Procedure for clinical sample collection

This appendix illustrates the protocol for clinical sample collection.

Control group. Ten samples of human plasma from healthy people were sourced by Cambridge Bioscience. Plasma samples of healthy people are herein referred to as 'non-PCa' and constituted the control group. Non-PCa donors were selected to be adult male subjects only. The average age of the non-PCa group was 34±10 years. The ethnicity of the group was diversified including, European, Asian, and African donors. Samples were already pre-screened for the most common infections, including HIV, syphilis, Hepatitis B, Hepatitis C, and all resulted negative. Approximately 10 mL of fresh blood samples were collected in various research clinical facilities in England, mixed with 10 mg of dipotassium ethylenediaminetetraacetic acid (K2EDTA) anticoagulant, centrifuged and the generated 4 mL of plasma samples were frozen at –80°. Frozen plasma samples were shipped under dry-ice. After collection, plasma samples were aliquoted in 200 µL vials and stored at –80°. No additional freeze and taw cycles were performed. A table listing details on the non-PCa group is reported below.

Prostate cancer group. Sixteen human plasma samples from people diagnosed with PCa were sourced from the Beatson Cancer Institute, Glasgow, UK, under ethical approval, with the collaboration with Dr Robert Jones and Prof Jeff Evans. Plasma samples from cancer patients herein are referred to as 'PCa' samples and constituted the cancer or PCa group. Donors were selected to be adults who had already been diagnosed with PCa. However, due to ethical reason, detailed information, such as age and ethnicity, about the samples was not available. General information about the therapeutic course of the treatment for the patients such as the use of drugs was available. All the patients were under similar standard therapy involving the administration of triptorelin (or similar), omeprazole/esomeprazole, and statins. Approximately 10 mL of blood samples were collected at the Beatson Cancer Institute, mixed with 10 mg of K2EDTA anticoagulant, centrifuged, and the resulting plasma samples were frozen at –80°C. Samples were collected from the Beatson Cancer Institute and transported to Institute of Infection Immunity and Inflammation (III), Glasgow Biomedical Research Centre, University of Glasgow, where most of the measurements were carried out in dry ice. Afterwards, plasma samples were aliquoted in 200 µL vials and stored at –80°C. No additional freeze and thaw cycles were performed except an initial thaw just before the testing. Samples were stored and tested in the same facilities as the non-PCa group.

Ischemic stroke group. Ten samples of human plasma from people diagnosed with ischemic stroke were sourced from the Queen Elizabeth University Hospital, Glasgow, UK, under ethical approval, thanks to the collaboration with Dr Samadhan B. Patil, lecturer in Medical Engineering at the University of York, and Prof Jessie Dawson, Professor of Stroke Medicine and Consultant Stroke Physician at The Queen Elizabeth Hospital, Glasgow. Donors were selected to be adults recently diagnosed with ischemic stroke. Due to ethical reasons, detailed information, such as age and ethnicity, related to patients were not available. The approximate available volume, for each sample, was 100 µL. Blood samples were collected from the West Glasgow Ambulatory Care Hospital, mixed with anticoagulant, centrifuged, and the resulting plasma samples were frozen at –80º. Samples were transported from West Glasgow Ambulatory Care Hospital in dry-ice. Afterwards, vials were stored into a –80º freezer. No additional freeze and taw cycle was performed except premeasurement thawing. Samples were stored and tested in the same facilities as the clinical cancer samples. Calibration samples (calibrators) were sourced from the Institute of Cardiovascular and Medical Sciences, University of Glasgow. Calibrators were used in diluted form.

Table L.1 General information of the control group.

Sample #	1	2	3	4	5	6	7	8	9	10	Average	Std
Collect. date	18/07/2019 12:12	18/07/2019 13:34	18/07/2019 11:51	18/07/2019 14:30	18/07/2019 11:44	18/07/2019 13:23	18/07/2019 14:09	18/07/2019 08:11	18/07/2019 12:22	18/07/2019 08:34	-	-
Blood Group	O RhD Pos	O RhD neg	A RhD neg	O RhD pos	O RhD pos	A RhD pos	A RhD pos	B RhD neg	0 RhD pos	A RhD pos	Various	-
Gender	Male	Male	Male	Male	Male	Male	Male	Male	Male	Male	Male	-
Male	32	22	36	45	20	53	27	29	29	40	33.3	9.8
Ethnicity	Asian	Brithis/Irish	Brithis/Irish	Brithis/Irish	Black	Brithis/Irish	Brithis/Irish	Black	Black	Brithis/Irish	Various	-
HIV 1&2, p24	Negative	Negative	Negative	Negative	Negative	Negative	Negative	Negative	Negative	Negative	Negative	-
HBsAg	Negative	Negative	Negative	Negative	Negative	Negative	Negative	Negative	Negative	Negative	Negative	-
HCV	Negative	Negative	Negative	Negative	Negative	Negative	Negative	Negative	Negative	Negative	Negative	-
Syphillis	Negative	Negative	Negative	Negative	Negative	Negative	Negative	Negative	Negative	Negative	Negative	-
WBC (1/L)	6.76E+09	5.04E+09	5.50E+09	5.20E+09	5.29E+09	5.88E+09	5.55E+09	2.44E+09	5.14E+09	5.13E+09	5.19E+09	1.04E+09
RBC (1/L)	4.82E+12	4.25E+12	5.12E+12	4.81E+12	5.45E+12	4.72E+12	4.92E+12	5.65E+12	4.78E+12	5.67E+12	5.019E+12	4.30E+11
HGB (g/L)	148	140	157	142	150	146	143	133	147	160	146.6	7.5
HCT (L/L)	0.425	0.394	0.453	0.422	0.452	0.422	0.425	0.417	0.425	0.482	0.4317	0.0
MCV (fL)	88.2	92.7	88.5	87.7	82.9	89.4	86.4	73.8	88.9	85	86.35	4.9
MCH (pg)	30.7	32.9	30.7	29.5	27.5	30.9	29.1	23.5	30.8	28.2	29.38	2.4
MCHC (g/L)	348	355	347	336	332	346	336	319	346	332	339.7	10.1
PLT (1/L)	3.32E+11	1.41E+11	2.45E+11	2.24E+11	2.9E+11	2.19E+11	2.24E+11	2.12E+11	2.28E+11	2.85E+11	2.4E+11	4.97E+10
RDW (%)	11.4	11.3	12.2	12.6	13.8	13	13.2	12.1	12.1	14.3	12.6	0.9
Neut (1/L)	3.29E+09	3.01E+09	2.88E+09	3.02E+09	2.33E+09	3.15E+09	3.62E+09	8.90E+08	2.69E+09	2.81E+09	2.77E+09	7.07E+08
Lymph (1/L)	2.73E+09	1.10E+09	1.69E+09	1.60E+09	2.09E+09	1.92E+09	1.31E+09	1.20E+09	1.73E+09	1.75E+09	1.71E+09	4.51E+08
Mono (1/L)	5.30E+08	5.20E+08	6.20E+08	4.00E+08	6.60E+08	5.20E+08	4.90E+08	2.70E+08	4.90E+08	4.10E+08	4.91E+08	1.06E+08
EO (1/L)	1.40E+08	3.80E+08	2.80E+08	1.70E+08	1.50E+08	2.40E+08	7.00E+07	5.00E+07	2.10E+08	1.20E+08	1.81E+08	9.47E+07
Baso (1/L)	7.00E+07	3.00E+07	3.00E+07	1.00E+07	6.00E+07	5.00E+07	6.00E+07	3.00E+07	2.00E+07	4.00E+07	4.00E+07	1.84E+07

M. PCA scores for classification

This appendix reports the dataset for prostate cancer clinical evaluation (after Principal Component Analysis – PCA).

Table M.1 PCA scores for prostate cancer samples.

Sample	PC 1 (88.33%)	PC 2 (7.56%)	PC 3 (4.11%)
1	1.696752	0.37309	-0.08331
2	1.737893	-0.39242	-0.02927
3	0.901266	-0.35921	0.295321
4	1.618211	0.021794	0.50435
5	1.640694	0.367556	-0.03393
6	1.58718	0.032493	0.024632
7	0.977501	-0.36137	0.142953
8	0.994047	0.268857	-0.00329
9	1.185934	-0.02453	-0.11917
10	1.129113	-0.19346	0.033888
11	1.448242	-0.68844	-0.29005
12	1.717073	0.973358	0.502618
13	2.350504	-0.09969	0.469352
14	2.381458	-0.55839	0.98048
15	2.307302	0.185646	0.548527
16	3.053422	-1.14177	-0.61908
17	1.904028	0.520958	0.277342
18	1.480935	0.104297	0.291933
19	1.519043	-0.25816	-0.17274
20	2.271879	0.821612	-0.10654
21	3.237712	1.315546	-0.93454
22	1.575352	-0.49917	-0.30436
23	1.661074	-0.22037	-0.03577
24	1.668592	-0.30158	-0.46687
25	1.56468	-0.43482	-0.19961
26	1.407768	-0.41207	0.026069

Bibliography

[1] A. St John and C. P. Price, "Existing and Emerging Technologies for Point-of-Care Testing.," *Clin. Biochem. Rev.*, vol. 35, no. 3, pp. 155–67, Aug. 2014.

[2] V. Gubala, L. F. Harris, A. J. Ricco, M. X. Tan, and D. E. Williams, "Point of care diagnostics: Status and future," *Anal. Chem.*, vol. 84, no. 2, pp. 487–515, 2012, doi: 10.1021/ac2030199.

[3] S. L. Weiss *et al.*, "Delayed antimicrobial therapy increases mortality and organ dysfunction duration in pediatric sepsis," *Crit. Care Med.*, vol. 42, no. 11, pp. 2409–2417, 2014.

[4] M. Hand, "Access to timely and optimal care of patients with acute coronary syndromes - Community planning considerations: A report by the National Heart Attack Alert Program," *J. Thromb. Thrombolysis*, vol. 6, no. 1, pp. 19–46, 1998, doi: 10.1023/A:1008820104852.

[5] G. Giordano *et al.*, *Modelling the COVID-19 epidemic and implementation of population-wide interventions in Italy*. 2020.

[6] P. C. Walsh, "Operating characteristics of prostate-specific antigen in men with an initial PSA level of 3.0 Ng/Ml or lower: Commentary," *J. Urol.*, vol. 175, no. 2, pp. 562–563, 2006, doi: 10.1016/S0022-5347(05)00385-X.

[7] N. Gómez-Cebrián, A. Rojas-Benedicto, A. Albors-Vaquer, J. A. López-Guerrero, A. Pineda-Lucena, and L. Puchades-Carrasco, "Metabolomics contributions to the discovery of prostate cancer biomarkers," *Metabolites*, vol. 9, no. 3, Mar. 2019, doi: 10.3390/metabo9030048.

[8] X. Ma *et al.*, "The cost implications of prostate cancer screening in the Medicare population," *Cancer*, vol. 120, no. 1, pp. 96–102, 2014, doi: 10.1002/cncr.28373.

[9] A. Fridhammar, U. Axelsson, U. Persson, A. Bjartell, and C. A. K. Borrebaeck, "The Value of a New Diagnostic Test for Prostate Cancer: A Cost-Utility Analysis in Early Stage of Development," *PharmacoEconomics - Open*, 2020, doi: 10.1007/s41669-020-00226-7.

[10] R. D. Beger *et al.*, "Metabolomics enables precision medicine: 'A White Paper, Community Perspective,'" *Metabolomics*, vol. 12, no. 10, Oct. 2016, doi: 10.1007/s11306-016-1094-6.

[11] U. Roessner and J. Bowne, "What is metabolomics all about?," *Biotechniques*, vol. 46, no. 5 SPEC. ISSUE, pp. 363–365, 2009, doi: 10.2144/000113133.

[12] D. K. Trivedi, K. A. Hollywood, and R. Goodacre, "Metabolomics for the masses: The future of metabolomics in a personalized world," *New Horizons in Translational Medicine*, vol. 3, no. 6. Elsevier Ltd, pp. 294–305, Mar. 01, 2017, doi: 10.1016/j.nhtm.2017.06.001.

[13] "WHO | World Health Organization." https://www.who.int/ (accessed Jan. 17, 2020).

[14] D. S. Wishart, "Emerging applications of metabolomics in drug discovery and precision medicine," *Nat. Rev. Drug Discov.*, vol. 15, no. 7, pp. 473–484, 2016, doi: 10.1038/nrd.2016.32.

[15] F. R. Pinu, S. A. Goldansaz, and J. Jaine, "Translational metabolomics: Current challenges and future opportunities," *Metabolites*, vol. 9, no. 6, Jun. 2019, doi: 10.3390/metabo9060108.

[16] S. B. Patil, V. F. Annese, and D. R. S. Cumming, "Commercial Aspects of Biosensors for Diagnostics and Environmental Monitoring," in *Advances in Nanosensors for Biological and Environmental Analysis*, Elsevier, 2019, pp. 133–142.

[17] S. Publications, "Statistical Problems in Assessing Methods of Medical Diagnosis , with Special Reference to X-Ray Techniques Author (s): Jacob Yerushalmy Source : Public Health Reports (1896-1970), Vol . 62 , No . 40 , Tuberculosis Control Issue No . 20 Stable URL : h," vol. 62, no. 40, pp. 1432–1449, 2020.

[18] I. M. Thompson *et al.*, "Operating Characteristics of Prostate-Specific Antigen in Men With an Initial PSA Level of 3 . 0 ng / mL or Lower," vol. 78229, 2005.

[19] J. P. Goddard and J. L. Reymond, "Recent advances in enzyme assays," *Trends in Biotechnology*, vol. 22, no. 7. pp. 363–370, Jul. 2004, doi: 10.1016/j.tibtech.2004.04.005.

[20] J. Kimura, Y. Kawana, and T. Kuriyama, "An immobilized enzyme membrane fabrication method using an ink jet nozzle," *Biosensors*, vol. 4, no. 1, pp. 41–52, 1989, doi: 10.1016/0265-928X(89)80033-1.

[21] C. D. Chin, V. Linder, and S. K. Sia, "Commercialization of microfluidic point-of-care diagnostic devices," *Lab Chip*, vol. 12, no. 12, pp. 2118–2134, 2012, doi: 10.1039/c2lc21204h.

[22] "The Multicorder." https://gow.epsrc.ukri.org/NGBOViewGrant.aspx?GrantRef=EP/K021966/1 (accessed May 07, 2020).

[23] "Glasgow university scientists invent hand-held Star Trek gizmo that scans your skin to find illness at the touch of a button." https://www.thescottishsun.co.uk/news/3256042/glasgow-university-hand-held-device-scan-skin-illness/ (accessed May 07, 2020).

[24] M. F. (Martin F. . Chaplin and C. Bucke, *Enzyme technology*. Cambridge University Press, 1990.

[25] M. Mascini, “A Brief Story of Biosensor Technology,” in *Biotechnological Applications of Photosynthetic Proteins: Biochips, Biosensors and Biodevices*, Springer US, 2007, pp. 4–10.

[26] A. P. F. Turner, “Biosensors: Sense and sensibility,” *Chem. Soc. Rev.*, vol. 42, no. 8, pp. 3184–3196, Mar. 2013, doi: 10.1039/c3cs35528d.

[27] L. C. Clark and C. Lyons, “ELECTRODE SYSTEMS FOR CONTINUOUS MONITORING IN CARDIOVASCULAR SURGERY,” *Ann. N. Y. Acad. Sci.*, vol. 102, no. 1, pp. 29–45, 1962, doi: 10.1111/j.1749-6632.1962.tb13623.x.

[28] M. Staiano *et al.*, *Enzymes as Sensors*, 1st ed., vol. 589. Elsevier Inc., 2017.

[29] R. Monošík, M. Streďanský, and E. Šturdík, “Biosensors-classifi cation, characterization and new trends,” doi: 10.2478/v10188-012-0017-z.

[30] F. Gorjikhah *et al.*, “Improving ‘lab-on-a-chip’ techniques using biomedical nanotechnology: a review,” *Artificial Cells, Nanomedicine and Biotechnology*, vol. 44, no. 7. Taylor and Francis Ltd., pp. 1609–1614, Oct. 02, 2016, doi: 10.3109/21691401.2015.1129619.

[31] J. P. Conde *et al.*, “Lab-on-chip systems for integrated bioanalyses,” *Essays Biochem.*, vol. 60, no. 1, pp. 121–131, Jun. 2016, doi: 10.1042/EBC20150013.

[32] S. D’Auria and J. R. Lakowicz, “Enzyme fluorescence as a sensing tool: New perspectives in biotechnology,” *Curr. Opin. Biotechnol.*, vol. 12, no. 1, pp. 99–104, Feb. 2001, doi: 10.1016/S0958-1669(00)00164-6.

[33] A. Mulchandani, K. Rogers, and A. Mulchandani, “Principles of Enzyme Biosensors,” in *Enzyme and Microbial Biosensors*, Humana Press, 2003, pp. 3–14.

[34] P. D. Boyer *et al.*, *The Enzymes*. Academic Press, 1970.

[35] E. Fischer, “Einfluss der Configuration auf die Wirkung der Enzyme. II,” *Berichte der Dtsch. Chem. Gesellschaft*, vol. 27, no. 3, pp. 3479–3483, Oct. 1894, doi: 10.1002/cber.189402703169.

[36] G. M. Cooper, *The cell : a molecular approach*. ASM Press, 2000.

[37] T. O. Tiffany, J. M. Jansen, C. A. Burtis, J. B. Overton, and C. D. Scott, “Enzymatic Kinetic Rate and End-Point Analyses of Substrate, by Use of a GeMSAEC Fast Analyzer,” *Clin. Chem.*, vol. 18, no. 8, 1972.

[38] P. Takhistov, “Biosensor technology for food processing, safety, and packaging,” in *Handbook of Food Science, Technology, and Engineering - 4 Volume Set*, CRC Press, 2005, pp. 2312–2331.

[39] Y. Song, Y. Y. Huang, X. Liu, X. Zhang, M. Ferrari, and L. Qin, “Point-of-care technologies for molecular diagnostics using a drop of blood,” *Trends Biotechnol.*, vol. 32, no. 3, pp. 132–139, 2014, doi: 10.1016/j.tibtech.2014.01.003.

[40] E. H. Yoo and S. Y. Lee, “Glucose biosensors: An overview of use in clinical practice,” *Sensors*, vol. 10, no. 5. pp. 4558–4576, May 2010, doi: 10.3390/s100504558.

[41] H. W. Yeh and H. W. Ai, “Development and Applications of Bioluminescent and Chemiluminescent Reporters and Biosensors,” *Annu. Rev. Anal. Chem.*, vol. 12, pp. 129–150, 2019, doi: 10.1146/annurev-anchem-061318-115027.

[42] J. W. Lichtman and J. Conchello, “Fluorescence microscopy,” vol. 2, no. 12, 2005, doi: 10.1038/NMETH817.

[43] O. Pashchenko, T. Shelby, T. Banerjee, and S. Santra, “A Comparison of Optical, Electrochemical, Magnetic, and Colorimetric Point-of-Care Biosensors for Infectious Disease Diagnosis,” *ACS Infectious Diseases*, vol. 4, no. 8. American Chemical Society, pp. 1162–1178, Aug. 10, 2018, doi: 10.1021/acsinfecdis.8b00023.

[44] W. Chen, S. Cai, Q. Q. Ren, W. Wen, and Y. Di Zhao, “Recent advances in electrochemical sensing for hydrogen peroxide: A review,” *Analyst*, vol. 137, no. 1. Royal Society of Chemistry, pp. 49–58, Jan. 07, 2012, doi: 10.1039/c1an15738h.

[45] C. Giagkoulovits *et al.*, “A 16 × 16 CMOS amperometric microelectrode array for Simultaneous Electrochemical Measurements,” *IEEE Trans. Circuits Syst. I Regul. Pap.*, vol. 65, no. 9, pp. 2821–2831, Sep. 2018, doi: 10.1109/TCSI.2018.2794502.

[46] J. K. Tung, K. Berglund, C.-A. Gutekunst, U. Hochgeschwender, and R. E. Gross, “Bioluminescence imaging in live cells and animals,” *Neurophotonics*, vol. 3, no. 02, p. 1, 2016, doi: 10.1117/1.nph.3.2.025001.

[47] F. Serra and E. M. Terentjev, “Nonlinear dynamics of absorption and photobleaching of dyes,” *J. Chem. Phys.*, vol. 128, no. 22, 2008, doi: 10.1063/1.2937455.

[48] G. C. Genshaw MA, “Optical bleaching in o-dianisidine glucose tests,” *Clin. Chem.*, vol. 19(10):122, 1973.

[49] “Enzyme Database - BRENDA.” https://www.brenda-enzymes.org/index.php (accessed Jan. 22, 2020).

[50] D. F. Swinehart, “The Beer-Lambert Law,” *J. Chem. Educ.*, vol. 39, no. 7, p. 333, Jul. 1962, doi:

10.1021/ed039p333.
[51] A. Dwevedi and A. Dwevedi, “Basics of Enzyme Immobilization,” in *Enzyme Immobilization*, Springer International Publishing, 2016, pp. 21–44.
[52] K. Nakagawa, A. Tamura, and C. Chaiya, “Preparation of proteolytic microreactors by freeze-drying immobilization,” *Chem. Eng. Sci.*, vol. 119, pp. 22–29, 2014, doi: 10.1016/j.ces.2014.07.054.
[53] A. Aksan, D. Irimia, X. He, and M. Toner, “Desiccation kinetics of biopreservation solutions in microchannels,” *J. Appl. Phys.*, vol. 99, no. 6, 2006, doi: 10.1063/1.2181280.
[54] John G. Day and Glyn N. Stacey, *Methods in molecular biology. Cryopreservation and freeze-drying protocols.*, 2nd ed., vol. 368. 2007.
[55] T. Garcia-Perez, S. G. Hong, J. Kim, and S. Ha, “Entrapping cross-linked glucose oxidase aggregates within a graphitized mesoporous carbon network for enzymatic biofuel cells,” *Enzyme Microb. Technol.*, vol. 90, pp. 26–34, Aug. 2016, doi: 10.1016/j.enzmictec.2016.04.010.
[56] S. Ghosh and C. H. Ahn, “Lyophilization of chemiluminescent substrate reagents for high-sensitive microchannel-based lateral flow assay (MLFA) in point-of-care (POC) diagnostic system,” *Analyst*, vol. 144, no. 6, pp. 2109–2119, Mar. 2019, doi: 10.1039/c8an01899e.
[57] N. Bhalla, P. Jolly, N. Formisano, and P. Estrela, “Introduction to biosensors,” *Essays Biochem.*, pp. 60–61, 2016, doi: 10.1042/EBC20150001.
[58] G. L. Long and J. D. Winefordner, “Limit of Detection: A Closer Look at the IUPAC Definition,” *Anal. Chem.*, vol. 55, no. 7, pp. 712A-724A, 1983, doi: 10.1021/ac00258a001.
[59] U. S. N. B. of Standards, *NBS Special Publication*, no. v. 1;v. 300. The Bureau, 1969.
[60] L. A. Currie’ and G. Svehla2, “INTERNATIONAL UNION OF PURE AND APPLIED CHEMISTRY ANALYTICAL CHEMISTRY DIVISION COMMISSION ON ANALYTICAL NOMENCLATURE* t NOMENCLATURE FOR THE PRESENTATION OF RESULTS OF CHEMICAL ANALYSIS,” 1994.
[61] K. Y. Mehta *et al.*, “Metabolomic biomarkers of pancreatic cancer: a meta-analysis study,” *Oncotarget*, vol. 8, no. 40, pp. 68899–68915, 2017, doi: 10.18632/oncotarget.20324.
[62] “Error Sum of Squares.” https://hlab.stanford.edu/brian/error_sum_of_squares.html (accessed Dec. 08, 2020).
[63] J. Benesty, J. Chen, Y. Huang, and I. Cohen, “Pearson Correlation Coefficient,” 2009, pp. 1–4.
[64] “Unmounted LEDs.” https://www.thorlabs.com/newgrouppage9.cfm?objectgroup_id=2814 (accessed Mar. 16, 2020).
[65] A. S. Sedra and K. C. Smith, “Microelectronic Circuits Revised Edition,” *Oxford Ser. Electr. Comput. Eng.*, p. 1392, 2007.
[66] S. Voinigescu, *High-frequency integrated circuits*. Cambridge University Press, 2013.
[67] G. E. Moore, “The role of fairchild in silicon technology in the early days of ‘Silicon Valley,’” *Proc. IEEE*, vol. 86, no. 1, pp. 53–62, 1998, doi: 10.1109/5.658759.
[68] R. J. (Robert J. Keyes, *Optical and infrared detectors*. Springer-Verlag, 1977.
[69] H. Photonics, “Si photodiodes.” https://www.hamamatsu-news.de/hamamatsu_optosemiconductor_handbook/14/ (accessed Oct. 28, 2020).
[70] O. Optoelectronics, “Photodiode Characteristics and Applications.” http://www.osioptoelectronics.com/application-notes/an-photodiode-parameters-characteristics.pdf (accessed Oct. 28, 2020).
[71] A. H., M. C-K., and V. P., “CMOS Photodetectors,” in *Photodiodes - World Activities in 2011*, InTech, 2011.
[72] R. A. Yotter and D. M. Wilson, “A review of photodetectors for sensing light-emitting reporters in biological systems,” *IEEE Sensors Journal*, vol. 3, no. 3. pp. 288–303, Jun. 2003, doi: 10.1109/JSEN.2003.814651.
[73] R. Hui, “Photodetectors,” *Introd. to Fiber-Optic Commun.*, pp. 125–154, 2020, doi: 10.1016/b978-0-12-805345-4.00004-4.
[74] and P. K. B. Deen, M. Jamal, *Silicon photonics: fundamentals and devices*, Vol. 44. J. .
[75] B. Van Zeghbroeck, *Principles of semiconductor devices*, 2004th ed. Colarado University.
[76] “Application Notes n4 - Modes of Operation - Photovoltaic vs. Photoconductive.” https://www.farnell.com/datasheets/2302133.pdf.
[77] B. Bahreyni, “Chapter 7 - Noise,” in *Fabrication and Design of Resonant Microdevices*, B. Bahreyni, Ed. Norwich, NY: William Andrew Publishing, 2009, pp. 129–141.
[78] A. S. Junhao Chu, *Device physics of narrow gap semiconductors*. Springer, 2010.
[79] R. F. Pires and V. D. B. Bonifácio, “J ournal of Materials NanoScience Photodiodes : Principles and recent advances,” vol. 6, no. 2, pp. 38–46, 2019.
[80] M. Bigas, E. Cabruja, J. Forest, and J. Salvi, “Review of CMOS image sensors,” 2005, doi:

10.1016/j.mejo.2005.07.002.
[81] S. A. Taylor, “CCD and CMOS Imaging Array Technologies : Technology Review - Technology Review -,” 1998.
[82] E. K. Bolton, et al., “Integrated CMOS photodetectors and signal processing for very low-level chemical sensing with the bioluminescent bioreporter integrated circuit,” *Sensors Actuators, B Chem.*, vol. 85, no. 1–2, pp. 179–185, Jun. 2002, doi: 10.1016/S0925-4005(02)00106-5.
[83] D. Sander, M. Dandin, H. Ji, N. Nelson, and P. Abshire, “Low-noise CMOS fluorescence sensor,” in *Proceedings - IEEE International Symposium on Circuits and Systems*, 2007, pp. 2007–2010, doi: 10.1109/iscas.2007.378431.
[84] S. B. Patil *et al.*, “An integrated portable system for single chip simultaneous measurement of multiple disease associated metabolites,” *Biosens. Bioelectron.*, vol. 122, no. August, pp. 88–94, 2018, doi: 10.1016/j.bios.2018.09.013.
[85] M. A. Al-Rawhani *et al.*, “Multimodal Integrated Sensor Platform for Rapid Biomarker Detection.,” *IEEE Trans. Biomed. Eng.*, Jun. 2019, doi: 10.1109/TBME.2019.2919192.
[86] C. Accarino *et al.*, “A 64×64 spad array for portable colorimetric sensing, fluorescence and x-ray imaging,” *IEEE Sens. J.*, vol. 19, no. 17, pp. 7319–7327, Sep. 2019, doi: 10.1109/JSEN.2019.2916424.
[87] W. Jiang, Y. Chalich, and M. J. Deen, “Sensors for positron emission tomography applications,” *Sensors (Switzerland)*, vol. 19, no. 22, 2019, doi: 10.3390/s19225019.
[88] N. Zurich, “CCD versus CMOS--has CCD imaging come to an end?,” 2001, Accessed: Jan. 17, 2020. [Online]. Available: http://citeseerx.ist.psu.edu/viewdoc/summary?doi=10.1.1.4.6048.
[89] D. Litwiller, “CCD vs. CMOS: Facts and Fiction. Phothonics Spectra,” 2001.
[90] N. Psychogios *et al.*, “The human serum metabolome,” *PLoS One*, vol. 6, no. 2, 2011, doi: 10.1371/journal.pone.0016957.
[91] M. Vailati-Riboni, V. Palombo, and J. J. Loor, “What Are Omics Sciences?,” in *Periparturient Diseases of Dairy Cows*, Cham: Springer International Publishing, 2017, pp. 1–7.
[92] A. K. Kosmides, K. Kamisoglu, S. E. Calvano, S. A. Corbett, and I. P. Androulakis, “Metabolomic fingerprinting: Challenges and opportunities,” *Crit. Rev. Biomed. Eng.*, vol. 41, no. 3, pp. 205–221, 2013, doi: 10.1615/CritRevBiomedEng.2013007736.
[93] D. J. Beale, A. V. Karpe, and W. Ahmed, “Beyond metabolomics: A review of multi-omics-based approaches,” in *Microbial Metabolomics: Applications in Clinical, Environmental, and Industrial Microbiology*, Springer International Publishing, 2016, pp. 289–312.
[94] J. L. Markley *et al.*, “The future of NMR-based metabolomics,” *Curr. Opin. Biotechnol.*, vol. 43, pp. 34–40, 2017, doi: 10.1016/j.copbio.2016.08.001.
[95] I. P. GEROTHANASSIS, A. TROGANIS, V. EXARCHOU, and K. BARBAROSSOU, “NUCLEAR MAGNETIC RESONANCE (NMR) SPECTROSCOPY: BASIC PRINCIPLES AND PHENOMENA, AND THEIR APPLICATIONS TO CHEMISTRY, BIOLOGY AND MEDICINE,” *Chem. Educ. Res. Pr.*, vol. 3, no. 2, pp. 229–252, 2002, doi: 10.1039/b2rp90018a.
[96] J. J. Pitt, “Principles and applications of liquid chromatography-mass spectrometry in clinical biochemistry.,” *Clin. Biochem. Rev.*, vol. 30, no. 1, pp. 19–34, Feb. 2009, Accessed: Jan. 20, 2020. [Online]. Available: http://www.ncbi.nlm.nih.gov/pubmed/19224008.
[97] J.-S. Kang, “Principles and Applications of LC-MS/MS for the Quantitative Bioanalysis of Analytes in Various Biological Samples,” *Tandem Mass Spectrom. - Appl. Princ.*, 2012, doi: 10.5772/32085.
[98] E. R. Perez, J. A. Knapp, C. K. Horn, S. L. Stillman, J. E. Evans, and D. P. Arfsten, “Comparison of LC-MS-MS and GC-MS analysis of benzodiazepine compounds included in the drug demand reduction urinalysis program,” *J. Anal. Toxicol.*, vol. 40, no. 3, pp. 201–207, Apr. 2016, doi: 10.1093/jat/bkv140.
[99] Cancer Research UK, “Cancer in the UK: Overview, Prevention, Early diagnosis, Treatment & Data,” pp. 1–20, 2018, [Online]. Available: stats.team@cancer.org.uk.
[100] R. Landy, F. Pesola, A. Castañón, and P. Sasieni, “Impact of cervical screening on cervical cancer mortality: Estimation using stage-specific results from a nested case-control study,” *Br. J. Cancer*, vol. 115, no. 9, pp. 1140–1146, Oct. 2016, doi: 10.1038/bjc.2016.290.
[101] S. Koo, L. J. Neilson, C. Von Wagner, and C. J. Rees, “The NHS bowel cancer screening program: Current perspectives on strategies for improvement,” *Risk Management and Healthcare Policy*, vol. 10. Dove Medical Press Ltd, pp. 177–187, Dec. 04, 2017, doi: 10.2147/RMHP.S109116.
[102] A. Zhang, H. Sun, G. Yan, P. Wang, Y. Han, and X. Wang, “Metabolomics in diagnosis and biomarker discovery of colorectal cancer,” *Cancer Lett.*, vol. 345, no. 1, pp. 17–20, Apr. 2014, doi: 10.1016/j.canlet.2013.11.011.
[103] B. Kalyanaraman, “Teaching the basics of cancer metabolism: Developing antitumor strategies by exploiting the differences between normal and cancer cell metabolism,” *Redox Biology*, vol. 12.

Elsevier B.V., pp. 833–842, Aug. 01, 2017, doi: 10.1016/j.redox.2017.04.018.

[104] J. Shen, L. Yan, S. Liu, C. B. Ambrosone, and H. Zhao, "Plasma metabolomic profiles in breast cancer patients and healthy controls: By race and tumor receptor subtypes," *Transl. Oncol.*, vol. 6, no. 6, pp. 757–765, 2013, doi: 10.1593/tlo.13619.

[105] T. Zhang *et al.*, "Discrimination between malignant and benign ovarian tumors by plasma metabolomic profiling using ultra performance liquid chromatography/mass spectrometry," *Clin. Chim. Acta*, vol. 413, no. 9–10, pp. 861–868, May 2012, doi: 10.1016/j.cca.2012.01.026.

[106] G. D. Dakubo, *Cancer Biomarkers in Body Fluids*. Springer International Publishing, 2017.

[107] A. B. Leichtle *et al.*, "Pancreatic carcinoma, pancreatitis, and healthy controls: Metabolite models in a three-class diagnostic dilemma," *Metabolomics*, vol. 9, no. 3, pp. 677–687, Jun. 2013, doi: 10.1007/s11306-012-0476-7.

[108] L. Wang *et al.*, "1H-NMR based metabonomic profiling of human esophageal cancer tissue," *Mol. Cancer*, vol. 12, no. 1, p. 25, Apr. 2013, doi: 10.1186/1476-4598-12-25.

[109] A. Vazquez, J. J. Kamphorst, E. K. Markert, Z. T. Schug, S. Tardito, and E. Gottlieb, "Cancer metabolism at a glance," *J. Cell Sci.*, vol. 129, no. 18, pp. 3367–3373, 2016, doi: 10.1242/jcs.181016.

[110] P. Jóźwiak, E. Forma, M. Bryś, and A. Krześlak, "O-GlcNAcylation and metabolic reprograming in cancer," *Frontiers in Endocrinology*, vol. 5, no. SEP. Frontiers Media S.A., 2014, doi: 10.3389/fendo.2014.00145.

[111] L. Vettore, R. L. Westbrook, and D. A. Tennant, "New aspects of amino acid metabolism in cancer," *British Journal of Cancer*. Springer Nature, 2019, doi: 10.1038/s41416-019-0620-5.

[112] T. B. Salisbury and S. Arthur, "The regulation and function of the L-type amino acid transporter 1 (LAT1) in cancer," *International Journal of Molecular Sciences*, vol. 19, no. 8. MDPI AG, Aug. 12, 2018, doi: 10.3390/ijms19082373.

[113] K. Glunde, M. F. Penet, L. Jiang, M. A. Jacobs, and Z. M. Bhujwalla, "Choline metabolism-based molecular diagnosis of cancer: An update," *Expert Review of Molecular Diagnostics*, vol. 15, no. 6. Expert Reviews Ltd., pp. 735–747, Jun. 01, 2015, doi: 10.1586/14737159.2015.1039515.

[114] U. E. Martinez-Outschoorn, M. Peiris-Pagés, R. G. Pestell, F. Sotgia, and M. P. Lisanti, "Cancer metabolism: A therapeutic perspective," *Nat. Rev. Clin. Oncol.*, vol. 14, no. 1, pp. 11–31, 2017, doi: 10.1038/nrclinonc.2016.60.

[115] S. R. V. Knott *et al.*, "Asparagine bioavailability governs metastasis in a model of breast cancer," *Nature*, vol. 554, no. 7692, pp. 378–381, Feb. 2018, doi: 10.1038/nature25465.

[116] O. Olivares, J. H. M. Däbritz, A. King, E. Gottlieb, and C. Halsey, "Research into cancer metabolomics: Towards a clinical metamorphosis," *Semin. Cell Dev. Biol.*, vol. 43, pp. 52–64, 2015, doi: 10.1016/j.semcdb.2015.09.008.

[117] C. Oakman *et al.*, "Identification of a serum-detectable metabolomic fingerprint potentially correlated with the presence of micrometastatic disease in early breast cancer patients at varying risks of disease relapse by traditional prognostic methods," *Ann. Oncol.*, vol. 22, no. 6, pp. 1295–1301, 2011, doi: 10.1093/annonc/mdq606.

[118] Y. Li, X. Song, X. Zhao, L. Zou, and G. Xu, "Serum metabolic profiling study of lung cancer using ultra high performance liquid chromatography/quadrupole time-of-flight mass spectrometry," *J. Chromatogr. B Anal. Technol. Biomed. Life Sci.*, vol. 966, pp. 147–153, Sep. 2014, doi: 10.1016/j.jchromb.2014.04.047.

[119] W. Lv and T. Yang, "Identification of possible biomarkers for breast cancer from free fatty acid profiles determined by GC-MS and multivariate statistical analysis," *Clin. Biochem.*, vol. 45, no. 1–2, pp. 127–133, Jan. 2012, doi: 10.1016/j.clinbiochem.2011.10.011.

[120] L. Tenori *et al.*, "Serum metabolomic profiles evaluated after surgery may identify patients with oestrogen receptor negative early breast cancer at increased risk of disease recurrence. Results from a retrospective study," *Mol. Oncol.*, vol. 9, no. 1, pp. 128–139, Jan. 2015, doi: 10.1016/j.molonc.2014.07.012.

[121] J. Budczies *et al.*, "Comparative metabolomics of estrogen receptor positive and estrogen receptor negative breast cancer: Alterations in glutamine and beta-alanine metabolism," *J. Proteomics*, vol. 94, pp. 279–288, Dec. 2013, doi: 10.1016/j.jprot.2013.10.002.

[122] N. Lefort *et al.*, "1H NMR metabolomics analysis of the effect of dichloroacetate and allopurinol on breast cancers," *J. Pharm. Biomed. Anal.*, vol. 93, pp. 77–85, 2014, doi: 10.1016/j.jpba.2013.08.017.

[123] A. S. Krall, S. Xu, T. G. Graeber, D. Braas, and H. R. Christofk, "Asparagine promotes cancer cell proliferation through use as an amino acid exchange factor," *Nat. Commun.*, vol. 7, pp. 1–13, Apr. 2016, doi: 10.1038/ncomms11457.

[124] H. Nam, B. C. Chung, Y. Kim, K. Y. Lee, and D. Lee, "Combining tissue transcriptomics and urine metabolomics for breast cancer biomarker identification," *Bioinformatics*, vol. 25, no. 23, pp. 3151–

3157, Sep. 2009, doi: 10.1093/bioinformatics/btp558.

[125] A. B. Leichtle *et al.*, "Serum amino acid profiles and their alterations in colorectal cancer," *Metabolomics*, vol. 8, no. 4, pp. 643–653, Aug. 2012, doi: 10.1007/s11306-011-0357-5.

[126] H. Wang, V. K. Tso, C. M. Slupsky, and R. N. Fedorak, "Metabolomics and detection of colorectal cancer in humans: A systematic review," *Future Oncology*, vol. 6, no. 9. pp. 1395–1406, Sep. 2010, doi: 10.2217/fon.10.107.

[127] Y. Qiu *et al.*, "Serum metabolite profiling of human colorectal cancer using GC-TOFMS and UPLC-QTOFMS," *J. Proteome Res.*, vol. 8, no. 10, pp. 4844–4850, 2009, doi: 10.1021/pr9004162.

[128] A. Huang, D. Fuchs, B. Widner, C. Glover, D. C. Henderson, and T. G. Allen-Mersh, "Tryptophan and quality of life in colorectal cancer," in *Advances in Experimental Medicine and Biology*, 2003, vol. 527, pp. 353–358, doi: 10.1007/978-1-4615-0135-0_39.

[129] S. A. Ritchie *et al.*, "Reduced levels of hydroxylated, polyunsaturated ultra long-chain fatty acids in the serum of colorectal cancer patients: Implications for early screening and detection," *BMC Med.*, vol. 8, Feb. 2010, doi: 10.1186/1741-7015-8-13.

[130] B. Jiménez *et al.*, "1H HR-MAS NMR spectroscopy of tumor-induced local metabolic 'field-effects' enables colorectal cancer staging and prognostication," *J. Proteome Res.*, vol. 12, no. 2, pp. 959–968, Feb. 2013, doi: 10.1021/pr3010106.

[131] K. Raina, K. Ravichandran, S. Rajamanickam, K. M. Huber, N. J. Serkova, and R. Agarwal, "Inositol hexaphosphate inhibits tumor growth, vascularity, and metabolism in TRAMP mice: A multiparametric magnetic resonance study," *Cancer Prev. Res.*, vol. 6, no. 1, pp. 40–50, Jan. 2013, doi: 10.1158/1940-6207.CAPR-12-0387.

[132] G. F. Giskeødegård *et al.*, "Spermine and Citrate as Metabolic Biomarkers for Assessing Prostate Cancer Aggressiveness," *PLoS One*, vol. 8, no. 4, Apr. 2013, doi: 10.1371/journal.pone.0062375.

[133] J. E. McDunn *et al.*, "Metabolomic signatures of aggressive prostate cancer," *Prostate*, vol. 73, no. 14, pp. 1547–1560, Oct. 2013, doi: 10.1002/pros.22704.

[134] O. F. Bathe *et al.*, "Feasibility of identifying pancreatic cancer based on serum metabolomics," *Cancer Epidemiol. Biomarkers Prev.*, vol. 20, no. 1, pp. 140–147, 2011, doi: 10.1158/1055-9965.EPI-10-0712.

[135] D. O. Yang, J. Xu, H. Huang, and Z. Chen, "Metabolomic profiling of serum from human pancreatic cancer patients Using 1 H NMR spectroscopy and principal component analysis," *Appl. Biochem. Biotechnol.*, vol. 165, no. 1, pp. 148–154, 2011, doi: 10.1007/s12010-011-9240-0.

[136] L. Zhang *et al.*, "Distinguishing pancreatic cancer from chronic pancreatitis and healthy individuals by 1H nuclear magnetic resonance-based metabonomic profiles," *Clin. Biochem.*, vol. 45, no. 13–14, pp. 1064–1069, Sep. 2012, doi: 10.1016/j.clinbiochem.2012.05.012.

[137] S. Chen *et al.*, "Pseudotargeted metabolomics method and its application in serum biomarker discovery for hepatocellular carcinoma based on ultra high-performance liquid chromatography/triple quadrupole mass spectrometry," *Anal. Chem.*, vol. 85, no. 17, pp. 8326–8333, 2013, doi: 10.1021/ac4016787.

[138] S. Urayama, W. Zou, K. Brooks, and V. Tolstikov, "Comprehensive mass spectrometry based metabolic profiling of blood plasma reveals potent discriminatory classifiers of pancreatic cancer," *Rapid Commun. Mass Spectrom.*, vol. 24, no. 5, pp. 613–620, Mar. 2010, doi: 10.1002/rcm.4420.

[139] J. F. Xiao *et al.*, "LC-MS based serum metabolomics for identification of hepatocellular carcinoma biomarkers in Egyptian cohort," *J. Proteome Res.*, vol. 11, no. 12, pp. 5914–5923, Dec. 2012, doi: 10.1021/pr300673x.

[140] S. A. Ritchie *et al.*, "Metabolic system alterations in pancreatic cancer patient serum: Potential for early detection," *BMC Cancer*, vol. 13, Sep. 2013, doi: 10.1186/1471-2407-13-416.

[141] P. Tripathi *et al.*, "Delineating metabolic signatures of head and neck squamous cell carcinoma: Phospholipase A2, a potential therapeutic target," *Int. J. Biochem. Cell Biol.*, vol. 44, no. 11, pp. 1852–1861, Nov. 2012, doi: 10.1016/j.biocel.2012.06.025.

[142] J. D. Clarke *et al.*, "Characterization of hepatocellular carcinoma related genes and metabolites in human nonalcoholic fatty liver disease," *Dig. Dis. Sci.*, vol. 59, no. 2, pp. 365–374, Feb. 2014, doi: 10.1007/s10620-013-2873-9.

[143] H. Wen *et al.*, "A new NMR-based metabolomics approach for the diagnosis of biliary tract cancer," *J. Hepatol.*, vol. 52, no. 2, pp. 228–233, Feb. 2010, doi: 10.1016/j.jhep.2009.11.002.

[144] X. H. He *et al.*, "Metabonomic studies of pancreatic cancer response to radiotherapy in a mouse xenograft model using magnetic resonance spectroscopy and principal components analysis," *World J. Gastroenterol.*, vol. 19, no. 26, pp. 4200–4208, Jul. 2013, doi: 10.3748/wjg.v19.i26.4200.

[145] W. Struck, D. Siluk, A. Yumba-Mpanga, M. Markuszewski, R. Kaliszan, and M. J. Markuszewski, "Liquid chromatography tandem mass spectrometry study of urinary nucleosides as potential cancer markers," *J. Chromatogr. A*, vol. 1283, pp. 122–131, Mar. 2013, doi: 10.1016/j.chroma.2013.01.111.

[146] J. V. Alberice *et al.*, "Searching for urine biomarkers of bladder cancer recurrence using a liquid

chromatography-mass spectrometry and capillary electrophoresis-mass spectrometry metabolomics approach," *J. Chromatogr. A*, vol. 1318, pp. 163–170, Nov. 2013, doi: 10.1016/j.chroma.2013.10.002.

[147] P. Tripathi *et al.*, "HR-MAS NMR tissue metabolomic signatures cross-validated by mass spectrometry distinguish bladder cancer from benign disease," *J. Proteome Res.*, vol. 12, no. 7, pp. 3519–3528, Jul. 2013, doi: 10.1021/pr4004135.

[148] J. Huang *et al.*, "Serum metabolomic profiling of prostate cancer risk in the prostate, lung, colorectal, and ovarian cancer screening trial," *Br. J. Cancer*, vol. 115, no. 9, pp. 1087–1095, Oct. 2016, doi: 10.1038/bjc.2016.305.

[149] M. Kdadra, S. Höckner, H. Leung, W. Kremer, and E. Schiffer, "Metabolomics biomarkers of prostate cancer: A systematic review," *Diagnostics*, vol. 9, no. 1, pp. 1–44, Feb. 2019, doi: 10.3390/diagnostics9010021.

[150] R. S. Kelly, M. G. V. Heiden, E. Giovannucci, and L. A. Mucci, "Metabolomic biomarkers of prostate cancer: Prediction, diagnosis, progression, prognosis, and recurrence," *Cancer Epidemiol. Biomarkers Prev.*, vol. 25, no. 6, pp. 887–906, Jun. 2016, doi: 10.1158/1055-9965.EPI-15-1223.

[151] G. F. Giskeødegård *et al.*, "Metabolic markers in blood can separate prostate cancer from benign prostatic hyperplasia," *Br. J. Cancer*, vol. 113, no. 12, pp. 1712–1719, Dec. 2015, doi: 10.1038/bjc.2015.411.

[152] M. Johansson *et al.*, "One-carbon metabolism and prostate cancer risk: Prospective investigation of seven circulating B vitamins and metabolites," *Cancer Epidemiol. Biomarkers Prev.*, vol. 18, no. 5, pp. 1538–1543, May 2009, doi: 10.1158/1055-9965.EPI-08-1193.

[153] C. Myers *et al.*, "Suramin: A novel growth factor antagonist with activity in hormone- refractory metastatic prostate cancer," *J. Clin. Oncol.*, vol. 10, no. 6, pp. 881–889, 1992, doi: 10.1200/JCO.1992.10.6.881.

[154] S. J. Weinstein, K. Mackrain, R. Z. Stolzenberg-Solomon, J. Selhub, J. Virtamo, and D. Albanes, "Serum creatinine and prostate cancer risk in a prospective study," *Cancer Epidemiol. Biomarkers Prev.*, vol. 18, no. 10, pp. 2643–2649, Oct. 2009, doi: 10.1158/1055-9965.EPI-09-0322.

[155] P. M. Quilty *et al.*, "A comparison of the palliative effects of strontium-89 and external beam radiotherapy in metastatic prostate cancer," *Radiother. Oncol.*, vol. 31, no. 1, pp. 33–40, 1994, doi: 10.1016/0167-8140(94)90411-1.

[156] B. J. Trock, "Application of metabolomics to prostate cancer," *Urologic Oncology: Seminars and Original Investigations*, vol. 29, no. 5. pp. 572–581, Sep. 2011, doi: 10.1016/j.urolonc.2011.08.002.

[157] A. Sreekumar *et al.*, "Metabolomic profiles delineate potential role for sarcosine in prostate cancer progression," *Nature*, vol. 457, no. 7231, pp. 910–914, Feb. 2009, doi: 10.1038/nature07762.

[158] E. Thysell *et al.*, "Metabolomic characterization of human prostate cancer bone metastases reveals increased levels of cholesterol," *PLoS One*, vol. 5, no. 12, 2010, doi: 10.1371/journal.pone.0014175.

[159] J. W. Locasale, "Serine, glycine and one-carbon units: Cancer metabolism in full circle," *Nature Reviews Cancer*, vol. 13, no. 8. pp. 572–583, Aug. 2013, doi: 10.1038/nrc3557.

[160] A. C. Ogilvie, et al., "Lactic Acidosis in Prostate Cancer: Consider the Warburg Effect Keywords Mutation · p53 mutations · PIK3CA mutations · PTEN mutations · IDH1 mutations · Prostate cancer · Lactic acidosis · Warburg effect · Metabolic reprogramming · Case report," *Case Rep Oncol*, vol. 10, pp. 1085–1091, 2017, doi: 10.1159/000485242.

[161] K. Fabyan, A. Holtzclaw, and J. Sherner, "PROSTATE LACTATE: A CASE OF SEVERE LACTIC ACIDOSIS WITH AN INTERESTING MECHANISM OF ACTION," *Chest*, vol. 156, no. 4, p. A2105, Oct. 2019, doi: 10.1016/j.chest.2019.08.2050.

[162] X. Zhang *et al.*, "Metabolic signatures of esophageal cancer: NMR-based metabolomics and UHPLC-based focused metabolomics of blood serum," *Biochim. Biophys. Acta - Mol. Basis Dis.*, vol. 1832, no. 8, pp. 1207–1216, Aug. 2013, doi: 10.1016/j.bbadis.2013.03.009.

[163] J. Zhang *et al.*, "Esophageal Cancer Metabolite Biomarkers Detected by LC-MS and NMR Methods," *PLoS One*, vol. 7, no. 1, p. e30181, Jan. 2012, doi: 10.1371/journal.pone.0030181.

[164] T. Wiggins, S. Kumar, S. R. Markar, S. Antonowicz, and G. B. Hanna, "Tyrosine, phenylalanine, and tryptophan in gastroesophageal malignancy: A systematic review," *Cancer Epidemiol. Biomarkers Prev.*, vol. 24, no. 1, pp. 32–38, Jan. 2015, doi: 10.1158/1055-9965.EPI-14-0980.

[165] Q. Y. *et al.*, "A distinct metabolic signature of human colorectal cancer with prognostic potential," *Clin. Cancer Res.*, vol. 20, no. 8, pp. 2136–2146, 2014, doi: 10.1158/1078-0432.CCR-13-1939 LK.

[166] K. Yonezawa *et al.*, "Serum and tissue metabolomics of head and neck cancer," *Cancer Genomics and Proteomics*, vol. 10, no. 5, pp. 233–238, 2013.

[167] T. Wen *et al.*, "Exploratory investigation of plasma metabolomics in human lung adenocarcinoma," *Mol. Biosyst.*, vol. 9, no. 9, pp. 2370–2378, 2013, doi: 10.1039/c3mb70138g.

[168] Y. Guo *et al.*, "Probing gender-specific lipid metabolites and diagnostic biomarkers for lung cancer

using Fourier transform ion cyclotron resonance mass spectrometry," *Clin. Chim. Acta*, vol. 414, pp. 135–141, Dec. 2012, doi: 10.1016/j.cca.2012.08.010.

[169] L. Gao, Z. Wen, C. Wu, T. Wen, and C. Ong, "Metabolic Profiling of Plasma from Benign and Malignant Pulmonary Nodules Patients Using Mass Spectrometry-Based Metabolomics," *Metabolites*, vol. 3, no. 3, pp. 539–551, Jul. 2013, doi: 10.3390/metabo3030539.

[170] M. Serizawa *et al.*, "Identification of metabolic signatures associated with erlotinib resistance of non-small cell lung cancer cells.," *Anticancer Res.*, vol. 34, no. 6, pp. 2779–87, Jun. 2014.

[171] A. P. J. Van Den Heuvel, J. Jing, R. F. Wooster, and K. E. Bachman, "Analysis of glutamine dependency in non-small cell lung cancer: GLS1 splice variant GAC is essential for cancer cell growth," *Cancer Biol. Ther.*, vol. 13, no. 12, pp. 1185–1194, Oct. 2012, doi: 10.4161/cbt.21348.

[172] S. Nakamizo *et al.*, "GC/MS-based metabolomic analysis of cerebrospinal fluid (CSF) from glioma patients," *J. Neurooncol.*, vol. 113, no. 1, pp. 65–74, May 2013, doi: 10.1007/s11060-013-1090-x.

[173] S. G. Musharraf, A. J. Siddiqui, T. Shamsi, M. I. Choudhary, and A. U. Rahman, "Serum metabonomics of acute leukemia using nuclear magnetic resonance spectroscopy," *Sci. Rep.*, vol. 6, Aug. 2016, doi: 10.1038/srep30693.

[174] D. A. MacIntyre *et al.*, "Serum metabolome analysis by 1H-NMR reveals differences between chronic lymphocytic leukaemia molecular subgroups," *Leukemia*, vol. 24, no. 4, pp. 788–797, 2010, doi: 10.1038/leu.2009.295.

[175] B. Tan *et al.*, "Metabonomics identifies serum metabolite markers of colorectal cancer," *J. Proteome Res.*, vol. 12, no. 6, pp. 3000–3009, 2013, doi: 10.1021/pr400337b.

[176] B. S. Li *et al.*, "The downregulation of asparagine synthetase expression can increase the sensitivity of cells resistant to L-asparaginase [13]," *Leukemia*, vol. 20, no. 12. Nature Publishing Group, pp. 2199–2201, 2006, doi: 10.1038/sj.leu.2404423.

[177] S. Holst *et al.*, "Investigations on aberrant glycosylation of glycosphingolipids in colorectal cancer tissues using liquid chromatography and matrix-assisted laser desorption time-of- flight mass spectrometry (MALDI-TOF-MS)," *Mol. Cell. Proteomics*, vol. 12, no. 11, pp. 3081–3093, Nov. 2013, doi: 10.1074/mcp.M113.030387.

[178] R. Etzioni *et al.*, "The case for early detection," *Nature Reviews Cancer*, vol. 3, no. 4. pp. 243–252, Apr. 2003, doi: 10.1038/nrc1041.

[179] S. O. Lilienfeld, G. Alliger, and K. Mitchell, "Why Integrity Testing Remains Controversial," *Am. Psychol.*, vol. 50, no. 6, pp. 457–458, 1995, doi: 10.1037/0003-066X.50.6.457.

[180] E. A. Struys, A. C. Heijboer, J. Van Moorselaar, C. Jakobs, and M. A. Blankenstein, "Serum sarcosine is not a marker for prostate cancer," *Annals of Clinical Biochemistry*, vol. 47, no. 3. p. 282, May 2010, doi: 10.1258/acb.2010.009270.

[181] A. R. Meyer and M. A. Gorin, "First point-of-care PSA test for prostate cancer detection," *Nat. Rev. Urol.*, vol. 16, no. 6, pp. 332–333, 2019, doi: 10.1038/s41585-019-0179-1.

[182] S. Koochekpour *et al.*, "Serum glutamate levels correlate with gleason score and glutamate blockade decreases proliferation, migration, and invasion and induces apoptosis in prostate cancer cells," *Clin. Cancer Res.*, vol. 18, no. 21, pp. 5888–5901, Nov. 2012, doi: 10.1158/1078-0432.CCR-12-1308.

[183] L. C. Soliman, Y. Hui, A. K. Hewavitharana, and D. D. Y. Chen, "Monitoring potential prostate cancer biomarkers in urine by capillary electrophoresis-tandem mass spectrometry," *J. Chromatogr. A*, vol. 1267, pp. 162–169, Dec. 2012, doi: 10.1016/j.chroma.2012.07.021.

[184] W. Johnson, O. Onuma, M. Owolabi, and S. Sachdev, "Stroke: A global response is needed," *Bulletin of the World Health Organization*, vol. 94, no. 9. World Health Organization, pp. 634A-635A, Sep. 01, 2016, doi: 10.2471/BLT.16.181636.

[185] R. W. McGarrah, S. B. Crown, G. F. Zhang, S. H. Shah, and C. B. Newgard, "Cardiovascular metabolomics," *Circulation Research*, vol. 122, no. 9. Lippincott Williams and Wilkins, pp. 1238–1258, 2018, doi: 10.1161/CIRCRESAHA.117.311002.

[186] S. M. Grundy and N. J. Stone, "2018 cholesterol clinical practice guidelines: Synopsis of the 2018 American Heart Association/American college of cardiology/ multisociety cholesterol guideline," *Annals of Internal Medicine*, vol. 170, no. 11. American College of Physicians, pp. 779–783, 2019, doi: 10.7326/M19-0365.

[187] C. Lazzeri, S. Valente, M. Chiostri, and G. F. Gensini, "Clinical significance of Lactate in acute cardiac patients," *World J. Cardiol.*, vol. 7, no. 8, p. 483, 2015, doi: 10.4330/wjc.v7.i8.483.

[188] V. Pucino, M. Bombardieri, C. Pitzalis, and C. Mauro, "Lactate at the crossroads of metabolism, inflammation, and autoimmunity," *Eur. J. Immunol.*, vol. 47, no. 1, pp. 14–21, Jan. 2017, doi: 10.1002/eji.201646477.

[189] E. Sidorov, D. K. Sanghera, and J. K. P. Vanamala, "Biomarker for ischemic stroke using metabolome: A clinician perspective," *J. Stroke*, vol. 21, no. 1, pp. 31–41, Jan. 2019, doi: 10.5853/jos.2018.03454.

[190] J. Bakker, M. W. N. Nijsten, and T. C. Jansen, "Clinical use of lactate monitoring in critically ill patients," *Ann. Intensive Care*, vol. 3, no. 1, pp. 1–8, 2013, doi: 10.1186/2110-5820-3-12.

[191] R. Cánovas, M. Cuartero, and G. A. Crespo, "Modern creatinine (Bio)sensing: Challenges of point-of-care platforms," *Biosens. Bioelectron.*, vol. 130, no. November 2018, pp. 110–124, 2019, doi: 10.1016/j.bios.2019.01.048.

[192] J. L. Griffin, H. Atherton, J. Shockcor, and L. Atzori, "Metabolomics as a tool for cardiac research," *Nature Reviews Cardiology*, vol. 8, no. 11. pp. 630–643, Nov. 2011, doi: 10.1038/nrcardio.2011.138.

[193] V. Chopra and K. A. Eagle, "PRACTITIONERS SECTION;Cardiac biomarkers in the diagnosis, prognosis and management of coronary artery disease: A primer for internists," *Indian J. Med. Sci.*, vol. 64, no. 12, pp. 564–576, Dec. 2010, doi: 10.4103/0019-5359.75934.

[194] A. A. Rasmiena, T. W. Ng, and P. J. Meikle, "Metabolomics and ischaemic heart disease," *Clin. Sci.*, vol. 124, no. 5, pp. 289–306, Mar. 2013, doi: 10.1042/CS20120268.

[195] V. Bodi, V. G. Marrachelli, O. Husser, F. J. Chorro, J. R. Viña, and D. Monleon, "Metabolomics in the diagnosis of acute myocardial ischemia," *J. Cardiovasc. Transl. Res.*, vol. 6, no. 5, pp. 808–815, Oct. 2013, doi: 10.1007/s12265-013-9505-9.

[196] Y. G. Y. Y.-G. Wang, Y. G. Y. Y.-G. Wang, T.-F. F. Ma, M. Li, and S.-L. L. Gu, "Dynamic metabolites profile of cerebral ischemia/reperfusion revealed by 1H NMR-based metabolomics contributes to potential biomarkers," *Int. J. Clin. Exp. Pathol.*, vol. 7, no. 7, pp. 4067–4075, 2014.

[197] P. P. Liu *et al.*, "Discovery of Metabolite Biomarkers for Acute Ischemic Stroke Progression," *J. Proteome Res.*, vol. 16, no. 2, pp. 773–779, Feb. 2017, doi: 10.1021/acs.jproteome.6b00779.

[198] E. Trushina and M. M. Mielke, "Recent advances in the application of metabolomics to Alzheimer's Disease," *Biochimica et Biophysica Acta - Molecular Basis of Disease*, vol. 1842, no. 8. Elsevier, pp. 1232–1239, 2014, doi: 10.1016/j.bbadis.2013.06.014.

[199] "Disposable paper-on-CMOS platform for real-time simultaneous detection of metabolites - Enlighten: Publications." https://eprints.gla.ac.uk/206483/ (accessed Jan. 20, 2020).

[200] B. Reddy *et al.*, "Point-of-care sensors for the management of sepsis," *Nature Biomedical Engineering*, vol. 2, no. 9. Nature Publishing Group, pp. 640–648, Sep. 01, 2018, doi: 10.1038/s41551-018-0288-9.

[201] M. Eckerle *et al.*, "Metabolomics as a Driver in Advancing Precision Medicine in Sepsis," *Pharmacotherapy*, vol. 37, no. 9, pp. 1023–1032, Sep. 2017, doi: 10.1002/phar.1974.

[202] B. Mickiewicz *et al.*, "Integration of metabolic and inflammatory mediator profiles as a potential prognostic approach for septic shock in the intensive care unit," *Crit. Care*, vol. 19, no. 1, pp. 1–12, Jan. 2015, doi: 10.1186/s13054-014-0729-0.

[203] S. M. Khan, A. Gumus, J. M. Nassar, and M. M. Hussain, "CMOS Enabled Microfluidic Systems for Healthcare Based Applications," *Adv. Mater.*, vol. 30, no. 16, pp. 1–26, 2018, doi: 10.1002/adma.201705759.

[204] G. M. Whitesides, "The origins and the future of microfluidics," *Nature*, vol. 442, no. 7101, pp. 368–373, 2006, doi: 10.1038/nature05058.

[205] L. Gervais, N. De Rooij, and E. Delamarche, "Microfluidic chips for point-of-care immunodiagnostics," *Adv. Mater.*, vol. 23, no. 24, 2011, doi: 10.1002/adma.201100464.

[206] P. Tabeling, *Introduction to microfluidics*. Oxford University Press, 2010.

[207] C. K. Dixit and A. Kaushik, *Micro uidics for Biologists*. 2016.

[208] H. Bruus, *Theoretical microfluidics*. Oxford University Press, 2008.

[209] J. Castillo-León, "Microfluidics and Lab-on-a-Chip Devices: History and Challenges," in *Lab-on-a-Chip Devices and Micro-Total Analysis Systems*, Cham: Springer International Publishing, 2015, pp. 1–15.

[210] V. Jokinen and S. Franssila, "Capillarity in microfluidic channels with hydrophilic and hydrophobic walls," *Microfluid. Nanofluidics*, vol. 5, no. 4, pp. 443–448, 2008, doi: 10.1007/s10404-008-0263-y.

[211] P. J. Ponce De Leon and L. F. Velásquez-Garcia, "Optimization of capillary flow through open-microchannel and open-micropillar arrays," *J. Phys. D. Appl. Phys.*, vol. 49, no. 5, 2016, doi: 10.1088/0022-3727/49/5/055501.

[212] E. Berthier, A. M. Dostie, U. N. Lee, J. Berthier, and A. B. Theberge, "Open Microfluidic Capillary Systems," *Analytical Chemistry*, vol. 91, no. 14. American Chemical Society, pp. 8739–8750, Jul. 01, 2019, doi: 10.1021/acs.analchem.9b01429.

[213] A. Olanrewaju, M. Beaugrand, M. Yafia, and D. Juncker, "Capillary microfluidics in microchannels: From microfluidic networks to capillaric circuits," *Lab Chip*, vol. 18, no. 16, pp. 2323–2347, 2018, doi: 10.1039/c8lc00458g.

[214] A. Kreider *et al.*, "Functionalization of PDMS modified and plasma activated two-component polyurethane coatings by surface attachment of enzymes," *Appl. Surf. Sci.*, vol. 273, pp. 562–569, 2013, doi: 10.1016/j.apsusc.2013.02.080.

[215] E. Fialová, K. Zdeňková, E. Jablonská, K. Demnerová, and J. Ovesná, "Digital polymerase chain reaction: Principle and applications," *Chem. List.*, vol. 113, no. 9, pp. 545–552, Sep. 2019, doi: 10.5772/intechopen.86491.

[216] B. Nagy, M. A. Al-Rawhani, B. C. Cheah, M. P. Barrett, and D. R. S. Cumming, "Immunoassay Multiplexing on a Complementary Metal Oxide Semiconductor Photodiode Array," *ACS Sensors*, vol. 3, no. 5, pp. 953–959, May 2018, doi: 10.1021/acssensors.7b00972.

[217] B. Hayes, C. Murphy, A. Crawley, and R. O'Kennedy, "Developments in Point-of-Care Diagnostic Technology for Cancer Detection," *Diagnostics*, vol. 8, no. 2, p. 39, Jun. 2018, doi: 10.3390/diagnostics8020039.

[218] Y. Uludag *et al.*, "An integrated lab-on-a-chip-based electrochemical biosensor for rapid and sensitive detection of cancer biomarkers," *Anal. Bioanal. Chem.*, vol. 408, no. 27, pp. 7775–7783, Nov. 2016, doi: 10.1007/s00216-016-9879-z.

[219] T. Zhang, Y. He, J. Wei, and L. Que, "Nanostructured optical microchips for cancer biomarker detection," *Biosens. Bioelectron.*, vol. 38, no. 1, pp. 382–388, Oct. 2012, doi: 10.1016/j.bios.2012.06.029.

[220] A. I. Barbosa, P. Gehlot, K. Sidapra, A. D. Edwards, and N. M. Reis, "Portable smartphone quantitation of prostate specific antigen (PSA) in a fluoropolymer microfluidic device," *Biosens. Bioelectron.*, vol. 70, pp. 5–14, Aug. 2015, doi: 10.1016/j.bios.2015.03.006.

[221] S. Sharma, J. Zapatero-Rodríguez, P. Estrela, and R. O'Kennedy, "Point-of-Care diagnostics in low resource settings: Present status and future role of microfluidics," *Biosensors*, vol. 5, no. 3. MDPI AG, pp. 577–601, 2015, doi: 10.3390/bios5030577.

[222] "United Kingdom | Sigma-Aldrich." https://www.sigmaaldrich.com/united-kingdom.html (accessed Jan. 31, 2020).

[223] C. S. Pundir, S. Lata, and V. Narwal, "Biosensors for determination of D and L- amino acids: A review," *Biosensors and Bioelectronics*, vol. 117. Elsevier Ltd, pp. 373–384, Oct. 15, 2018, doi: 10.1016/j.bios.2018.06.033.

[224] B. Hoeben, F. Gunneweg Bsc, and B. W. Hoeben Bsc, "A critical review on glutamate sensing," doi: 10.13140/RG.2.1.2450.7360.

[225] P. Rahimi and Y. Joseph, "Enzyme-based biosensors for choline analysis: A review," *TrAC - Trends Anal. Chem.*, vol. 110, pp. 367–374, 2019, doi: 10.1016/j.trac.2018.11.035.

[226] V. Yamkamon *et al.*, "Development of sarcosine quantification in urine based on enzyme-coupled colorimetric method for prostate cancer diagnosis," *EXCLI J.*, vol. 17, pp. 467–478, May 2018, doi: 10.17179/excli2018-1245.

[227] M. M. F. Choi, "Progress in enzyme-based biosensors using optical transducers," *Microchimica Acta*, vol. 148, no. 3–4. pp. 107–132, Dec. 2004, doi: 10.1007/s00604-004-0273-8.

[228] P. Fossati, L. Prencipe, and G. Berti, "Enzymic creatinine assay: a new colorimetric method based on hydrogen peroxide measurement.," *Clin. Chem.*, vol. 29, no. 8, pp. 1494–1496, Aug. 1983, doi: 10.1093/clinchem/29.8.1494.

[229] Y. H. Kwak *et al.*, "A simple and low-cost biofilm quantification method using LED and CMOS image sensor," *J. Microbiol. Methods*, vol. 107, pp. 150–156, 2014, doi: 10.1016/j.mimet.2014.10.004.

[230] Y. W. Chang, P. C. Yu, Y. T. Huang, and Y. S. Yang, "A CMOS-compatible optical biosensing system based on visible absorption spectroscopy," *IEEE Conf. Electron Devices Solid-State Circuits 2007, EDSSC 2007*, pp. 1099–1102, 2007, doi: 10.1109/EDSSC.2007.4450320.

[231] C. Dincer, R. Bruch, A. Kling, P. S. Dittrich, and G. A. Urban, "Multiplexed Point-of-Care Testing – xPOCT," *Trends Biotechnol.*, vol. 35, no. 8, pp. 728–742, 2017, doi: 10.1016/j.tibtech.2017.03.013.

[232] V. Srinivasan, V. Pamula, M. Pollack, and R. Fair, "A digital microfluidic biosensor for multianalyte detection," in *Proceedings of the IEEE Micro Electro Mechanical Systems (MEMS)*, 2003, pp. 327–330, doi: 10.1109/memsys.2003.1189752.

[233] D. Wang, C. Ha, C. B. Park, and Y. Joo, "Spectrophotometer on a focal-plane-array chip for the high-throughput analysis of enzymatic reaction," *Conf. Proc. - Lasers Electro-Optics Soc. Annu. Meet.*, vol. 1, pp. 19–20, 2003, doi: 10.1109/leos.2003.1251579.

[234] Y. T. Wu, C. E. Yang, C. H. Ko, Y. N. Wang, C. C. Liu, and L. M. Fu, "Microfluidic detection platform with integrated micro-spectrometer system," *Chem. Eng. J.*, vol. 393, no. February, p. 124700, 2020, doi: 10.1016/j.cej.2020.124700.

[235] J. Liu, Z. Geng, Z. Fan, J. Liu, and H. Chen, "Point-of-care testing based on smartphone: The current state-of-the-art (2017–2018)," *Biosens. Bioelectron.*, vol. 132, pp. 17–37, May 2019, doi: 10.1016/j.bios.2019.01.068.

[236] C. Fernández-Sánchez, C. J. McNeil, K. Rawson, O. Nilsson, H. Y. Leung, and V. Gnanapragasam, "One-step immunostrip test for the simultaneous detection of free and total prostate specific antigen in

serum," *J. Immunol. Methods*, vol. 307, no. 1–2, pp. 1–12, Dec. 2005, doi: 10.1016/j.jim.2005.08.014.
[237] L. Ekhlaspour *et al.*, "Comparative Accuracy of 17 Point-of-Care Glucose Meters," *J. Diabetes Sci. Technol.*, vol. 11, no. 3, pp. 558–566, 2017, doi: 10.1177/1932296816672237.
[238] "Abbott | Global Healthcare & Research." https://www.abbott.co.uk/ (accessed Jan. 20, 2020).
[239] "Ion Torrent | Thermo Fisher Scientific - UK." https://www.thermofisher.com/uk/en/home/brands/ion-torrent.html (accessed Jan. 30, 2020).
[240] "US8691509B2 - Multi-primer amplification method for barcoding of target nucleic acids - Google Patents." https://patents.google.com/patent/US8691509B2/en?q=~patent%2FUS20100291666A1 (accessed Jan. 17, 2020).
[241] V. Haag, "(12) United States Patent," 2017, doi: 10.1109/MEMSYS.
[242] C. Accarino *et al.*, "Noise characteristics with CMOS sensor array scaling," *Meas. J. Int. Meas. Confed.*, vol. 152, Feb. 2020, doi: 10.1016/j.measurement.2019.107325.
[243] C. Hu, M. A. Al-Rawhani, B. C. Cheah, S. Velugotla, and D. R. S. Cumming, "Hybrid Dual Mode Sensor for Simultaneous Detection of Two Serum Metabolites," *IEEE Sens. J.*, vol. 18, no. 2, pp. 484–493, Jan. 2018, doi: 10.1109/JSEN.2017.2774359.
[244] B. M. P. Brigham, W. H. Stein, and S. Moore, "THE CONCENTRATIONS OF CYSTEINE AND CYSTINE IN Phenyianlne ETyposine," pp. 1633–1638, 1960.
[245] M. J. Hirsch, J. H. Growdon, and R. J. Wurtman, "Relations between dietary choline or lecithin intake, serum choline levels, and various metabolic indices," *Metabolism*, vol. 27, no. 8, pp. 953–960, 1978, doi: 10.1016/0026-0495(78)90139-7.
[246] A. B. R. Garnotel and A. H. C. Arndt, "CASE REPORT A Young Adult with Sarcosinemia . No Benefit from Long Duration Treatment with Memantine," 2012, doi: 10.1007/8904.
[247] J. Bakker, "Increased blood lactate levels : a marker of ...?," no. June, pp. 1–10, 2003.
[248] K. D. EDWARDS and H. M. WHYTE, "Plasma creatinine level and creatinine clearance as tests of renal function," *Australas. Ann. Med.*, vol. 8, p. 218—224, Aug. 1959, doi: 10.1111/imj.1959.8.3.218.
[249] S. Natarajan, D. A. Chang-Yen, and B. K. Gale, "Large-area, high-aspect-ratio SU-8 molds for the fabrication of PDMS microfluidic devices," *J. Micromechanics Microengineering*, vol. 18, no. 4, 2008, doi: 10.1088/0960-1317/18/4/045021.
[250] V. F. Annese *et al.*, "The Multicorder: A Handheld Multimodal Metabolomics-on-CMOS Sensing Platform," in *Proceedings - 2019 8th International Workshop on Advances in Sensors and Interfaces, IWASI 2019*, 2019, doi: 10.1109/IWASI.2019.8791347.
[251] B. C. Cheah *et al.*, "An Integrated Circuit for Chip-Based Analysis of Enzyme Kinetics and Metabolite Quantification," *IEEE Trans. Biomed. Circuits Syst.*, vol. 10, no. 3, pp. 721–730, Jun. 2016, doi: 10.1109/TBCAS.2015.2487603.
[252] B. C. Cheah, "METABOLOMIC SENSING SYSTEM FOR PERSONALISED MEDICINE USING AN INTEGRATED CMOS SENSOR," no. July, 2016.
[253] M. Al-Rawhani, D. Cumming, D. Chitnis, and S. Collins, "Photocurrent dependent response of a SPAD biased by a charge pump," *Proc. - IEEE Int. Symp. Circuits Syst.*, pp. 789–792, 2011, doi: 10.1109/ISCAS.2011.5937684.
[254] "NUCLEO-F334R8 - STM32 Nucleo-64 development board with STM32F334R8 MCU, supports Arduino and ST morpho connectivity - STMicroelectronics." https://www.st.com/en/evaluation-tools/nucleo-f334r8.html (accessed Feb. 05, 2020).
[255] ST, "STM32F303CC - Mainstream Mixed signals MCUs ARM Cortex-M4 core with DSP and FPU, 256 Kbytes Flash, 72 MHz CPU, MPU, CCM, 12-bit ADC 5 MSPS, PGA, comparators - STMicroelectronics." https://www.st.com/en/microcontrollers-microprocessors/stm32f303cc.html (accessed Nov. 25, 2020).
[256] "Mbed Compiler Workspace Management." https://ide.mbed.com/compiler/#nav:/; (accessed Feb. 05, 2020).
[257] P. Abgrall and A. M. Gué, "Lab-on-chip technologies: Making a microfluidic network and coupling it into a complete microsystem - A review," *J. Micromechanics Microengineering*, vol. 17, no. 5, 2007, doi: 10.1088/0960-1317/17/5/R01.
[258] B. C. Cheah and D. R. S. Cumming, "Metabolomics on CMOS for personalised medicine," in *CMOS Circuits for Biological Sensing and Processing*, Springer International Publishing, 2017, pp. 23–46.
[259] T. Datta-Chaudhuri, E. Smela, and P. A. Abshire, "System-on-Chip Considerations for Heterogeneous Integration of CMOS and Fluidic Bio-Interfaces," *IEEE Trans. Biomed. Circuits Syst.*, vol. 10, no. 6, pp. 1129–1142, Dec. 2016, doi: 10.1109/TBCAS.2016.2522402.
[260] B. K. Gale *et al.*, "A review of current methods in microfluidic device fabrication and future commercialization prospects," *Inventions*, vol. 3, no. 3, 2018, doi: 10.3390/inventions3030060.
[261] G. T. Roman and R. T. Kennedy, "Fully integrated microfluidic separations systems for biochemical

analysis," *J. Chromatogr. A*, vol. 1168, no. 1–2, pp. 170–188, 2007, doi: 10.1016/j.chroma.2007.06.010.

[262] F. Bragheri, R. Martínez Vázquez, and R. Osellame, "Microfluidics," in *Three-Dimensional Microfabrication Using Two-Photon Polymerization*, Elsevier, 2020, pp. 493–526.

[263] J. M. Bustjllo, R. T. Howe, and R. S. Muller, "Surface micromachining for microelectromechanical systems," *Proc. IEEE*, vol. 86, no. 8, pp. 1552–1573, 1998, doi: 10.1109/5.704260.

[264] Y.-K. Hsieh *et al.*, "Direct Micromachining of Microfluidic Channels on Biodegradable Materials Using Laser Ablation," *Polymers (Basel).*, vol. 9, no. 12, p. 242, Jun. 2017, doi: 10.3390/polym9070242.

[265] "Fluidic Factory 3D Printing System (Using Coc)." https://www.dolomite-microfluidics.com/product/fluidic-factory-3d-printer/ (accessed Jan. 23, 2020).

[266] R. Mukhopadhyay, "When PDMS isn't the best," *Anal. Chem.*, vol. 79, no. 9, pp. 3249–3253, 2007, doi: 10.1021/ac071903e.

[267] F. Rusmini, Z. Zhong, and J. Feijen, "Protein immobilization strategies for protein biochips," *Biomacromolecules*, vol. 8, no. 6, pp. 1775–1789, 2007, doi: 10.1021/bm061197b.

[268] Y. Asanomi, H. Yamaguchi, M. Miyazaki, and H. Maeda, "Enzyme-immobilized microfluidic process reactors," *Molecules*, vol. 16, no. 7, pp. 6041–6059, 2011, doi: 10.3390/molecules16076041.

[269] K. A. Heyries, C. A. Marquette, and L. J. Blum, "Straightforward protein immobilization on Sylgard 184 PDMS microarray surface," *Langmuir*, vol. 23, no. 8, pp. 4523–4527, 2007, doi: 10.1021/la070018o.

[270] C. A. Marquette and L. J. Blum, "Direct immobilization in poly(dimethylsiloxane) for DNA, protein and enzyme fluidic biochips," *Anal. Chim. Acta*, vol. 506, no. 2, pp. 127–132, 2004, doi: 10.1016/j.aca.2003.11.015.

[271] L. Betancor *et al.*, "Glutaraldehyde in Protein Immobilization," pp. 57–64, 2006, doi: 10.1007/978-1-59745-053-9_5.

[272] T. Honda, M. Miyazaki, H. Nakamura, and H. Maeda, "Immobilization of enzymes on a microchannel surface through cross-linking polymerization," *Chem. Commun.*, no. 40, pp. 5062–5064, 2005, doi: 10.1039/b510605b.

[273] R. A. Williams and H. W. Blanch, "Covalent immobilization of protein monolayers for biosensor applications," *Biosens. Bioelectron.*, vol. 9, no. 2, pp. 159–167, 1994, doi: 10.1016/0956-5663(94)80108-8.

[274] E. Ghafar-Zadeh, M. Sawan, and D. Therriault, "Novel direct-write CMOS-based laboratory-on-chip: Design, assembly and experimental results," *Sensors Actuators, A Phys.*, vol. 134, no. 1, pp. 27–36, 2007, doi: 10.1016/j.sna.2006.05.022.

[275] F. J. Blanco *et al.*, "Microfluidic-optical integrated CMOS compatible devices for label-free biochemical sensing," *J. Micromechanics Microengineering*, vol. 16, no. 5, pp. 1006–1016, 2006, doi: 10.1088/0960-1317/16/5/018.

[276] B. Zhang, Q. Dong, C. E. Korman, Z. Li, and M. E. Zaghloul, "Flexible packaging of solid-state integrated circuit chips with elastomeric microfluidics," *Sci. Rep.*, vol. 3, pp. 1–8, 2013, doi: 10.1038/srep01098.

[277] K. F. Brennan and A. S. Brown, *Theory of Modern Electronic Semiconductor Devices*. Hoboken, NJ, USA: John Wiley & Sons, Inc., 2002.

[278] Y. Huang and A. J. Mason, "Lab-on-CMOS integration of microfluidics and electrochemical sensors," *Lab Chip*, vol. 13, no. 19, pp. 3929–3934, 2013, doi: 10.1039/c3lc50437a.

[279] C. P. Hsu, P. C. Chen, and Y. L. Wang, "A novel packaging technology for disposable FET-based biosensors with microfluidic channels," *2017 IEEE 12th Int. Conf. Nano/Micro Eng. Mol. Syst. NEMS 2017*, pp. 375–378, 2017, doi: 10.1109/NEMS.2017.8017045.

[280] H. Lee, Y. Liu, D. Ham, and R. M. Westervelt, "Integrated cell manipulation system - CMOS/microfluidic hybrid," *Lab Chip*, vol. 7, no. 3, pp. 331–337, 2007, doi: 10.1039/b700373k.

[281] Y. Hwang and R. N. Candler, "Non-planar PDMS microfluidic channels and actuators: A review," *Lab Chip*, vol. 17, no. 23, pp. 3948–3959, 2017, doi: 10.1039/c7lc00523g.

[282] A. Wu, L. Wang, E. Jensen, R. Mathies, and B. Boser, "Modular integration of electronics and microfluidic systems using flexible printed circuit boards," *Lab Chip*, vol. 10, no. 4, pp. 519–521, 2010, doi: 10.1039/b922830f.

[283] D. Welch and J. B. Christen, "Seamless integration of CMOS and microfluidics using flip chip bonding," *J. Micromechanics Microengineering*, vol. 23, no. 3, 2013, doi: 10.1088/0960-1317/23/3/035009.

[284] M. Muluneh and D. Issadore, "A multi-scale PDMS fabrication strategy to bridge the size mismatch between integrated circuits and microfluidics," *Lab Chip*, vol. 14, no. 23, pp. 4552–4558, 2014, doi:

10.1039/c4lc00869c.
[285] T. Trantidou, Y. Elani, E. Parsons, and O. Ces, “Hydrophilic surface modification of pdms for droplet microfluidics using a simple, quick, and robust method via pva deposition,” *Microsystems Nanoeng.*, vol. 3, no. April 2016, 2017, doi: 10.1038/micronano.2016.91.
[286] “DDBST - DDBST GmbH.” http://www.ddbst.com/ (accessed Feb. 17, 2020).
[287] “Viscosity of Blood Plasma and Serum.” https://www.rheosense.com/application/viscosity-of-blood-plasma-and-serum (accessed Feb. 17, 2020).
[288] S. Lewin, “Blood Serum Surface Tension and its Potential,” *Br. J. Haematol.*, vol. 22, no. 5, pp. 561–566, May 1972, doi: 10.1111/j.1365-2141.1972.tb05702.x.
[289] E. Hrnčíř and J. Rosina1, “Surface Tension of Blood,” 1997.
[290] A. Syakur, Hermawan, and H. Sutanto, “Determination of hydrophobic contact angle of epoxy resin compound silicon rubber and silica,” in *International Conference on Electrical Engineering, Computer Science and Informatics (EECSI)*, 2016, vol. 3, no. 1, p. 012025, doi: 10.1088/1757-899X/190/1/012025.
[291] Microchem, “SU-8 3000 Permanent Epoxy,” *Prod. Datasheet*, vol. 20, 2000, doi: 10.1146/annurev.matsci.28.1.153.
[292] R. Seghir and S. Arscott, “Sensors and Actuators A : Physical Extended PDMS stiffness range for flexible systems,” *Sensors Actuators A. Phys.*, vol. 230, pp. 33–39, 2015, doi: 10.1016/j.sna.2015.04.011.
[293] “EUROPRACTICE | IC Service.” https://europractice-ic.com/ (accessed Feb. 10, 2020).
[294] “EPO-TEK ® H74,” 2017. Accessed: Feb. 10, 2020. [Online]. Available: www.epotek.com.
[295] “EPO-TEK ® 302-3M Technical Data Sheet For Reference Only Optically Transparent Epoxy,” 2018. Accessed: Feb. 10, 2020. [Online]. Available: www.epotek.com.
[296] Abbott, “Alere Afinion AS100 Analyzer,” 2018, [Online]. Available: https://www.alere.com/en/home/product-details/afinion-as100-analyzer.html.
[297] “Optical Interface - an overview | ScienceDirect Topics.” https://www.sciencedirect.com/topics/engineering/optical-interface (accessed Mar. 25, 2020).
[298] “Refractive index of (C2H6OSi)n (Polydimethylsiloxane, PDMS) - Querry-NIR.” https://refractiveindex.info/?shelf=organic&book=polydimethylsiloxane&page=Querry-NIR (accessed Mar. 25, 2020).
[299] G. M. Hale and M. R. Querry, “Optical Constants of Water in the 200-nm to 200-μm Wavelength Region,” *Appl. Opt.*, vol. 12, no. 3, p. 555, Mar. 1973, doi: 10.1364/ao.12.000555.
[300] *IUPAC Compendium of Chemical Terminology*. IUPAC, 2009.
[301] C. Rensch, “Creation of Small Microdrops,” *MicroFab Technol. Inc.*, pp. 1–51, 2006.
[302] D. Ioannou, W. Huda, and A. F. Laine, “Circle recognition through a 2D Hough Transform and radius histogramming,” *Image Vis. Comput.*, vol. 17, no. 1, pp. 15–26, Jan. 1999, doi: 10.1016/S0262-8856(98)00090-0.
[303] H. Liu, S. Lin, and Y. Qian, “Detecting Persons using Hough Circle Transform in Surveillance Video. DETECTING PERSONS USING HOUGH CIRCLE TRANSFORM IN SURVEILLANCE VIDEO,” 2010.
[304] I. Roy and M. N. Gupta, “Freeze-drying of proteins: some emerging concerns,” *Biotechnol. Appl. Biochem.*, vol. 39, no. 2, p. 165, 2004, doi: 10.1042/ba20030133.
[305] Astm, “Standard Guide for Accelerated Aging of Sterile Medical Device Packages 1,” *Astm F1980-02*, vol. 11, pp. 1–6, 2002, doi: 10.1520/D7102-10.Copyright.
[306] C. Hu *et al.*, “Disposable Paper-on-CMOS Platform for Real-time Simultaneous Detection of Metabolites,” *IEEE Trans. Biomed. Eng.*, pp. 1–1, 2020, doi: 10.1109/tbme.2019.2962239.
[307] X. Yang, O. Forouzan, T. P. Brown, and S. S. Shevkoplyas, “Integrated separation of blood plasma from whole blood for microfluidic paper-based analytical devices,” *Lab Chip*, vol. 12, no. 2, pp. 274–280, 2012, doi: 10.1039/c1lc20803a.
[308] T. Songjaroen, W. Dungchai, O. Chailapakul, C. S. Henry, and W. Laiwattanapaisal, “Blood separation on microfluidic paper-based analytical devices,” *Lab Chip*, vol. 12, no. 18, pp. 3392–3398, 2012, doi: 10.1039/c2lc21299d.
[309] J. A. Hanley and B. J. McNeil, “The Meaning and Use of the Area under a Receiver Operating Characteristic (ROC) Curve1.”
[310] I. T. Jollife and J. Cadima, “Principal component analysis: A review and recent developments,” *Philosophical Transactions of the Royal Society A: Mathematical, Physical and Engineering Sciences*, vol. 374, no. 2065. Royal Society of London, Apr. 13, 2016, doi: 10.1098/rsta.2015.0202.
[311] S. B. Kotsiantis, “Decision trees: A recent overview,” *Artificial Intelligence Review*, vol. 39, no. 4. Springer, pp. 261–283, Apr. 29, 2013, doi: 10.1007/s10462-011-9272-4.

[312] Q. Mai, "A review of discriminant analysis in high dimensions," *Wiley Interdisciplinary Reviews: Computational Statistics*, vol. 5, no. 3. John Wiley & Sons, Ltd, pp. 190–197, May 01, 2013, doi: 10.1002/wics.1257.

[313] D. De Venuto and G. Mezzina, "FPGA-embedded serial SVM classifier for neuromuscular disorders assessment," in *Proceedings - 2018 International Conference on Computational Science and Computational Intelligence, CSCI 2018*, Dec. 2018, pp. 1392–1397, doi: 10.1109/CSCI46756.2018.00269.

[314] A. Kataria, and M. D. Singh, "International Journal of Emerging Technology and Advanced Engineering A Review of Data Classification Using K-Nearest Neighbour Algorithm," 2008.

[315] A. Yadav and J. M. Johnson, "Fault detection and classification technique for HVDC transmission lines using KNN," 2016. Accessed: Mar. 10, 2020. [Online]. Available: https://www.researchgate.net/publication/304526301.

[316] T. Chen *et al.*, "Random forest in clinical metabolomics for phenotypic discrimination and biomarker selection," *Evidence-based Complement. Altern. Med.*, vol. 2013, 2013, doi: 10.1155/2013/298183.

[317] A. L. and M. Wiener, "Classification and Regression by randomForest. R News 2," vol. 3, no. December 2002, pp. 18–22, 2003.

[318] M. Kuhn, "Building predictive models in R using the caret package," *J. Stat. Softw.*, vol. 28, no. 5, pp. 1–26, 2008, doi: 10.18637/jss.v028.i05.

[319] E. D. Crawford and P. A. Abrahamsson, "PSA-based Screening for Prostate Cancer: How Does It Compare with Other Cancer Screening Tests?," *European Urology*, vol. 54, no. 2. pp. 262–273, Aug. 2008, doi: 10.1016/j.eururo.2008.05.032.

[320] Roche, "Cobas C 311 Analyzer," pp. 1–12, 2009, [Online]. Available: http://www.roche.hu/content/dam/roche_hungary/hu_HU/docs/cobas_c_311_en.pdf.

[321] B. Hall, D. D. Wong, W. D. Rawlinson, M. B. Tracy, and S. K. Tracy, "A validation study: Assessing the reliability of the hand held StatStripXPress lactate meter to test lactate in amniotic fluid," *BMC Res. Notes*, vol. 7, no. 1, p. 935, Dec. 2014, doi: 10.1186/1756-0500-7-935.

[322] J. X. J. Zhang and K. Hoshino, "Electrical Transducers," in *Molecular Sensors and Nanodevices*, Elsevier, 2014, pp. 169–232.

[323] C. Shivinder Singh, M. Abhishek Bhardawaj, L. Col Ratnesh Shukla, M. Trimbak Jhadav, S. Lt Cdr Anoop Sharma, and D. Basannar, "The handheld blood lactate analyser versus the blood gas based analyser for measurement of serum lactate and its prognostic significance in severe sepsis," *Med. J. Armed Forces India*, vol. 72, pp. 325–331, 2016, doi: 10.1016/j.mjafi.2016.05.007.

[324] J. M. Bonaventura, K. Sharpe, E. Knight, K. L. Fuller, R. K. Tanner, and C. J. Gore, "Reliability and accuracy of six hand-held blood lactate analysers," *J. Sport. Sci. Med.*, vol. 14, no. 1, pp. 203–214, 2014.

[325] V. F. Annese and D. De Venuto, "On-line shelf-life prediction in perishable goods chain through the integration of WSN technology with a 1st order kinetic model," in *2015 IEEE 15th International Conference on Environment and Electrical Engineering, EEEIC 2015 - Conference Proceedings*, 2015, doi: 10.1109/EEEIC.2015.7165232.

[326] V. F. Annese, G. E. Biccario, S. Cipriani, and D. De Venuto, "Organoleptic properties remote sensing and life-time prediction along the perishables goods supply-chain," in *Proceedings of the International Conference on Sensing Technology, ICST*, 2014, vol. 2014-Janua.

[327] G. Maltezos, J. Lee, A. Rajagopal, K. Scholten, E. Kartalov, and A. Scherer, "Microfluidic blood filtration device," *Biomed. Microdevices*, vol. 13, no. 1, pp. 143–146, 2011, doi: 10.1007/s10544-010-9479-1.

[328] K. Iwai, R. D. Sochol, and L. Lin, "Finger-powered, pressure-driven microfluidic pump," *Proc. IEEE Int. Conf. Micro Electro Mech. Syst.*, pp. 1131–1134, 2011, doi: 10.1109/MEMSYS.2011.5734629.

[329] Hans Stork (Texas Instrument), "Economies of CMOS Scaling," 2005. [Online]. Available: https://www.nist.gov/system/files/documents/pml/div683/conference/Stork_2005.pdf.

[330] "Multicorder DX – Multi-task Diagnostics." https://www.multicorderdx.co.uk/ (accessed Jan. 20, 2020).

[331] "University of Glasgow - Schools - School of Physics & Astronomy - Research - Research Groups - Particle Physics Experiment - Research Overview - GLADD - Infrastructure." https://www.gla.ac.uk/schools/physics/research/groups/particlephysicsexperiment/research/gladd/infrastructure/ (accessed Feb. 10, 2020).

[332] "Hesse & Knipps Bondjet 710 Wedge Bonder - TaraSemi.com." https://www.tarasemi.com/product/hesse-knipps-bondjet-710-wedge-bonder/ (accessed Feb. 10, 2020).